





Nieuwe eindigedifferentietechnieken voor het modelleren  
van elektromagnetische multischaalproblemen in het tijdsdomein

Novel Finite-Difference Time-Domain Techniques to Model  
Multiscale Electromagnetic Problems

Arne Van Londersele

Promotoren: prof. dr. ir. D. Vande Ginste, em. prof. dr. ir. D. De Zutter  
Proefschrift ingediend tot het behalen van de graad van  
Doctor in de ingenieurswetenschappen: toegepaste natuurkunde



UNIVERSITEIT  
GENT

Vakgroep Informatietechnologie  
Voorzitter: prof. dr. ir. B. Dhoedt  
Faculteit Ingenieurswetenschappen en Architectuur  
Academiejaar 2017 - 2018

ISBN 978-94-6355-124-3  
NUR 959  
Wettelijk depot: D/2018/10.500/42

# Novel Finite-Difference Time-Domain Techniques to Model Multiscale Electromagnetic Problems

Arne Van Londersele

Dissertation submitted to obtain the academic degree of  
Doctor of Engineering Physics

Publicly defended at Ghent University on June 4, 2018

## Supervisor:

prof. dr. ir. D. Vande Ginste  
Electromagnetics group  
Department of Information Technology  
Faculty of Engineering and Architecture  
Ghent University  
Technologiepark-Zwijnaarde 15  
B-9052 Ghent, Belgium  
<http://emweb.intec.ugent.be>

## Supervisor:

em. prof. dr. ir. D. De Zutter  
Electromagnetics group  
Department of Information Technology  
Faculty of Engineering and Architecture  
Ghent University  
Technologiepark-Zwijnaarde 15  
B-9052 Ghent, Belgium  
<http://emweb.intec.ugent.be>

## Members of the examining board:

prof. dr. ir. F. De Turck (chairman)  
prof. dr. ir. H. Rogier (secretary)  
prof. dr. ir. D. Vande Ginste (supervisor)  
em. prof. dr. ir. D. De Zutter (supervisor)  
prof. dr. ir. F. L. Teixeira  
prof. dr. ir. R. Remis  
dr. ir. J. Van Hese  
prof. dr. ir. G. Crevecoeur

Ghent University, Belgium  
Ghent University, Belgium  
Ghent University, Belgium  
Ghent University, Belgium  
The Ohio State University, United States  
TU Delft, Netherlands  
Keysight Technologies, Belgium  
Ghent University, Belgium



## Dankwoord

Net als de golven die ik simuleerde, ging mijn gemoed de voorbije vier jaar op en neer met elk nieuw “baanbrekend” idee en de vaak hieropvolgende teleurstelling dat er toch iets aan schort. De paar uitzonderingen hierop hebben geleid tot het boek dat nu voor u ligt. Het is een eerder theoretisch getinte bundeling van academisch werk dat werd gepubliceerd in verscheidene wetenschappelijke tijdschriften, maar dat wel degelijk ook onmiddellijke praktische toepassingen heeft zoals blijkt uit de interesse vanuit de industrie.

Ik ben mijn beide promotoren, Daniël en Dries, enorm dankbaar voor het vertrouwen en de kansen die ze mij de voorbije jaren geschonken hebben. Enerzijds heeft hun *hands-off approach* me de nodige vrijheid gegeven om zorgeloos mijn technische kennis te verbreden van net die deeldomeinen die me het meest interesseren, maar anderzijds stonden ze ook altijd — en dit mag vrij letterlijk genomen worden: ook tijdens avonden, weekends of zelfs vakantie — klaar met een antwoord, suggestie of interessante paper wanneer dat nodig was. Hun enthousiasme en passie voor hun werk is inspirerend.

Tijdens dit doctoraat heb ik het geluk gehad in het gezelschap van heel wat leuke collega's te mogen vertoeven, zowel tijdens als naast het werk. Simon, “Chef”, bedankt voor de ontelbare keren dat je me geholpen hebt met Linux, Python en C. Martijn en Michiel, bedankt om jullie elektromagnetisme- en talenkennis met mij te delen, maar ook voor de sporadische, ludieke “M&M” discussies à la ‘Is een Mars een koek of een chocoladereep?’. Thomas, dankzij u is het posteridee niet louter een idee gebleven. Bedankt om zoveel initiatief aan de dag te leggen om de kale gang van het iGent gebouw op te vrolijken met een prachtig staaltje *nerdiness*. Gert-Jan, het spijt me, maar je zal nooit een goede geest zijn. Laat het a.u.b. los. Nick, bedankt voor de dagelijkse portie soep en de leuke babbels. Quinten, je bent een man met veel kwaliteiten, maar ik hoop dat je tijdens je doctoraat wat strategischer te werk gaat dan bij het spelen van Game of Thrones. Giorgos, bedankt om gedurende lange tijd enige vorm van normaliteit aan de groep toe te voegen — op de periode na waarbij je er een uur over deed om op je werk te geraken, omdat je onderweg pokemons aan het vangen was — en voor de vele leuke momenten zoals het poolen en de 10 Miles. Irven, bedankt om toch wel voor enkele zeer memorabele gebeurtenissen te zorgen zoals dat epische kotfeest in onze studententijd waar zelfs Hollywoodfilms nog een puntje kunnen aan zuigen, of uw *dance-off* in Londen, of de prachtfoto in Dublin. *Kamil, you really are the kindest and hardest working PhD student I've ever met. I wish you succeed in achieving your ambitious goals. Marco, thanks for the nice time in Fajardo and for making my neighbors familiar with so many beautiful English curses. Mykola, thanks for hosting me and my friends so well in Munich, for mocking the Belgian Eurosong participants — every*

*single year — and for being such an exceptional person. Ook de andere collega's en ex-collega's zou ik graag oprecht willen bedanken voor de aangename werksfeer.*

*In the fall of 2017, I got the opportunity to collaborate with prof. Robert Lee and prof. Fernando Teixeira from the Electrosience Laboratory. I'm very grateful for our discussions about differential forms, finite elements, subgridding, some historical facts about ESL and Ansoft, and the differences between the academic and the entrepreneurial view. Also, I would like to thank Dr. Ryan Chilton for the Starbucks meeting in Dayton, which was of utmost importance for the joint letter.*

*During my stay in Ohio, I was lucky to share a huge office with a very motivated Spanish PhD student. Adrián, thank you for introducing me to your Spanish and Mexican friends, for making so many stupid jokes (“meh”), for crossing a graveyard together in total darkness, and most of all... for printing my documents. I would also like to express my gratitude to Yiqi. I could not imagine a more helpful roommate. Thank you, Yiqi, for telling such fascinating stories about China, for dining together, for driving to Cleveland and watch the opening game of the Cavs, for watching the Buckeye's football game, ... See you back in August, Yiqi!*

Dat ontspanning immens belangrijk is voor een creatieve job als deze, bewijst het feit dat het grote eureka-moment van dit doctoraat, namelijk de sluitsteen voor het wiskundig bewijs in Hoofdstuk 4, uit het niets plaatsvond starend naar het Vogezijsche sneeuwlandschap vanuit een skilift. Ik zou daarom ook een heleboel mensen die ogenschijnlijk niets met dit doctoraat te maken hebben, maar toch meer bijgedragen hebben dan ze zelf beseffen, willen bedanken: de “Ninovierters” (Daaf, Jorrit, Nico, Ojs, Pidgey, Svenno, Uvijn, Yen), de “burgies”, mijn huisgenoten, de carnavalisten, de padellers, de frisbeegroep, ... maar in het bijzonder vooral Arend, Berg, Nele en Marie. Het laatste anderhalf jaar was niet gemakkelijk en ik ben jullie enorm dankbaar voor al jullie steun. Arend, bedankt onder andere voor de leuke tijd aan Dampoort en voor uw absurde humor. Marie, bedankt voor de Kastart-momentjes en het ongegeneerd onnozel doen. Berg, de dag dat wij naast elkaar gaan zitten zijn op de achterste schoolbank heeft mijn leven veranderd. Je bent een vriend uit de duizend, nee uit de miljoenen. Ik twijfel er niet aan dat we nog een heleboel hoogtepunten in ons leven samen zullen meemaken.

Tot slot zou ik ook nog mijn familie willen bedanken. Papa, je bent een voorbeeld van doorzettingsvermogen en bescheidenheid. Je kocht me in mijn kindertijd geen PlayStation, maar toonde me hoe al lopend regen, wind, kou en milt te trotseren. Bedankt hiervoor. Mama, bedankt voor de vele liefde en warmte die je me altijd al gegeven hebt. Yentel, door de jaren heen voel ik dat we elkaar steeds beter en beter begrijpen en steeds meer en meer aan elkaar hebben. Ik ben een trotse grote broer. En *last but not least*... Nonkel Clement en tante Cécile, bedankt om altijd naschools zo goed gezorgd te hebben voor Yentel en mij. Jullie hebben indertijd, samen met papa en mama, het fundament gelegd voor dit doctoraat.

*Gent, juni 2018  
Arne Van Londersele*

*Just do it.*

DAN WIEDEN



# Contents

<b>Samenvatting</b>	<b>vii</b>
<b>Summary</b>	<b>xi</b>
<b>List of Abbreviations</b>	<b>xv</b>
<b>List of Symbols</b>	<b>xvii</b>
<b>List of Publications</b>	<b>xxi</b>
<b>Part I: Introductory Chapters</b>	<b>3</b>
<b>1 Introduction</b>	<b>5</b>
1.1 Background and Motivation . . . . .	5
1.2 Contributions . . . . .	7
1.3 Outline . . . . .	8
<b>2 Maxwell's Equations and Their Numerical Solution</b>	<b>11</b>
2.1 Maxwell's equations . . . . .	11
2.2 Full-wave solvers . . . . .	19
<b>3 The Finite-Difference Time-Domain Method</b>	<b>27</b>
3.1 Space discretization . . . . .	28
3.2 Time discretization . . . . .	30
3.3 Yee's finite-difference scheme . . . . .	32
3.4 Consequences of discretization . . . . .	45
3.5 Subgridding . . . . .	49
<b>Part II: Novel Contributions</b>	<b>59</b>
<b>4 Stability of Locally Implicit Methods</b>	<b>61</b>
4.1 Introduction . . . . .	62
4.2 Update equations . . . . .	63
4.3 Lyapunov stability . . . . .	65
4.4 Numerical validation: conservation of discrete energy . . . . .	77
4.5 Conclusion . . . . .	85
4.6 Addendum: CN implicitization of subgrids . . . . .	85

<b>5</b>	<b>3-D Cell-by-Cell Subgridding based on Finite Elements</b>	<b>93</b>
5.1	Introduction . . . . .	94
5.2	From finite elements to finite integrations . . . . .	94
5.3	Numerical example: ridge waveguide . . . . .	100
5.4	Conclusion . . . . .	102
<b>6</b>	<b>The Fully-Collocated Implicit FDTD Method</b>	<b>105</b>
6.1	Introduction . . . . .	106
6.2	Finite-element derivation . . . . .	106
6.3	Properties . . . . .	110
6.4	Numerical example: 2-D anisotropic slab . . . . .	113
<b>7</b>	<b>The Unidirectionally-Collocated HIE-FDTD Method</b>	<b>119</b>
7.1	Introduction . . . . .	120
7.2	Finite-element interpretation . . . . .	120
7.3	UCHIE/Yee hybridization . . . . .	123
7.4	Drude media and uniaxial PML . . . . .	125
7.5	Numerical stability . . . . .	131
7.6	Numerical dispersion . . . . .	134
7.7	Numerical examples . . . . .	136
<b>Part III:</b>	<b>Conclusion</b>	<b>155</b>
<b>8</b>	<b>Conclusion</b>	<b>157</b>
8.1	Comparative overview . . . . .	157
8.2	Overall conclusion . . . . .	159
8.3	Possible future work . . . . .	160

# Samenvatting

Computerondersteund ontwerp en computationeel elektromagnetisme laten elektrotechnische ingenieurs toe om hun ontwerpen te valideren en te optimaliseren in een vroeg stadium van het ontwerpsproces. Op die manier kan de totaalkost geminimaliseerd worden. Computerondersteund ontwerp en computationeel elektromagnetisme zijn quasi onmisbaar geworden voor ieder bedrijf dat elektronische componenten produceert en assembleert. De aanhoudende trend om steeds verder te miniaturiseren, om meer functionaliteiten aan te bieden en samen te brengen, gecombineerd met de nood aan hogere datadebiten en hoogfrequente signalen met meer bandbreedte, dwingt de ontwerpers van elektromagnetische simulatie-software om steeds betere en efficiëntere software op de markt te brengen. Enkel dan kunnen complexe ontwerpen nog binnen een aanvaardbare tijd en met blijvende nauwkeurigheid gesimuleerd worden.

Aangezien elektronische bouwstenen klein geworden zijn t.o.v. de golflengte, moet het golfgedrag van spanningen en stromen mee in rekening gebracht worden. Men spreekt dan van “full-wave” software waarmee veld distributies berekend worden uitgaande van de vergelijkingen van Maxwell zonder daarbij quasi-statische voorveronderstellingen te maken. Eén van de belangrijke “full-wave” technieken is de eindige-differentie-in-de-tijd of FDTD-methode. De FDTD-methode discretiseert de vierdimensionale ruimtetijd in een geschrinkt kubisch rooster en benadert de afgeleiden in de vergelijkingen van Maxwell door centrale differenties om op die manier een algoritme te bekomen waarbij elektrische en magnetische velden afwisselend geüpdatet worden in een haasje-over iteratieschema. Multischaal en multifysische problemen vormen een grote uitdaging voor alle “full-wave” softwarepakketten en voor de FDTD-methode in het bijzonder. Inderdaad, de steeds verder doorgedreven miniaturisering van transistoren en andere componenten hebben er voor gezorgd dat men bij de co-simulatie van IC's en hun verpakking te maken krijgt met verschillen van grootte-orde één miljoen in de typische afmetingen. Daarnaast zijn de opwarmingseffecten, de ladingdynamica en soms zelfs kwantumverschijnselen niet langer verwaarloosbaar.

De FDTD-methode heeft veel aantrekkelijke eigenschappen zoals rekentechnische eenvoud, lineaire complexiteit, massieve paralleliseerbaarheid, robuustheid, de mogelijkheid om niet-lineaire materialen te modelleren, breedband data-output, behoud van lading en energie, enzovoort. De FDTD-methode is dan ook de preferentiële methode om multifysische problemen te modelleren. Als het echter op multischaalproblemen aankomt, dan is de achilleshiel van de methode de ruimtelijke afhankelijkheid van de tijdstap, welbekend als de Courant stabiliteitslimiet. In ruwe benadering komt het er op neer dat een lokale roosterverfijning een globaal doorwegend effect heeft op de rekentijd. Indien de kleinste celdimensie uit het

rooster met een factor  $r$  verfijnd wordt, dan zal de totale rekentijd met minstens een factor  $r$  toenemen. Dit nadeel kan vermeden worden door over te stappen op impliciete tijdsintegratietechnieken die niet gebonden zijn aan een stabiliteitscriterium en die dus toelaten om het aantal iteraties in multischaalproblemen te reduceren. Dit gaat wel gepaard met een toename van de rekencomplexiteit bij iedere tijdstap.

Hierboven zijn al een aantal, voor dit proefschrift belangrijke, aspecten opgesomd: lokale roosterverfijning, impliciete methodes en stabiliteit. De meeste nieuwe onderzoeksbijdragen in dit proefschrift situeren zich binnen deze drie domeinen. Lokale roosterverfijning wordt gerealiseerd door het invoeren van niet-uniforme en geneste roosters. Het nesten van roosters is zeer delicaat zowel met betrekking tot de numerieke stabiliteit als met betrekking tot de nauwkeurigheid. Dit is te wijten aan het feit dat de hoeken en randoppervlakken van de interface tussen grof en fijn rooster vaak bronnen zijn van valse reflecties en valse ladingsofstapelingen. Het verbeteren van geneste roosters is reeds gedurende meer dan een kwarteeuw één van de meest uitdagende takken van het FDTD-onderzoek. Het “per cel” nesten van roosters dat in Hoofdstuk 5 voorgesteld wordt, is gebaseerd op goedgearchuteerde fysische inzichten. Dit leidt tot de gezochte nauwkeurighedsverbetering t.o.v. gekende technieken. Bovendien is de methode zeer flexibel en bijgevolg bruikbaar voor adaptieve roosterverfijning.

Impliciete methodes worden in Hoofdstuk 4 besproken als een valabele manier om de ruimtediscretisatie lokaal los te koppelen van de Courantlimiet. Dit houdt meteen in dat numerieke stabiliteit ook in dit hoofdstuk een belangrijke rol speelt. Om de efficiëntie van de voorgestelde impliciete technieken te verbeteren, worden deze technieken enkel daar waar nodig in het rooster toegepast. Bovendien worden ze ook anisotroop toegepast, t.t.z. enkel volgens de richting(en) die relevant zijn, bijvoorbeeld loodrecht op een gelaagd medium. Op die manier wordt het beste van twee werelden gecombineerd: “goedkope” expliciete berekeningen in het grof rooster en “dure” impliciete berekeningen in de fijne roosters om er voor te zorgen dat de tijdstap voldoende groot kan gekozen worden. Drie dergelijke hybride impliciete-expliciete (HIE) methodes werden ontwikkeld en geanalyseerd: de Newmark- $\beta$ , de Crank-Nicolson en de haasje-over alternerende-richting FDTD-methode.

Daarnaast is een belangrijk deel van dit doctoraat gewijd aan de hybridizatie van de conventionele expliciete FDTD-methode en de volledig samen-gelokalizeerde impliciete FDTD-methode (Hoofdstuk 6). Deze methode heeft een samenvallende ruimtetijddiscretisatie voor de zes veldcomponenten, heeft geen bovenlimiet voor de tijdstap en wordt gekenmerkt door een betere accuraatheid bij niet-uniforme roosters. Dergelijke samen-gelokalizeerde methodes zijn ook bijzonder geschikt voor de modellering van media beschreven door meer ingewikkelde constitutieve wetmatigheden zoals bijvoorbeeld anisotrope media. Bovendien wordt in Hoofdstuk 7 een efficiëntere unidirectioneel samen-gelokalizeerde HIE-methode in drie dimensies voorgesteld, die dan ook toegepast wordt op tweedimensionale proble-

men op een geneste wijze. Het bleek daarbij noodzakelijk om over een absorberende randvoorwaarde, de zogenaamde perfect aangepaste laag (PML), te beschikken. Deze PML wordt in Hoofdstuk 7 besproken samen met een hulpvergelijking voor dispersieve Drude materialen, noodzakelijk voor het modelleren van grafen in het microgolf- en terahertz-bereik.

In dit doctoraatsonderzoek is veel aandacht besteed aan de rigoureuze stabiliteitsanalyse van elk van de voorgestelde technieken. Uitgaande van de numerieke stabiliteitsproblemen eigen aan FDTD-technieken en van de gewenste efficiëntiewinst voor multischaalproblemen, werd bij het onderzoek gaandeweg meer en meer het “hou het eenvoudig” principe toegepast. Van zodra de dimensies van de matrices slecht schalen met het aantal onbekenden of indien de geheugenorganisatie te complex wordt, heeft het geen zin meer tijd aan de ontwikkeling van een vooropgestelde, nieuwe methode te besteden. Inderdaad, één van de belangrijkste troeven van de FDTD-methode is haar conceptuele en aritmetische eenvoud die aan de basis ligt van een aantal, hierboven reeds opgesomde, aantrekkelijke eigenschappen. Verder is gebleken dat eindige differenties op zichzelf niet volstaan om het effect van roosteranomalieën, zoals geneste roosters, te begrijpen. Bijgevolg werden in het onderzoek en in dit proefschrift veel inspanningen geleverd om de eindigedifferentiemethodes te complementeren met eindige-integratie- en eindige-elementenanalyses. Het belang van deze technieken is dubbel: enerzijds zijn ze toepasbaar op een willekeurig roostertype; anderzijds incorporeren ze ook de differentiaalgeometrische principes waaraan de vergelijkingen van Maxwell voldoen. Dit laatste heeft dan weer tot gevolg dat alle fysische behoudswetten ook na discretisatie gerespecteerd blijven.

Samenvattend kan gesteld worden dat de technieken die in dit proefschrift aan bod komen tot doel hebben FDTD-simulaties van multischaalproblemen te versnellen door het aantal ruimtelijke variabelen te reduceren mits het behoud van het oorspronkelijk aantal tijditaties. Dat gereduceerde aantal variabelen levert dan de extra computationele capaciteit op om, o.a., het huideffect in geleiders met eindige geleidbaarheid correct te modelleren door middel van volumediscretisatie i.p.v. de vaak gebruikte, maar benaderende oppervlakte-impedantierandvoorwaarden of randvoorwaarden gebaseerd op impedantienetwerkbenaderingen.



## Summary

Computer-aided design (CAD) and computational electromagnetic (CEM) tools allow electrical engineers to validate and optimize their designs at an early stage in the development process, minimizing the overall costs. They have become indispensable in virtually every industry that produces or closely deals with electrical components. The everlasting urge for more compact technology with more functionality, together with the need for higher data rates and high-frequency signals with more bandwidth, forces CEM software to reinvent itself continuously such that these complex configurations can still be simulated in a reasonable time span retaining sufficient accuracy.

As electronic devices have become small compared to the wavelength, the wave behavior of the current and voltage signals needs to be taken into account by dedicated software, the so-called full-wave solvers, which compute the field distribution starting from Maxwell's equations without quasi-static assumptions. One of the prevalent full-wave solutions is provided by the finite-difference time-domain (FDTD) method, which discretizes the four dimensions of spacetime on a staggered cubic lattice and approximates the derivatives occurring in Maxwell's equations by central differences as to render a marching-on-in-time scheme where electric and magnetic fields are alternately updated. The present-day challenges of full-wave solvers, and the FDTD method in particular, are focused on multiscale and multiphysics problems. Indeed, the sustained downscaling of transistors and other components have made the chip-package cosimulation in essence a complex problem where the minimum feature size is likely to differ from the package dimensions by a factor in the order of magnitude of millions. Besides, the effects from heating, charge dynamics and quantum tunneling, to name a few, are no longer negligible at the present-day small scales and small pitches.

The FDTD method has many favorable properties such as arithmetic simplicity, linear complexity, massive parallelizability, robustness, broadband output generation, nonlinear material modeling capability, conservation of discrete charge and energy, etcetera. For multiphysics problems, FDTD is undoubtedly the best suited approach. However, when it comes to the modeling of multiscale geometries, its Achilles' heel is its spatial dependency of the time step, known as the Courant stability limit. Roughly speaking, it implies that local refinements of the grid have a global effect on the CPU time because they invoke a larger number of time iterations, i.e., if the smallest cell edge occurring in the grid is refined by a factor  $r$ , the CPU time will rise by at least a factor  $r$ . This drawback can be circumvented by means of implicit time integration techniques that are not bounded to a stability criterion and, hence, are able to reduce the number of time iterations in multiscale problems, but at the expense of more complex operations per time step.

In the above paragraph, several important aspects of this dissertation are already put into perspective: local refinement, implicit methods and stability. The novel contributions of this doctoral thesis are related to each of these domains. The first one, local refinement of the spatial grid, is realized by means of nonuniform gridding and subgridding. The latter is a delicate operation, in particular with regard to the numerical stability, but also with respect to the accuracy because the edges and corners of the interface between main grid and subgrid are a common source of spurious reflections and spurious charges. As such, subgridding has been a compelling branch of FDTD research during the past quarter century. The cell-by-cell subgridding method proposed in Chapter 5 of this dissertation has a well-argued physical backbone, resulting in the desired accuracy boost, and shows the level of flexibility needed for adaptive mesh refinement.

The second aspect, implicit methods, is discussed in Chapter 4 as a viable way to locally decouple the spatial discretization from Courant's time step limit. Consequently, the third aspect, namely the numerical stability, readily comes into play in this chapter as well. In order to improve the efficiency of the proposed implicit techniques, they are only applied locally, there where needed, as well as anisotropically, along the preferred dimension(s). Hence, we combine "the best of both worlds": cheap explicit computations in the coarse part of the grid and expensive implicit computations in the dense part as to be able to tune the time step to our needs. Three such hybrid implicit-explicit (HIE) methods were developed and analysed: the Newmark- $\beta$ , the Crank-Nicolson and the leapfrog alternating-direction HIE-FDTD method.

Furthermore, an important part of this doctoral research has been devoted to a fourth domain: the hybridization of the conventional explicit FDTD scheme with the fully-collocated implicit (FCI) FDTD method, which has no time step upper bound and features improved accuracy for nonuniform gridding (Chapter 6). Collocated methods are attractive to model media exhibiting complex constitutive relations, e.g. anisotropic media. Besides, a more efficient unidirectionally-collocated hybrid implicit-explicit (UCHIE) FDTD method is developed in 3-D and hybridized with the conventional FDTD method in 2-D (Chapter 7). The UCHIE-FDTD method is extended with a uniaxial perfectly matched layer as to absorb outgoing waves in open-space simulations and with an auxiliary differential equation to model dispersive Drude media, such as graphene in the microwave and terahertz regime.

Throughout this doctoral research, much attention has been devoted to rigorous stability analysis for each of the proposed contributions. Partially because of the numerical stability issues that are typical for the FDTD method and partially because of the desired efficiency boost with regard to multiscale problems, the main thought throughout this doctoral research has become "keep it simple": once the occurring matrices do not scale well with the number of unknowns or the memory organization gets too complicated, the idea is aborted. After all, one of the main assets of the FDTD method is its conceptual and arithmetic simplicity, which

lies at the root of other strongly appreciated properties mentioned earlier. Also, since finite differences are often not sufficient to understand the behavior of grid anomalies such as subgridding, much effort has been put into finite-integration and finite-element analysis. Their main asset, apart from being applicable to any type of grid, is that they inherently comply to the differential-geometric principles that underpin Maxwell's equations, such that important physical conservation properties are preserved on the discrete level.

In summary, the novel techniques proposed in this dissertation aim to speed up multiscale FDTD simulations by reducing the number of spatial variables and, at the same time, avoid oversampling in time due to the Courant stability limit. This leverages extra computational capacity, which is then, for example, exploited to resolve the skin depth of thin conductive layers with finite conductivity by means of a standard volume discretization instead of a less accurate surface impedance or impedance network boundary condition.



# List of Abbreviations

ABC	Absorbing Boundary Condition
ADE	Auxiliary Differential Equation
ADI	Alternating-Direction Implicit
ADHIE	Alternating-Direction Hybrid Implicit-Explicit
AMR	Adaptive Mesh Refinement
BEM	Boundary Element Method
CAD	Computer-Aided Design
CEM	Computational Electromagnetics
CFA	Complex-Frequency Analysis
CFS	Complex-Frequency-Shifted
CN	Crank-Nicolson
CPU	Central Processing Unit
DC	Direct Current
DD	Domain Decomposition
DEC	Discrete Exterior Calculus
DFT	Discrete Fourier Transform
DGTD	Discontinuous-Galerkin Time-Domain
DtN	Dirichlet-to-Neumann
FCI	Fully-Collocated Implicit
FDFD	Finite-Difference Frequency-Domain
FDTD	Finite-Difference Time-Domain
FET	Field-Effect Transistor
FETD	Finite-Element Time-Domain
FEM	Finite-Element Method
FIT	Finite Integration Technique
FVTD	Finite-Volume Time-Domain
GTS	Global Time-Stepping
GO	Geometrical Optics
GPU	Graphics Processing Unit
HIE	Hybrid Implicit-Explicit
HSG	Huygens Subgridding
INBC	Impedance Network Boundary Condition
LEP	Linear Eigenvalue Problem
LOD	Locally One-Dimensional
LTS	Local Time-Stepping
MoM	Method of Moments
MOO	Marching-On-in-Order
MOT	Marching-On-in-Time
MLFMM	Multilevel Fast Multipole Method

N $\beta$ HIE	Newmark- $\beta$ Hybrid Implicit-Explicit
NTFF	Near-To-Far-Field
PEC	Perfect Electric Conductor
PBC	Periodic Boundary Condition
PO	Physical Optics
PMC	Perfect Magnetic Conductor
PML	Perfectly Matched Layer
PSTD	Pseudo-Spectral Time-Domain
QED	Quantum Electrodynamics
QEP	Quadratic Eigenvalue Problem
UCHIE	Unidirectionally-Collocated Hybrid Implicit-Explicit
UPML	Uniaxial PML
UTD	Uniform Theory of Diffraction
SE	Shielding Effectiveness
SG	Subgrid(ding)
SW	Scattering Width
TE	Transverse Electric
TFSF	Total-Field Scattered-Field
TM	Transverse Magnetic
TSV	Through-Silicon Via

# List of Symbols

$J$	Imaginary unit
$\dots^*$	Complex conjugate
$ \dots $	Modulus of a scalar also, $k$ -dimensional volume of a $k$ -dimensional manifold
$\text{Re}(\dots)$	Real part of a complex number
$\text{Im}(\dots)$	Imaginary part of a complex number
$\dots^T$	Transpose
$\dots^\dagger$	Hermitian transpose
$\ \mathbf{a}\ _2$	Vector two-norm of $\mathbf{a}$
$\ A\ _2$	Matrix two-norm of $A$
$\lambda_{\max}(A)$	Maximum eigenvalue of $A$
$\sigma_{\max}(A)$	Maximum singular value of $A$
$\text{null}(A)$	Nullity of $A$
$\text{diag}(\dots)$	Diagonal matrix with specified elements
$\epsilon$	Permittivity of a general medium
$\epsilon_0$	Permittivity of vacuum ( $8.854187817\dots \cdot 10^{-12}$ F/m)
$\epsilon_r$	Relative permittivity
$\mu$	Permeability of a general medium
$\mu_0$	Permeability of vacuum ( $4\pi \cdot 10^{-7}$ H/m)
$\mu_r$	Relative permeability
$\sigma$	Electrical conductivity
$f$	Frequency
$\omega$	Angular frequency ( $2\pi f$ )
$\Gamma$	(Waveguide) wavenumber
$k_0$	Wavenumber in vacuum
$\tilde{k}$	Numerical wavenumber
$c$	Phase velocity in a general medium
$c_0$	Phase velocity in vacuum (299792458 m/s)
$Z$	Wave impedance in a general medium
$Z_0$	Wave impedance in vacuum ( $376.730313\dots \Omega$ )
$Z_c$	Modal characteristic impedance
$\alpha$	Modal attenuation constant
$\beta$	Modal propagation constant
$\delta_{\text{skin}}$	Skin depth

$E$	Electric field intensity
$H$	Magnetic field intensity
$D$	Electric flux density
$B$	Magnetic flux density
$J$	Electric current density
$\rho$	Electric charge density
$\phi$	Electric potential
$\varphi$	Magnetic potential
$\mathbf{E}$	Continuous electric field vector
$\mathbf{e}$	Discrete electric field vector
$i$	Index w.r.t. the $x$ -axis
$j$	Index w.r.t. the $y$ -axis
$k$	Index w.r.t. the $z$ -axis
$n$	Time-index
$N_x$	Number of cells in the $x$ -dimension
$n_x$	Number of cells in the $x$ -dimension minus one ( $N_x - 1$ )
$\Delta x$	Discretization length (or step size) along the $x$ -dimension
$r$	Refinement ratio
$E _{i,j,k}^n$	Spatio-temporal evaluation of the state variable $E$ in the discrete grid
$\mathbf{a} _i$	$i^{\text{th}}$ element of vector $\mathbf{a}$
$D_x$	Central difference incidence matrix w.r.t. $x$
$A_x$	Central interpolation matrix w.r.t. $x$
$C$	Curl incidence matrix
$I_{n_x}$	Identity matrix of rank $n_x$
$\delta_x$	Diagonal step-size matrix with elements $\Delta x$
$[\varepsilon]$	Standard diagonal permittivity matrix (only non-diagonal if explicitly mentioned)
$[\star_\varepsilon]$	Not necessarily diagonal Hodge permittivity matrix
$[\star_\varepsilon^4]$	Not necessarily diagonal 4-D Hodge permittivity matrix
$M_\varepsilon$	Diagonal FIT permittivity matrix
$\sim$	Rescaled quantity
$\dots$	also, numerical quantity in the context of numerical dispersion
$\overline{\dots}$	Averaged quantity
$\dots$	One-form state variable
$\hat{\dots}$	Two-form state variable
$\dots$	Auxiliary variable
$\dots$	Auxiliary variable
$\dots^*$	Dual operator
$\dots^\circ$	Periodic boundary conditions (related to FCI-FDTD)

---

$\dots_c$	Coarse-grid operators
$\dots_f$	Fine-grid operators
$\dots_r$	Restricted/coarsenend/assembled operators
$\Pi$	Pulse function
$\hat{\Pi}$	Normalized pulse function
$\Pi^*$	Shifted (or dual) pulse function
$\Lambda$	Triangle function
$\Lambda^*$	Shifted (or dual) triangle function
$\partial_x$	Continuous derivative w.r.t. $x$
$\partial M$	Boundary of the manifold $M$
$\star$	3-D Hodge star operator
$\star_4$	4-D Hodge star operator
$d$	3-D exterior derivative
$d_4$	4-D exterior derivative
$\wedge$	Exterior (or wedge) product
$\mathcal{W}^1$	Whitney one-form brick element
$\mathcal{W}^2$	Whitney two-form brick element
$\mathcal{N}^1$	Nodal Whitney one-form brick element
$\mathcal{N}^2$	Nodal Whitney two-form brick element
$\hat{\mathbf{w}}^1$	Whitney one-form vector with normalized pulses
$\hat{\mathbf{w}}^2$	Whitney two-form vector with normalized pulses
$\hat{\mathbf{n}}^1$	Nodal Whitney one-form vector with normalized pulses
$\hat{\mathbf{n}}^2$	Nodal Whitney two-form vector with normalized pulses
$\mathcal{E}$	Electric one-form (3-D)
$\mathcal{H}$	Magnetic one-form (3-D)
$\mathcal{D}$	Electric two-form (3-D)
$\mathcal{B}$	Magnetic two-form (3-D)
$\mathcal{J}$	Current two-form (3-D)
$\mathcal{Q}$	Charge three-form (3-D)
$\mathcal{F}$	Faraday two-form (4-D)
$\mathcal{G}$	Maxwell two-form (4-D)
$\mathcal{J}_4$	Four-current three-form (4-D)
$z$	complex number introduced by the $z$ -transform also, the $z$ -coordinate
$\zeta$	Bilinear transformation
$\mathcal{K}(\dots)$	DEC's causality operator
$\mathcal{O}(\dots)$	Order of the truncation term

$\mathcal{H}_0^{(2)}(\dots)$	Zero-order Hankel function of the second kind
$S_{21}$	Transmission scattering parameter
$\sigma_{2D}$	2-D scattering width
$\{\dots\}$	Set of numbers

# List of Publications

## Articles in international journals

- B. De Deckere, A. Van Londersele, D. De Zutter, and D. Vande Ginste, “Birefringent dispersive FDTD subgridding scheme”, *Electronics Letters*, vol. 52, no. 17, pp. 1455–1457, 2016.
- A. Van Londersele, D. De Zutter, and D. Vande Ginste, “A new hybrid implicit-explicit FDTD method for local subgridding in multiscale 2-D TE scattering problems”, *IEEE Transactions on Antennas and Propagation*, vol. 64, no. 8, pp. 3509–3520, 2016.
- A. Van Londersele, D. De Zutter, and D. Vande Ginste, “An in-depth stability analysis of nonuniform FDTD combined with novel local implicitization techniques”, *Journal of Computational Physics*, vol. 342, pp. 177–193, 2017.
- A. Van Londersele, D. De Zutter, and D. Vande Ginste, “A collocated 3-D HIE-FDTD scheme with PML”, *IEEE Microwave and Wireless Components Letters*, vol. 27, no. 7, pp. 609–611, 2017.
- A. Van Londersele, D. De Zutter, and D. Vande Ginste, “Full-wave analysis of the shielding effectiveness of thin graphene sheets with the 3D unidirectionally collocated HIE-FDTD method”, *International Journal of Antennas and Propagation*, vol. 2017, Article ID 5860854, 8 pages, 2017.
- A. Van Londersele, R. Lee, F. L. Teixeira, D. De Zutter, and D. Vande Ginste, “Systematic cell-by-cell FDTD subgridding in 3-D”, *IEEE Microwave and Wireless Components Letters*, accepted.

## Articles in conference proceedings

- A. Van Londersele, D. De Zutter, and D. Vande Ginste, “HIE-subgridding for TM scattering problems”, in *2016 IEEE International Symposium on Antennas and Propagation (APSURSI)*, Fajardo, Puerto Rico, 26 June - 1 July 2016, pp. 2029–2030.
- A. Van Londersele, D. De Zutter, and D. Vande Ginste, “Huygens subgridding combined with the 2D fully collocated implicit FDTD method”, in *2016 IEEE International Symposium on Antennas and Propagation (APSURSI)*, Fajardo, Puerto Rico, 26 June - 1 July 2016, pp. 2025–2026.

- A. Van Londersele, D. De Zutter, and D. Vande Ginste, “A leapfrog alternating-direction hybrid implicit-explicit FDTD method”, in *2017 IEEE International Symposium on Antennas and Propagation (APSURSI)*, San Diego, United States, 9-14 July 2017, pp. 2393–2394.
- A. Van Londersele, D. De Zutter, and D. Vande Ginste, “A leapfrog alternating-direction hybrid implicit-explicit FDTD method for local grid refinement”, in *7th International Conference on Advanced Computational Methods in Engineering (ACOMEN)*, Ghent, Belgium, 18-22 September 2017, pp. 131–132.
- A. Van Londersele, D. De Zutter, and D. Vande Ginste, “Provably stable local application of Crank-Nicolson time integration to the FDTD method with nonuniform gridding and subgridding”, in *ACES Conference*, Denver, United States, accepted.

**NOVEL FINITE-DIFFERENCE TIME-DOMAIN TECHNIQUES  
TO MODEL MULTISCALE ELECTROMAGNETIC PROBLEMS**



PART I

Introductory Chapters



# 1

## Introduction

*“A state-of-the-art calculation requires 100 hours of CPU time on the state-of-the-art computer, independent of the decade.”*

Edward Teller

### 1.1 Background and Motivation

Computer-aided design (CAD) and computational electromagnetic (CEM) tools allow electrical engineers to validate and optimize their designs at an early stage in the development process, minimizing the overall costs. They have become indispensable in virtually every industry that produces or closely deals with electrical components. The everlasting urge for more compact technology with more functionality, which establishes itself as Moore’s “the transistor count doubles every two years” law, together with the need for higher data rates and high-frequency signals with more bandwidth, forces CEM software to reinvent itself continuously such that these complex configurations can still be simulated in a reasonable time span retaining sufficient accuracy.

For example, the Intel Core i7-8700K processor, which has recently been launched in October 2017 [1], uses tri-gate transistors with 8 nm-wide fins that are separated 42 nm from each other (Fig. 1.1). Billions of these transistors are placed inside an electronic package measuring 37.5 mm × 37.5 mm × 4.4 mm. Since the processor operates at a base frequency of 3.7 GHz, corresponding to a vacuum wavelength of 81 mm, the package cannot be considered electrically small anymore, such that the wave propagation happening inside it has to be taken into account by dedicated software. This cannot be achieved by the traditional circuit simulators, which essentially apply Kirchhoff’s voltage and current laws, neither by

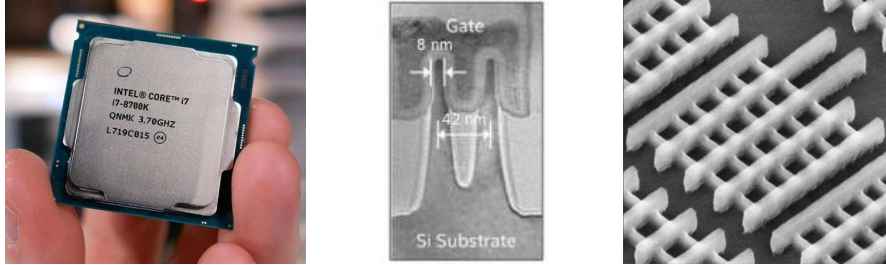


**Figure 1.1:** Intel's Core i7-8700K processor (left) and tri-gate transistors (right) [1].

transmission line theory. Ideally, the electromagnetic interactions should be derived from first principles, that is, directly from Maxwell's equations. There exists a multitude of numerical techniques that are able to compute the electromagnetic fields starting from Maxwell's equations. They all fall under the umbrella of *full-wave* simulators. One of them, the finite-difference time-domain (FDTD) method, which essentially approximates the continuous derivatives occurring in the time-domain formulation of Maxwell's curl equations by discrete differences, is the subject of this dissertation.

Returning to the example of the Intel processor, it should be pointed out that the ratio between the smallest dimension of the fins and the largest dimension of the package is about 1 : 5 000 000. In other words, the chip-package problem is *multi-scale*, which poses a huge burden on full-wave simulations and the FDTD method in particular. Also, due to the high transistor density, the heat produced by switch operations causes a considerable amount of mechanical stress as the occurring materials all have different expansion coefficients. This is why, over the last decade, the performance of processors is mainly improved by increasing the number of cores in one processor, rather than increasing the clock frequency. Moreover, due to the downscaling of transistors, the gate length and oxide thickness merely comprise a countable number of atoms, such that quantum tunneling effects come into play. Hence, Intel deals with what is typically called a *multi-physics* problem: Maxwell's theory of electromagnetics should be coupled with other physics domains such as thermodynamics, classical mechanics, quantum mechanics, and so on.

Not the transistor switching speed, but the signal delay and distortion introduced by the metal interconnections between electrical components forms the main performance bottleneck of present integrated circuits (IC). To mitigate this, modern ICs are stacked above each other along the third dimension (Fig. 1.2). One of the most promising 3-D integration technologies are the through-silicon via (TSV) interconnections between two dies. Despite their potential to drastically reduce the interconnection path length, they require a whole new manufacturing process and entail numerous unprecedented effects, such as the metal-oxide-semiconductor capacitance, that are likely to result in signal and power integrity problems and, hence, require careful numerical modeling. Since the TSVs, which have a diameter

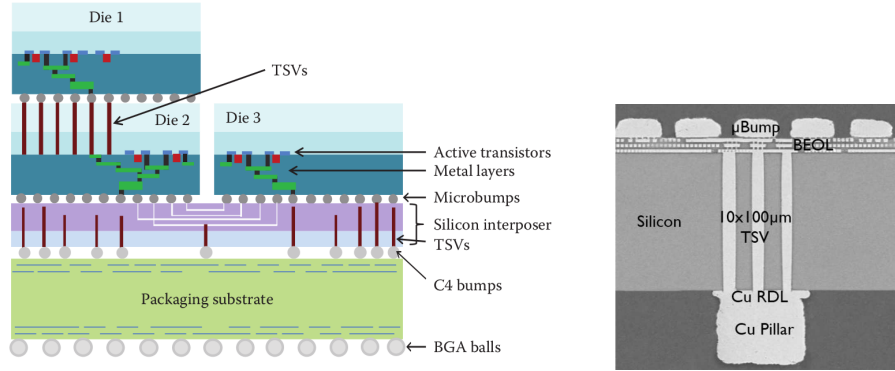


**Figure 1.2:** 3-D integration example (left) [2] and cross section of a silicon interposer with TSVs (right) [3].

in the range 2-20  $\mu\text{m}$  and a length of 10-100  $\mu\text{m}$ , are orders of magnitude smaller than the surrounding electronic package but orders of magnitude larger than the planar interconnects, this again poses a complex multiscale problem. Moreover, the desired level of accuracy requires the semiconductor charge dynamics inside the silicon to be taken into account, which makes this problem again multiphysics as well.

Although CEM has a long tradition that harks back to World War II, the continuous innovation in the semiconductor industry keeps challenging software developers to make their code more accurate and more efficient, with the current emphasis being on multiscale and multiphysics problems. In fact, this is a vicious circle: CEM software is needed to develop devices with more computational power, which are in turn needed to perform more complex CEM simulations.

## 1.2 Contributions

In this dissertation, multiple efficiency and accuracy improvements with regard to multiscale problems are added to the conventional finite-difference time-domain method:

- reduction of grid samples by means of nonuniform gridding and subgridding
- reduction of time samples by means of hybrid implicit-explicit methods
- better geometrical modeling with a (partially) collocated grid

Then, for example, the reduced number of unknowns leverages extra computational capacity, which is exploited to resolve the skin depth of good conductors by means of a standard volume discretization instead of a less accurate surface

impedance or impedance network boundary condition. Much effort has been devoted to rigorous stability proofs for each of the proposed improvements. Because of the numerical stability issues that are typical for the FDTD method and because of the desired efficiency boost, the main thought throughout this doctoral research has become “keep it simple”: once the occurring matrices do not scale well with the number of unknowns or the memory organization gets too complicated, the idea is aborted. After all, one of the main assets of the FDTD method is its conceptual and arithmetic simplicity, which lies at the root of other strongly appreciated properties such as linear computational complexity and massive parallelism.

### 1.3 Outline

Part I of this manuscript is meant to introduce the reader to the basics of theoretical and computational electromagnetics (Chapter 2) and the FDTD method in particular (Chapter 3). The latter discusses, amongst others, the equivalence of finite differences, finite integrations and finite elements on cubic lattices, which will be extensively utilized in Part II of this dissertation, where the new contributions are presented, one at a time. Part II (Chapters 4-7) is based on the author’s publications in international journals and conference proceedings. Chapter 4 presents a theoretical assessment of the numerical stability of nonuniform gridding in combination with different types of hybrid implicit-explicit time integrations. Next, Chapter 5 proposes an elegant and flexible subgridding method based on finite-element and finite-integration insights, applied to a 3-D rectangular waveguide example with a ridge discontinuity. In Chapter 6, the finite-element analysis of the fully-located implicit FDTD method described in [4], [5] is reconsidered, and the FCI-FDTD method is applied to a 2-D anisotropic slab example. In Chapter 7, the novel unidirectionally-located hybrid implicit-explicit FDTD method is proposed, which combines the advantages of staggered explicit updates and located implicit updates to gain the best possible trade-off between accuracy and efficiency. Also, a 2-D subgridding version of the UCHIE-FDTD method is put forward. This UCHIE-FDTD method is tested on several examples such as a thin conductive layer, a graphene sheet, a metal grating far-field scattering problem, and a microstrip line. In Part III, the author’s final remarks and conclusions are listed as well as a comparative overview of the proposed multiscale techniques and some prospects for possible future research.

## References

- [1] [www.intel.com](http://www.intel.com).
- [2] B. K. Kaushik, V. R. Kumar, M. K. Majumder, and A. Alam, *Through Silicon Vias*. Taylor & Francis Group, 2017.
- [3] M. Detalle, B. Vandeveld, P. Nolmans, A. Miller, A. La Manna, G. Beyer, and E. Beyne, “Stress and bowing engineering in passive silicon interposer”, in *2015 IEEE 65th Electronic Components and Technology Conference (ECTC)*, 2015, pp. 287–292.
- [4] W. Tierens and D. De Zutter, “An unconditionally stable time-domain discretization on cartesian meshes for the simulation of nonuniform magnetized cold plasma”, *Journal of Computational Physics*, vol. 231, pp. 5144–5156, 2012.
- [5] W. Tierens, “Finite Element and Finite Difference Based Approaches for the Time-Domain Simulation of Plasma-Wave Interactions”, PhD thesis, Ghent University, 2013.



# 2

## Maxwell's Equations and Their Numerical Solution

*“Differential forms illuminate electromagnetic theory,  
and electromagnetic theory illuminates differential forms.”*

Misner, Thorne and Wheeler

### 2.1 Maxwell's equations

In 1865, the Scottish scientist James Clerk Maxwell unified the theory of electricity and magnetism under a set of twenty quaternion equations, which were later, in 1881, simplified by Oliver Heaviside to the four vector equations that are nowadays most often studied and used by physicists and engineers. Maxwell's work got experimentally validated and acknowledged after his death: Heinrich Hertz demonstrated remote induction in 1888, Nikola Tesla and Guglielmo Marconi set up wireless transmission links in 1893 and 1897 respectively. With the advent of Albert Einstein's special relativity in 1905, Maxwell's equations were shown to be relativistically invariant, and the speed of electromagnetic waves in vacuum was proclaimed to be the universal upper speed limit. Moreover, Paul Dirac's work on quantum electrodynamics (QED) in 1927 made it clear that Maxwell's equations emerge from quantum mechanics in a smooth and consistent manner. So far, QED is the only fundamental theory that is valid in both the relativistic and the quantum regime, and even in the overlap of both regimes. The discrepancy between the classical field theory of Maxwell and QED is only significant to the electrical engineer for a few very advanced problems, e.g. quantum computing. Needless to say that, over the last 150 years, Maxwell's equations have affected a large number of

scientific technologies, and that they will keep on influencing the next generations of technology. [1]

### 2.1.1 Time domain

The basic equations describing electromagnetic phenomena are the two curl equations

$$\nabla \times \mathbf{E}(\mathbf{r}, t) = -\partial_t \mathbf{B}(\mathbf{r}, t) \quad (2.1)$$

$$\nabla \times \mathbf{H}(\mathbf{r}, t) = \partial_t \mathbf{D}(\mathbf{r}, t) + \mathbf{J}(\mathbf{r}, t) \quad , \quad (2.2)$$

which are typically named after Michael Faraday and André-Marie Ampère respectively. Here,  $\mathbf{E}$  and  $\mathbf{H}$  are the electric and magnetic field intensities,  $\mathbf{D}$  and  $\mathbf{B}$  are the electric and magnetic flux densities, and  $\mathbf{J}$  is the electric current density. Taking the divergence of both sides of the curl equations, yields the so-called divergence equations

$$\nabla \cdot \mathbf{B}(\mathbf{r}, t) = 0 \quad (2.3)$$

$$\nabla \cdot \mathbf{D}(\mathbf{r}, t) = \rho(\mathbf{r}, t) \quad , \quad (2.4)$$

complemented with the continuity equation

$$\partial_t \rho(\mathbf{r}, t) + \nabla \cdot \mathbf{J}(\mathbf{r}, t) = 0 \quad . \quad (2.5)$$

Here,  $\rho$  denotes the electric charge density. (2.4) is often named after Carl Friedrich Gauss. In the derivation of the divergence equations, it was silently assumed that the occurring time integral does not introduce a constant or, equivalently, that (2.3)–(2.4) hold at a particular time instance. The set of four Maxwell equations (2.1)–(2.4) is closed by the constitutive relations

$$\mathbf{B}(\mathbf{r}, t) = \mu(\mathbf{r}) \mathbf{H}(\mathbf{r}, t) \quad (2.6)$$

$$\mathbf{D}(\mathbf{r}, t) = \varepsilon(\mathbf{r}) \mathbf{E}(\mathbf{r}, t) \quad , \quad (2.7)$$

where  $\mu$  and  $\varepsilon$  denote the possibly inhomogeneous permeability and permittivity of the medium. They define the phase velocity and wave impedance

$$c(\mathbf{r}) = 1 / \sqrt{\varepsilon(\mathbf{r}) \mu(\mathbf{r})} \quad (2.8)$$

$$Z(\mathbf{r}) = \sqrt{\mu(\mathbf{r}) / \varepsilon(\mathbf{r})} \quad . \quad (2.9)$$

The current term in (2.2) may have different contributions. Besides the external current sources  $\mathbf{J}_{ext}$  that excite the initial-boundary-value problem, a typical other contribution is the conduction current

$$\mathbf{J}_c(\mathbf{r}, t) = \sigma(\mathbf{r}) \mathbf{E}(\mathbf{r}, t) \quad , \quad (2.10)$$

which represents the Ohmic losses inside a conductor with conductivity  $\sigma$ . The constitutive relations (2.6), (2.7) and (2.10) are a simplification of the complex

field-matter interaction, which actually should take into account the coupling between Maxwell's equations and other partial differential equations originating from charge dynamics, mechanics, quantum mechanics, thermodynamics, and so on. Instead, they encompass simple linear relations between the flux densities and the field intensities that result from well-grounded physical assumptions and that are fitted to measured data. Although more complex constitutive relations exist describing e.g. (bi)anisotropic, dispersive or nonlinear media, (2.6)–(2.10) suffice for most problems that are tackled in this dissertation. It should also be mentioned that often magnetic current sources and charges are added to Maxwell's equations to introduce extra symmetry and to make numerical solutions more convenient. However, the physical existence of these quantities has not been observed.

### 2.1.2 Frequency domain

In the frequency domain or sine regime, which is achieved by application of the Fourier transform with respect to time, Maxwell's equations (2.1)–(2.4) reduce to

$$\nabla \times \mathbf{E}(\mathbf{r}, \omega) = -j \omega \mathbf{B}(\mathbf{r}, \omega) \quad (2.11)$$

$$\nabla \times \mathbf{H}(\mathbf{r}, \omega) = j \omega \mathbf{D}(\mathbf{r}, \omega) + \mathbf{J}(\mathbf{r}, \omega) \quad (2.12)$$

$$\nabla \cdot \mathbf{B}(\mathbf{r}, \omega) = 0 \quad (2.13)$$

$$\nabla \cdot \mathbf{D}(\mathbf{r}, \omega) = \rho(\mathbf{r}, \omega) \quad , \quad (2.14)$$

with angular frequency  $\omega$  and complex-valued frequency-domain variables. It is often preferred to search analytical or numerical solutions for Maxwell's equations in the frequency domain, because the problem is now essentially 3-D instead of 4-D and, consequently, easier to solve.

### 2.1.3 Wave equation

The first-order Maxwell equations (2.1)–(2.2), which, after substitution of the constitutive relations (2.6)–(2.10), depend on both the electric and magnetic field, can be reduced to a single second-order differential equation solely depending on one field quantity. Thereto, we take the curl of (2.1) and substitute (2.2) in the right-hand side, which yields the electric-field wave equation

$$\left[ \nabla \times \mu(\mathbf{r})^{-1} \nabla \times + \sigma(\mathbf{r}) \partial_t + \varepsilon(\mathbf{r}) \partial_t^2 \right] \mathbf{E}(\mathbf{r}, t) = -\partial_t \mathbf{J}_{ext}(\mathbf{r}, t) \quad . \quad (2.15)$$

A similar expression can be derived for the magnetic field.

### 2.1.4 Integral formulation

Until now, we focused on the differential-equation formulation of Maxwell's equations. An alternative formulation, which makes Maxwell's equations easier to grasp through intuitive visualizations, is deduced by taking the integral of both sides of

the curl equations (2.1)–(2.2) over an arbitrary surface  $S$  and the integral of both sides of the divergence equations (2.3)–(2.4) over an arbitrary volume  $V$ . The resulting expressions are then simplified by means of Stoke's theorem

$$\int_S (\nabla \times \mathbf{A}) \cdot d\mathbf{s} = \int_{\partial S} \mathbf{A} \cdot d\mathbf{l} \quad , \quad (2.16)$$

where the infinitesimal segment  $d\mathbf{l}$  runs over the contour  $\partial S$  according to the right-hand-rule with respect to the vector  $d\mathbf{s}$  normal to the surface  $S$ , and the divergence theorem

$$\int_V (\nabla \cdot \mathbf{A}) dv = \int_{\partial V} \mathbf{A} \cdot d\mathbf{s} \quad , \quad (2.17)$$

where  $d\mathbf{s}$  is the infinitesimal vector normal to the closed surface  $\partial V$  and pointing outwards with respect to the enclosed volume  $V$ . The resulting time-domain integral formulation of Maxwell's equations (2.1)–(2.4) is

$$\int_{\partial S} \mathbf{E}(\mathbf{r}, t) \cdot d\mathbf{l} = -\partial_t \int_S \mathbf{B}(\mathbf{r}, t) \cdot d\mathbf{s} \quad (2.18)$$

$$\int_{\partial S} \mathbf{H}(\mathbf{r}, t) \cdot d\mathbf{l} = \partial_t \int_S \mathbf{D}(\mathbf{r}, t) \cdot d\mathbf{s} + \int_S \mathbf{J}(\mathbf{r}, t) \cdot d\mathbf{s} \quad (2.19)$$

$$\int_{\partial V} \mathbf{B}(\mathbf{r}, t) \cdot d\mathbf{s} = 0 \quad (2.20)$$

$$\int_{\partial V} \mathbf{D}(\mathbf{r}, t) \cdot d\mathbf{s} = \int_V \rho(\mathbf{r}, t) dv \quad . \quad (2.21)$$

### 2.1.5 Boundary conditions

By applying (2.18)–(2.21) to an infinitesimally small contour or closed surface crossing the boundary between two media, it is readily found that the tangential components of the electric field and the normal component of the magnetic flux density need to be continuous, whereas the tangential components of the magnetic field and the normal component of the electric flux density are allowed to exhibit jumps ascribed to surface currents and surface charges respectively. For a perfect electric conductor (PEC), it can be shown in a similar way that the tangential electric field and normal magnetic flux density need to be zero at the PEC's surface. For a perfect magnetic conductor (PMC), the tangential magnetic field and normal electric flux density vanish.

### 2.1.6 Differential forms

Vector calculus has limited capabilities as it allows only two types of quantities: scalars and vectors. To see why the notion of vectors is too restrictive, notice, for example, that the reflection transformation with respect to the origin, i.e. the sign change of the coordinate axes, flips the orientation of vectors but leaves the orientation of the cross product of two vectors unaltered, such that they actually constitute two very similar yet distinct vector classes, respectively called polar and axial vectors. In 1945, the French mathematician Élie Cartan understood that the language of vector calculus is too concise to uncover the distinct behavior of each of the electromagnetic quantities occurring in Maxwell's equations and, so, he reformulated them in terms of differential forms. Indeed, in 3-D, the exterior calculus of differential forms allows four types of quantities: zero-forms (scalars), one-forms (polar vectors), two-forms (axial vectors), and three-forms (pseudoscalars). Although tensor calculus provides an even more general picture of the mathematics and symmetry under the hood of Maxwell's equations, exterior calculus suffices for our engineering purposes. The remainder of this section is mainly based on [2]–[10].

#### (3 + 1)-D representation

In the (3 + 1)-D representation, that is, if time is not treated the same way as the three spatial dimensions, Maxwell's equations in terms of differential forms are given by

$$d\mathcal{E} = -\partial_t \mathcal{B} \quad (2.22)$$

$$d\mathcal{H} = \partial_t \mathcal{D} + \mathcal{J} \quad (2.23)$$

$$d\mathcal{B} = 0 \quad (2.24)$$

$$d\mathcal{D} = \varrho \quad (2.25)$$

$$\mathcal{B} = \mu \star \mathcal{H} \quad (2.26)$$

$$\mathcal{D} = \varepsilon \star \mathcal{E} \quad (2.27)$$

$$\mathcal{J} = \sigma \star \mathcal{E} \quad (2.28)$$

Here, the field intensities are one-forms, the flux densities and current densities are two-forms, and the electric charge density is a three-form. In Cartesian coordinates, they are given by

$$\mathcal{E} = E_x dx + E_y dy + E_z dz \quad (2.29)$$

$$\mathcal{H} = H_x dx + H_y dy + H_z dz \quad (2.30)$$

$$\mathcal{D} = D_x dy \wedge dz + D_y dz \wedge dx + D_z dx \wedge dy \quad (2.31)$$

$$\mathcal{B} = B_x dy \wedge dz + B_y dz \wedge dx + B_z dx \wedge dy \quad (2.32)$$

$$\mathcal{J} = J_x dy \wedge dz + J_y dz \wedge dx + J_z dx \wedge dy \quad (2.33)$$

$$\varrho = \rho dx \wedge dy \wedge dz \quad , \quad (2.34)$$

where the exterior product ' $\wedge$ ' is the distributive and anticommutative operator, which, applied between two one- or two-forms, resembles<sup>1</sup> the cross product and dot product from vector calculus respectively. Note that the anticommutativity of the exterior product implies that  $dx \wedge dx = 0$ , such that, in 3-D space, any  $k$ -form of degree  $k > 3$  is zero. The exterior derivative is defined as

$$d = [\partial_x dx + \partial_y dy + \partial_z dz] \wedge . \quad (2.35)$$

It is the exterior-calculus analog of the gradient, curl and divergence operators depending on whether its argument is a zero-, one- or two-form respectively. From (2.22)–(2.25), it is observed that the exterior derivative maps  $k$ -forms to  $(k + 1)$ -forms. In (2.26)–(2.28), the tensors  $\mu$ ,  $\varepsilon$ ,  $\sigma$  account for the material properties, whereas the Hodge star operator  $\star$  takes care of the metric and maps  $k$ -forms to  $(n - k)$ -forms, with  $n$  the number of dimensions, here  $n = 3$ . The action of the Hodge star operator on differential forms of different degrees is

$$\star dx = dy \wedge dz \quad \star dy \wedge dz = dx \quad (2.36)$$

$$\star dy = dz \wedge dx \quad \star dz \wedge dx = dy \quad (2.37)$$

$$\star dz = dx \wedge dy \quad \star dx \wedge dy = dz \quad (2.38)$$

$$\star 1 = dx \wedge dy \wedge dz \quad \star dx \wedge dy \wedge dz = 1 , \quad (2.39)$$

with, obviously,

$$\star \star = 1 . \quad (2.40)$$

Differential forms have a clear-cut graphical representation:  $\alpha dx$  can be visualized by  $\alpha$  surfaces normal to the  $x$ -axis, whereas  $\beta dx \wedge dy$  corresponds to the superposition of two sets of surfaces yielding  $\beta$  tubes along the  $z$ -axis, and  $\gamma dx \wedge dy \wedge dz$  is the superposition of three sets of surfaces giving rise to  $\gamma$  boxes. For example, Ampère's law (2.23) is elegantly represented by two-form  $\mathcal{J}$  tubes giving rise to one-form  $\mathcal{H}$  surfaces (Fig. 2.1). This representation is in agreement with the fact that one-forms should be integrable over a curve and two-forms over a surface: one can count the number of surfaces pierced by a curve and the number of tubes cut by a surface.

The differential forms needed to describe all quantities occurring in Maxwell's equations are elegantly summarized by the Tonti diagram [10], which consists

<sup>1</sup>Strictly speaking, the cross product is the superposition of the exterior product and the Hodge star operator. Thus, the exterior product could be interpreted as a metric-free generalization of the cross product.

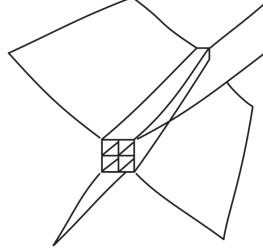


**Figure 2.1:** A graphical representation of Ampère's law in terms of differential forms: tubes (two-forms) of current generate surfaces (one-forms) of magnetic field intensity. The current flows along the tubes, whereas the field intensity is normal to the surfaces, giving rise to a circulating magnetic field that is only zero at the location of the current source. [3]

of two de Rham complexes connected by the Hodge star operators:

$$\begin{array}{ccccccc}
 \begin{array}{c} \text{0-form} \\ \varphi \end{array} & \xrightarrow{\nabla} & \begin{array}{c} \text{1-form} \\ \mathcal{H} \end{array} & \xrightarrow{\nabla \times} & \begin{array}{c} \text{2-form} \\ \mathcal{D}, \mathcal{J} \end{array} & \xrightarrow{\nabla \cdot} & \begin{array}{c} \text{3-form} \\ \varrho \end{array} \\
 & & \mu \star \downarrow & & \uparrow \varepsilon \star, \sigma \star & & \\
 \begin{array}{c} \text{3-form} \\ 0 \end{array} & \xleftarrow{\nabla \cdot} & \begin{array}{c} \text{2-form} \\ \mathcal{B} \end{array} & \xleftarrow{\nabla \times} & \begin{array}{c} \text{1-form} \\ \mathcal{E} \end{array} & \xleftarrow{\nabla} & \begin{array}{c} \text{0-form} \\ \phi \end{array}
 \end{array} \quad (2.41)$$

A de Rham complex has the exact sequence property: each differential operator maps its domain into the kernel of the next differential operator, i.e.

$$\nabla \times \nabla = 0 \quad (2.42)$$

$$\nabla \cdot \nabla \times = 0 \quad (2.43)$$

In exterior calculus, this corresponds to the nilpotency of the exterior derivative

$$dd = 0 \quad (2.44)$$

The exact sequence property is crucial with regard to physical conservation laws. Depending on what is more important, conservation of electric charge or magnetic flux, the top or bottom complex is chosen for the actual implementation in electromagnetic simulation software.

As a last remark, in terms of differential forms, (2.16) and (2.17) are two instances of the same generalized Stokes' theorem, namely

$$\int_M d\alpha = \oint_{\partial M} \alpha \quad (2.45)$$

where  $M$  is a general  $(k+1)$ -dimensional manifold,  $\partial M$  is its  $k$ -dimensional boundary,  $d$  is the exterior derivative, and  $\alpha$  is a  $k$ -form. Integration plays a central role in exterior calculus: the integral of a  $k$ -form over a  $k$ -dimensional manifold yields a scalar. These scalars are the true measurable quantities. The fields themselves are not.

#### 4-D representation

In the 4-D Minkowski spacetime representation, Maxwell's equations are even more compact:

$$d_4 \mathcal{F} = 0 \quad (2.46)$$

$$d_4 \mathcal{G} = \mathcal{J}_4 \quad (2.47)$$

$$\mathcal{G} = \star_4 \mathcal{F} \quad , \quad (2.48)$$

with the spacetime exterior derivative defined as

$$d_4 = [\partial_x dx + \partial_y dy + \partial_z dz + \partial_t dt] \wedge \quad , \quad (2.49)$$

and with Faraday and Maxwell two-forms and four-current three-form given by

$$\mathcal{F} = \mathcal{B} + \mathcal{E} \wedge dt \quad (2.50)$$

$$\mathcal{G} = \mathcal{D} - \mathcal{H} \wedge dt \quad (2.51)$$

$$\mathcal{J}_4 = \varrho - \mathcal{J} \wedge dt \quad . \quad (2.52)$$

The continuity relation (2.5) is translated to

$$d_4 \mathcal{J}_4 = 0 \quad . \quad (2.53)$$

Analogously to vector calculus, (2.53) is redundant because of (2.47) in combination with the exact sequence property  $d_4 d_4 = 0$ . The 4-D Hodge star operator  $\star_4$  accounts for both the material and the metric. As dictated by special relativity, the spacetime metric is not positive definite, such that  $\star_4 \star_4 = \pm 1$  as opposed to (2.40). More details about the 4-D Hodge star operator is out of the scope of this short introduction. Although the level of abstraction is quite high, the two-forms (2.50) and (2.51) contain valuable information about how a spacetime discretization should look like.

#### Whitney forms and discrete exterior calculus

In this paragraph, it is briefly explained how to define differential forms on a discrete grid. The idea to expand the electromagnetic quantities in basis functions that are derived from differential forms, was first proposed by Alain Bossavit in 1988 [11]. In his work, he relied on a particular class of forms defined by Hassler Whitney in 1957 [12]. The so-called Whitney elements were found to be a generalization of Jean-Claude Nédélec's seminal edge and face elements [13]. The beauty

of these basis functions is that they automatically satisfy the boundary conditions listed in Section 2.1.5 and correctly discretize the kernel of the curl, whereas former nodal basis functions introduced spurious solutions.

From (2.45), it is observed that continuous  $k$ -forms are typically integrated over  $k$ -dimensional manifolds, such that it makes common sense to assign zero-forms to vertices, one-forms to edges, two-forms to faces, and three-forms to volumes<sup>2</sup>. A dual grid is constructed, e.g. with a barycentric or circumcentric approach, and the discrete  $k$ -forms are anchored to  $k$ -dimensional manifolds of the primary or dual grid depending on which de Rham complex they belong to in the Tonti diagram (2.41). The discrete Hodge star operator maps primary-grid  $k$ -forms to dual-grid  $(n - k)$ -forms, and vice versa.

A well-explained derivation of the Whitney elements for simplicial meshes, starting from barycentric coordinates for zero-forms and generalizing to higher-degree forms, can be found in [8]. To the author's knowledge, there does not exist a similar derivation for cubic grids, although the Whitney forms on simplices can be deduced from those on cubic grids by pinching vertices together in a continuous manner.

In recent years, the direct full spacetime discretization of Maxwell's equations based on the differential forms outlined in paragraph 2.1.6 has been gaining popularity under the buzzword "discrete exterior calculus" (DEC) [9]. Here, a simplicial spacetime mesh is used in combination with the diagonal Hodge star operator

$$\star \alpha = \mathcal{K}(s) \frac{|\star s|}{|s|} \alpha, \quad (2.54)$$

where  $\alpha$  is a discrete  $k$ -form defined on the  $k$ -simplex  $s$ .  $\star \alpha$  and  $\star s$  are the dual  $(n - k)$ -form and the dual  $(n - k)$ -simplex respectively.  $|s|$  denotes the  $k$ -dimensional volume of  $s$  and  $\mathcal{K}(s)$  is the causality operator, which equals +1 if  $s$  is spacelike and -1 otherwise. A simplex is said to be spacelike if all its points  $(x, y, z, t)$  satisfy  $x^2 + y^2 + z^2 > (c t)^2$ , with  $c$  the phase velocity defined in (2.8).

## 2.2 Full-wave solvers

Roughly speaking, there are three main categories of full-wave modeling techniques: boundary integrals, finite elements and finite differences. As shown in Fig. 2.2, all of them have their own application domain, but no single one is a panacea. Therefore, commercial software packages are often specialized in one of these full-wave modeling techniques, but typically offer all three of them, mostly even hybridized. For electrically very large objects such as ships and airplanes, a fourth category of ray-tracing methods exists that encompasses the uniform theory of diffraction (UTD), physical optics (PO) and geometrical optics (GO).

<sup>2</sup>In case of a 4-D spacetime lattice, four-forms could theoretically be assigned to hypervolumes, but, in practice, there is no electromagnetic quantity corresponding to four-forms.

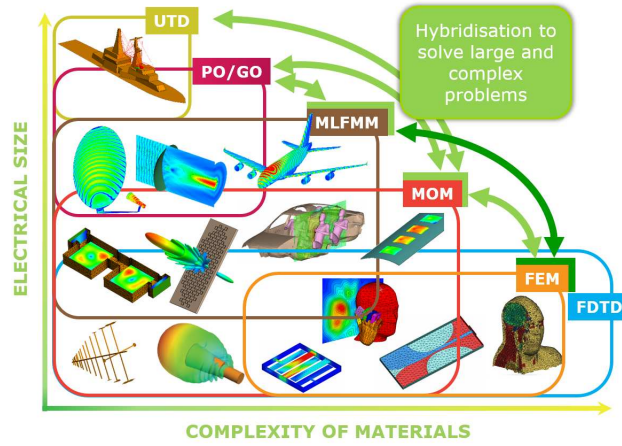


Figure 2.2: Different electromagnetic simulation techniques offered by FEKO [14].

### 2.2.1 Boundary integrals

The boundary element method (BEM) discretizes only the boundary of scattering objects and computes the equivalent currents arising in the boundary-integral equations by means of the method of moments (MoM) [15]. For electrically large objects, the MoM is accelerated with the multilevel fast multipole method (MLFMM) [16]. The salient advantage of the BEM is the discretization of a surface instead of a volume, which heavily reduces the size of the MoM matrix. Also, there is no need for a computationally expensive absorbing boundary condition to mimic open space. But, as always, there is no free lunch: the MoM-matrix is dense and becomes ill-conditioned for low frequencies as well as dense discretizations. Also, the Green's function, which is the kernel of the boundary integrals, is inflexible with regard to complex media. Most often, the BEM is implemented in the frequency domain. This prohibits the modeling of transient phenomena as well as nonlinear or active systems in which frequency is not conserved. There have been many investigations in a time-domain analog [17]. However, besides the usual BEM drawbacks mentioned earlier, the time-domain BEM suffers from poorly-understood stability issues. One of the most rewarded commercial frequency-domain BEM software is the Momentum solver delivered by Keysight Technologies.

### 2.2.2 Finite elements

The finite-element method (FEM) [18] tessellates the full 3-D domain of interest with an unstructured mesh consisting of tetrahedral elements. The fields are expanded in basis functions with local support anchored to the simplices belonging to a particular element. A variational or weak formulation of the frequency-

domain<sup>3</sup> Maxwell equations is then solved by the Galerkin method, resulting in large sparse matrices. The FEM is arguably the most mature full-wave modeling technique with highly accurate solutions and adaptive meshes. However, it also is the computationally most demanding method and, hence, it is only preferred if accuracy is the top priority, as is for example the case for highly inhomogeneous and geometrically complex structures. FEM solvers are usually equipped with efficient frequency sweeps to generate broadband solutions, making them competitive with time-domain methods. However, they cannot deal with nonlinear media as is often needed to solve multiphysics problems. Also, they have troubles with multiscale structures. The bestselling FEM software is HFSS delivered by Ansoft.

### 2.2.3 Finite differences

The finite-difference time-domain (FDTD) method was pioneered by Kane Yee in 1966 [19] and popularized by Allen Taflov, who coined the term ‘FDTD’ in 1980 [20]. Basically, the FDTD method discretizes the full 3-D domain on a staggered cubic grid and approximates the continuous derivatives occurring in the time-domain Maxwell equations by discrete central differences. The algorithm marches on in time, alternately updating the electric and magnetic fields in an explicit manner, that is, without the need to invert a matrix. The FDTD method outshines in terms of conceptual simplicity, which, on the one hand, makes it easy to implement, and, on the other hand, makes it also computationally very efficient owing to the absence of advanced linear algebra in its formulation, its linear computational complexity, its well-structured memory, and its possibility to run in parallel on a central processing unit (CPU) and/or a graphics processing unit (GPU). Furthermore, being a time-domain method, broadband data can be generated with a single run, transient phenomena can be modeled, and nonlinear media are treated naturally. Moreover, its stability is well understood to be guaranteed for a spatially reciprocal discretization and a time step below the Courant limit. Also, in contrast to some other time-domain methods, the FDTD method translates physical conservation laws correctly to the discrete level. At last, the FDTD method is compatible with circuit simulators and it is relatively easy to extend to multiphysics problems.

Probably the main drawback of the conventional FDTD method is the low level of geometric flexibility due to its cubic grid. Several popular full-wave techniques that are branched from the FDTD method tackle this problem, such as the finite integration technique (FIT) [21], the finite-element time-domain (FETD) method [22], the finite-volume time-domain (FVTD) method [23], and the discontinuous-Galerkin time-domain (DGTD) method [24]. Also, the numerical dispersion error

<sup>3</sup>The FEM is most often formulated in the frequency domain, but there exists a time-domain counterpart called the finite-element time-domain (FETD) method, which is taken up in Section 2.2.3 as part of a series of time-domain techniques. Analogously, finite differences are almost exclusively applied in the time domain, but a so-called finite-difference frequency-domain (FDFD) method exists as well and is, for example, used for the modal analysis that is required for wave port excitations in the FDTD method.

of the FDTD method can be reduced by means of higher-order approximations of the derivatives, instead of the conventional central differences. However, these higher-order schemes complicate the accurate modeling of material boundaries [25], the most extreme example being the pseudo-spectral time-domain (PSTD) method [26]. Finally, a third disadvantage of the conventional FDTD method is that the Courant stability limit is in many cases too restrictive in terms of accuracy such that, especially for multiscale problems, the fields are oversampled, leading to unnecessarily long computation times. This is countered by many different implicit reformulations such as Crank-Nicolson (CN) [27], alternating-direction implicit (ADI) [28] and locally one-dimensional (LOD) [29] FDTD methods. In contrast to the FEM, the latter all yield (sparse) matrices that are well conditioned by construction owing to the cubic grid.

The most prominent FDTD software is CST Microwave Studio, which has recently been acquired by Dassault Systèmes.

For a well-written basic introduction to the FDTD method, the reader is referred to [30]. More application-oriented notes on the FDTD method can be found in [31], and more implementation details in [32]. The universally accepted standard book about the FDTD method is [33].

## References

- [1] W. C. Chew, A. Y. Liu, C. Salazar-Lazaro, and W. E. I. Sha, “Quantum electromagnetics: A new look (part I)”, *IEEE Journal on Multiscale and Multiphysics Computational Techniques*, vol. 1, pp. 73–84, 2016.
- [2] K. F. Warnick, R. H. Selfridge, and D. V. Arnold, “Teaching electromagnetic field theory using differential forms”, *IEEE Transactions on Education*, vol. 40, no. 1, pp. 53–68, 1997.
- [3] K. F. Warnick and P. H. Russer, “Two, three and four-dimensional electromagnetics using differential forms”, *Turkish Journal of Electrical Engineering and Computer Sciences*, 2006.
- [4] —, “Differential forms and electromagnetic field theory (invited paper)”, *Progress In Electromagnetics Research*, vol. 148, pp. 83–112, 2014.
- [5] F. L. Teixeira and W. C. Chew, “Lattice electromagnetic theory from a topological viewpoint”, *Journal of mathematical physics*, vol. 40, no. 1, pp. 169–187, 1999.
- [6] B. He and F. L. Teixeira, “Geometric finite element discretization of Maxwell equations in primal and dual spaces”, *Physics Letters A*, vol. 349, no. 1, pp. 1–14, 2006.
- [7] F. L. Teixeira, “Differential forms in lattice field theories: An overview”, *ISRN Mathematical Physics*, 2013.
- [8] —, “Lattice Maxwell’s equations (invited paper)”, *Progress In Electromagnetics Research*, vol. 148, pp. 113–128, 2014.
- [9] A. Stern, Y. Tong, M. Desbrun, and J. E. Marsden, *Geometry, Mechanics, and Dynamics*. New York: Springer, 2015, vol. 73, ch. Geometric Computational Electrodynamics with Variational Integrators and Discrete Differential Forms, pp. 437–475.
- [10] P. B. Bochev and A. C. Robinson, “Matching algorithms with physics: Exact sequences of finite element spaces”, in *Lectures on the Preservation of Stability under Discretization*, Philadelphia: SIAM, 2002, ch. 8.
- [11] A. Bossavit, “Whitney forms: A class of finite elements for three-dimensional computations in electromagnetism”, *IEE Proceedings A - Physical Science, Measurement and Instrumentation, Management and Education - Reviews*, vol. 135, no. 8, pp. 493–500, 1988.
- [12] H. Whitney, *Geometric Integration Theory*. Princeton University Press, 1957.
- [13] J.-C. Nédélec, “Mixed finite elements in  $R^3$ ”, *Numerische Mathematik*, vol. 35, pp. 315–341, 1980.

- [14] [www.feko.info](http://www.feko.info).
- [15] R. F. Harrington, *Field Computation by Moment Methods*. Macmillan, 1968.
- [16] W. Chew, J. Jin, E. Michielssen, and J. Song, *Fast and Efficient Algorithms in Computational Electromagnetics*. Artech House, 2001.
- [17] Y. Beghein, "Advanced discretization and preconditioning techniques for electromagnetic boundary integral equations", PhD thesis, Ghent University, 2015.
- [18] Y. Zhu and A. C. Cangellaris, *Multigrid Finite Element Methods for Electromagnetic Field Modeling*. IEEE Press, 2006.
- [19] K. Yee, "Numerical solution of initial boundary value problems involving Maxwell's equations in isotropic media", *IEEE Transactions on Antennas and Propagation*, vol. 14, no. 3, pp. 302–307, 1966.
- [20] A. Taflovie, "Application of the finite-difference time-domain method to sinusoidal steady-state electromagnetic-penetration problems", *IEEE Transactions on Electromagnetic Compatibility*, vol. EMC-22, no. 3, pp. 191–202, 1980.
- [21] M. Clemens and T. Weiland, "Discrete electromagnetism with the finite integration technique", *Journal of Electromagnetic Waves and Applications*, vol. 15, no. 1, pp. 79–80, 2001.
- [22] J.-F. Lee, R. Lee, and A. Cangellaris, "Time-domain finite-element methods", *IEEE Transactions on Antennas and Propagation*, vol. 45, no. 3, pp. 430–442, 1997.
- [23] N. K. Madsen and R. W. Ziolkowski, "A three-dimensional modified finite volume technique for Maxwell's equations", *Electromagnetics*, vol. 10, no. 1-2, pp. 147–161, 1990.
- [24] G. E. K. B. Cockburn and C.-W. Shu, *Discontinuous Galerkin Methods: Theory, Computation and Applications*. Springer-Verlag Telos, 2000.
- [25] J. Hesthaven, "High-order accurate methods in time-domain computational electromagnetics: A review", in, ser. *Advances in Imaging and Electron Physics*, P. W. Hawkes, Ed., vol. 127, Elsevier, 2003, pp. 59–123.
- [26] Q. H. Liu, "The PSTD algorithm: A time-domain method requiring only two cells per wavelength", *Microwave and Optical Technology Letters*, vol. 15, no. 3, pp. 158–165, 1997.
- [27] C. Sun and C. W. Trueman, "Unconditionally stable Crank-Nicolson scheme for solving two-dimensional Maxwell's equations", *Electronics Letters*, vol. 39, no. 7, pp. 595–597, 2003.
- [28] F. Zheng, Z. Chen, and J. Zhang, "A finite-difference time-domain method without the Courant stability conditions", *IEEE Microwave and Guided Wave Letters*, vol. 9, no. 11, pp. 441–443, 1999.

- [29] J. Shibayama, M. Muraki, J. Yamauchi, and H. Nakano, "Efficient implicit FDTD algorithm based on locally one-dimensional scheme", *Electronics Letters*, vol. 41, no. 19, pp. 1046–1047, 2005.
- [30] S. D. Gedney, *Introduction to the Finite-Difference Time-Domain (FDTD) Method for Electromagnetics*. Morgan & Claypool publishers, 2011.
- [31] W. Yu, X. Yang, Y. Liu, and R. Mittra, *Electromagnetic Simulation Techniques Based on the FDTD Method*. John Wiley & Sons, Inc., 2009.
- [32] J. B. Schneider, *Understanding the finite-difference time-domain method*, [www.eecs.wsu.edu/~schneidj/ufdtd](http://www.eecs.wsu.edu/~schneidj/ufdtd), 2017.
- [33] S. Taflove and S. C. Hagness, *Computational Electrodynamics: The Finite-Difference Time-Domain Method (Third Edition)*. Artech House, 2005.



# 3

## The Finite-Difference Time-Domain Method

*“Less is more.”*

Felix De Laet

★ ★ ★

*In this chapter, we will embark on an exciting journey into the discrete world of finite differences, where less is more: less assumptions when solving Maxwell’s equations result in more areas of application where the method is valid, less degrees of approximation between the continuous derivatives and the discrete differences yield more geometric flexibility, less far-reaching modifications to the standard algorithm yield better performance. After a short discussion on the discretization of space and time with emphasis on important computational aspects such as accuracy and efficiency in Sections 3.1 and 3.2, Maxwell’s curl equations are cast into the framework of finite differences in Section 3.3, giving rise to the FDTD update stencil as originally proposed by Kane Yee. Next, the finite integration technique (FIT) and the finite-element time-domain (FETD) method are demonstrated to be valid generalizations of the FDTD method. In contrast to the conventional FDTD method, the latter are not bounded to regular cubic grids. As such, they provide valuable insights with respect to the novel nonuniform gridding and subgridding techniques that will be proposed in Part II of this dissertation. Section 3.4 summarizes the side effects of discretization, such as numerical dispersion and discrete-time stability. Many of the complications associated to subgridding are highlighted. Finally, in Section 3.5, we list the state-of-the-art subgridding methods and briefly reflect on possible avenues of progress.*

### 3.1 Space discretization

The Yee cell, depicted in Fig. 3.1, is the elementary unit used to discretize the 3-D simulation domain. The different field components are staggered as to yield second-order accuracy in space with minimal computational effort. It is the natural discretization of the differential forms that underpin Maxwell's equations: fields (one-forms) are anchored to one-dimensional edges and flux densities (two-forms) are anchored to two-dimensional faces, and the constitutive relations convert edge quantities of the primary grid into face quantities of the dual grid and vice versa. However, the Yee cell tessellation has some clear disadvantages:

- Any small deviation such as nonuniform gridding and subgridding forces the Yee grid to become locally first-order accurate, albeit with second-order supraconvergence [1], [2].
- The unbounded local error due to field singularities emerging near sharp metallic edges and corners cannot be alleviated by supraconvergence [3], [4].
- The staggered nature requires the material constants to be averaged.
- The tangential-field continuity across (axis-aligned) boundaries of materials exhibiting both electric and magnetic properties cannot be satisfied, again due to the staggering [5, Sec. 3.7].
- The constitutive relations of (bi)anisotropic media are more naturally modeled by a collocated grid [6]–[8].

Therefore, in this dissertation, we investigate the use of fully collocated and partially collocated unit cells (Fig. 3.2). Although from a finite-element/differential-form perspective nodal discretizations, such as the one in Fig. 3.2(a), are strongly discouraged, the collocated FDTD scheme proposed in [7] exhibits enhanced accuracy thanks to a correct mixture of interpolation and differentiation operations to evaluate Maxwell's equations right in the middle between adjacent anchor points. Similar arguments hold for the unidirectionally collocated cell shown in Fig. 3.2(b), which projects the traditional Yee cell from Fig. 3.1 along one axis, here chosen to be the  $x$ -axis, such that a layered discretization is retrieved. The proposed FDTD scheme for the unidirectionally collocated cell preserves second-order accuracy in the direction of collocation.

Now that we have defined the building blocks, we can assemble them into a grid. Several ways to do this are clarified in the remainder of this section by discretizing a 2-D disc (Fig. 3.3). A first rudimentary discretization approach uses three invariant spatial steps  $\Delta x$ ,  $\Delta y$  and  $\Delta z$ , one for each dimension. This corresponds to the uniform grid with staircased boundary in Fig. 3.3(a).

A second straightforward approach allows the spatial steps to vary along their respective axes, i.e.  $\Delta x(x)$ ,  $\Delta y(y)$  and  $\Delta z(z)$ . This so-called nonuniform grid,

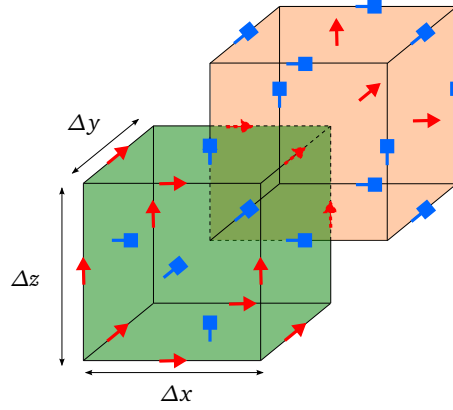


**Figure 3.1:** Primary (green) and dual (orange) Yee cell. The electric fields (*triangle arrows*) and magnetic flux densities (*square arrows*) are discretized along the edges and faces respectively of the primary grid. Equivalently, the magnetic fields (*square arrows*) and electric flux densities (*triangle arrows*) are discretized along the edges and faces respectively of the dual grid. Flux densities are coinciding with their associated fields. Red and blue markers are staggered in time.

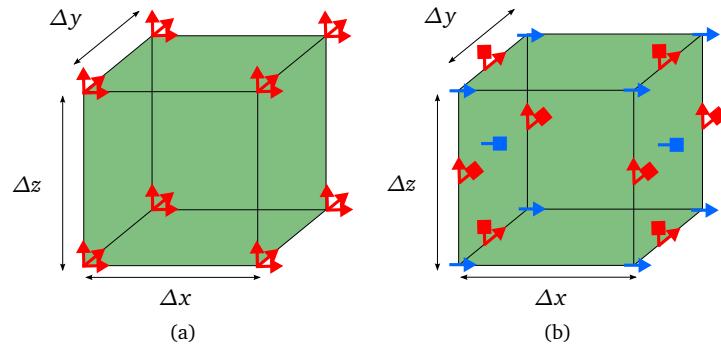


**Figure 3.2:** (a) Fully collocated cell with all electric and magnetic field components anchored to the vertices. (b) Unidirectionally collocated cell with electric field components (*triangle arrows*) and magnetic field components (*square arrows*) collocated along the x-axis but staggered along the y- and z-axis. Red and blue markers are staggered in time.

shown in Fig. 3.3(b), involves minimal changes to the uniform grid and its associated stability requirements, but allows much more geometrical flexibility. For the traditional Yee scheme, the nonuniformities are locally first-order accurate, but the global accuracy is still acceptable owing to second-order supraconvergence if 1) the dual-grid edges cross the centroids of the primary-grid faces and 2) two adjacent steps do not differ by a factor larger than 1.5 [1], [3], [9].

A third approach, named subgridding, uses nested uniform grids, as is illustrated in Fig. 3.3(c). This may seem straightforward at first sight, but deriving the physically correct and numerically stable interpolation rules along the subgrid interface is far from evident and has been a compelling FDTD research topic during the last decades. Also, the reflection errors at the subgrid interface pose a larger issue than the errors introduced by nonuniform grids.

A fourth approach discretizes the boundary exactly by means of a nonorthogonal curvilinear grid (Fig. 3.3(d)), obtained by a coordinate transformation. However, this may lead to very small and even singular cells, which is detrimental with respect to the numerical stability of the traditional leapfrog time-stepping scheme.

A fifth category constitutes the so-called conformal techniques and subcell techniques. Here, not the grid but the weights of the finite differences themselves are adapted to the geometry by using the integral formulation of Maxwell's equations. This is a supplementary technique to reduce the staircasing error without changing the grid itself. As such, this category is kind of a cheater and Fig. 3.3(e) is an idealization of the actual situation.

At last, a sixth approach does not use the earlier described cubic unit cells, but, instead, appeals to tetrahedrons (or triangles in 2-D, such as in Fig. 3.3(f)). This is called an unstructured grid and is typically used by the FIT, the FETD method, the FVTD method and the DGTD method in regions that have complex geometrical features.

## 3.2 Time discretization

Unless there are time-dependent media that require special treatment, there is no reason not to choose standard uniformly spaced time samples. Analogously to the spatial discretization, the time samples can be staggered (e.g. Yee-FDTD) or collocated (e.g. CN-FDTD). The time discretization determines to a great extent the efficiency of the finite-difference scheme. Causal schemes, where new fields depend on current and past fields, are explicit in the sense that they can be computed directly and do not require any kind of matrix inversion. On the contrary, non-causal schemes are implicit: they require the simultaneous computation of multiple new fields. Although, for finite-difference schemes, the resulting matrices are always sparse and positive definite by construction, which permits a fast iterative solution with a suitable preconditioner, implicit methods are always computationally more demanding.

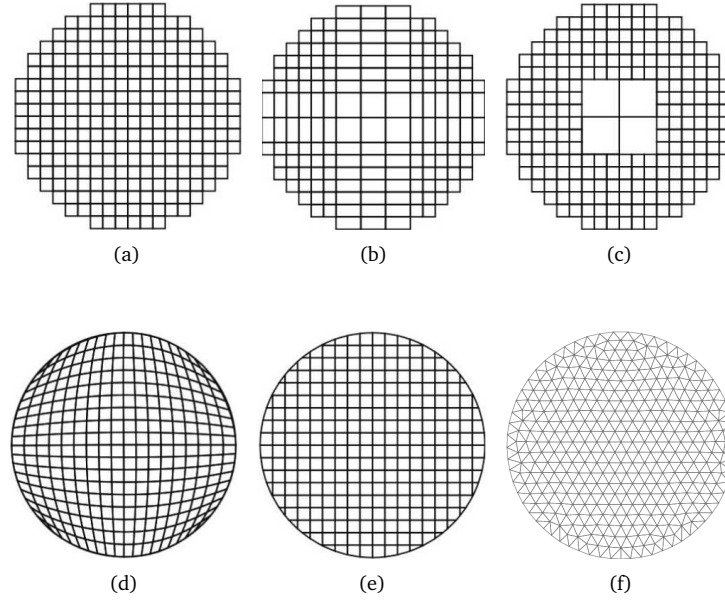


**Figure 3.3:** The different types of gridding techniques applied to a circular object: (a) uniform, (b) nonuniform, (c) subgridding, (d) nonorthogonal, (e) conformal, and (f) unstructured. [4]

There is a good reason why sometimes implicit methods are preferred over explicit ones. If they are well constructed, they feature unconditional stability, which means that the time step can be picked purely based on accuracy. Examples are the Crank-Nicolson (CN), the alternating-direction implicit (ADI) and the locally-one-dimensional (LOD) FDTD method. They are used if the working wavelength is orders of magnitude larger than the smallest structure that needs to be resolved. It is definitely not true that any implicit scheme is unconditionally stable! From a digital-filtering perspective, unconditionally stable schemes act as a notch filter that removes the Nyquist frequency. Not every non-causal time discretization has this property. Also, there exist hybrid implicit-explicit (HIE) schemes that are “the best of both worlds” if objects that are small in at least one but not all dimensions need to be modeled. Fully implicit and hybrid implicit-explicit methods, as well as the local application of each of them in combination with a fully explicit scheme, are viable approaches for the efficient solution of multiscale problems. This is one of the main tracks that will be addressed thoroughly in this dissertation.

For classical time discretizations, the time samples have a local support: only neighboring time samples interact with each other. They adopt a so-called marching-on-in-time (MOT) strategy: the algorithm iterates over time and updates the field unknowns at each discrete time instance. In contrast, there exist finite-difference methods that expand time in orthogonal polynomials spanning the full time inter-

val of interest. These so-called marching-on-in-order (MOO) schemes iterate over the order of the polynomials. Examples of orthogonal polynomials used to construct MOO finite-difference schemes include Laguerre [10]–[12], Hermite [13] and Chebyshev [14] polynomials. They give rise to implicit and unconditionally stable MOO schemes with a sparse system matrix.

### 3.3 Yee's finite-difference scheme

#### 3.3.1 Finite differences

Yee's original scheme [15] uses the staggered unit cell (Fig. 3.1) and approximates all derivatives occurring in Maxwell's curl equations by the central difference

$$(\partial_x \phi)|_i \approx \frac{\phi|_{i+\frac{1}{2}} - \phi|_{i-\frac{1}{2}}}{\Delta x}, \quad (3.1)$$

where the index  $i$  denotes the evaluation of the function at  $x = i \Delta x$ . Upon substitution of the Taylor series expansions

$$\phi|_{i+\frac{1}{2}} = \phi|_i + \frac{\Delta x}{2}(\partial_x \phi)|_i + \frac{\Delta x^2}{8}(\partial_x^2 \phi)|_i + \mathcal{O}(\Delta x^3) \quad (3.2)$$

$$\phi|_{i-\frac{1}{2}} = \phi|_i - \frac{\Delta x}{2}(\partial_x \phi)|_i + \frac{\Delta x^2}{8}(\partial_x^2 \phi)|_i + \mathcal{O}(\Delta x^3), \quad (3.3)$$

the central difference operator (3.1) is found to be second-order accurate. In practice, this means that the error decreases quadratically with decreasing  $\Delta x$ . FDTD solvers typically perform several runs with increasing refinement until the error between consecutive solutions achieves a predefined tolerance. Therefore, quadratic convergence is often stated to be the minimum acceptable rate. Finite-difference schemes based on higher-order difference operators exist, but they impede the accurate modeling of material boundaries and, consequently, they should only be applied to homogeneous problems.

If the difference operator (3.1) loses its central character, the quadratic terms in the Taylor series expansions (3.2)–(3.3) no longer balance each other out, and the operator becomes merely first-order accurate. As discussed in Section 3.1, this happens amongst others in nonuniform grids and along the interfaces of subgrids, but supraconvergence still yields second-order global convergence.

Not only the spatial but also the temporal derivatives are approximated by the central difference (3.1). With electric and magnetic fields discretized in a staggered fashion along the time axis, this gives rise to the explicit leapfrog update scheme, where electric and magnetic fields are alternately updated.

### Update equations

We now apply Yee's scheme to the curl equations (2.1)–(2.2) in the case of a nonuniform spatial grid and in the absence of external sources. It is a silent convention in the FDTD community to use the indices  $\{i, j, k, n\}$  to denote the dimensions  $\{x, y, z, t\}$ . Ampère's law (2.2) gives rise to the electric-field update equations

$$\begin{aligned}\hat{E}_x|_{i,j,k}^{n+1} &= s_x^e|_{i,j,k} \hat{E}_x|_{i,j,k}^n + c_x^e|_{i,j,k} \left( \hat{H}_z|_{i,j,k}^n - \hat{H}_z|_{i,j-1,k}^n \right. \\ &\quad \left. - \hat{H}_y|_{i,j,k}^n + \hat{H}_y|_{i,j,k-1}^n \right) \\ \hat{E}_y|_{i,j,k}^{n+1} &= s_y^e|_{i,j,k} \hat{E}_y|_{i,j,k}^n + c_y^e|_{i,j,k} \left( \hat{H}_x|_{i,j,k}^n - \hat{H}_x|_{i,j,k-1}^n \right. \\ &\quad \left. - \hat{H}_z|_{i,j,k}^n + \hat{H}_z|_{i-1,j,k}^n \right) \\ \hat{E}_z|_{i,j,k}^{n+1} &= s_z^e|_{i,j,k} \hat{E}_z|_{i,j,k}^n + c_z^e|_{i,j,k} \left( \hat{H}_y|_{i,j,k}^n - \hat{H}_y|_{i-1,j,k}^n \right. \\ &\quad \left. - \hat{H}_x|_{i,j,k}^n + \hat{H}_x|_{i,j-1,k}^n \right) .\end{aligned}\tag{3.4}$$

whereas Faraday's law (2.1) yields the magnetic-field update equations

$$\begin{aligned}\hat{H}_x|_{i,j,k}^{n+1} &= \hat{H}_x|_{i,j,k}^n + c_x^h|_{i,j,k} \left( \hat{E}_z|_{i,j+1,k}^{n+1} - \hat{E}_z|_{i,j,k}^{n+1} \right. \\ &\quad \left. - \hat{E}_y|_{i,j,k+1}^{n+1} + \hat{E}_y|_{i,j,k}^{n+1} \right) \\ \hat{H}_y|_{i,j,k}^{n+1} &= \hat{H}_y|_{i,j,k}^n + c_y^h|_{i,j,k} \left( \hat{E}_x|_{i,j,k+1}^{n+1} - \hat{E}_x|_{i,j,k}^{n+1} \right. \\ &\quad \left. - \hat{E}_z|_{i+1,j,k}^{n+1} + \hat{E}_z|_{i,j,k}^{n+1} \right) \\ \hat{H}_z|_{i,j,k}^{n+1} &= \hat{H}_z|_{i,j,k}^n + c_z^h|_{i,j,k} \left( \hat{E}_y|_{i+1,j,k}^{n+1} - \hat{E}_y|_{i,j,k}^{n+1} \right. \\ &\quad \left. - \hat{E}_x|_{i,j+1,k}^{n+1} + \hat{E}_x|_{i,j,k}^{n+1} \right) ,\end{aligned}\tag{3.5}$$

where we adopted the “implementation notation” instead of the conventional “half-integer notation”<sup>1</sup>. Although the latter, used in (3.1), makes the staggering more clear, the former is more compact and can be readily copied for implementation. Also, the electric and magnetic field components are rescaled by the length of their associated edges. In agreement with FIT terminology, we call these quantities grid voltages. The electric and magnetic grid voltages are given by

$$\begin{aligned}\hat{E}_x|_{i,j,k} &= \Delta x_i E_x|_{i,j,k} & \hat{H}_x|_{i,j,k} &= \Delta x_i^* H_x|_{i,j,k} \\ \hat{E}_y|_{i,j,k} &= \Delta y_j E_y|_{i,j,k} & \hat{H}_y|_{i,j,k} &= \Delta y_j^* H_y|_{i,j,k} \\ \hat{E}_z|_{i,j,k} &= \Delta z_k E_z|_{i,j,k} & \hat{H}_z|_{i,j,k} &= \Delta z_k^* H_z|_{i,j,k} ,\end{aligned}\tag{3.6}$$

<sup>1</sup>The “half-integer notation” is easily retrieved by adding one half to the tangential space index of the electric field and its coefficients as well as to the normal space indices of the magnetic field and its coefficients, and by subtracting one half from the time index of the electric field.

with the dual-grid steps (see Fig. 3.4)

$$\begin{aligned}\Delta x_i^* &= (\Delta x_{i-1} + \Delta x_i)/2 \\ \Delta y_j^* &= (\Delta y_{j-1} + \Delta y_j)/2 \\ \Delta z_k^* &= (\Delta z_{k-1} + \Delta z_k)/2 .\end{aligned}\tag{3.7}$$

This rescaling reduces the number of floating-point operations by one unit per update equation. Using the time-average discretization of the conduction current, the self-term coefficients in (3.4) are

$$\begin{aligned}s_x^e|_{i,j,k} &= \frac{\frac{\bar{\epsilon}_x|_{i,j,k}}{\Delta t} - \frac{\bar{\sigma}_x|_{i,j,k}}{2}}{\frac{\bar{\epsilon}_x|_{i,j,k}}{\Delta t} + \frac{\bar{\sigma}_x|_{i,j,k}}{2}} \\ s_y^e|_{i,j,k} &= \frac{\frac{\bar{\epsilon}_y|_{i,j,k}}{\Delta t} - \frac{\bar{\sigma}_y|_{i,j,k}}{2}}{\frac{\bar{\epsilon}_y|_{i,j,k}}{\Delta t} + \frac{\bar{\sigma}_y|_{i,j,k}}{2}} \\ s_z^e|_{i,j,k} &= \frac{\frac{\bar{\epsilon}_z|_{i,j,k}}{\Delta t} - \frac{\bar{\sigma}_z|_{i,j,k}}{2}}{\frac{\bar{\epsilon}_z|_{i,j,k}}{\Delta t} + \frac{\bar{\sigma}_z|_{i,j,k}}{2}} ,\end{aligned}\tag{3.8}$$

and the curl coefficients are

$$\begin{aligned}c_x^e|_{i,j,k} &= \frac{\frac{\Delta x_i}{\Delta y_j^* \Delta z_k^*}}{\frac{\bar{\epsilon}_x|_{i,j,k}}{\Delta t} + \frac{\bar{\sigma}_x|_{i,j,k}}{2}} \\ c_y^e|_{i,j,k} &= \frac{\frac{\Delta y_j}{\Delta z_k^* \Delta x_i^*}}{\frac{\bar{\epsilon}_y|_{i,j,k}}{\Delta t} + \frac{\bar{\sigma}_y|_{i,j,k}}{2}} \\ c_z^e|_{i,j,k} &= \frac{\frac{\Delta z_k}{\Delta x_i^* \Delta y_j^*}}{\frac{\bar{\epsilon}_z|_{i,j,k}}{\Delta t} + \frac{\bar{\sigma}_z|_{i,j,k}}{2}} ,\end{aligned}\tag{3.9}$$

whereas the curl coefficients belonging to (3.5) are

$$\begin{aligned}c_x^h|_{i,j,k} &= -\frac{\Delta x_i^*}{\Delta y_j \Delta z_k} \frac{\Delta t}{\bar{\mu}_x|_{i,j,k}} \\ c_y^h|_{i,j,k} &= -\frac{\Delta y_j^*}{\Delta z_k \Delta x_i} \frac{\Delta t}{\bar{\mu}_y|_{i,j,k}} \\ c_z^h|_{i,j,k} &= -\frac{\Delta z_k^*}{\Delta x_i \Delta y_j} \frac{\Delta t}{\bar{\mu}_z|_{i,j,k}} .\end{aligned}\tag{3.10}$$

Here, the material constants  $\bar{\mu}_d$ ,  $\bar{\epsilon}_d$  and  $\bar{\sigma}_d$  with  $d \in \{x, y, z\}$ , are properly averaged over the cuboid volume covered by the associated field component, possibly

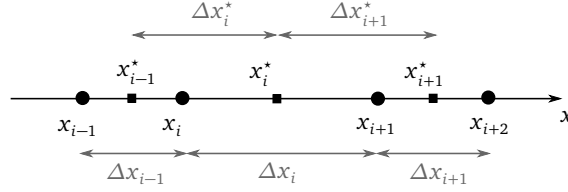


**Figure 3.4:** Spatial indexing of the nodes and steps in primary and dual grid. The dual-grid nodes are equidistant with respect to the nearest primary-grid nodes, i.e.  $x_i^* = (x_i + x_{i+1})/2$ . The nodes and steps come in pairs  $(x_i, \Delta x_i^*)$  and  $(x_i^*, \Delta x_i)$ .

by means of some conformal technique (recall Fig. 3.3(e)). Since the Yee scheme preserves the exact sequence property (2.44) on the discrete level, Maxwell's divergence equations are automatically satisfied and the curl equations suffice to model any electromagnetic problem as long as the source is charge-conserving. The most basic FDTD code repeatedly performs the updates (3.4)–(3.5) with the inclusion of boundary conditions and sources and with the extraction of the electromagnetic quantities of interest, e.g., scattering parameters. Note that the electric and magnetic grid voltages are updated in-place such that the memory usage is proportional to the number of cells but not to the number of time iterations.

#### Matrix notation

For a nonuniform grid composed of  $N_x \times N_y \times N_z$  primary cells and terminated by PEC boundary conditions, the matrix-form update equation corresponding to (3.4)–(3.5) can be written as

$$\begin{bmatrix} M^* \left( \frac{[\epsilon]}{\Delta t} + \frac{[\sigma]}{2} \right) & 0 \\ C^T & M \frac{[\mu]}{\Delta t} \end{bmatrix} \begin{bmatrix} \hat{\mathbf{e}}_{n+1} \\ \hat{\mathbf{h}}_{n+1} \end{bmatrix} = \begin{bmatrix} M^* \left( \frac{[\epsilon]}{\Delta t} - \frac{[\sigma]}{2} \right) & C \\ 0 & M \frac{[\mu]}{\Delta t} \end{bmatrix} \begin{bmatrix} \hat{\mathbf{e}}_n \\ \hat{\mathbf{h}}_n \end{bmatrix}. \quad (3.11)$$

with Cartesian components of the grid voltages stacked into column vectors

$$\hat{\mathbf{e}} = \begin{bmatrix} \hat{e}_x \\ \hat{e}_y \\ \hat{e}_z \end{bmatrix} \quad \hat{\mathbf{h}} = \begin{bmatrix} \hat{h}_x \\ \hat{h}_y \\ \hat{h}_z \end{bmatrix}, \quad (3.12)$$

with row-major vectorized components

$$\begin{aligned} \hat{\mathbf{e}}_{\mathbf{x}}|_{(i n_y + j) n_z + k} &= \hat{E}_{\mathbf{x}}|_{i,j,k} & \{i, j, k\} &= 1, \dots, \{N_x, n_y, n_z\} \\ \hat{\mathbf{e}}_{\mathbf{y}}|_{(i n_y + j) n_z + k} &= \hat{E}_{\mathbf{y}}|_{i,j,k} & \{i, j, k\} &= 1, \dots, \{n_x, N_y, n_z\} \\ \hat{\mathbf{e}}_{\mathbf{z}}|_{(i n_y + j) n_z + k} &= \hat{E}_{\mathbf{z}}|_{i,j,k} & \{i, j, k\} &= 1, \dots, \{n_x, n_y, N_z\} \\ \hat{\mathbf{h}}_{\mathbf{x}}|_{(i n_y + j) n_z + k} &= \hat{H}_{\mathbf{x}}|_{i,j,k} & \{i, j, k\} &= 1, \dots, \{n_x, N_y, N_z\} \\ \hat{\mathbf{h}}_{\mathbf{y}}|_{(i n_y + j) n_z + k} &= \hat{H}_{\mathbf{y}}|_{i,j,k} & \{i, j, k\} &= 1, \dots, \{N_x, n_y, N_z\} \\ \hat{\mathbf{h}}_{\mathbf{z}}|_{(i n_y + j) n_z + k} &= \hat{H}_{\mathbf{z}}|_{i,j,k} & \{i, j, k\} &= 1, \dots, \{N_x, N_y, n_z\} \end{aligned}.$$

We here used the notation

$$n_d = N_d - 1 \quad d \in \{x, y, z\} . \quad (3.13)$$

Hence, the total lengths of  $\hat{\mathbf{e}}$  and  $\hat{\mathbf{h}}$  are respectively

$$n_e = N_x n_y n_z + n_x N_y n_z + n_x n_y N_z \quad (3.14)$$

$$n_h = n_x N_y N_z + N_x n_y N_z + N_x N_y n_z . \quad (3.15)$$

The diagonal material matrices  $[\mu]$ ,  $[\varepsilon]$ ,  $[\sigma]$  contain the properly averaged material constants  $\mu$ ,  $\varepsilon$  and  $\sigma$ . The curl incidence matrix is given by

$$C = \begin{bmatrix} 0 & -I_{N_x} \otimes I_{n_y} \otimes D_z & I_{N_x} \otimes D_y \otimes I_{n_z} \\ I_{n_x} \otimes I_{N_y} \otimes D_z & 0 & -D_x \otimes I_{N_y} \otimes I_{n_z} \\ -I_{n_x} \otimes D_y \otimes I_{N_z} & D_x \otimes I_{n_y} \otimes I_{N_z} & 0 \end{bmatrix}_{n_e \times n_h} , \quad (3.16)$$

where ‘ $\otimes$ ’ denotes the Kronecker product,  $I_n$  the  $n$ -dimensional identity matrix, and  $D_d$  the central-difference incidence matrix acting on the  $d$ -dimension

$$D_d = \begin{bmatrix} -1 & 1 & & \\ & -1 & 1 & \\ & & \ddots & \ddots \\ & & & -1 & 1 \end{bmatrix}_{n_d \times N_d} \quad d \in \{x, y, z\} . \quad (3.17)$$

The metric of the grid is included in the diagonal metric operators

$$M = \begin{bmatrix} (\delta_x^*)^{-1} \otimes \delta_y \otimes \delta_z & & \\ & \delta_x \otimes (\delta_y^*)^{-1} \otimes \delta_z & \\ & & \delta_x \otimes \delta_y \otimes (\delta_z^*)^{-1} \end{bmatrix} \quad (3.18)$$

$$M^* = \begin{bmatrix} (\delta_x)^{-1} \otimes \delta_y^* \otimes \delta_z^* & & \\ & \delta_x^* \otimes (\delta_y)^{-1} \otimes \delta_z^* & \\ & & \delta_x^* \otimes \delta_y^* \otimes (\delta_z)^{-1} \end{bmatrix} \quad (3.19)$$

with  $\delta_d$  and  $\delta_d^*$  diagonal matrices containing the  $N_d$  and  $n_d$  spatial increments in the  $d$ -dimension of the primary and dual grid respectively. For instance,

$$\delta_x = \begin{bmatrix} \Delta x_1 & & & \\ & \Delta x_2 & & \\ & & \ddots & \\ & & & \Delta x_{N_x} \end{bmatrix} . \quad (3.20)$$

Remarkably, (3.11) exhibits spatial reciprocity: the curl incidence matrices occurring in Faraday’s and Ampère’s laws are related to each other by transposition. This property is indispensable with regard to the numerical stability of the FDTD method.

### 3.3.2 Finite integrations

The finite integration technique (FIT) [16] is a generalization of the FDTD method based on the time-domain integral formulation of Maxwell's equations. It is applicable to nonorthogonal and unstructured dual grid pairs. All grid edges and faces are given an integer label<sup>2</sup> and their corresponding FIT unknowns are stacked in column vectors according to this label. With dual edge-face pairs denoted as  $(L, A^*)$  and  $(L^*, A)$ , the state variables in the FIT are the grid voltages

$$\hat{\mathbf{e}}_i(t) = \int_{L_i} \mathbf{E}(\mathbf{r}, t) \cdot d\mathbf{l} \quad \hat{\mathbf{h}}_j(t) = \int_{L_j^*} \mathbf{H}(\mathbf{r}, t) \cdot d\mathbf{l} \quad , \quad (3.21)$$

and the grid fluxes

$$\hat{\mathbf{b}}_j(t) = \int_{A_j} \mathbf{B}(\mathbf{r}, t) \cdot d\mathbf{A} \quad \hat{\mathbf{d}}_i(t) = \int_{A_i^*} \mathbf{D}(\mathbf{r}, t) \cdot d\mathbf{A} \quad \hat{\mathbf{j}}_i(t) = \int_{A_i^*} \mathbf{J}(\mathbf{r}, t) \cdot d\mathbf{A} \quad . \quad (3.22)$$

Each edge of one grid pierces a face of the other grid, and each vertex of one grid is in the center of a cell volume of the other grid. This duality property is via cellular contour integrations translated to spatially reciprocal curl equations

$$C \hat{\mathbf{h}}(t) = \partial_t \hat{\mathbf{d}}(t) + \hat{\mathbf{j}}(t) \quad (3.23)$$

$$C^T \hat{\mathbf{e}}(t) = -\partial_t \hat{\mathbf{b}}(t) \quad , \quad (3.24)$$

with  $C$  earlier defined in (3.16). Note that (3.23)–(3.24) are purely topological relations. As such, they are exact. The only approximation made by the FIT is in the discretization of the constitutive relations,

$$\hat{\mathbf{b}}(t) = M_\mu \hat{\mathbf{h}}(t) \quad \hat{\mathbf{d}}(t) = M_\epsilon \hat{\mathbf{e}}(t) \quad \hat{\mathbf{j}}(t) = M_\sigma \hat{\mathbf{e}}(t) \quad , \quad (3.25)$$

which include both the material characteristics and the grid metric. There exist quite advanced techniques, some of them even based on Whitney forms borrowed from the FETD method [17], to approximate the material matrices  $M_\mu$ ,  $M_\epsilon$  and  $M_\sigma$  for general dual grid pairs. For simplicity, we will only consider their derivation for dual-orthogonal grid pairs, where all edge-face intersections are orthogonal even though the grids themselves are not necessarily orthogonal. In that case, since the elementary vectors  $d\mathbf{l}$  and  $d\mathbf{A}$  occurring in (3.21)–(3.22) are collinear in the intersection points, the grid voltages and fluxes can be mapped to each other in a one-to-one sense. In other words, the material matrices are diagonal. Also, we assume that all primary cells are homogeneously filled with material, such that tangential electric field continuity and normal magnetic flux continuity are satisfied by construction. Then, the FIT material matrices are

$$M_\mu|_{j,j} = \bar{\mu}_j \frac{|A_j|}{|L_j^*|} \quad M_\epsilon|_{i,i} = \bar{\epsilon}_i \frac{|A_i^*|}{|L_i|} \quad M_\sigma|_{i,i} = \bar{\sigma}_i \frac{|A_i^*|}{|L_i|} \quad , \quad (3.26)$$

<sup>2</sup>Do not confuse the labels  $i$  and  $j$  in this section with the spatial indices used in other sections.

where  $\bar{\mu}$ ,  $\bar{\varepsilon}$  and  $\bar{\sigma}$  are properly averaged over the associated faces and the vertical bars represent the line and surface integrals over edges and faces. Their derivation is briefly illustrated for the FIT permittivity matrix:

$$M_{\varepsilon}|_{i,i} = \frac{\hat{\mathbf{d}}_i(t)}{\hat{\mathbf{e}}_i(t)} = \frac{\int_{A_i^*} \varepsilon(\mathbf{r}) \mathbf{E}(\mathbf{r}, t) \cdot d\mathbf{A}}{\int_{L_i} \mathbf{E}(\mathbf{r}, t) \cdot d\mathbf{l}} \approx \frac{\int_{A_i^*} \varepsilon(\mathbf{r}) dA}{\int_{L_i} dl} = \bar{\varepsilon}_i \frac{|A_i^*|}{|L_i|}, \quad (3.27)$$

with, obviously,

$$\bar{\varepsilon}_i = \frac{1}{|A_i^*|} \int_{A_i^*} \varepsilon(\mathbf{r}) dA. \quad (3.28)$$

Mind the similarity between the FIT material matrix (3.27) and the diagonal Hodge star operator (2.54) used in discrete exterior calculus. The approximation step in (3.27) assumes that the electric field is both constant along the primary edge  $L_i$  and along the dual face  $A_i^*$ . The latter does not comply to the linear-normal behavior of the Whitney one-form (Section 3.3.3). This should not be alarming: the Whitney one-form has this property mainly to guarantee the tangential electric field continuity across material boundaries, but this is already satisfied in the FIT thanks to the piecewise homogeneous discretization on the primary grid. As a rule of thumb, in the derivation of the material matrices, the material constants should be integrated over dual-grid manifolds, because the dual grid comprises the electromagnetic quantities that can feature jumps across material discontinuities. To further illustrate this principle, we find for the FIT permeability matrix

$$M_{\mu}|_{j,j} = \frac{\hat{\mathbf{b}}_j(t)}{\hat{\mathbf{h}}_j(t)} = \frac{\int_{A_j} \mathbf{B}(\mathbf{r}, t) \cdot d\mathbf{A}}{\int_{L_j^*} \mu(\mathbf{r})^{-1} \mathbf{H}(\mathbf{r}, t) \cdot d\mathbf{l}} \approx \frac{\int_{A_j} dA}{\int_{L_j^*} \mu(\mathbf{r})^{-1} dl} = \bar{\mu}_j \frac{|A_j|}{|L_j^*|}, \quad (3.29)$$

with

$$\bar{\mu}_j = \frac{1}{\frac{1}{|L_j^*|} \int_{L_j^*} \mu(\mathbf{r})^{-1} dl}. \quad (3.30)$$

For the nonuniform Yee grid, the edges and faces are Cartesian (axis-aligned) straight lines and flat surfaces. They give rise to simple line and surface integrals that can be expressed in terms of the primary and dual spatial steps. For example, for the edges and faces highlighted in Fig. 3.5,

$$|L_i| = \Delta z \quad |A_i^*| = \Delta x^* \Delta y^* \quad (3.31)$$

$$|L_j^*| = \Delta y^* \quad |A_j| = \Delta z \Delta x \quad (3.32)$$

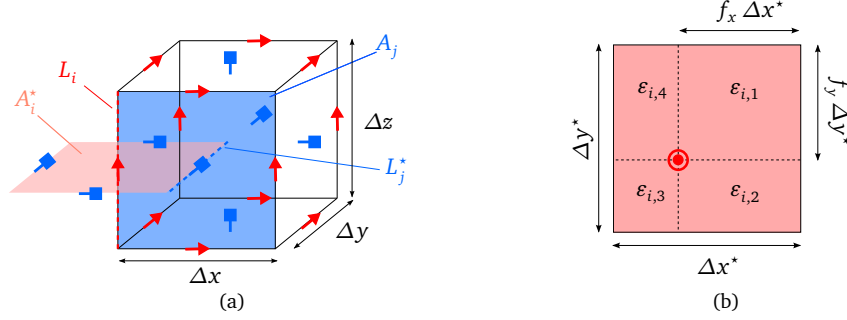


**Figure 3.5:** (a) Yee cell with indication of the dual edge-face pair  $(L_i, A_i^*)$  belonging to the  $i^{\text{th}}$  electric voltage sample and the dual edge-face pair  $(L_j^*, A_j)$  belonging to the  $j^{\text{th}}$  magnetic voltage sample. (b) 2-D view of the face  $A_i^*$  with indication of the permittivity constants assigned to each of the four primary cells that are involved. For a nonuniform grid, the edge  $L_i$  is not necessarily located in the center of the face  $A_i^*$ .

holds, such that (3.26) yields

$$M_\mu|_{j,j} = \frac{2\mu_{j,1}\mu_{j,2}}{\mu_{j,1} + \mu_{j,2}} \frac{\Delta z \Delta x}{\Delta y^*} \quad (3.33)$$

$$M_\epsilon|_{i,i} = (f_x f_y \epsilon_{i,1} + f_x (1-f_y) \epsilon_{i,2} + (1-f_x)(1-f_y) \epsilon_{i,3} + (1-f_x) f_y \epsilon_{i,4}) \frac{\Delta x^* \Delta y^*}{\Delta z} \quad (3.34)$$

$$M_\sigma|_{i,i} = (f_x f_y \sigma_{i,1} + f_x (1-f_y) \sigma_{i,2} + (1-f_x)(1-f_y) \sigma_{i,3} + (1-f_x) f_y \sigma_{i,4}) \frac{\Delta x^* \Delta y^*}{\Delta z} , \quad (3.35)$$

with  $f_x$  and  $f_y$  the dual-step fractions indicated in Fig. 3.5. The conventional FDTD method uses the same material discretization and averaging procedure. Now, it is easily seen that the FIT material matrices are related to the FDTD metric and material matrices as follows:

$$M_\mu = M[\mu] \quad M_\epsilon = M^*[\epsilon] \quad M_\sigma = M^*[\sigma] , \quad (3.36)$$

such that, after leapfrog time integration, (3.23)–(3.24) indeed yield the FDTD update equation (3.11).

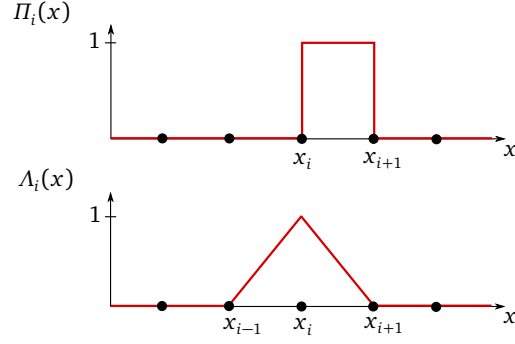


Figure 3.6: Pulse and triangle basis functions.

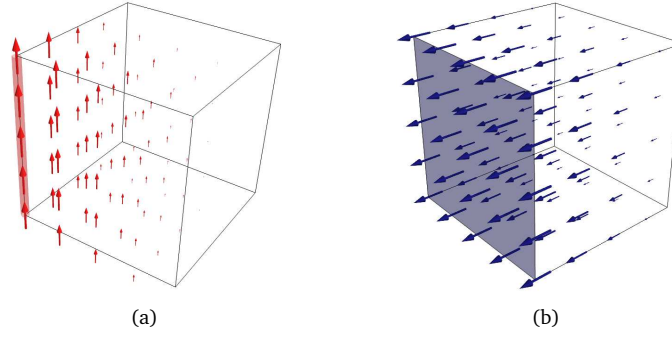


Figure 3.7: Visualization of (a) the Whitney one-form anchored to an edge and (b) the Whitney two-form anchored to a face.

### 3.3.3 Finite elements

#### Space discretization

On a Cartesian grid, the Whitney one- and two-forms of lowest polynomial order are (see [18])

$$\begin{aligned}\mathcal{W}_x^1|_{i,j,k} &= \Pi_i(x) \Lambda_j(y) \Lambda_k(z) \\ \mathcal{W}_y^1|_{i,j,k} &= \Lambda_i(x) \Pi_j(y) \Lambda_k(z) \\ \mathcal{W}_z^1|_{i,j,k} &= \Lambda_i(x) \Lambda_j(y) \Pi_k(z)\end{aligned}\tag{3.37}$$

$$\begin{aligned}\mathcal{W}_x^2|_{i,j,k} &= \Lambda_i(x) \Pi_j(y) \Pi_k(z) \\ \mathcal{W}_y^2|_{i,j,k} &= \Pi_i(x) \Lambda_j(y) \Pi_k(z) \\ \mathcal{W}_z^2|_{i,j,k} &= \Pi_i(x) \Pi_j(y) \Lambda_k(z) \ ,\end{aligned}\tag{3.38}$$

with pulse and triangle functions (Fig. 3.6)

$$\Pi_i(x) = \begin{cases} 1 & x_i \leq x < x_{i+1} \\ 0 & \text{elsewhere} \end{cases}, \quad (3.39)$$

$$\Lambda_i(x) = \begin{cases} \frac{x-x_{i-1}}{x_i-x_{i-1}} & x_{i-1} \leq x < x_i \\ \frac{x_{i+1}-x}{x_{i+1}-x_i} & x_i \leq x < x_{i+1} \\ 0 & \text{elsewhere} \end{cases}. \quad (3.40)$$

Here,  $x_i$  is the location of the  $i^{\text{th}}$  primary node. The primary-grid steps are defined as (see Fig. 3.4)

$$\Delta x_i = x_{i+1} - x_i. \quad (3.41)$$

As illustrated in Fig. 3.7, the Whitney one-form is a constant-tangent/linear-normal edge element and the Whitney two-form a linear-tangent/constant-normal face element. Hence, if we opt for the  $(E, B)$  de Rham complex in the Tonti diagram, the electric field intensity and magnetic flux density are expanded into grid voltages and grid fluxes respectively as follows:

$$\begin{aligned} E_x(x, y, z, t) &= \sum_{i,j,k} \hat{e}_x|_{i,j,k}(t) \mathcal{W}_x^1|_{i,j,k}(x, y, z) / \Delta x_i \\ E_y(x, y, z, t) &= \sum_{i,j,k} \hat{e}_y|_{i,j,k}(t) \mathcal{W}_y^1|_{i,j,k}(x, y, z) / \Delta y_j \\ E_z(x, y, z, t) &= \sum_{i,j,k} \hat{e}_z|_{i,j,k}(t) \mathcal{W}_z^1|_{i,j,k}(x, y, z) / \Delta z_k \end{aligned} \quad (3.42)$$

$$\begin{aligned} B_x(x, y, z, t) &= \sum_{i,j,k} \hat{b}_x|_{i,j,k}(t) \mathcal{W}_x^2|_{i,j,k}(x, y, z) / (\Delta y_j \Delta z_k) \\ B_y(x, y, z, t) &= \sum_{i,j,k} \hat{b}_y|_{i,j,k}(t) \mathcal{W}_y^2|_{i,j,k}(x, y, z) / (\Delta z_k \Delta x_i) \\ B_z(x, y, z, t) &= \sum_{i,j,k} \hat{b}_z|_{i,j,k}(t) \mathcal{W}_z^2|_{i,j,k}(x, y, z) / (\Delta x_i \Delta y_j). \end{aligned} \quad (3.43)$$

After row-major vectorization and edge-length/face-area rescaling of the Whitney vectors, this can be rewritten in matrix-form as

$$\mathbf{E}(x, y, z, t) = \left( \hat{\mathbf{w}}^1(x, y, z) \right)^T \hat{\mathbf{e}}(t) \quad (3.44)$$

$$\mathbf{B}(x, y, z, t) = \left( \hat{\mathbf{w}}^2(x, y, z) \right)^T \hat{\mathbf{b}}(t). \quad (3.45)$$

The rescaling of the Whitney vectors can be interpreted as a normalization of the constituent pulse basis functions, i.e.

$$\begin{aligned} \hat{\Pi}_i(x) &= \Pi_i(x) / \Delta x_i \\ \hat{\Pi}_j(y) &= \Pi_j(y) / \Delta y_j \\ \hat{\Pi}_k(z) &= \Pi_k(z) / \Delta z_k. \end{aligned} \quad (3.46)$$

Now, note that the space spanned by the derivatives of the triangle basis functions resides in the space of pulse basis functions, since

$$\frac{d}{dx} \Lambda_i(x) = \frac{\Pi_{i-1}(x)}{x_i - x_{i-1}} - \frac{\Pi_i(x)}{x_{i+1} - x_i} = \hat{\Pi}_{i-1}(x) - \hat{\Pi}_i(x) . \quad (3.47)$$

As a matter of fact, this property is extendable to higher dimensions and gives rise to the curl-inclusion property

$$\nabla \times \hat{\mathbf{w}}^1(x, y, z) = C \hat{\mathbf{w}}^2(x, y, z) , \quad (3.48)$$

with  $C$  again the curl incidence matrix defined in (3.16). The substitution of the finite-element expansions (3.44)–(3.45) into Faraday's law (2.1) results in

$$\nabla \times (\hat{\mathbf{w}}^1(x, y, z))^T \hat{\mathbf{e}}(t) = -(\hat{\mathbf{w}}^2(x, y, z))^T \partial_t \hat{\mathbf{b}}(t) , \quad (3.49)$$

such that the curl-inclusion property (3.48) yields

$$(\hat{\mathbf{w}}^2(x, y, z))^T C^T \hat{\mathbf{e}}(t) = -(\hat{\mathbf{w}}^2(x, y, z))^T \partial_t \hat{\mathbf{b}}(t) , \quad (3.50)$$

or, since the elements of the vector  $\hat{\mathbf{w}}^2(x, y, z)$  are linearly independent functions,

$$C^T \hat{\mathbf{e}}(t) = -\partial_t \hat{\mathbf{b}}(t) . \quad (3.51)$$

Consequently, Faraday's law is said to be satisfied in the strong sense. In contrast, Ampère's law causes more trouble. If the constitutive relations (2.6)–(2.7) are discretized and substituted into the sourceless law of Ampère (2.2), the finite-element analysis gives rise to

$$\nabla \times (\hat{\mathbf{w}}^2(x, y, z))^T [\mu]^{-1} \hat{\mathbf{b}}(t) = [\varepsilon] (\hat{\mathbf{w}}^1(x, y, z))^T \partial_t \hat{\mathbf{e}}(t) . \quad (3.52)$$

However, since the pulse functions are not differentiable, the curl of the Whitney two-forms occurring in (3.52) cannot be evaluated unless a trick is employed: instead of looking for the solution of the original problem, a weak formulation is adopted by taking the inner product of (3.52) with respect to a suitable differentiable function, called a testing function, and applying integration by parts as to shift the curl operator from the nondifferentiable basis function to the differentiable testing function. This approach is usually named after Boris Galerkin. Here, the appropriate testing function is  $\hat{\mathbf{w}}^1$ . Hence, Galerkin testing gives rise to

$$\iiint (\nabla \times \hat{\mathbf{w}}^1) [\mu]^{-1} (\hat{\mathbf{w}}^2)^T dx dy dz \hat{\mathbf{b}}(t) = \iiint \hat{\mathbf{w}}^1 [\varepsilon] (\hat{\mathbf{w}}^1)^T dx dy dz \partial_t \hat{\mathbf{e}}(t) , \quad (3.53)$$

where the spatial dependence of the Whitney elements was omitted to enhance the readability. (3.48) permits to rewrite (3.53) as

$$C [\star_{\mu^{-1}}] \hat{\mathbf{b}}(t) = [\star_{\varepsilon}] \partial_t \hat{\mathbf{e}}(t) , \quad (3.54)$$

with the finite-element material matrices

$$[\star_\varepsilon] = \iiint \hat{\mathbf{w}}^1[\varepsilon] (\hat{\mathbf{w}}^1)^T dx dy dz \quad (3.55)$$

$$[\star_{\mu^{-1}}] = \iiint \hat{\mathbf{w}}^2[\mu]^{-1} (\hat{\mathbf{w}}^2)^T dx dy dz . \quad (3.56)$$

From their differential-geometric interpretation, (3.55)–(3.56) are called Hodge matrices. In the finite-element jargon, they are called mass matrices, a name originating from mechanics where finite elements were introduced for the first time. They are symmetric positive definite by construction. However, they are not diagonal, since the triangle basis functions (3.40) are not orthogonal. This can be remedied by evaluating the integrals using a low-order quadrature rule, which is also called mass lumping. With the trapezoid rule

$$\int_{x_i}^{x_{i+1}} f(x) dx \approx (x_{i+1} - x_i) \frac{f(x_i) + f(x_{i+1})}{2} , \quad (3.57)$$

applied to the primary nodes  $x_i$ , orthogonality of the triangle functions is yet enforced:

$$\int_{-\infty}^{+\infty} \Lambda_{i_1}(x) \Lambda_{i_2}(x) dx \approx \begin{cases} \Delta x_i^* & \text{if } i_1 = i_2 = i \\ 0 & \text{else} \end{cases} , \quad (3.58)$$

with the dual-grid step  $\Delta x_i^*$  as defined in (3.7). The normalized pulse functions are orthogonal, even for continuous integration:

$$\int_{-\infty}^{+\infty} \hat{\Pi}_{i_1}(x) \hat{\Pi}_{i_2}(x) dx = \begin{cases} \frac{1}{\Delta x_i} & \text{if } i_1 = i_2 = i \\ 0 & \text{else} \end{cases} . \quad (3.59)$$

Hence, the mass-lumped material matrices from the FETD method on a Cartesian grid are equivalent to the material matrices from the FIT. As such, the finite-element equations (3.51) and (3.54) are demonstrated to be equivalent to the ones derived from finite integrations and finite differences, if mass lumping is applied. As a side note, there exist tetrahedral Whitney-form elements as well. In fact, the FETD method mostly uses unstructured tetrahedral grids.

### Time discretization

Interestingly, a similar finite-element approach can be applied to the time axis. Thereto, it is observed from (2.50) and (2.51) that the electric field is naturally expanded in normalized time pulses and the magnetic flux density in time trian-

gles, i.e.

$$\hat{\mathbf{e}}(t) = \sum_n \hat{\mathbf{e}}_n \hat{\Pi}_{n-1}(t) \quad (3.60)$$

$$\hat{\mathbf{b}}(t) = \sum_n \hat{\mathbf{b}}_n \Lambda_n(t) \quad , \quad (3.61)$$

with

$$\hat{\mathbf{e}}_n = \Delta t \hat{\mathbf{e}}_n \quad . \quad (3.62)$$

In agreement with differential geometry in 4-D spacetime, both the electric and magnetic state variables are now two-forms. Substitution of these time expansions into (3.51) and application of the derivative-inclusion property (3.47), reveals that Faraday's law preserves its strong formulation and gives rise to the purely topological update equation

$$\hat{\mathbf{b}}_{n+1} = \hat{\mathbf{b}}_n - C^T \hat{\mathbf{e}}_{n+1} \quad . \quad (3.63)$$

Again, Ampère's law can only be satisfied in the weak sense. Testing (3.54) with  $\Lambda_n(t)$ , it is found that

$$\hat{\mathbf{e}}_{n+1} = \hat{\mathbf{e}}_n + \Delta t [\star_\varepsilon]^{-1} C [\star_{\mu^{-1}}] \sum_{n'} \int \Lambda_{n'}(t) \Lambda_n(t) dt \hat{\mathbf{b}}_{n'} \quad . \quad (3.64)$$

Here, we used integration by parts as well as the derivative-inclusion property (3.47) and the unique definition of the inner product of two normalized pulses (3.59). The inner product remaining in the right-hand side of (3.64) is not diagonal and needs to be evaluated by means of a low-order quadrature rule in order to obtain an explicit update scheme. With the trapezoid rule (3.57), we retrieve the leapfrog scheme:

$$\hat{\mathbf{e}}_{n+1} = \hat{\mathbf{e}}_n + [\star_\varepsilon^4]^{-1} C [\star_{\mu^{-1}}^4] \hat{\mathbf{b}}_n \quad , \quad (3.65)$$

with the 4-D Hodge matrices

$$[\star_\varepsilon^4] = [\star_\varepsilon] / \Delta t \quad [\star_{\mu^{-1}}^4] = [\star_{\mu^{-1}}] \Delta t \quad . \quad (3.66)$$

With the midpoint rule

$$\int_{x_i}^{x_{i+1}} f(x) dx = (x_{i+1} - x_i) f\left(\frac{x_i + x_{i+1}}{2}\right) \quad , \quad (3.67)$$

we find the Newmark- $\beta$  scheme with  $\beta = 0.25$  as proposed in [19], [20]. More specifically,

$$\hat{\mathbf{e}}_{n+1} = \hat{\mathbf{e}}_n + [\star_\varepsilon^4]^{-1} C [\star_{\mu^{-1}}^4] \frac{\hat{\mathbf{b}}_{n+1} + 2\hat{\mathbf{b}}_n + \hat{\mathbf{b}}_{n-1}}{4} \quad . \quad (3.68)$$

Interestingly, this implicit and unconditionally stable scheme naturally comes to light from the finite-element analysis. A similar result was found for the wave equation in [21].

### 3.4 Consequences of discretization

#### 3.4.1 Round-off errors

The FDTD method is quite robust against round-off errors due to the finite machine precision if, in the actual implementation, the electric field  $E$  is rescaled by the vacuum wave impedance  $Z_0$  in the  $(E, H)$  scheme or by the vacuum phase velocity  $c_0$  in the  $(E, B)$  scheme, such that all variables have the same order of magnitude [4].

#### 3.4.2 Numerical dispersion and stability

The numerical error introduced by the central difference operator (3.1) is often characterized in the spatio-temporal frequency domain by substituting the discrete plane-wave solution

$$E_x|_{i,j,k}^n = E_{x_0} e^{J(n\omega\Delta t - i\tilde{k}_x\Delta x - j\tilde{k}_y\Delta y - k\tilde{k}_z\Delta z)} \quad (3.69)$$

$$E_y|_{i,j,k}^n = E_{y_0} e^{J(n\omega\Delta t - i\tilde{k}_x\Delta x - j\tilde{k}_y\Delta y - k\tilde{k}_z\Delta z)} \quad (3.70)$$

$$E_z|_{i,j,k}^n = E_{z_0} e^{J(n\omega\Delta t - i\tilde{k}_x\Delta x - j\tilde{k}_y\Delta y - k\tilde{k}_z\Delta z)} \quad (3.71)$$

$$H_x|_{i,j,k}^n = H_{x_0} e^{J(n\omega\Delta t - i\tilde{k}_x\Delta x - j\tilde{k}_y\Delta y - k\tilde{k}_z\Delta z)} \quad (3.72)$$

$$H_y|_{i,j,k}^n = H_{y_0} e^{J(n\omega\Delta t - i\tilde{k}_x\Delta x - j\tilde{k}_y\Delta y - k\tilde{k}_z\Delta z)} \quad (3.73)$$

$$H_z|_{i,j,k}^n = H_{z_0} e^{J(n\omega\Delta t - i\tilde{k}_x\Delta x - j\tilde{k}_y\Delta y - k\tilde{k}_z\Delta z)} , \quad (3.74)$$

into the six update equations (3.4)–(3.5) for a lossless homogeneous medium with phase velocity  $c$  and in the absence of grid nonuniformities. This yields the well-known numerical dispersion relation of the Yee scheme (see e.g. [22])

$$\left[ \frac{\sin\left(\frac{\omega\Delta t}{2}\right)}{c\Delta t} \right]^2 = \left[ \frac{\sin\left(\frac{\tilde{k}_x\Delta x}{2}\right)}{\Delta x} \right]^2 + \left[ \frac{\sin\left(\frac{\tilde{k}_y\Delta y}{2}\right)}{\Delta y} \right]^2 + \left[ \frac{\sin\left(\frac{\tilde{k}_z\Delta z}{2}\right)}{\Delta z} \right]^2 , \quad (3.75)$$

which relates the angular frequency  $\omega$  to the numerical wavevector  $\tilde{\mathbf{k}} = [\tilde{k}_x, \tilde{k}_y, \tilde{k}_z]$ . For a well-resolved wavelength and period, the sine arguments are small and the numerical dispersion relation (3.75) converges to its continuous counterpart

$$\left( \frac{\omega}{c} \right)^2 = \tilde{k}_x^2 + \tilde{k}_y^2 + \tilde{k}_z^2 . \quad (3.76)$$

The numerical error inherent to (3.75) is a phase error and not an amplitude error as long as  $\omega \in \mathbb{R}$ , which is guaranteed for (see e.g. [22])

$$c\Delta t < \frac{1}{\sqrt{\frac{1}{\Delta x^2} + \frac{1}{\Delta y^2} + \frac{1}{\Delta z^2}}} . \quad (3.77)$$

This is the notorious Courant stability criterion. For time steps that defy this criterion,  $\omega$  can become complex-valued such that the amplitude of the plane-wave

solution (3.69)–(3.74) nonphysically increases while iterating over the time index  $n$ , making the numerical solution worthless. However,  $\Delta t$  should be chosen as close as possible to the upper bound (3.77) for reasons of computational efficiency, but also because this alleviates the phase error. The phase error due to undersampling in time is isotropic, whereas the phase error due to undersampling in space is anisotropic with the highest error occurring along the cell edges and the lowest error along the cell diagonals. Most textbooks recommend a minimum of ten samples per wavelength in order to guarantee a decent level of accuracy. The Courant limit (3.77) automatically translates an accurate spatial resolution to an (over)accurate temporal resolution.

In the case of nonuniform grids, the Courant limit (3.77) employs the minimum cell size along each dimension, which means that the coarse cells dominate the numerical dispersion. In the case of inhomogeneous media,  $c$  in (3.77) should be the maximum occurring phase velocity, which is typically that of vacuum. In Chapter 4 of this dissertation, however, a rigorous algebraic stability analysis shows that the necessary and sufficient stability limit is given by the matrix two-norm

$$\Delta t < \frac{2}{\|M_\varepsilon^{-1/2} C M_\mu^{-1/2}\|_2}, \quad (3.78)$$

which depends on the curl incidence matrix (3.16) and the FIT material matrices (3.36). Recall that the latter include both the material properties and the grid metric. The derivation of (3.78) shows that the *spatial reciprocity* of the update equations, i.e. the curl incidence matrices being each others transposition, plays an important role with regard to the numerical stability, which cannot be deduced from the complex-frequency analysis above. The traditional Courant limit (3.77) is an overestimation of the algebraic limit (3.78) and, consequently, a sufficient but not a necessary condition for stability. It is a necessary condition if the medium is homogeneous and the grid is uniform and infinite.

In view of solving multiscale problems, it is important to decouple the time step from the smallest grid cells. Hence, the Courant limit should be surpassed somehow. This could be achieved by locally applying implicit or hybrid implicit-explicit techniques, which are not bounded to the Courant limit. Alternatively, instead of adapting the time integration to the space discretization, the time step could be picked solely based on accuracy and the discrete curl could be adapted to the time step by means of eigenvalue perturbation as to reduce the two-norm in (3.78) [23]. Yet another trick is to filter out the high spatial frequencies during time-stepping such that the right-hand side of (3.75) is low enough to ensure stability [24].

### 3.4.3 Spurious reflections

The above dispersion analysis considered the ideal case of a uniform grid. Any nonuniformity introduced in the grid changes the numerical dispersion relation along the two sides of the nonuniformity, yielding a discrepancy in both numerical

phase velocity and numerical wave impedance. This causes an additional undesired artifact of discretization: spurious (or numerical) reflections.

To clarify this from another point of view, note that in the FIT material matrices (3.36) the material properties and grid metric are intertwined, such that changing the local cell size in a homogeneous region is equivalent to changing the local material properties in a uniform region, which obviously causes scattering.

Numerical reflections are more critical to subgridding than to nonuniform gridding. Especially the edges and corners of the subgrid pose a serious issue.

#### 3.4.4 Spurious charges

In the source-free regions, the divergence of the electric and magnetic flux densities should be zero according to (2.3)-(2.4). Otherwise, spurious charges pollute the solution. It can be shown that the conventional FDTD method preserves the exact sequence property (2.44) of the de Rahm complex (2.41), implying that the discrete divergence acting on the discrete curl is zero [18], [25]. However, badly designed subgridding methods often lack the exact sequence property and, consequently, suffer from spurious charge accumulation along the interface.

#### 3.4.5 Convergence

In order to have any practical significance, the FDTD solution should converge to the real-world solution in the limit  $\{\Delta x, \Delta y, \Delta z, \Delta t\} \rightarrow 0$ . This is indeed the case and can be proven with the help of the Lax-Richtmyer equivalence theorem, which states that a *consistent* finite-difference approximation of a well-posed linear initial-value problem is *convergent* if and only if it is *stable* [26, Thm. 1.5.1]. The consistency requirement is easily verified with local Taylor series expansions and the stability requirement boils down to the Courant criterion (3.77).

#### 3.4.6 Time reversibility and energy conservation

Owing to the spatial reciprocity, the lossless FDTD method is time-reversible: if the time step flips sign after a certain number of iterations, the fields will return to their original state after an equal number of iterations, even if the simulation is unstable. According to the discrete version of Noether's theorem, this time symmetry is an indication of energy conservation [27]. Indeed, there exists a discrete energy measure that is always conserved, namely [18], [28], [29]

$$w_n = \frac{1}{2\Delta t} \left( \hat{\mathbf{e}}_{n+1}^T [\star_\epsilon^4] \hat{\mathbf{e}}_n + \hat{\mathbf{b}}_n^T [\star_\mu^4] \hat{\mathbf{b}}_n \right) . \quad (3.79)$$

Mind the “geometric averaging” in time of the electric-field contribution, such that all energy contributions are collocated in time<sup>3</sup>. It can be verified by substituting

<sup>3</sup>Recall that we are not using the “half-integer notation”.

the update equations (3.63) and (3.65) into (3.79) that  $w_n = w_{n-1}$ , independently of the time step. Hence, this energy measure is of no practical use when it comes to confirming FDTD stability by means of numerical experiments.

Nonetheless, an interesting observation can be made. Substitution of (3.65) into (3.79) reveals that

$$w_n = \frac{1}{2\Delta t} \begin{bmatrix} \hat{\mathbf{e}}_n \\ \hat{\mathbf{b}}_n \end{bmatrix}^T \begin{bmatrix} [\star_\varepsilon^4] & 0 \\ [\star_{\mu^{-1}}^4] C^T & [\star_{\mu^{-1}}^4] \end{bmatrix} \begin{bmatrix} \hat{\mathbf{e}}_n \\ \hat{\mathbf{b}}_n \end{bmatrix}. \quad (3.80)$$

Since the energy  $w_n$  is a scalar, it is found that

$$w_n = \frac{1}{2}(w_n + w_n^T) = \frac{1}{2\Delta t} \begin{bmatrix} \hat{\mathbf{e}}_n \\ \hat{\mathbf{b}}_n \end{bmatrix}^T \begin{bmatrix} [\star_\varepsilon^4] & \frac{1}{2}C [\star_{\mu^{-1}}^4] \\ \frac{1}{2}[\star_{\mu^{-1}}^4] C^T & [\star_{\mu^{-1}}^4] \end{bmatrix} \begin{bmatrix} \hat{\mathbf{e}}_n \\ \hat{\mathbf{b}}_n \end{bmatrix}, \quad (3.81)$$

where we used the fact that the Hodge matrices are symmetric. A physically meaningful energy measure cannot become negative. As is proven in [28]–[30], the matrix occurring in (3.81) is only positive definite if

$$\|[\star_\varepsilon^4]^{-1/2} C [\star_{\mu^{-1}}^4]^{1/2}\|_2 < 2, \quad (3.82)$$

which, in FIT terminology, corresponds to the exact stability criterion (3.78). Nevertheless, as stated before, the conservation of the discrete energy  $w_n$  does not necessarily imply stability.

### 3.4.7 Aliasing

In the conventional FDTD method, the high-frequency content of the source is usually well-resolved by the ten-samples-per-wavelength rule. There are no (spatial) frequencies above the Nyquist limit and, hence, there is nothing to worry about aliasing. However, for subgridding methods, high frequencies excited in the fine grid can be transferred to the coarse grid, where they cause spurious effects due to aliasing. What is even worse, they are likely to excite instabilities if the spatio-temporal interpolation along the interface does not filter out the small band of frequencies around the Nyquist limit of the coarse grid [31]. A first attempt to fully theoretically describe the aliasing effects occurring in the FDTD method was presented in [32].

### 3.4.8 Absorbing boundary conditions

Open-space simulations theoretically require an infinite grid or, at least, a grid that is large enough as to avoid contamination of the region of interest with fields that are back-scattered from the outer boundaries within the simulated time. As this is

computationally very expensive, early FDTD research mainly focused on the development of absorbing boundary conditions (ABC), which can be placed close to the region of interest and absorb all outgoing waves with negligible reflections for traveling as well as evanescent waves and for all angles of incidence. This has resulted in the invention of the perfectly matched layer (PML). Although originally derived as an impedance-matched non-Maxwellian absorbing medium [33] and later as a uniaxial anisotropic medium [34], the PML is most frequently interpreted as a complex-coordinate stretch [35]. Arguably the most efficient and most accurate formulation of the PML is the complex-frequency-shifted (CFS) PML implemented with a recursive convolution [36]. Despite its universal use in academic and commercial software packages in several branches of physics, the stability of the PML is still poorly understood. In fact, [37, Sect. 4.8] quotes an example of an open cavity with loaded conductor, where the simulation gets unstable for certain PML parameters. A succinct summary of the evolution of absorbing boundary conditions in the past half century can be found in [38].

### 3.4.9 Spurious solutions of the wave equation

A vast body of literature, e.g. [23], [39], discretizes the wave equation (2.15) instead of Maxwell's curl equations. It may look tempting to do this as to reduce the number of unknowns since only the electric and not the magnetic field is computed, but it should be kept in mind that a second-order time derivative requires the storage of two instead of one time sample, such that both the wave equation and the set of curl equations have six unknowns per Yee cell. There is, nonetheless, one real but mostly overlooked advantage of the wave equation: the stability requirement of the curls being reciprocal is reduced to the curl-curl operator being symmetric and positive definite, which facilitates many geometric modifications to the wave equation-based FDTD method such as subgridding and model order reduction. However, this advantage does not outweigh the huge drawback that the wave equation supports spurious solutions [40].

## 3.5 Subgridding

### 3.5.1 Why subgridding?

Subgridding is used to reduce the CPU time and memory usage of the FDTD method by means of local instead of global refinement<sup>4</sup>. Although it is essentially a spatial operation, subgridding affects the time step via the Courant limit (3.77). The ideal subgridding method allows to apply local refinement without changing the time step in the original grid. In the Author's opinion, there are two applications of subgridding: domain decomposition (DD) and adaptive mesh refinement (AMR).

<sup>4</sup>There is, however, only an actual speedup if the reduction in number of variables counters the increased complexity in memory architecture [41], [42]. Otherwise, nonuniform tensor-product grids are more lucrative.

DD aims to resolve electrically small features arising in multiscale setups. Here, the combination of a nonuniform main grid with a nonuniform subgrid comprising several coarse cells, provides optimal geometric flexibility as well as the possibility to reduce the impedance mismatch between main grid and subgrid by gradually changing the cell size. The user can specify the delicate parts of the geometry and the mesher generates the subgrids prior to time-stepping. The subgrids are not likely to share edges or faces. As a consequence, they can be updated implicitly without the matrices of each subgrid combining to one large matrix. Hence, the local use of (semi)-implicit techniques inside the subgrids allows to preserve the original time step throughout the whole grid.

AMR aims to accelerate convergence. An error is assigned to each cell. Once it exceeds a certain threshold, the cell is refined on-the-fly, i.e. during time-stepping. For the FDTD method based on the  $(E,B)$  de Rham complex, a good error measure is, for example, based on the nonphysical jumps between tangential magnetic fields. Subgrids with different refinement ratios are likely to share edges and faces. There is no room for a buffer zone. Together with the adaptive aspect, this makes AMR in attractive to implicit techniques. A better solution would be a local time-stepping (LTS) procedure, where each subgrid has its own local time step determined by its local Courant limit. The late-time stability of LTS schemes, however, is one of the main concerns of FDTD research during the past quarter century.

### 3.5.2 State of the art

The term “subgridding” was coined in [43], where an LTS approach was readily proposed. This scheme was unstable, as was the case for many early publications about subgridding, such as the very accurate scheme described in [44]. It became clear very soon that the reciprocity of Maxwell’s equations needed to be preserved on the discrete level. The fulfillment of spatial reciprocity led to the symmetric (or reciprocal) subgridding methods. In first instance, they used a small global time step depending on the cell size of the subgrid [45]. Later, a separate spatial and temporal interface allowed to delay the instability of reciprocal LTS schemes [46]. A very promising stable subgridding scheme with explicit local time-stepping and implicit interfacing is reported in [47], but has, to the author’s best knowledge, never been further pursued. The ad hoc use of fully implicit time integration inside the subgrid as to enlarge the subgrid’s time step without stability issues has been proposed in e.g. [48]–[50], but is theoretically not well founded. Besides, these fully implicit subgridding methods are often either inaccurate (ADI-FDTD) or inefficient (CN-FDTD). In [51], spatial filters based on expensive discrete Fourier transforms are employed to stabilize subgridding methods with a single global time step that can be picked based on accuracy.

A new category of LTS subgridding schemes based on grid overlap instead of grid stitching was introduced in [52], where digital filters were employed as spatial decimators and interpolators along the interface to suppress instabilities. This idea was further developed in [31], [53], [54], disguised as “Huygens subgrid-

ding” (HSG). HSG is a typical example of a subgridding method that should be used for DD purposes: it allows much flexibility inside the subgrid, but it has difficulties placing multiple subgrids next to each other. The Huygens subgrid can be nonuniform and rotated [55], it can be updated implicitly [56], it can be spatially and temporally collocated [57], etcetera. However, despite the many efforts, HSG is late-time unstable.

In [18], [58], another interesting type of subgridding is proposed, derived from finite element principles. Interestingly, this method preserves the exact sequence property and exhibits spatial reciprocity by construction. In contrast to many of the aforementioned methods, this approach suffers minimally from spurious reflections arising from the subgrid edges and corners owing to the correct discretization of the differential forms underpinning Maxwell’s equations. In Chapter 5 of this dissertation, it is shown that the subgrid interfacing can be interpreted in terms of finite integrations, which allows to place subgrids with different refinement ratios next to each other. Hence, this is an example of a subgridding method that is perfectly suited for AMR purposes, albeit with a small global time step. A stable extension of this subgridding technique with a local time-stepping scheme for arbitrary refinement ratios, would, without any doubt, make this the state-of-the-art subgridding method.

In [29], [59], a modular approach to prove subgridding stability is put forward based on the theory of dissipative systems and the earlier work in [30]. The name ‘dissipative systems’ is misleading as the theory also holds in the lossless case. Although drafted for global time-stepping methods, this type of stability analysis could maybe cause the breakthrough that is needed for LTS schemes such as the one alluded to above.



## References

- [1] P. Monk and E. Suli, “A convergence analysis of Yee’s scheme on nonuniform grids”, *SIAM Journal on Numerical Analysis*, vol. 31, no. 2, pp. 393–412, 1994.
- [2] P. Monk, “Sub-gridding FDTD schemes”, *Applied Computational Electromagnetics Society Journal*, vol. 11, no. 1, pp. 37–46, 1996.
- [3] W. Heinrich, K. Beilenhoff, P. Mezzanotte, and L. Roselli, “Optimum mesh grading for finite-difference method”, *IEEE Transactions on Microwave Theory and Techniques*, vol. 44, no. 9, pp. 1569–1574, 1996.
- [4] M. Celuch and W. K. Gwarek, “Properties of the FDTD method relevant to the analysis of microwave power problems”, *Journal of Microwave Power & Electromagnetic Energy*, vol. 41, no. 4, pp. 62–80, 2007.
- [5] S. D. Gedney, *Introduction to the Finite-Difference Time-Domain (FDTD) Method for Electromagnetics*. Morgan & Claypool publishers, 2011.
- [6] M. Nauta, M. Okoniewski, and M. Potter, “FDTD method on a Lebedev grid for anisotropic materials”, *Transactions on Antennas and Propagation*, vol. 61, no. 6, pp. 3161–3171, 2013.
- [7] W. Tierens and D. De Zutter, “An unconditionally stable time-domain discretization on cartesian meshes for the simulation of nonuniform magnetized cold plasma”, *Journal of Computational Physics*, vol. 231, pp. 5144–5156, 2012.
- [8] F. L. Teixeira, “Compatible discretizations for multiphysics: A brief review and some future challenges”, in *2016 IEEE International Symposium on Antennas and Propagation (APSURSI)*, 2016, pp. 1289–1290.
- [9] M. K. Berens, I. D. Flintoft, and J. F. Dawson, “Structured mesh generation: Open-source automatic nonuniform mesh generation for FDTD simulation.”, *IEEE Antennas and Propagation Magazine*, vol. 58, no. 3, pp. 45–55, 2016.
- [10] Y.-S. Chung, T. K. Sarkar, B. H. Jung, and M. Salazar-Palma, “An unconditionally stable scheme for the finite-difference time-domain method”, *IEEE Transactions on Microwave Theory and Techniques*, vol. 51, no. 3, pp. 697–704, 2003.
- [11] K. Srinivasan, “Multiscale EM and circuit simulation using the Laguerre-FDTD scheme for package-aware integrated-circuit design”, PhD thesis, Georgia Institute of Technology, 2008.

- [12] M. Yi, “Transient simulation for multiscale chip-package structures using the Laguerre-FDTD scheme”, PhD thesis, Georgia Institute of Technology, 2015.
- [13] Z. Y. Huang, L. H. Shi, B. Chen, and Y. H. Zhou, “A new unconditionally stable scheme for FDTD method using associated Hermite orthogonal functions”, *IEEE Transactions on Antennas and Propagation*, vol. 62, no. 9, pp. 4804–4809, 2014.
- [14] H. D. Raedt, K. Michielsen, J. S. Kile, and M. T. Figge, “Solving the Maxwell equations by the Chebyshev method: A one-step finite-difference time-domain algorithm”, *IEEE Transactions on Antennas and Propagation*, vol. 51, no. 11, pp. 3155–3160, 2003.
- [15] K. Yee, “Numerical solution of initial boundary value problems involving Maxwell’s equations in isotropic media”, *IEEE Transactions on Antennas and Propagation*, vol. 14, no. 3, pp. 302–307, 1966.
- [16] M. Clemens and T. Weiland, “Discrete electromagnetism with the finite integration technique”, *Journal of Electromagnetic Waves and Applications*, vol. 15, no. 1, pp. 79–80, 2001.
- [17] R. Schuhmann, P. Schmidt, and T. Weiland, “A new Whitney-based material operator for the finite-integration technique on triangular grids”, *IEEE Transactions on Magnetics*, vol. 38, no. 2, pp. 409–412, 2002.
- [18] R. Chilton, “H-, P- and T-refinement strategies for the Finite-Difference-Time-Domain (FDTD) method developed via Finite-Element (FE) principles”, PhD thesis, Ohio State University, 2008.
- [19] B. De Deckere, A. Van Londersele, D. De Zutter, and D. Vande Ginste, “Birefringent dispersive FDTD subgridding scheme”, *Electronics Letters*, vol. 52, no. 17, pp. 1455–1457, 2016.
- [20] A. Van Londersele, D. De Zutter, and D. Vande Ginste, “An in-depth stability analysis of nonuniform FDTD combined with novel local implicitization techniques”, *Journal of Computational Physics*, vol. 342, pp. 177–193, 2017.
- [21] R. Lee, “A note on mass lumping in the finite element time domain method”, *IEEE Transactions on Antennas and Propagation*, vol. 54, no. 2, pp. 760–762, 2006.
- [22] S. Taflov and S. C. Hagness, *Computational Electrodynamics: The Finite-Difference Time-Domain Method (Third Edition)*. Artech House, 2005.
- [23] M. Gaffar and D. Jiao, “An explicit and unconditionally stable FDTD method for electromagnetic analysis”, *IEEE Transactions on Microwave Theory and Techniques*, vol. 62, no. 11, pp. 2538–2550, 2014.
- [24] C. Chang and C. D. Sarris, “A spatially filtered finite-difference time-domain scheme with controllable stability beyond the CFL limit: Theory and applications”, *IEEE Transactions on Microwave Theory and Techniques*, vol. 61, no. 1, pp. 351–359, 2013.

- [25] R. Schuhmann and T. Weiland, "Conservation of discrete energy and related laws in the finite integration technique", *Progress In Electromagnetics Research (PIER)*, vol. 32, pp. 301–316, 2001.
- [26] J. C. Strikwerda, *Finite Difference Schemes and Partial Differential Equations (Second Edition)*. Society for Industrial and Applied Mathematics (SIAM), 2004.
- [27] S. Wang and F. L. Teixeira, "Some remarks on the stability of time-domain electromagnetic simulations", *IEEE Transactions on Antennas and Propagation*, vol. 52, no. 3, pp. 895–898, 2004.
- [28] F. Edelvik, R. Schuhmann, and T. Weiland, "A general stability analysis of FIT/FDTD applied to lossy dielectrics and lumped elements", *International Journal of Numerical Modelling: Electronic Networks, Devices and Fields*, vol. 17, pp. 407–419, 2004.
- [29] F. Bekmambetova, X. Zhang, and P. Triverio, "A dissipative systems theory for FDTD with application to stability analysis and subgridding", *IEEE Transactions on Antennas and Propagation*, vol. PP, no. 99, pp. 1–1, 2016.
- [30] B. Denecker, L. Knockaert, F. Olyslager, and D. De Zutter, "A new state-space-based algorithm to assess the stability of the finite-difference time-domain method for 3D finite inhomogeneous problems", *AEU - International Journal of Electronics and Communications*, vol. 58, no. 5, pp. 339–348, 2004.
- [31] J.-P. Bérenger, "A Huygens subgridding for the FDTD method", *IEEE Transactions on Antennas and Propagation*, vol. 54, no. 12, pp. 3797–3804, 2006.
- [32] —, "Propagation and aliasing of high frequencies in the FDTD grid", *IEEE Transactions on Electromagnetic Compatibility*, vol. 58, no. 1, pp. 117–124, 2016.
- [33] —, "A perfectly matched layer for the absorption of electromagnetic waves", *Journal of Computational Physics*, vol. 114, no. 2, pp. 185–200, 1994.
- [34] S. D. Gedney, "An anisotropic perfectly matched layer-absorbing medium for the truncation of FDTD lattices", *IEEE Transactions on Antennas and Propagation*, vol. 44, no. 12, pp. 1630–1639, 1996.
- [35] W. C. Chew and W. H. Weedon, "A 3D perfectly matched medium from modified Maxwell's equations with stretched coordinates", *Microwave and Optical Technology Letters*, vol. 7, no. 13, pp. 599–604, 1994.
- [36] J. A. Roden and S. D. Gedney, "Convolution PML: An efficient FDTD implementation of the CFS-PML for arbitrary media", *Microwave and Optical Technology Letters*, vol. 27, no. 5, pp. 334–339, 2000.
- [37] W. Yu, X. Yang, Y. Liu, and R. Mittra, *Electromagnetic Simulation Techniques Based on the FDTD Method*. John Wiley & Sons, Inc., 2009.

- [38] J.-P. Bérenger, “A historical review of the absorbing boundary conditions for electromagnetics”, *Forum for Electromagnetic Research Methods and Application Technologies (FERMAT)*, vol. 9, 2015.
- [39] L. Kulas and M. Mrozowski, “Stability of the FDTD scheme containing macromodels”, *IEEE Microwave and Wireless Components Letters*, vol. 14, no. 10, pp. 484–486, 2004.
- [40] B.-N. Jiang, J. Wu, and L. Povinelli, “The origin of spurious solutions in computational electromagnetics”, *Journal of Computational Physics*, vol. 125, no. 1, pp. 104–123, 1996.
- [41] I. Valuev, A. Deinega, A. Knizhnik, and B. Potapkin, “Creating numerically efficient FDTD simulations using generic C++ programming”, in *International Conference on Computational Science and Its Applications (ICCSA)*, vol. 4707, 2007, pp. 213–226.
- [42] S. Van Den Berghe, “Object-oriented electromagnetic simulations with the finite-difference time-domain method”, PhD thesis, Ghent University, 2000.
- [43] S. S. Zivanovic, K. S. Yee, and K. K. Mei, “A subgridding method for the time-domain finite-difference method to solve Maxwell’s equations”, *IEEE Transactions on Microwave Theory and Techniques*, vol. 39, no. 3, pp. 471–479, 1991.
- [44] M. Okoniewski, E. Okoniewska, and M. A. Stuchly, “Three-dimensional subgridding algorithm for FDTD”, *IEEE Transactions on Antennas and Propagation*, vol. 45, no. 3, pp. 422–429, 1997.
- [45] T. Weiland, “A consistent subgridding scheme for the finite difference time domain method”, *International Journal of Numerical Modelling Electronic Networks Devices and Fields*, vol. 9, no. 5, pp. 359–374, 1996.
- [46] K. Xiao, D. J. Pommerenke, and J. L. Drewniak, “A three-dimensional FDTD subgridding algorithm with separated temporal and spatial interfaces and related stability analysis”, *IEEE Transactions on Antennas and Propagation*, vol. 55, no. 7, pp. 1981–1990, 2007.
- [47] F. Collino, T. Fouquet, and P. Joly, “Conservative space-time mesh refinement methods for the FDTD solution of Maxwell’s equations”, *Journal of Computational Physics*, vol. 211, no. 1, pp. 9–35, 2006.
- [48] B.-Z. Wang, Y. Wang, W. Yu, and R. Mittra, “A hybrid 2-D ADI-FDTD subgridding scheme for modeling on-chip interconnects”, *IEEE Transactions on Advanced Packaging*, vol. 24, no. 4, pp. 528–533, 2001.
- [49] T.-C. Lin and C.-W. Kuo, “A novel and efficient subgridding scheme in FDTD method using the Crank-Nicolson algorithm”, *Microwave and Optical Technology Letters*, vol. 49, no. 12, pp. 3103–3106, 2007.
- [50] M. R. Cabello, L. D. Angulo, J. Alvarez, I. D. Flintoft, S. Bourke, J. F. Dawson, R. G. Martin, and S. G. Garcia, “A hybrid Crank-Nicolson FDTD subgridding boundary condition for lossy thin-layer modeling”, *IEEE Transactions on Microwave Theory and Techniques*, vol. 65, no. 5, pp. 1397–1406, 2017.

- [51] C. Chang and C. D. Sarris, "An efficient implementation of a 3D spatially-filtered FDTD subgridding scheme", in *Proceedings of the 2012 IEEE International Symposium on Antennas and Propagation*, 2012, pp. 1–2.
- [52] B. Donderici and F. L. Teixeira, "Improved FDTD subgridding algorithms via digital filtering and domain overriding", *IEEE Transactions on Antennas and Propagation*, vol. 53, no. 9, pp. 2938–2951, 2005.
- [53] J.-P. Bérenger, "Extension of the FDTD Huygens subgridding algorithm to two dimensions", *IEEE Transactions on Antennas and Propagation*, vol. 57, no. 12, pp. 3860–3867, 2009.
- [54] —, "The Huygens subgridding for the numerical solution of the Maxwell equations", *Journal of Computational Physics*, vol. 230, no. 14, pp. 5635 – 5659, 2011.
- [55] C. J. Railton, "Rotated subgrids in the FDTD method", *IEEE Transactions on Antennas and Propagation*, vol. 64, no. 7, pp. 3047–3054, 2016.
- [56] Z. Huang, G. G. Pan, and K. S. Chen, "A synchronized multigrid time domain method via Huygens subgridding and implicit algorithms", *IEEE Transactions on Antennas and Propagation*, vol. 61, no. 5, pp. 2605–2614, 2013.
- [57] A. Van Londersele, D. De Zutter, and D. Vande Ginste, "Huygens subgridding combined with the 2D fully collocated implicit FDTD method", in *2016 IEEE International Symposium on Antennas and Propagation (APSURSI)*, Fajardo, Puerto Rico, 26 June - 1 July 2016, pp. 2025–2026.
- [58] R. A. Chilton and R. Lee, "Conservative and provably stable FDTD subgridding", *IEEE Transactions on Antennas and Propagation*, vol. 55, no. 9, pp. 2537–2549, 2007.
- [59] F. Bekmambetova, X. Zhang, and P. Triverio, "A dissipative systems theory for FDTD with application to stability analysis and subgridding", *IEEE Transactions on Antennas and Propagation*, vol. 65, no. 2, pp. 751–762, 2017.



PART II

Novel Contributions



# 4

## Stability of Locally Implicit Methods

*“Almost anything you can do with  $A^{-1}$  can be done without it.”*

Forsythe and Moler

★ ★ ★

*In this chapter, three local implicitization techniques are proposed and carefully analyzed in order to relax the traditional time step limit of the FDTD method on a nonuniform, staggered, tensor-product grid: Newmark, Crank-Nicolson (CN) and alternating-direction implicit (ADI) implicitization. All of them are applied in preferable directions, alike hybrid implicit-explicit (HIE) methods, as to limit the rank of the sparse linear systems. Both exponential and polynomial stability are rigorously investigated for arbitrary grid spacings and arbitrary inhomogeneous, possibly lossy, isotropic media. Numerical examples confirm the conservation of energy inside a cavity for a million iterations if the time step is chosen below the proposed relaxed limit. Apart from the theoretical contributions, new accomplishments such as the development of the leapfrog alternating-direction hybrid implicit-explicit (ADHIE) FDTD method and a less stringent Courant-like time step limit for the conventional, fully explicit FDTD method on a nonuniform grid, have immediate practical applications.*

## 4.1 Introduction

As stated in the previous chapters, the finite-difference time-domain method is one of the prevalent numerical techniques to predict electromagnetic behavior by solving Maxwell's equations in the time domain. Often, the second-order accuracy of the uniform Yee grid (Fig. 3.1) is locally given up in favor of more flexible nonuniform grids, which preserve the tensor-product nature but have step sizes that vary along the respective axis (e.g.  $\Delta x$  varies along the  $x$ -axis). One of the major drawbacks of the nonuniform FDTD method is the dependence of the time step on the smallest cell size, as dictated by the Courant stability limit (3.77). Hence, multiscale problems that require a locally increased resolution, are usually temporally oversampled to guarantee numerical stability. Various implicit and semi-implicit techniques have been proposed to sidestep (3.77) such that fewer time iterations are needed at the cost of more expensive computations per iteration. Generally, these techniques are applied throughout the whole grid because little is known about their influence on the stability limit if they would be applied locally.

The aim of this chapter is to put the stability of the FDTD method on nonuniform tensor-product grids, as well as its combination with several local implicitization techniques, on a firm mathematical footing. The proposed techniques permit implicitization in preferable directions as to end up with low-rank banded matrices, such that the reduced number of iterations outweighs the slightly increased computational cost per iteration for multiscale problems. The typical configurations that will be tackled are illustrated in Fig. 4.1. If a thin layer or thin wire needs to be modeled, the nonuniform grid is locally much more dense. It will be demonstrated, both analytically and numerically, that the proposed local implicitization techniques allow to eliminate the small step sizes enforced by the thin object from the stability limit.

The remainder of this chapter first lays out the update equations of each of the three proposed local implicitization techniques: Newmark, CN and ADI implicitization. Next, in Section 4.3, the stability of each technique is discussed. Two types of stability analyses are put forward: one based on  $z$ -transform theory and one extending the state-space-based method described in [1]. The Newmark implicitization technique is meticulously analyzed using the first approach. As a bonus, it leads to an explicit Courant-like time step limit for the conventional FDTD method on nonuniform grids that is less stringent than the one found in [2]. This new relaxed time step limit is directly applicable in classical FDTD software that leverages nonuniform gridding. The ADI implicitization technique is handled by the state-space approach, whereas the CN implicitization method is concisely analyzed using both approaches. In Section 4.4, the analytical results are numerically validated using the example of Fig. 4.1(a). The chapter concludes with a summary of the pros and cons of each local implicitization technique.

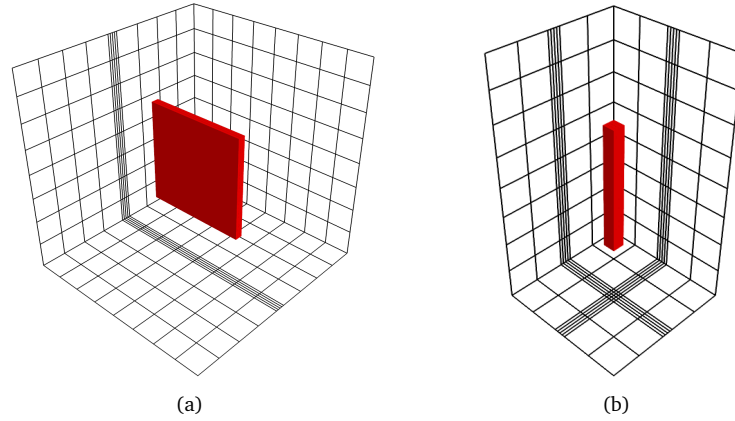


**Figure 4.1:** 3-D representation of a nonuniform tensor-product grid obtained by projecting the primary-grid edges on each of the three coordinate planes for **(a)** a thin plate and **(b)** a thin wire.

## 4.2 Update equations

We summarize the update equations for each of the three implicitization techniques, where we choose to implicitize the magnetic fields. A dual scheme, implicitizing the electric fields, of course, exists as well and is discussed in [3]. All proposed FDTD techniques use the spatial discretization described in Section 3.3.1. More specifically, the electric and magnetic fields are discretized on a nonuniform tensor-product grid terminated by perfectly electrically conducting (PEC) boundary conditions. The considered medium is isotropic, inhomogeneous and possibly lossy.

### 4.2.1 Newmark implicitization

The Newmark- $\beta$  technique is frequently used in finite-element time-domain simulations (e.g. [4]), but it is only recently investigated in the FDTD context. In one variant [5], both curls are time averaged as prescribed by the Newmark- $\beta$  scheme, whereas in another variant [6] only a single one is. Indeed, the unconditionally stable technique proposed in [6] is the Newmark- $\beta$  time integration method with  $\beta = 0.25$ , perceived as a dispersive background medium, which allows to interpret partial implicitization in one instead of two directions as a manifestation of anisotropy. Here, the unconditionally stable technique of [6] is extended to 3-D

and applied locally, which gives rise to the update scheme

$$\begin{aligned} & \begin{bmatrix} \frac{M_\varepsilon}{\Delta t} + \frac{M_\sigma}{2} & -\frac{C}{4}(I_{n_h} - P) \\ C^T & \frac{M_\mu}{\Delta t} \end{bmatrix} \mathbf{x}_{n+2} \\ &= \begin{bmatrix} \frac{M_\varepsilon}{\Delta t} - \frac{M_\sigma}{2} & \frac{C}{2}(I_{n_h} + P) \\ 0 & \frac{M_\mu}{\Delta t} \end{bmatrix} \mathbf{x}_{n+1} + \begin{bmatrix} 0 & \frac{C}{4}(I_{n_h} - P) \\ 0 & 0 \end{bmatrix} \mathbf{x}_n + \mathbf{s}_{n+1} \end{aligned} \quad (4.1)$$

with

$$\mathbf{x}_n = \begin{bmatrix} \hat{\mathbf{e}}((n-0.5)\Delta t) \\ \hat{\mathbf{h}}(n\Delta t) \end{bmatrix} \quad \mathbf{s}_n = \begin{bmatrix} -\hat{\mathbf{j}}(n\Delta t) \\ 0 \end{bmatrix} \quad (4.2)$$

and  $P$  the  $n_h$ -dimensional diagonal matrix with elements

$$P|_{i,i} = \begin{cases} 1 & \text{if } \hat{\mathbf{h}}_i \text{ is updated explicitly} \\ 0 & \text{if } \hat{\mathbf{h}}_i \text{ is updated implicitly} \end{cases}, \quad (4.3)$$

and with  $M_\mu$ ,  $M_\varepsilon$  and  $M_\sigma$  the FIT material matrices defined in (3.26) and (3.36). Interestingly, this Newmark- $\beta$  method naturally entered the scene in the finite-element analysis performed in Section 3.3.3, provided that the mass matrices pertaining to the space discretization are lumped by the trapezoid rule and the mass matrices pertaining to the time discretization by the midpoint rule. Indeed, the finite-element update equations (3.63) and (3.68) are identical to (4.1) for  $P = 0$ .

#### 4.2.2 CN implicitization

The Crank-Nicolson method is well-known in the FDTD community (e.g. [7]). If applied locally, its update scheme is

$$\begin{aligned} & \begin{bmatrix} \frac{M_\varepsilon}{\Delta t} + \frac{M_\sigma}{2} & -\frac{C}{2}(I_{n_h} - P) \\ (I_{n_h} + P)\frac{C^T}{2} & \frac{M_\mu}{\Delta t} \end{bmatrix} \mathbf{x}_{n+1} \\ &= \begin{bmatrix} \frac{M_\varepsilon}{\Delta t} - \frac{M_\sigma}{2} & \frac{C}{2}(I_{n_h} + P) \\ -(I_{n_h} - P)\frac{C^T}{2} & \frac{M_\mu}{\Delta t} \end{bmatrix} \mathbf{x}_n + \mathbf{s}_n \end{aligned} \quad (4.4)$$

with

$$\mathbf{x}_n = \begin{bmatrix} \hat{\mathbf{e}}((n-0.5)\Delta t) \\ P\hat{\mathbf{h}}(n\Delta t) + (I_{n_h} - P)\hat{\mathbf{h}}((n-0.5)\Delta t) \end{bmatrix} \quad (4.5)$$

and  $P$  given by (4.3). The time discretization of the implicitized magnetic fields is identical to that of the electric fields. A similar time discretization holds for the source term.

### 4.2.3 ADI implicitization

Although the original ADI-FDTD method was a split-step method where additional field variables were needed at intermediate time instances, it has evolved to a one-step leapfrog update scheme with the same dispersion and stability properties but improved computation time and memory requirements [8]. Both the split-step and the leapfrog ADI method split the curl incidence matrix into two parts, e.g.  $C = C_1 + C_2$ , and this in a clever way as to end up with tridiagonal matrices that scale with the number of cells in only one dimension. We call this *complete curl splitting* as opposed to *incomplete curl splitting*, which will be presented in this chapter. Our new curl splitting technique generalizes the traditional leapfrog ADI method, which is fully implicit and unconditionally stable, to a hybrid implicit-explicit version of the ADI method, named the “leapfrog ADHIE-FDTD method”, which is only partially implicit and weakly conditionally stable. Without going into the details yet, both the traditional leapfrog ADI and the newly proposed leapfrog ADHIE update scheme can be cast as:

$$\begin{aligned} & \begin{bmatrix} \frac{M_\varepsilon}{\Delta t} + \frac{M_\sigma}{2} + \frac{\Delta t}{4\alpha^2} C_1 M_\mu^{-1} C_1^T & 0 \\ C^T & \frac{M_\mu}{\Delta t} + \frac{\Delta t}{4\alpha^2} C_2^T M_\varepsilon^{-1} C_2 \end{bmatrix} \mathbf{x}_{n+1} \\ &= \begin{bmatrix} \frac{M_\varepsilon}{\Delta t} - \frac{M_\sigma}{2} + \frac{\Delta t}{4\alpha^2} C_1 M_\mu^{-1} C_1^T & C \\ 0 & \frac{M_\mu}{\Delta t} + \frac{\Delta t}{4\alpha^2} C_2^T M_\varepsilon^{-1} C_2 \end{bmatrix} \mathbf{x}_n + \mathbf{s}_n \end{aligned} \quad (4.6)$$

where  $\mathbf{x}_n$  and  $\mathbf{s}_n$  are given by (4.2). The scalar  $\alpha$  is a tunable parameter that has to be chosen in the interval  $]0, 1[$  for incomplete curl splitting and equals one for complete curl splitting. The curl parts  $C_1$  and  $C_2$  do not necessarily sum up to  $C$ . They will be defined in Section 4.3.3. Note that, if they were zero, (4.6) would reduce to the conventional, fully explicit FDTD method. Hence, they constitute a perturbation, which results in the so-called ADI splitting error [9, Eq. 11]. This leads to non-negligible numerical errors for time steps considerably exceeding the Courant limit and for electromagnetic fields with large spatial gradients.

## 4.3 Lyapunov stability

### 4.3.1 Newmark implicitization

#### Exponential stability

The discrete-time system (4.1) is transformed to the  $z$ -domain for the most delicate case where all energy is trapped inside a lossless cavity, resulting in the linear system

$$A\mathbf{x} = \mathbf{s} \quad , \quad (4.7)$$

where

$$\mathbf{x} = \sum_{n=0}^{\infty} \mathbf{x}_n z^{-n} \quad \mathbf{s} = \sum_{n=0}^{\infty} \mathbf{s}_n z^{-n} , \quad (4.8)$$

with initial conditions

$$\mathbf{x}_0 = \mathbf{x}_1 = \mathbf{s}_0 = 0 , \quad (4.9)$$

and system matrix

$$A = \begin{bmatrix} (z-1)\frac{M_\varepsilon}{\Delta t} & -C \mathcal{I} \\ z C^T & (z-1)\frac{M_\mu}{\Delta t} \end{bmatrix} . \quad (4.10)$$

The diagonal *implicitization matrix*  $\mathcal{I} \in \mathbb{C}^{n_h \times n_h}$ , occurring in (4.10), has elements

$$\mathcal{I}_{i,i} = \begin{cases} 1 & \text{if } \hat{\mathbf{h}}_i \text{ is updated explicitly} \\ (z+1)^2/(4z) & \text{if } \hat{\mathbf{h}}_i \text{ is updated implicitly} \end{cases} \quad (4.11)$$

Exponentially growing instabilities are excluded if the poles of the transfer function matrix belonging to (4.7), which are the solutions for  $z$  fulfilling  $\det(A) = 0$ , do not lie outside the unit disk [10]. Note that these solutions do not change upon replacement of  $A$  with

$$\tilde{A} = \Delta t \begin{bmatrix} M_\varepsilon & \\ & M_\mu \end{bmatrix}^{-1/2} A \begin{bmatrix} M_\varepsilon & \\ & M_\mu \end{bmatrix}^{-1/2} = \begin{bmatrix} (z-1)I_{n_e} & -2\tilde{C} \mathcal{I} \\ 2z\tilde{C}^T & (z-1)I_{n_h} \end{bmatrix} , \quad (4.12)$$

with the modified curl operator

$$\tilde{C} = \frac{\Delta t}{2} M_\varepsilon^{-1/2} C M_\mu^{-1/2} . \quad (4.13)$$

We used the fact that all matrices occurring in (4.12) are diagonal and regular, and that  $\mathcal{I}$  is diagonal as well. The remainder of this stability analysis focuses on the matrix  $\tilde{A}$ , which exhibits more symmetry than the original matrix  $A$ .

Similarly to [4], [11], [12], we need to distinguish between the static modes with  $z = 1$  and the dynamic modes with  $z \neq 1$ . The former obviously have unit-circle-bounded  $z$  and reside in the nullspace of the system matrix (4.10) with insertion of  $z = 1$ . They can also be found upon inspection of the nullspace of

$$\frac{1}{2}\tilde{A}_{z=1} = \begin{bmatrix} 0 & -\tilde{C} \\ \tilde{C}^T & 0 \end{bmatrix} . \quad (4.14)$$

For the dynamic modes, the block matrices on the diagonal of (4.12) are nonsingular and the stability analysis amounts to locating the roots of

$$\begin{aligned} \det(\tilde{A}_{z \neq 1}) &= \det((z-1)I_{n_h}) \det((z-1)I_{n_e} + 4z(z-1)^{-1} \tilde{C} \mathcal{I} \tilde{C}^T) \\ &= ((z-1))^{n_e+n_h} \det(I_{n_e} + 4z(z-1)^{-2} \tilde{C} \mathcal{I} \tilde{C}^T) , \end{aligned} \quad (4.15)$$

where we used the partitioned-matrix determinant rule [13, Eq. 2.8.13]. Along the lines of [14], substituting the bilinear transformation

$$z = \frac{\zeta - 1}{\zeta + 1}, \quad (4.16)$$

which projects the unit disk in  $z$ -space to the right half-plane in  $\zeta$ -space, into the remaining determinant in (4.15), yields

$$\det(I_{n_e} + \tilde{C}(\zeta^2 I_{n_h} - P)\tilde{C}^T) = 0, \quad (4.17)$$

with  $P$  given by (4.3). Searching the roots of (4.17) is equivalent to solving the generalized eigenvalue problem

$$\zeta^2 \tilde{C} \tilde{C}^T \mathbf{v} = (\tilde{C} P \tilde{C}^T - I_{n_h}) \mathbf{v}. \quad (4.18)$$

The zero eigenvalues of the curl-curl matrix in the l.h.s. of (4.18) give rise to so-called infinite eigenvalues  $\zeta^2 = \infty$  of the generalized eigenvalue problem, which are doubly mapped to  $z = 1$ . They correspond to static modes, which have already been treated above and which were not allowed in the derivation of (4.15). Therefore, we only consider the finite eigenvalues of (4.18), which correspond to the dynamic modes. Left-multiplying (4.18) by the Hermitian transpose of  $\mathbf{v}$  and subsequently subtracting/adding the Hermitian-transposed equation, yields respectively

$$\text{Im}(\zeta^2) \|\tilde{C}^T \mathbf{v}\|_2^2 = 0 \quad \forall \mathbf{v} \neq 0 \quad (4.19)$$

$$\text{Re}(\zeta^2) \|\tilde{C}^T \mathbf{v}\|_2^2 = \|P \tilde{C}^T \mathbf{v}\|_2^2 - \|\mathbf{v}\|_2^2 \quad \forall \mathbf{v} \neq 0, \quad (4.20)$$

where we readily replaced the occurring inner products by vector two-norms and used the fact that  $P = P^T P$ . Now, recall that exponentially growing instabilities are excluded by demanding that  $|z| \leq 1$ , which is, via the bilinear transformation (4.16), translated to  $\text{Re}(\zeta) \geq 0$ . From (4.19), we conclude that  $\text{Im}(\zeta^2) = 0$ , such that any solution  $\zeta^2$  yields either two real or two purely imaginary values for  $\pm\zeta$ . Since the first scenario always implies that one of the two values  $\pm\zeta$  resides on the negative real axis, the only way both  $\pm\zeta$  satisfy  $\text{Re}(\zeta) \geq 0$  is the case where they are purely imaginary. These purely imaginary values for  $\pm\zeta$  yield two complex conjugate roots  $z$  lying on the unit circle. From a physical perspective, this is exactly what we expect from a passive, lossless electromagnetic system; no energy is created, nor is there energy lost. In conclusion, stability is guaranteed if  $\text{Re}(\zeta^2) \leq 0$ , which is satisfied if and only if the r.h.s. of (4.20) cannot become positive. This gives rise to the stability criterion

$$\boxed{\|\tilde{C} P\|_2 \leq 1}, \quad (4.21)$$

with the matrix two-norm defined as [13, Eq. 8.4.3]

$$\|\tilde{C} P\|_2 = \|P \tilde{C}^T\|_2 = \max_{\mathbf{v} \neq 0} \frac{\|P \tilde{C}^T \mathbf{v}\|_2}{\|\mathbf{v}\|_2} = \sigma_{\max}(P \tilde{C}^T) = \sqrt{\lambda_{\max}(\tilde{C} P \tilde{C}^T)}. \quad (4.22)$$

The functions  $\sigma_{\max}()$  and  $\lambda_{\max}()$  denote the largest singular value and eigenvalue respectively. For a uniform grid that is homogeneously filled with vacuum and for which we fully explicitly advance in time, i.e.  $P = I_{n_h}$ , this upper bound is identical to the one found in [1], apart from the strict inequality. In Section 4.3.1, it will be shown that thoughtful implicitization, which eliminates all small spatial steps beneath a certain threshold from the r.h.s. of (4.21) by selecting the pertinent  $P|_{i,i}$  to be zero, can considerably reduce the time step limit for configurations with strongly varying spatial step sizes.

### Polynomial stability

Up till now, we only discussed *exponential* stability, meaning that the fields cannot diverge exponentially, which is achieved by the condition  $|z| \leq 1$ . As pointed out in [15], however, unit circle boundedness of  $z$  does not fully guarantee Lyapunov stability [13, Def. 11.10.1], which simply means that the fields cannot diverge to infinity in any kind of fashion. In addition, the poles located *on* the unit circle should be semisimple. In other words, they should have equal algebraic and geometric multiplicities [13, Def. 5.5.4], which is identical to the corresponding eigenvectors being linearly independent or, equivalently, to the corresponding matrix being diagonalizable. For a two-level update scheme, a violation of this condition manifests itself in a subtle polynomial growth because the amplification matrix then has at least one Jordan block of the form

$$\begin{bmatrix} \lambda & 1 \\ 0 & \lambda \end{bmatrix}, \quad (4.23)$$

with  $|\lambda| = 1$ , which is clearly unbounded upon self-multiplication. The same reasoning holds for higher-level schemes, as it is always possible to reduce them to a two-level scheme via a proper change of variables, e.g. companion linearization. In [4], the FETD method with Newmark- $\beta$  time integration of the second-order wave equation is shown to be prone to this type of late-time instability.

We will show now that our proposed Newmark implicitization method, and by extension also the conventional FDTD method, is free of polynomial instabilities. Therefore, note that there are  $2(n_e + n_h)$  poles  $z$  that satisfy  $\det(A) = 0$ , which can be essentially categorized into four types:

- complex conjugate pole pairs  $(z, z^*)$  with  $|z| = 1$ , yielding dynamic modes
- the repeated pole  $z = 1$ , yielding static modes
- the repeated pole  $z = -1$ , yielding “almost unstable” dynamic modes
- the non-physical repeated pole  $z = 0$

First, we discuss the last category, which in our scheme only appears as an algebraic artifact due to the linearization of the three-level Newmark scheme (4.1). If we shortly write (4.1) as

$$M_2 \mathbf{x}_{n+2} = M_1 \mathbf{x}_{n+1} + M_0 \mathbf{x}_n + \mathbf{s}_{n+1}, \quad (4.24)$$

then the companion linearization is

$$\begin{bmatrix} M_2 & 0 \\ 0 & I_{n_e+n_h} \end{bmatrix} \begin{bmatrix} \mathbf{x}_{n+2} \\ \mathbf{x}_{n+1} \end{bmatrix} = \begin{bmatrix} M_1 & M_0 \\ I_{n_e+n_h} & 0 \end{bmatrix} \begin{bmatrix} \mathbf{x}_{n+1} \\ \mathbf{x}_n \end{bmatrix} + \begin{bmatrix} \mathbf{s}_{n+1} \\ 0 \end{bmatrix}. \quad (4.25)$$

The block structure of the matrix in the r.h.s. of (4.25) is given by

$$\begin{bmatrix} B_{n_e \times n_e} & B_{n_e \times n_h} & 0 & B_{n_e \times n_h} \\ 0 & B_{n_h \times n_h} & 0 & 0 \\ B_{n_e \times n_e} & 0 & 0 & 0 \\ 0 & B_{n_h \times n_h} & 0 & 0 \end{bmatrix}, \quad (4.26)$$

where  $B_{n_1 \times n_2}$  denotes an arbitrary block of size  $n_1 \times n_2$  that has at least one non-zero element. A block permutation of the second and third row followed by a block permutation of the second and third column yields

$$\left[ \begin{array}{cc|cc} B_{n_e \times n_e} & 0 & B_{n_e \times n_h} & B_{n_e \times n_h} \\ B_{n_e \times n_e} & 0 & 0 & 0 \\ \hline 0 & 0 & B_{n_h \times n_h} & 0 \\ 0 & 0 & B_{n_h \times n_h} & 0 \end{array} \right]. \quad (4.27)$$

This is a two-by-two block upper triangular matrix. Hence, the eigenvalues are solely determined by the two blocks on its diagonal. The first block has at least  $n_e$  zero eigenvalues, the second block at least  $n_h$ . Hence, this reveals that the matrix in the r.h.s. of (4.25) has at least  $n_e + n_h$  zero eigenvalues or, equivalently, that the transfer function of the linear system (4.25) has a pole  $z = 0$  with multiplicity  $n_e + n_h$  or more. This pole would also have been found in the analysis of Section 4.3.1, if the source in (4.1) was shifted one step back in time;  $\mathbf{s}_n$  instead of  $\mathbf{s}_{n+1}$ . Anyway, since  $z = 0$  lies inside the unit disk, it is harmless. However, this zero pole, which originates from the sparsity of the matrix  $M_0$ , poses a fundamental difference between our proposed Newmark implicitization technique and the Newmark FETD method [4], because the linearized system (4.25) only requires  $n_e + n_h$  instead of  $2(n_e + n_h)$  linearly independent modes. For this reason, it is very likely that the Newmark- $\beta$  FDTD method described in [5] suffers from polynomially growing non-physical fields analogous to [4].

We will now prove that the remaining  $n_e + n_h$  poles belong to one of the above three mentioned categories on the unit circle and we will propose a sufficient condition such that they are guaranteed to be semisimple. The poles from the first category give rise to linearly independent dynamic modes in the  $\zeta^2$ -domain due to Lemma 1.

**Lemma 1.** *If  $A, B \in \mathbb{C}^{n \times n}$  are Hermitian and  $A$  is regular, then there exist  $n$  linearly independent vectors  $\mathbf{v} \in \mathbb{C}^{n \times 1}$  satisfying  $A\mathbf{v} = \lambda B\mathbf{v}$ .*

*Proof.* Since the matrices  $A$  and  $B$  are Hermitian, all eigenvalues  $\lambda$  must reside in  $\mathbb{R} \cup \{\infty\}$ . We prove the existence of a full linearly independent set of eigenvectors by ruling out the existence of non-trivial Jordan blocks in the Weierstrass canonical form. First, suppose that the finite eigenvalue  $\lambda_r \in \mathbb{R}$  gives rise to a Jordan block of size  $k > 1$ , then there must exist a Jordan chain [16, Def. 3.1]

$$(A - \lambda_r B) \mathbf{v}_1 = 0 \quad (4.28)$$

$$(A - \lambda_r B) \mathbf{v}_i = B \mathbf{v}_{i-1} \quad i = 2, \dots, k. \quad (4.29)$$

Consequently,

$$\mathbf{v}_1^\dagger B \mathbf{v}_1 = \mathbf{v}_2^\dagger (A - \lambda_r B)^\dagger \mathbf{v}_1 = \mathbf{v}_2^\dagger (A - \lambda_r B) \mathbf{v}_1 = 0, \quad (4.30)$$

where the first equality holds because of (4.29) with  $i = 2$ , the second equality uses the Hermitian symmetry of the matrix pencil  $(A - \lambda_r B)$ , and the third equality uses (4.28). Since  $\lambda_r$  is finite,  $\mathbf{v}_1$  cannot reside in the nullspace of  $B$ . Hence, (4.30) implies  $\mathbf{v}_1 = 0$ , which is in contradiction with the existence of the Jordan block.

Second, suppose that  $\infty$  is an eigenvalue corresponding to a Jordan block of size  $k > 1$ , then there must exist a Jordan chain [16, Def. 3.1]

$$B \mathbf{v}_1 = 0 \quad (4.31)$$

$$B \mathbf{v}_i = A \mathbf{v}_{i-1} \quad i = 2, \dots, k \quad (4.32)$$

Repeating the steps from (4.30), now yields

$$\mathbf{v}_1^\dagger A \mathbf{v}_1 = 0. \quad (4.33)$$

Since  $A$  is regular, we conclude that  $\mathbf{v}_1 = 0$ , which rules out the existence of the Jordan block. ■

Since every  $\zeta^2$  is, in a one-to-one sense, mapped to a complex conjugate pair  $(z, z^*)$  with  $z \neq z^*$ , this linear independence is preserved in the  $z$ -domain. Thus, the first category of poles is semisimple. A similar reasoning could be repeated for the second category, but since  $z = z^* = -1$ , linear independence of the dynamic modes in the  $z$ -domain cannot be guaranteed. This is, however, easily remedied by imposing a strict inequality

$$\boxed{\|\tilde{C} P\|_2 < 1}, \quad (4.34)$$

instead of (4.21). Now, we must show that the third category of poles, corresponding to the static modes, is semisimple. Since these modes are known to span the nullspace of the skew-symmetric matrix (4.14), the number of linearly independent static modes is given by

$$n_{\text{stat}} = \text{null}(\tilde{C}) + \text{null}(\tilde{C}^T), \quad (4.35)$$

where  $\text{null}()$  denotes the nullity, i.e. the dimension of the nullspace. It now suffices to show that these static modes together with the dynamic modes span the entire space  $\mathbb{R}^{(n_e+n_h) \times (n_e+n_h)}$ . From (4.18), it is found that the number of dynamic modes is

$$n_{\text{dyn}} = 2 \left( n_e - \text{null}(\tilde{C} \tilde{C}^T) \right). \quad (4.36)$$

Since from [13, Cor. 2.5.1],

$$\text{null}(\tilde{C} \tilde{C}^T) = \text{null}(\tilde{C}^T), \quad (4.37)$$

we obtain

$$n_{\text{stat}} + n_{\text{dyn}} = 2 n_e + \text{null}(\tilde{C}) - \text{null}(\tilde{C}^T) = n_e + n_h, \quad (4.38)$$

where the last equality uses [13, Cor. 2.5.3], namely

$$\text{null}(\tilde{C}) = \text{null}(\tilde{C}^T) + n_h - n_e. \quad (4.39)$$

In conclusion, Lyapunov stability, which encompasses both polynomial and exponential stability, is guaranteed if the time step satisfies (4.34). For uniform grids with explicit time-stepping, i.e.  $P = I_{n_h}$ , this agrees with [17], where the strict inequality (4.34) is found to be a necessary and sufficient condition for Lyapunov stability, and agrees with [18], where linear instability is numerically observed for a one-dimensional conventional FDTD simulation running at the “magic time step”, i.e., corresponding to an equality sign in (4.34).

Note that for a fully implicit grid, i.e.  $P = 0$ , it holds that  $\det(\tilde{A}_{z=-1}) \neq 0$ , such that the standalone Newmark FDTD method (4.1) is free of polynomial instability.

#### A Courant-like stability limit for fully explicit, nonuniform grids

To obtain a more transparent expression for the maximum allowed time step, we first derive an upper bound for the denominator of (4.34) in the simplified case that  $P = I_{n_h}$ . In other words, we consider a conventional FDTD scheme with explicit leapfrog time-stepping in each point of the grid. It is helpful to introduce the matrix

$$K = \begin{bmatrix} 0 & -I_{N_x} \otimes I_{n_y} \otimes K_z & I_{N_x} \otimes K_y \otimes I_{n_z} \\ I_{n_x} \otimes I_{N_y} \otimes K_z & 0 & -K_x \otimes I_{N_y} \otimes I_{n_z} \\ -I_{n_x} \otimes K_y \otimes I_{N_z} & K_x \otimes I_{n_y} \otimes I_{N_z} & 0 \end{bmatrix}, \quad (4.40)$$

with

$$K_d = (\delta_d^*)^{-1/2} D_d (\delta_d)^{-1/2} \quad d \in \{x, y, z\}. \quad (4.41)$$

As proven in [1, Eq. 44], a matrix of this particular form has the property

$$\|K\|_2^2 = \|K_x\|_2^2 + \|K_y\|_2^2 + \|K_z\|_2^2. \quad (4.42)$$

Now, it is left to the reader as an exercise to verify that

$$\tilde{C} = \frac{\Delta t}{2} [\varepsilon]^{-1/2} K [\mu]^{-1/2}. \quad (4.43)$$

In contrast to (4.13), the metric is now included in  $K$  instead of in the material matrices. Using submultiplicativity of the matrix two-norm [13, Eq. 9.3.4], yields

$$\|\tilde{C}\|_2^2 \leq \frac{\Delta t}{2} \frac{\|K\|_2^2}{\varepsilon_{\min} \mu_{\min}}, \quad (4.44)$$

with  $\varepsilon_{\min}$  and  $\mu_{\min}$  the lowest permittivity and permeability among all cells, which are often those of vacuum. A similar reasoning shows that

$$\|K_d\|_2^2 \leq \frac{\|D_d\|_2^2}{\delta_{d,\min} \delta_{d,\min}^*} \quad d \in \{x, y, z\}, \quad (4.45)$$

with  $\delta_{d,\min}$  and  $\delta_{d,\min}^*$  the smallest spatial step along the  $d$ -dimension present in the primary and dual grid respectively, and [1, Eq. 50]

$$\|D_d\|_2 = 2 \cos\left(\frac{\pi}{2N_d}\right) \quad d \in \{x, y, z\}. \quad (4.46)$$

So, if no implicitization is applied, (4.42) together with (4.44)–(4.46) substituted into (4.34) yields the time step limit

$$\Delta t < \frac{1}{\sqrt{\frac{1}{\varepsilon_{\min} \mu_{\min}} \sqrt{\frac{\cos^2(\frac{\pi}{2N_x})}{\delta_{x,\min} \delta_{x,\min}^*} + \frac{\cos^2(\frac{\pi}{2N_y})}{\delta_{y,\min} \delta_{y,\min}^*} + \frac{\cos^2(\frac{\pi}{2N_z})}{\delta_{z,\min} \delta_{z,\min}^*}}}}, \quad (4.47)$$

which is a generalization of the conventional Courant limit (3.77) to nonuniform grids. The upper bound (4.47) is tighter than the one proposed in [2]. Note that, due to the definition of the dual step (3.7), essentially being the average of two adjacent primary steps, holds that

$$\delta_{d,\min}^* \geq \delta_{d,\min} \quad d \in \{x, y, z\}. \quad (4.48)$$

#### Local implicitization to relax the stability limit

Now, we elaborate on how local implicitization affects the explicit stability limit (4.47) and, more importantly, how  $P$  can be tuned to get a more loose constraint. Suppose  $\delta_{x,\min} = \delta_x|_{i,i}$ , then we could implicitize all  $H_y$  and  $H_z$  with  $x$ -index  $i$ , which corresponds to

$$P = \begin{bmatrix} I_{n_x} \otimes I_{N_y} \otimes I_{N_z} & & \\ & P_x^i \otimes I_{n_y} \otimes I_{N_z} & \\ & & P_x^i \otimes I_{N_y} \otimes I_{n_z} \end{bmatrix}, \quad (4.49)$$

where we used the notation  $P_d^k$  to denote the diagonal projection matrix that is constructed by setting the  $k^{\text{th}}$  element of the  $N_d$ -dimensional identity matrix to

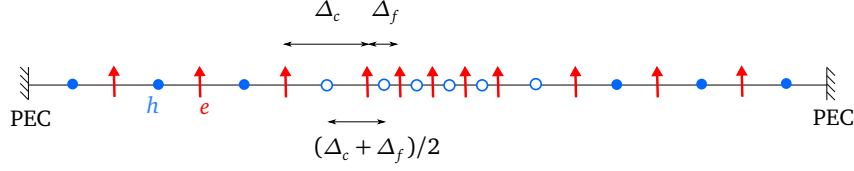


**Figure 4.2:** A one-dimensional refinement scheme with coarse step  $\Delta_c$ , fine step  $\Delta_f$  and average-sized transition step. Explicitly and implicitly updated magnetic fields are denoted by full and empty circles respectively. Electric field samples in between two implicitly updated magnetic field samples are involved in the implicit update, i.e. the matrix that needs to be inverted has rank 11. The Courant limit solely depends on  $\Delta_c$ .

zero with  $d \in \{x, y, z\}$ . Now, (4.44) changes to

$$\|\tilde{C}P\|_2^2 \leq \frac{\Delta t}{2} \frac{\|KP\|_2^2}{\varepsilon_{\min} \mu_{\min}}. \quad (4.50)$$

Because of the specific structure of  $P$ , essentially being a projection matrix, one can see that

$$KP = \begin{bmatrix} 0 & -I_{N_x} \otimes I_{N_y} \otimes K_z & I_{N_x} \otimes K_y \otimes I_{N_z} \\ I_{N_x} \otimes I_{N_y} \otimes K_z & 0 & -K_x P_x^i \otimes I_{N_y} \otimes I_{N_z} \\ -I_{N_x} \otimes K_y \otimes I_{N_z} & K_x P_x^i \otimes I_{N_y} \otimes I_{N_z} & 0 \end{bmatrix} P. \quad (4.51)$$

Consequently, submultiplicativity implies that (4.42) gives rise to

$$\|KP\|_2^2 \leq \|K_x P_x^i\|_2^2 + \|K_y\|_2^2 + \|K_z\|_2^2. \quad (4.52)$$

Since  $P_x^i$  directly acts on  $\delta_x$ , we succeeded in eliminating  $\delta_x|_{i,i}$  from the stability limit, and  $\delta_{x,\min}$  in (4.47) is replaced by the smallest step amongst those that were not eliminated via implicitization. If we would like to eliminate  $\delta_x^*|_{i,i}$ , it suffices to implicitize all  $H_y$  and  $H_z$  with  $x$ -index  $i-1$  and  $i$ , because the central-difference operator  $D_x$  is a bidiagonal matrix. This means that the one-dimensional refinement scheme illustrated in Fig. 4.2 is stable under the Courant limit imposed by the coarse step  $\Delta_c$ , if the magnetic fields indicated by empty circular markers are implicitly updated. Note that the dual Newmark scheme with implicitization of the electric instead of the magnetic fields would reduce the rank of the occurring matrix by two, because the transition step in the dual grid can be eliminated directly instead of eliminating the surrounding steps in the primary grid.

### 4.3.2 CN implicitization

The conditional stability of the local application of Crank-Nicolson time integration will be proven in two different ways. The first one is inspired by the previous analysis for Newmark implicitization. The second one is built on the insights of [1].

It forms the bridge to the third and last implicitization technique which locally applies the leapfrog ADI method in preferable directions. Both arrive at the same conclusion.

### First stability analysis

The  $z$ -transform of the discrete-time system (4.4), again in the lossless case, yields the system matrix

$$A_{\text{cn}} = \begin{bmatrix} (z-1)\frac{M_\varepsilon}{\Delta t} & -C \mathcal{I}_1 \\ z \mathcal{I}_2 C^T & (z-1)\frac{M_\mu}{\Delta t} \end{bmatrix}. \quad (4.53)$$

where

$$\mathcal{I}_1|_{i,i} = \begin{cases} 1 \\ (z+1)/2 \end{cases} \quad \mathcal{I}_2|_{i,i} = \begin{cases} 1 & \text{if } \hat{\mathbf{h}}_i \text{ is updated explicitly} \\ (1+z^{-1})/2 & \text{if } \hat{\mathbf{h}}_i \text{ is updated implicitly} \end{cases} \quad (4.54)$$

The steps in Section 4.3.1 that led to (4.15), can be repeated yielding the characteristic equation

$$\det(I_{n_e} + 4z(z-1)^{-2} \tilde{C} \mathcal{I}_1 \mathcal{I}_2 \tilde{C}^T) = 0. \quad (4.55)$$

Somewhat surprisingly, this characteristic equation is identical to the one of Newmark implicitization since  $\mathcal{I}_1 \mathcal{I}_2 = \mathcal{I}$ . Hence, the exact same conclusions can be drawn for the relaxation of the Courant limit using CN implicitization as was the case for Newmark implicitization.

### Second stability analysis

The update equation (4.4), including losses but omitting the source term, can be rewritten as

$$(E_{\text{cn}} + F_{\text{cn}}) \tilde{\mathbf{x}}_{n+1} = (E_{\text{cn}} - F_{\text{cn}}) \tilde{\mathbf{x}}_n, \quad (4.56)$$

with decomposed update matrices

$$E_{\text{cn}} = \begin{bmatrix} I_{n_e} & \tilde{C} P \\ P \tilde{C}^T & I_{n_h} \end{bmatrix} \quad (4.57)$$

$$F_{\text{cn}} = \begin{bmatrix} \frac{1}{2} M_\varepsilon^{-1} M_\sigma & -\tilde{C} \\ \tilde{C}^T & 0 \end{bmatrix}, \quad (4.58)$$

new state vectors

$$\tilde{\mathbf{x}} = \begin{bmatrix} \tilde{\mathbf{e}} \\ \tilde{\mathbf{h}} \end{bmatrix} = \begin{bmatrix} M_\varepsilon^{1/2} \hat{\mathbf{e}} \\ M_\mu^{1/2} \hat{\mathbf{h}} \end{bmatrix}, \quad (4.59)$$

and the modified curl  $\tilde{C}$  specified in (4.13). According to [1], stability is assured if the matrix  $E_{\text{cn}}$  is positive definite and  $F_{\text{cn}} + F_{\text{cn}}^T$  is positive semi-definite. The latter is trivially true for physically existing materials. Further, the theory presented in [1, Eq. 22-30] shows that  $E_{\text{cn}}$  is positive definite if the time step satisfies (4.34). Rather unexpectedly, losses do not alter the stability limit.

Both stability analyses of CN implicitization lead to the same conclusion, being that — similar as was the case for Newmark implicitization — proper choices of  $\mathcal{I}_1$  and  $\mathcal{I}_2$  or, equivalently, of  $P$ , i.e. well-chosen implicitization, leads to a relaxation of the stability limit.

### 4.3.3 ADI implicitization

We start this section by presenting a rather atypical stability proof of the traditional leapfrog ADI method, again inspired by [1]. Next, we use the acquired insights to construct a leapfrog ADI formalism that allows implicitization in preferable directions. Finally, the novel leapfrog ADHIE method is used for local implicitization of the conventional FDTD method.

#### Stability analysis of leapfrog ADI-FDTD

The standard ADI-FDTD method splits the curl incidence matrix (3.16) into a sum  $C = C_1 + C_2$  with the two contributions given by

$$C_1 = \begin{bmatrix} 0 & 0 & I_{N_x} \otimes D_y \otimes I_{N_z} \\ I_{N_x} \otimes I_{N_y} \otimes D_z & 0 & 0 \\ 0 & D_x \otimes I_{N_y} \otimes I_{N_z} & 0 \end{bmatrix} \quad (4.60)$$

$$C_2 = \begin{bmatrix} 0 & -I_{N_x} \otimes I_{N_y} \otimes D_z & 0 \\ 0 & 0 & -D_x \otimes I_{N_y} \otimes I_{N_z} \\ -I_{N_x} \otimes D_y \otimes I_{N_z} & 0 & 0 \end{bmatrix} . \quad (4.61)$$

The update equation (4.6), without sources and with  $\alpha = 1$ , is rewritten as

$$(E_{\text{adi}} + F_{\text{adi}}) \tilde{\mathbf{x}}_{n+1} = (E_{\text{adi}} - F_{\text{adi}}) \tilde{\mathbf{x}}_n , \quad (4.62)$$

with decomposed update matrices

$$E_{\text{adi}} = \begin{bmatrix} I_{n_e} + \tilde{C}_1 \tilde{C}_1^T & (\tilde{C}_1 + \tilde{C}_2) \\ (\tilde{C}_1 + \tilde{C}_2)^T & I_{n_h} + \tilde{C}_2^T \tilde{C}_2 \end{bmatrix} \quad (4.63)$$

$$F_{\text{adi}} = \begin{bmatrix} \frac{1}{2} M_\varepsilon^{-1} M_\sigma & -(\tilde{C}_1 + \tilde{C}_2) \\ (\tilde{C}_1 + \tilde{C}_2)^T & 0 \end{bmatrix} , \quad (4.64)$$

and state vector  $\tilde{\mathbf{x}}$  defined in (4.59). The curl parts have undergone the same left- and right-multiplication as the total curl in (4.13). Since clearly  $F_{\text{adi}} + F_{\text{adi}}^T$  is positive semi-definite, stability is guaranteed if  $E_{\text{adi}}$  is positive definite. Note that  $E_{\text{adi}}$  can be factorized into  $E_{\text{adi}} = Q^T Q$  with

$$Q = \begin{bmatrix} I_{n_e} & \tilde{C}_2 \\ \tilde{C}_1^T & I_{n_h} \end{bmatrix}. \quad (4.65)$$

Consequently,

$$\mathbf{v}^T E_{\text{adi}} \mathbf{v} = \mathbf{v}^T Q^T Q \mathbf{v} = \|Q \mathbf{v}\|_2^2 \geq 0 \quad \forall \mathbf{v} \neq 0. \quad (4.66)$$

In other words,  $E_{\text{adi}}$  is positive semi-definite. In theory, linear instability could still occur for infelicitous time steps which render a singular matrix  $E_{\text{adi}}$ , corresponding to the pole  $z = -1$ . Even if this theoretical case exists, in practice, it is very unlikely to exactly pick such an unstable time step within the range of the machine precision. Therefore, as also reported in literature [8], the traditional leapfrog ADI-FDTD method may indeed be considered as unconditionally stable.

#### Leapfrog ADHIE-FDTD to implicitize selected dimensions

Suppose that we want to implicitize the  $x$ -dimension but not the  $y$ - and  $z$ -dimension, then we propose the following *incomplete* curl splitting

$$C_{x1} = \begin{bmatrix} 0 & 0 & 0 \\ 0 & 0 & 0 \\ 0 & D_x \otimes I_{n_y} \otimes I_{n_z} & 0 \end{bmatrix} \quad (4.67)$$

$$C_{x2} = \begin{bmatrix} 0 & 0 & 0 \\ 0 & 0 & -D_x \otimes I_{n_y} \otimes I_{n_z} \\ 0 & 0 & 0 \end{bmatrix} \quad (4.68)$$

$$C_{yz} = \begin{bmatrix} 0 & -I_{n_x} \otimes I_{n_y} \otimes D_z & I_{n_x} \otimes D_y \otimes I_{n_z} \\ I_{n_x} \otimes I_{n_y} \otimes D_z & 0 & 0 \\ -I_{n_x} \otimes D_y \otimes I_{n_z} & 0 & 0 \end{bmatrix}, \quad (4.69)$$

such that the total curl is given by  $C = C_{x1} + C_{x2} + C_{yz}$ . We now insert these three curl parts into (4.6) and proceed as in the previous paragraph. The only change to (4.62), is a modified matrix  $E_{\text{adi}}$ , given by

$$\begin{aligned} E_{\text{adi}} &= \begin{bmatrix} I_{n_e} + \frac{1}{\alpha^2} \tilde{C}_{x1} \tilde{C}_{x1}^T & (\tilde{C}_{x1} + \tilde{C}_{x2} + \tilde{C}_{yz}) \\ (\tilde{C}_{x1} + \tilde{C}_{x2} + \tilde{C}_{yz})^T & I_{n_h} + \frac{1}{\alpha^2} \tilde{C}_{x2}^T \tilde{C}_{x2} \end{bmatrix} \\ &= \underbrace{\begin{bmatrix} \alpha I_{n_e} & \frac{1}{\alpha} \tilde{C}_{x2} \end{bmatrix}^T}_{Q_x^T} \underbrace{\begin{bmatrix} \alpha I_{n_e} & \frac{1}{\alpha} \tilde{C}_{x2} \\ \frac{1}{\alpha} \tilde{C}_{x1}^T & \alpha I_{n_h} \end{bmatrix}}_{Q_x} + \underbrace{\begin{bmatrix} (1 - \alpha^2) I_{n_e} & \tilde{C}_{yz} \\ \tilde{C}_{yz}^T & (1 - \alpha^2) I_{n_h} \end{bmatrix}}_{Q_{yz}}. \end{aligned} \quad (4.70)$$

$Q_x^T Q_x$  is positive semi-definite. Consequently, stability is ensured if  $Q_{yz}$  is positive definite, which, along the lines of [1, Eq. 22-30], is found to be the case if

$$\|\tilde{C}_{yz}\|_2 < 1 - \alpha^2. \quad (4.71)$$

This is the 2-D Courant limit in the  $yz$ -plane reduced by a factor  $1 - \alpha^2$ . Based on the conventional leapfrog ADI scheme, the most intuitive value for  $\alpha$  would be one. In this case, however, (4.71) does not yield a valid upper bound for the time step. The scalar  $\alpha$  poses a trade-off: the smaller  $\alpha$ , the larger the maximum time step, but the more splitting error is introduced into the ADHIE scheme. Compared to the splitting error of the traditional split-step and one-step leapfrog ADI schemes [9, Eq. 11], the overall splitting error of our ADHIE scheme is heavily reduced due to the increased sparsity of the split curl parts  $C_{x1}$  and  $C_{x2}$ . Most importantly, (4.71) shows that all  $x$ -dependence is eliminated from the stability limit.

#### ADHIE local implicitization to relax the stability limit

Suppose we want to locally refine our 3-D grid in the  $x$ -direction. In contrast to the above, the difficulty is now that  $C_{x1}$  and  $C_{x2}$  do not encompass the whole  $x$ -dimension of the grid. Hence, the incomplete curl splitting looks as follows:

$$C_{x1} = \begin{bmatrix} 0 & 0 & 0 \\ 0 & 0 & 0 \\ 0 & D_x(I_{n_x} - P_x) \otimes I_{n_y} \otimes I_{n_z} & 0 \end{bmatrix} \quad (4.72)$$

$$C_{x2} = \begin{bmatrix} 0 & 0 & 0 \\ 0 & 0 & -D_x(I_{n_x} - P_x) \otimes I_{n_y} \otimes I_{n_z} \\ 0 & 0 & 0 \end{bmatrix} \quad (4.73)$$

$$C_{yz} = \begin{bmatrix} 0 & -I_{n_x} \otimes I_{n_y} \otimes D_z & I_{n_x} \otimes D_y \otimes I_{n_z} \\ I_{n_x} \otimes I_{n_y} \otimes D_z & 0 & -D_x P_x \otimes I_{n_y} \otimes I_{n_z} \\ -I_{n_x} \otimes D_y \otimes I_{n_z} & D_x P_x \otimes I_{n_y} \otimes I_{n_z} & 0 \end{bmatrix} \quad (4.74)$$

$P_x$  is the diagonal projection matrix that is zero if the corresponding primary step needs to be eliminated from the stability limit. It is readily observed that stability is again guaranteed if (4.71) is satisfied, but this time with  $\|\tilde{C}_{yz}\|_2$  derived from (4.74). Consequently, a proper choice of  $P_x$  can lead to a relaxation of the traditional Courant limit without having to implicitize the entire  $x$ -dimension.

## 4.4 Numerical validation: conservation of discrete energy

Consider the example depicted in Fig. 4.1(a), where a grid with  $12 \times 8 \times 8$  cells and main step size  $\Delta = 2.5$  mm is locally refined in the  $x$ -dimension by a factor

ten as follows:

$$\delta_x = \Delta \text{diag}\left(1, 1, 1, 1, \frac{1}{10}, \frac{1}{10}, \frac{1}{10}, \frac{1}{10}, 1, 1, 1, 1\right) \quad (4.75)$$

$$\delta_y = \delta_z = \Delta \text{diag}(1, 1, 1, 1, 1, 1, 1, 1, 1, 1, 1, 1) \quad (4.76)$$

The dual nodes are placed halfway the primary nodes, i.e.

$$\delta_x^* = \Delta \text{diag}\left(1, 1, 1, \frac{11}{20}, \frac{1}{10}, \frac{1}{10}, \frac{1}{10}, \frac{11}{20}, 1, 1, 1, 1\right) \quad (4.77)$$

$$\delta_y^* = \delta_z^* = \Delta \text{diag}(1, 1, 1, 1, 1, 1, 1, 1, 1, 1, 1, 1) \quad (4.78)$$

The most delicate case where all energy is trapped inside a PEC cavity filled with vacuum is analyzed. The cavity is excited by randomly initializing one of the electric field components to 1 V/m. Each simulation performs one million iterations and records the discrete energy

$$q_n = \frac{1}{2} \left( \tilde{\mathbf{e}}_n^T \tilde{\mathbf{e}}_n + \tilde{\mathbf{h}}_n^T \tilde{\mathbf{h}}_n \right) \quad (4.79)$$

with  $\tilde{\mathbf{e}}$  and  $\tilde{\mathbf{h}}$  defined in (4.59). Electric and magnetic energy are not necessarily collocated in time. In contrast to (3.79), the energy measure (4.79) can only have positive contributions from every electromagnetic field sample, such that diverging fields give rise to a diverging energy. The goal of the proposed implicitization techniques is to arrive at an efficient and flexible update scheme that preserves this energy measure when the time step equals the traditional Courant limit (3.77) of the coarse part of the grid, i.e.

$$\Delta t_{\text{coarse}} = \frac{\Delta}{c_0 \sqrt{3}} = 4.8145319 \text{ ps} \quad (4.80)$$

#### 4.4.1 Fully explicit

For conventional leapfrog time-stepping, the explicit Courant-like limit (4.47) and the numerically computed norm-based limit (4.21) are respectively given by

$$\Delta t_{\text{expl}}^{\text{fe}} = 0.8329849 \text{ ps} \quad (4.81)$$

$$\Delta t_{\text{num}}^{\text{fe}} = 0.8890071 \text{ ps} \quad (4.82)$$

As expected, the submultiplicativity (4.45) used to find (4.47) gives rise to a 6.7% smaller maximum time step. Fig. 4.3 shows the discrete energy (4.79) normalized to the initial energy  $q_0$  for three different time steps close to  $\Delta t_{\text{num}}^{\text{fe}}$ . For a time step slightly below  $\Delta t_{\text{num}}^{\text{fe}}$ , the simulation remains stable (Fig. 4.3(a)). For a time step slightly above  $\Delta t_{\text{num}}^{\text{fe}}$ , the simulation is exponentially unstable (Fig. 4.3(c)). For a time step that is exactly  $\Delta t_{\text{num}}^{\text{fe}}$ , the simulation is polynomially unstable

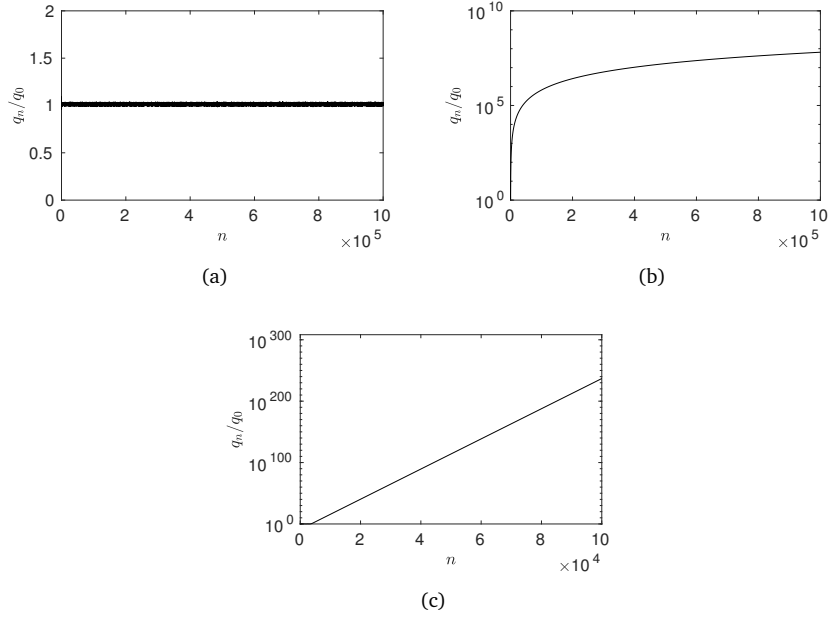


**Figure 4.3:** Normalized discrete energy  $q_n/q_0$  per iteration for conventional leapfrog time-stepping with  $\Delta t = (1 + \kappa) \Delta t_{\text{num}}^{\text{fe}}$ . **(a)** For  $\kappa = -10^{-6}$ , the total amount of energy in the cavity is conserved. **(b)** For  $\kappa = 0$ , the energy increases slower than exponentially. **(c)** For  $\kappa = 10^{-6}$ , the energy grows exponentially.

(Fig. 4.3(b)). This is in line with the algebraic stability analysis in Section 4.3.1. Note that the energy is not conserved from one iteration to the next, as was also observed in e.g. [11]. Fig. 4.3 confirms that (4.21) is the exact stability limit for nonuniform grids. Fig. 4.4 shows the relative error of the energy measure (3.79), which is conserved between two iterations, independently of the time step. Exponential instability is clearly observed due to round-off errors (Fig. 4.4(c)). However, the more subtle polynomial instability is well hidden by this energy measure (Fig. 4.4(b)), but is nevertheless still present. Hence, at this point, it needs to be stated that without round-off errors, i.e., with infinite floating-point precision, the energy measure (3.79) would not reveal the instabilities for time steps that are not below  $\Delta t_{\text{num}}^{\text{fe}}$ . The poles of the FDTD system are plotted in Fig. 4.5. They are numerically determined by constructing the amplification matrix and computing its eigenvalues with Matlab's built-in function `eig`. As expected, all poles of the lossless cavity are located on the unit circle. The number of poles inside the disk with center  $z = 1$  and a radius of thousand times the machine precision is 1306, which is found to be in exact agreement with (4.35). The poles also accumulate at  $z = -1$ , because the time step coincides with the exact stability limit. For time steps exceeding (4.82), the poles start diverging along the real axis. They come

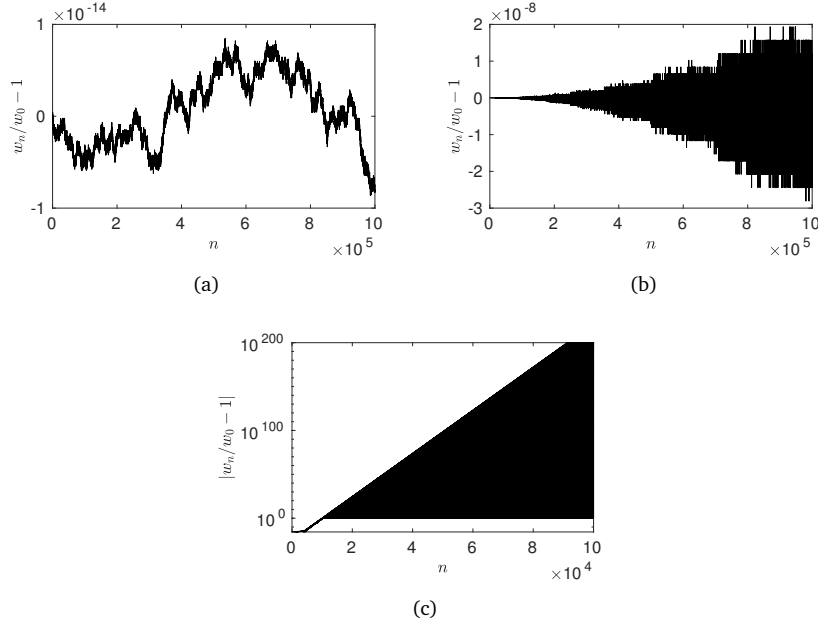


**Figure 4.4:** Relative error of the discrete energy  $w_n$  compared to the initial energy  $w_0$  per iteration for conventional leapfrog time-stepping with  $\Delta t = (1 + \kappa) \Delta t_{\text{num}}^{\text{fe}}$ . (a) For  $\kappa = -10^{-6}$ , the total amount of energy in the cavity is conserved from one iteration to the next aside from numerical noise that is of the order of magnitude of the machine precision. (b) For  $\kappa = 0$ , the energy is still conserved even though the fields are diverging, which causes the numerical noise to grow gradually due to round-off errors in the finite-sized floating-point numbers. (c) For  $\kappa = 10^{-6}$ , the energy is conserved, despite the diverging fields, until the round-off errors cause exponential instability.

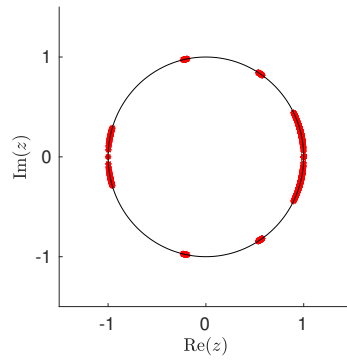


**Figure 4.5:** Location of the poles in the complex plane for the fully explicit simulation with  $\Delta t = \Delta t_{\text{num}}^{\text{fe}}$ .

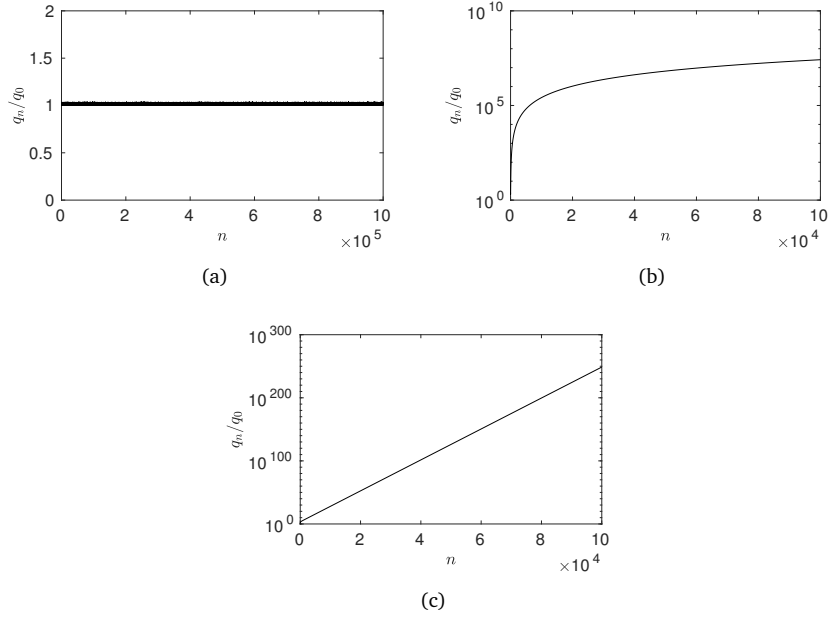


**Figure 4.6:** Normalized discrete energy  $q_n/q_0$  per iteration for Newmark implicitization with  $\Delta t = (1 + \kappa) \Delta t_{\text{num}}^{\text{cn}}$ . **(a)** For  $\kappa = -10^{-6}$ , the total amount of energy in the cavity is conserved. **(b)** For  $\kappa = 0$ , the energy increases slower than exponentially. **(c)** For  $\kappa = 10^{-6}$ , the energy grows exponentially.

in pairs: one left and one right of  $z = -1$ . The former category of poles causes numerical instability.

#### 4.4.2 Newmark and CN implicitization

Due to the high degree of resemblance between the Newmark and the Crank-Nicolson implicitization techniques, they are treated simultaneously in this section. Both techniques use a projection operator of the form (4.49) eliminating the step sizes of (4.75) and (4.77) that are smaller than  $\Delta$ . For our example,  $P_x^i$  in (4.49) is given by

$$P_x = \text{diag}(1, 1, 1, 0, 0, 0, 0, 0, 1, 1, 1) . \quad (4.83)$$

Both implicitization techniques have an identical maximum time step specified by (4.34), which is numerically determined to be

$$\Delta t_{\text{num}}^{\text{cn}} = 5.0418099 \text{ ps} . \quad (4.84)$$

The late-time behavior of the normalized energy (4.79) is studied in Fig. 4.6 and Fig. 4.7 for small perturbations of (4.84) and confirms that this is indeed the exact

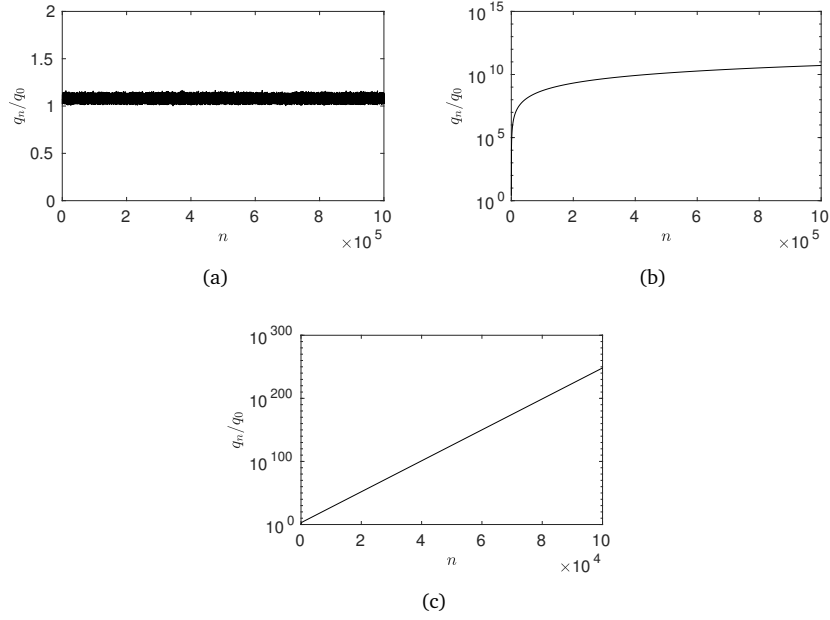


**Figure 4.7:** Normalized discrete energy  $q_n/q_0$  per iteration for Crank-Nicolson implicitization with  $\Delta t = (1 + \kappa) \Delta t_{\text{num}}^{\text{cn}}$ . **(a)** For  $\kappa = -10^{-6}$ , the total amount of energy in the cavity is conserved. **(b)** For  $\kappa = 0$ , the energy is still conserved but shows large fluctuations, indicating nearly unstable behavior. **(c)** For  $\kappa = 10^{-6}$ , the energy grows exponentially.

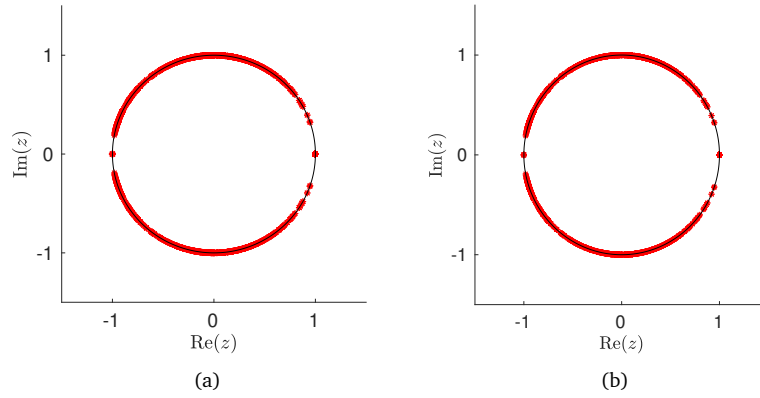


**Figure 4.8:** Location of the poles in the complex plane for  $\Delta t = \Delta t_{\text{num}}^{\text{cn}}$ . **(a)** Newmark implicitization, where the non-physical zero pole of the quadratic eigenvalue problem is omitted. **(b)** CN implicitization.

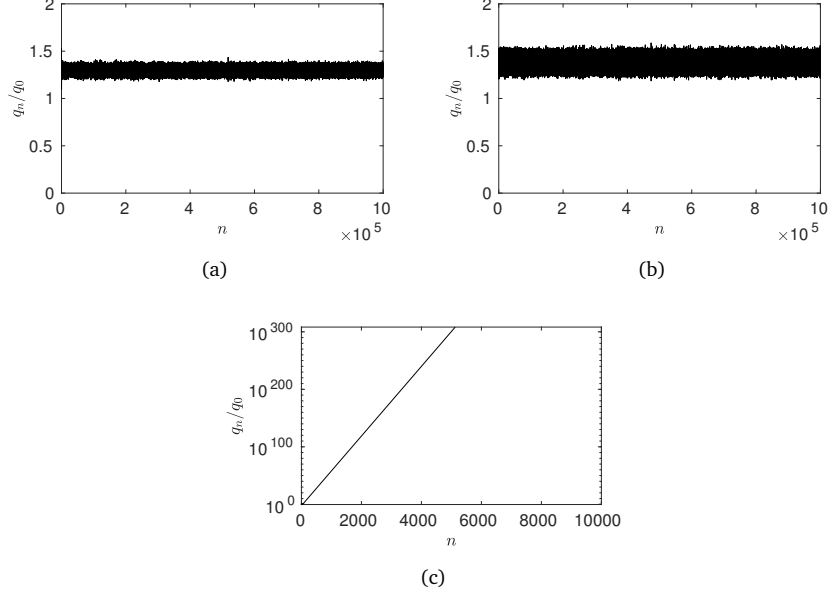


**Figure 4.9:** Normalized discrete energy per iteration for ADI implicitization with different time steps: (a)  $\Delta t = \Delta t_{\text{num}}^{\text{adi}}$ , (b)  $\Delta t = 1.30 \Delta t_{\text{num}}^{\text{adi}}$ , and (c)  $\Delta t = 1.33 \Delta t_{\text{num}}^{\text{adi}}$ .

upper bound on the time step to guarantee Lyapunov stability. As a side note, the spectra of both amplification matrices (Fig. 4.8) are identical, as could be expected from our stability analysis in Section 4.3.2. Compared to the conventional FDTD method (Fig. 4.5), the dynamic poles are pushed towards  $z = -1$  due to the larger time step. All three spectra have the same number of static modes. In conclusion, both implicitization techniques render a stable system for the pursued coarse time step (4.80).

#### 4.4.3 ADI implicitization

We adopt the split curl stencil (4.72)–(4.74) with projection operator (4.83). For this example, the leapfrog ADHIE update scheme employs  $\alpha = 0.5$ . A numerical estimation of the maximum time step (4.71) is then given by

$$\Delta t_{\text{num}}^{\text{adi}} = 3.7813574 \text{ ps} . \quad (4.85)$$

The small steps are clearly eliminated from the time step since (4.85) is four times larger than (4.82), but unfortunately (4.85) is smaller than the desired time step (4.80). Fig. 4.9 confirms that the local implicitization technique is stable, but also shows that the upper bound (4.71) is an underestimation of the exact upper bound. Numerical experiments to determine the actual upper bound (e.g. Fig. 4.10) reveal that, for this case, the upper bound (4.85) is underestimated by a factor of

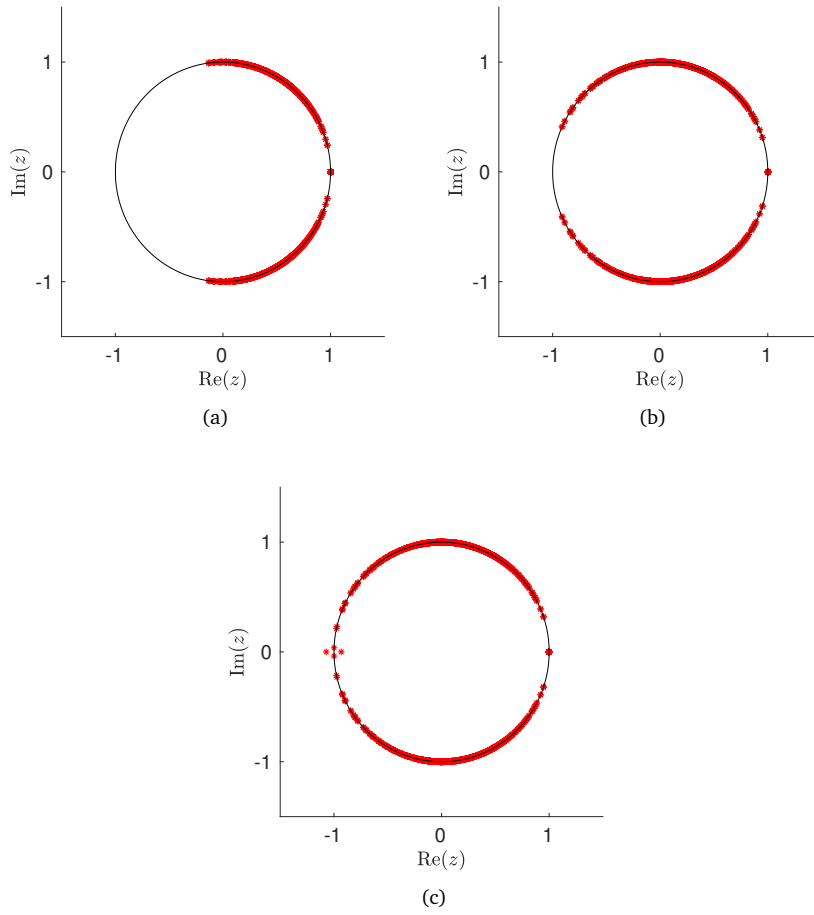


**Figure 4.10:** Pole tracking for ADI implicitization with different time steps: (a)  $\Delta t = \Delta t_{\text{num}}^{\text{adi}}$ , (b)  $\Delta t = 1.30 \Delta t_{\text{num}}^{\text{adi}}$ , and (c)  $\Delta t = 1.33 \Delta t_{\text{num}}^{\text{adi}}$ .

circa 1.3. Consequently, the system also remains stable for the desired time step (4.80). This can be explained as follows. The maximum time step allowed by (4.71) corresponds to  $\lambda_{\min}(Q_{yz}) = 0$  but not necessarily to  $\lambda_{\min}(Q_x^T Q_x) = 0$ . There is additional margin hidden in the latter, since it is known that [13, Thm. 8.4.11]

$$\lambda_{\min}(E_{\text{adi}}) \geq \lambda_{\min}(Q_x^T Q_x) + \lambda_{\min}(Q_{yz}) \quad . \quad (4.86)$$

## 4.5 Conclusion

The stability of three different local implicitization techniques was rigorously proven for nonuniform tensor-product grids with isotropic, inhomogeneous, possibly lossy media enclosed in a PEC box. This resulted in an exact norm-based upper bound for the time step in case of Newmark and Crank-Nicolson implicitization, and a more loose upper bound for ADI implicitization. Also, an explicit, Courant-like maximum time step was determined for fully explicit, nonuniform grids. Among the proposed methods, Newmark implicitization is the most computationally expensive technique, as it has a three-level update scheme. The ADI implicitization method is the most efficient one, because, no matter how many dimensions are implicitized, the occurring matrices are tridiagonal and scale with only one dimension. However, it suffers from a splitting error. Fortunately, for the newly proposed leapfrog ADHIE-FDTD method, this splitting error is heavily reduced compared to the traditional (leapfrog) ADI-FDTD method since the split curl parts are more sparse.

Possible future work includes the extension of the stability analysis to perfectly matched layers (PMLs). By means of a final, short discussion on this matter, it is worth mentioning that our  $z$ -domain stability analysis is well-suited to analyze the convolutional PML as the discrete convolution is transformed to a simple multiplication in the  $z$ -domain. Multiplying the step sizes by the  $z$ -domain stretching factors, our stability analysis can be repeated up to formula (4.18), but then the  $z$ -dependence of the step size matrices inside the modified curl operator (4.13) gives rise to a nonlinear eigenvalue problem with complex (instead of real) symmetry, which strongly impedes further conclusions about the location of  $z$  (or  $\zeta$ ) in the complex plane.

## 4.6 Addendum: CN implicitization of subgrids

The  $z$ -domain stability analysis from this chapter is repeated for nonuniform subgridding with local (semi-)implicit Crank-Nicolson time integration. Thereto, consider a nonuniform coarse grid that is locally overlapped by a nonuniform fine subgrid, whose outer edges coincide with coarse primary edges (see Fig. 4.11 in the uniform 2-D case). Along the interface, coarse-grid electric fields are coupled to fine-grid magnetic fields. If the overlapped coarse part would be filled with perfect

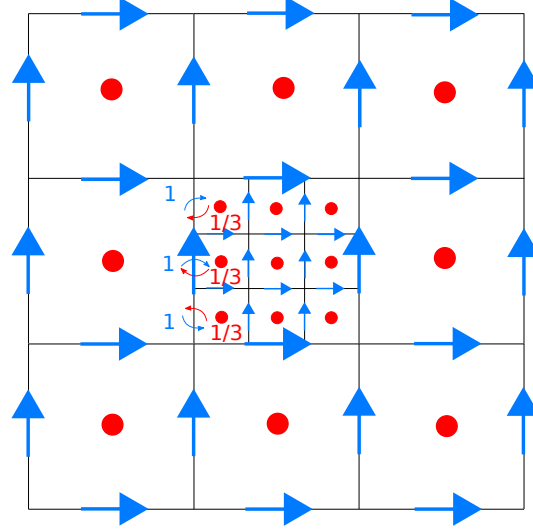


**Figure 4.11:** Sketch of a 2-D subgrid. The coarse-grid electric and magnetic fields are denoted by large arrows and dots respectively, the subgrid electric and magnetic fields by small arrows and dots. Coarse-grid electric fields are symmetrically coupled to fine-grid magnetic fields: the coarse-to-fine coupling weights (*blue*) equal the fine-to-coarse coupling weights (*red*) apart from a normalization factor 3. If there is overlap, the coarse-grid electric fields also couple to the coarse-grid magnetic field that is “underlying” the subgrid. This coupling coefficient is zero if the coarse cell “underlying” the subgrid is filled with PMC material.

magnetic conductors (PMCs) having infinite permeability, the resulting scheme is equivalent to a conventional grid stitching scheme without overlap. PMCs can only enhance the stability since they introduce zeros in the modified curl  $\tilde{C}$  defined in (4.13), which can only reduce its norm. Of course, for the subgridding scheme, the curl incidence matrix  $C$  occurring in (4.13) is not (3.16), but the same principle holds for a general matrix  $C$ . Hence, stability with overlap is a sufficient condition for stability without overlap. This insight allows us to detach coarse-grid curl  $C_c$ , fine-grid curl  $C_f$  and coupling operator  $S$  from each other, such that, for the subgridding scheme with overlap, the leapfrog update equation reads

$$\begin{bmatrix} \frac{M_{e,c}}{\Delta t} & & \\ C_c^T & \frac{M_{\mu,c}}{\Delta t} & \\ & \frac{M_{e,f}}{\Delta t} & \\ a S^T & C_f^T & \frac{M_{\mu,f}}{\Delta t} \end{bmatrix} \begin{bmatrix} \hat{e}_c \\ \hat{h}_c \\ \hat{e}_f \\ \hat{h}_f \end{bmatrix}^{n+1} = \begin{bmatrix} \frac{M_{e,c}}{\Delta t} & C_c & & S \\ & \frac{M_{\mu,c}}{\Delta t} & & \\ & & \frac{M_{e,f}}{\Delta t} & C_f \\ & & & \frac{M_{\mu,f}}{\Delta t} \end{bmatrix} \begin{bmatrix} \hat{e}_c \\ \hat{h}_c \\ \hat{e}_f \\ \hat{h}_f \end{bmatrix}^n. \quad (4.87)$$

Here, coarse-grid (main grid) and fine-grid (subgrid) variables and operators are highlighted by ‘c’ and ‘f’ subscripts respectively. The coarse-to-fine coupling matrix

is the transposition and normalization of the fine-to-coarse coupling matrix. The factor  $a$  embodies this normalization. Its scalar nature implies that the refinement is uniform and isotropic. This FDTD scheme is stable if and only if the poles of its transfer function matrix or, equivalently, the roots  $z$  of the characteristic equation,

$$\det \left[ \begin{array}{cc|cc} (z-1)\frac{M_{e,c}}{\Delta t} & -C_c & & -S \\ z C_c^T & (z-1)\frac{M_{\mu,c}}{\Delta t} & & \\ \hline & & (z-1)\frac{M_{e,f}}{\Delta t} & -C_f \\ z a S^T & & z C_f^T & (z-1)\frac{M_{\mu,f}}{\Delta t} \end{array} \right] = 0 \quad , \quad (4.88)$$

do not exit the unit circle. Furthermore, repeated poles lying on the unit circle must have linearly independent eigenvectors to avoid polynomially growing solutions. A good subgridding method does not alter the time step of the original grid. Therefore, the fields inside the subgrid and the fields involved in the interfacing should be updated implicitly by means of an unconditionally stable method, here chosen to be the Crank-Nicolson method. Hence, electric-field implicitization operators similar to (4.54) are added to both the fine-grid curl and the coupling operator occurring in (4.88), which yields

$$\det \left[ \begin{array}{cc|cc} (z-1)\frac{M_{e,c}}{\Delta t} & -C_c & & -\mathcal{I}_{1,s} S \\ z C_c^T & (z-1)\frac{M_{\mu,c}}{\Delta t} & & \\ \hline & & (z-1)\frac{M_{e,f}}{\Delta t} & -\mathcal{I}_{1,f} C_f \\ z a S^T \mathcal{I}_{2,s} & & z C_f^T \mathcal{I}_{2,f} & (z-1)\frac{M_{\mu,f}}{\Delta t} \end{array} \right] = 0 \quad . \quad (4.89)$$

Along the lines of (4.12), the roots of (4.89) are identical to those of

$$\det \left[ \begin{array}{cc|cc} (z-1)I_{n_{e,c}} & -2\tilde{C}_c & & -2\mathcal{I}_{1,s}\tilde{S} \\ 2z\tilde{C}_c^T & (z-1)I_{n_{h,c}} & & \\ \hline & & (z-1)I_{n_{e,f}} & -2\sqrt{a}\mathcal{I}_{1,f}\tilde{C}_f \\ 2z\tilde{S}^T\mathcal{I}_{2,s} & & \frac{2z}{\sqrt{a}}\tilde{C}_f^T\mathcal{I}_{2,f} & (z-1)I_{n_{h,f}} \end{array} \right] = 0 \quad , \quad (4.90)$$

with

$$\tilde{C}_c = \frac{\Delta t}{2} M_{e,c}^{-1/2} C_c M_{\mu,c}^{-1/2} \quad (4.91)$$

$$\tilde{C}_f = \frac{\Delta t}{2} M_{e,f}^{-1/2} C_f M_{\mu,f}^{-1/2} \quad (4.92)$$

$$\tilde{S} = \sqrt{a} \frac{\Delta t}{2} M_{e,c}^{-1/2} S M_{\mu,f}^{-1/2} \quad . \quad (4.93)$$

Since the determinant is invariant under block permutation, we can simplify the problem by locating the roots of

$$\det \left[ \begin{array}{cc|cc} (z-1)I_{n_e,c} & -2\mathcal{I}_{1,s}\tilde{S} & & -2\tilde{C}_c \\ 2z\tilde{S}^T\mathcal{I}_{2,s} & (z-1)I_{n_h,f} & \frac{2z}{\sqrt{a}}\tilde{C}_f^T\mathcal{I}_{2,f} & \\ \hline & -2\sqrt{a}\mathcal{I}_{1,f}\tilde{C}_f & (z-1)I_{n_e,f} & \\ 2z\tilde{C}_c^T & & & (z-1)I_{n_h,c} \end{array} \right] = 0, \quad (4.94)$$

which, after applying the partitioned-determinant rule [13, Eq. 2.8.13], yields

$$\det \left[ \begin{array}{cc} I_{n_e,c} + \frac{4z}{(z-1)^2}\tilde{C}_c\tilde{C}_c^T & -\frac{2}{z-1}\mathcal{I}_{1,s}\tilde{S} \\ \frac{2z}{z-1}\tilde{S}^T\mathcal{I}_{2,s} & I_{n_h,f} + \frac{4z}{(z-1)^2}\tilde{C}_f^T\mathcal{I}_{2,f}\mathcal{I}_{1,f}\tilde{C}_f \end{array} \right] = 0, \quad (4.95)$$

where we discarded the static solutions. We now substitute the bilinear transformation (4.16), which maps  $|z| \leq 1$  to  $\text{Re}(\zeta) \geq 0$ . This gives rise to the quadratic eigenvalue problem (QEP)

$$(\zeta^2 Q_2 + \zeta Q_1 + Q_0)\mathbf{u} = 0, \quad (4.96)$$

with

$$Q_2 = Q_2^T = \begin{bmatrix} \tilde{C}_c\tilde{C}_c^T & 0 \\ 0 & \tilde{C}_f^T\tilde{C}_f \end{bmatrix} \quad (4.97)$$

$$Q_1 = -Q_1^T = \begin{bmatrix} 0 & \tilde{S} \\ -\tilde{S}^T & 0 \end{bmatrix} \quad (4.98)$$

$$Q_0 = Q_0^T = \begin{bmatrix} I_{n_e,c} - \tilde{C}_c\tilde{C}_c^T & P_s\tilde{S} \\ \tilde{S}^T P_s & I_{n_h,f} - \tilde{C}_f^T P_f \tilde{C}_f \end{bmatrix}. \quad (4.99)$$

The diagonal projection operators  $P_f$  and  $P_s$  are analogous to (4.3). A QEP with this particular symmetry is well-known in mechanical engineering, where it is also called *gyroscopic*. Generally, its spectrum consists of quadruplets that are symmetric with respect to the real and the imaginary axis. In the more specific case that  $Q_0$  is positive definite, the eigenvalues are known to be purely imaginary and semisimple [19]. With respect to our Maxwellian eigenmode analysis, this conservative behavior is exactly what we would expect from a passive, lossless system. Indeed, if  $Q_0$  is regular, which is a nontrivial condition that will be discussed later on, the QEP (4.96) can be linearized to

$$(\zeta L_1 + L_0)\mathbf{v} = 0, \quad (4.100)$$

with

$$L_1 = L_1^T = \begin{bmatrix} Q_2 & 0 \\ 0 & Q_0 \end{bmatrix} \quad (4.101)$$

$$L_0 = -L_0^T = \begin{bmatrix} Q_1 & Q_0 \\ -Q_0 & 0 \end{bmatrix} , \quad (4.102)$$

and

$$\mathbf{v} = \begin{bmatrix} \zeta \mathbf{u} \\ \mathbf{u} \end{bmatrix} . \quad (4.103)$$

Left-multiplying (4.100) with the Hermitian transpose of  $\mathbf{v}$  and superposing the Hermitian-transposed equation, yields

$$\text{Re}(\zeta) \mathbf{v}^\dagger L_1 \mathbf{v} = 0 \quad \forall \mathbf{v} \neq 0 . \quad (4.104)$$

As a matter of fact, (4.104) readily shows that the eigenvalues  $\zeta$  are purely imaginary if

$$\mathbf{v}^\dagger L_1 \mathbf{v} \neq 0 \quad \forall \mathbf{v} \neq 0 . \quad (4.105)$$

With  $\lambda_i$  and  $\mathbf{v}_i$  the eigenvalues and eigenvectors belonging to  $L_1$  respectively, the spectral theorem for symmetric matrices states that

$$L_1 = \sum_i \lambda_i \mathbf{v}_i \mathbf{v}_i^T , \quad (4.106)$$

such that (4.105) translates to

$$\mathbf{v}^\dagger L_1 \mathbf{v} = \sum_i \lambda_i \|\mathbf{v}^\dagger \mathbf{v}_i\|_2^2 \neq 0 \quad \forall \mathbf{v} \neq 0 . \quad (4.107)$$

Since this inequality must hold for any non-zero vector  $\mathbf{v}$ , (4.105) can only be satisfied if  $L_1$  is either positive or negative definite. Given the fact that  $Q_2$  and  $Q_0$  inevitably have some positive eigenvalues, positive definiteness is the rule. Note that  $Q_2$  is “formally” positive definite, being the product of a matrix and its transposition, whose zero eigenvalues correspond to the static solutions that were discarded in (4.95). For  $Q_0$ , real symmetric positive definiteness, i.e.

$$\mathbf{u}^T Q_0 \mathbf{u} > 0 \quad \forall \mathbf{u} \neq 0 , \quad (4.108)$$

is not trivially satisfied. If  $Q_0$  is decomposed into  $Q_0 = I - R$ , the requirement (4.108) leads to [13, Eq. 8.4.3]

$$\max_{\mathbf{u} \neq 0} \frac{\mathbf{u}^T R \mathbf{u}}{\|\mathbf{u}\|_2^2} = \lambda_{\max}(R) < 1 . \quad (4.109)$$

Since

$$R = \begin{bmatrix} \tilde{C}_c \tilde{C}_c^T & 0 \\ 0 & \tilde{C}_f^T P_f \tilde{C}_f \end{bmatrix} - \begin{bmatrix} 0 & P_s \tilde{S} \\ \tilde{S}^T P_s & 0 \end{bmatrix} , \quad (4.110)$$

the triangle inequality [13, Eq. 8.4.15] yields a sufficient condition for the numerical stability of the locally implicitized subgridding scheme:

$$\boxed{\max(\|\tilde{C}_c\|_2^2, \|P_f \tilde{C}_f\|_2^2) + \|P_s \tilde{S}\|_2^2 < 1} . \quad (4.111)$$

All occurring operators are defined in (4.91)–(4.93). In case the subgrid and coupling are fully implicit, (4.111) reduces to the coarse-grid Courant limit

$$\|\tilde{C}_c\|_2^2 < 1 . \quad (4.112)$$

In case of hybrid implicit-explicit subgridding, i.e., if the projectors  $P_f$  and  $P_s$  are neither zero nor one, a reduced time step limit can be found with (4.111). Note that, due to the use of the triangle inequality and the overlap, (4.111) can be a large overestimation of the exact time step limit if main grid and subgrid are updated fully explicitly.

## References

- [1] B. Denecker, L. Knockaert, F. Olyslager, and D. De Zutter, “A new state-space-based algorithm to assess the stability of the finite-difference time-domain method for 3D finite inhomogeneous problems”, *AEU - International Journal of Electronics and Communications*, vol. 58, no. 5, pp. 339–348, 2004.
- [2] R. F. Remis, “Stability of FDTD on nonuniform grids for Maxwell’s equations in lossless media”, *Journal of Computational Physics*, vol. 218, no. 2, pp. 594–606, 2006.
- [3] A. Van Londersele, D. De Zutter, and D. Vande Ginste, “An in-depth stability analysis of nonuniform FDTD combined with novel local implicitization techniques”, *Journal of Computational Physics*, vol. 342, pp. 177–193, 2017.
- [4] R. A. Chilton and R. Lee, “The discrete origin of FETD-Newmark late time instability, and a correction scheme”, *Journal of Computational Physics*, vol. 224, no. 2, pp. 1293–1306, 2007.
- [5] S. B. Shi, W. Shao, X. K. Wei, X. S. Yang, and B. Z. Wang, “A new unconditionally stable FDTD method based on the Newmark-beta algorithm”, *IEEE Transactions on Microwave Theory and Techniques*, vol. 64, no. 12, pp. 4082–4090, 2016.
- [6] B. De Deckere, A. Van Londersele, D. De Zutter, and D. Vande Ginste, “Birefringent dispersive FDTD subgridding scheme”, *Electronics Letters*, vol. 52, no. 17, pp. 1455–1457, 2016.
- [7] C. Sun and C. W. Trueman, “Unconditionally stable Crank-Nicolson scheme for solving two-dimensional Maxwell’s equations”, *Electronics Letters*, vol. 39, no. 7, pp. 595–597, 2003.
- [8] S. C. Yang, Z. Chen, Y. Yu, and W. Y. Yin, “An unconditionally stable one-step arbitrary-order leapfrog ADI-FDTD method and its numerical properties”, *IEEE Transactions on Antennas and Propagation*, vol. 60, no. 4, pp. 1995–2003, 2012.
- [9] A. Grande and J. A. Pereda, “Accuracy limitations of the locally one-dimensional FDTD technique”, *IEEE Antennas and Wireless Propagation Letters*, vol. 13, pp. 1180–1183, 2014.
- [10] K. Abdijalilov and H. Grebel, “Z-transform theory and FDTD stability”, *IEEE Transactions on Antennas and Propagation*, vol. 52, no. 11, pp. 2950–2954, 2004.
- [11] R. A. Chilton and R. Lee, “Conservative and provably stable FDTD subgridding”, *IEEE Transactions on Antennas and Propagation*, vol. 55, no. 9, pp. 2537–2549, 2007.

- [12] R. Schuhmann and T. Weiland, “Conservation of discrete energy and related laws in the finite integration technique”, *Progress In Electromagnetics Research (PIER)*, vol. 32, pp. 301–316, 2001.
- [13] D. Bernstein, *Matrix Mathematics (2nd edition)*. Princeton University Press, 2009.
- [14] T. Rylander and A. Bondeson, “Stability of explicit-implicit hybrid time-stepping schemes for Maxwell’s equations”, *Journal of Computational Physics*, vol. 179, no. 2, pp. 426–438, 2002.
- [15] S. Wang and F. L. Teixeira, “Some remarks on the stability of time-domain electromagnetic simulations”, *IEEE Transactions on Antennas and Propagation*, vol. 52, no. 3, pp. 895–898, 2004.
- [16] T. Berger, A. Ilchmann, and S. Trenn, “The quasi-Weierstrass form for regular matrix pencils”, *Linear Algebra and its Applications*, vol. 436, no. 10, pp. 4052–4069, 2012.
- [17] R. F. Remis, “On the stability of the Finite-Difference Time-Domain method”, *Journal of Computational Physics*, vol. 163, no. 1, pp. 249–261, 2000.
- [18] M. Min and C. Teng, “The instability of the Yee scheme for the magic time step”, *Journal of Computational Physics*, vol. 166, no. 2, pp. 418–424, 2001.
- [19] F. Tisseur and K. Meerbergen, “The quadratic eigenvalue problem”, *SIAM Rev.*, vol. 43, no. 2, pp. 235–286, 2001.

# 5

## 3-D Cell-by-Cell Subgridding based on Finite Elements

*“I suppose it is tempting,  
if the only tool you have is a hammer,  
to treat everything as if it were a nail.”*

Abraham Maslow

★ ★ ★

*The finite-element-based subgridding algorithm for the 3-D FDTD method proposed in [1] is shown to be closely related to the finite integration technique. This new insight permits the straightforward derivation of coupling coefficients for complex configurations without the need for arduous finite-element pre-processing. The result is a flexible cell-by-cell subgridding algorithm that allows different refinement ratios without buffer zone and that preserves highly desired physical conservation properties on the discrete level. Its accuracy is validated by the S-parameter analysis of a rectangular waveguide with a ridge discontinuity.*

## 5.1 Introduction

In the past quarter century, a considerable amount of FDTD research has been devoted to subgridding, i.e. the nesting of structured grids to judiciously reduce the discretization error. Obviously, the interfacing between main grid and subgrid is the crux of the problem. Most of the proposed subgridding methods use ad hoc interpolation rules. As a consequence, numerical artifacts such as spurious reflections, mainly arising from the corners of the interface, pollute the solution. In addition, numerical instabilities may ensue. Among the few exceptions, the work presented in [1] provides a more rigorous and systematic methodology to FDTD subgridding. Based on the finite-element time-domain method, the interpolation rules are carefully derived from first principles according to the differential-geometric principles that underpin Maxwell's equations. Besides the discrete fulfillment of the correct field and flux continuity, the resulting scheme guarantees the conservation of energy and charge, features inherent spatial reciprocity, and appropriately takes care of the interface corners. Two drawbacks, however, are the extra programming effort required to construct the finite-element restriction operators and the implicitness of the resulting coupling scheme. Therefore, in [2, p.77-78], the subgrid was mass lumped to enable explicit updates, and formulas for the coupling weights were heuristically derived for some specific cases. However, for more general configurations, the derivation of such heuristic coupling weights is infeasible.

In this chapter, it will be demonstrated that more general coupling coefficients can be generated with the help of the finite integration technique [3]. As such, we bridge the gap between three prominent computational electromagnetic time-domain methods: FDTD, FETD and FIT. Section 5.2 describes the finite-integration formulation of the subgridding method and provides implementation details. Section 5.3 verifies the accuracy of the proposed method by computing the transmission  $S_{21}$  of a rectangular waveguide with an  $E$ -step ridge discontinuity. Finally, Section 5.4 lists some concluding remarks and some perspectives for future work.

## 5.2 From finite elements to finite integrations

On the one hand, as explained in Section 3.3.3, the FDTD method can be recognized as a special case of the FETD method with lowest-order mixed-order Whitney elements on a hexahedral grid and mass lumping of the Hodge star operators. The constant-tangent/linear-normal and linear-tangent/constant-normal functional behavior of the Whitney one- and two-forms reflects the correct boundary conditions of the electric field and magnetic flux density respectively. On the other hand, as pointed out in Section 3.3.2, the FDTD method can also be perceived as a special case of the FIT on a hexahedral grid. Instead of fields and flux densities, the FIT uses voltages and fluxes, i.e. line and surface integrals, which are related to one- and two-forms respectively [3]. Since the same fundamentals from differential geometry that characterize the FETD method also underpin the FIT, it is not sur-

prising that some aspects of the subgridding method proposed in [1] can be cast in the FIT framework.

The relation between the FETD and the FDTD method is particularly interesting with respect to the development of subgridding schemes that obey the correct field and flux continuity. Since the space of pulses and triangles with step  $\Delta$  resides in the space of pulses and triangles with step  $\Delta/r$  (with  $r \in \mathbb{N}$ ), restriction operators  $R_e$  and  $R_b$  can be constructed that relate coarse to fine Whitney elements:

$$\hat{\mathbf{w}}_c^1 = R_e \hat{\mathbf{w}}_f^1 \quad \hat{\mathbf{w}}_c^2 = R_b \hat{\mathbf{w}}_f^2 . \quad (5.1)$$

These are rectangular matrices with full row rank. Starting from a completely fine grid, we can now *coarsen* the parts whose resolution is not crucial with regard to the accuracy of the numerical solution. Alternatively, starting from two separate grids, the restriction operators permit to *assemble* them. The key finding in [1] is the coarsened/assembled/restricted version of the update equations (3.51) and (3.54). More specifically,

$$\partial_t \hat{\mathbf{b}}(t) = -C_r^T \hat{\mathbf{e}}(t) \quad (5.2)$$

$$\partial_t \hat{\mathbf{e}}(t) = [\star_\varepsilon]_r^{-1} C_r [\star_{\mu^{-1}}]_r \hat{\mathbf{b}}(t) . \quad (5.3)$$

with

$$C_r = R_e C R_b (R_b R_b^T)^{-1} \quad (5.4)$$

$$[\star_\varepsilon]_r = R_e [\star_\varepsilon] R_e^T \quad (5.5)$$

$$[\star_{\mu^{-1}}]_r = R_b [\star_{\mu^{-1}}] R_b^T \quad (5.6)$$

Here,  $C_r$  denotes the curl incidence matrix of the grid after restriction.  $[\star_\varepsilon]$  and  $[\star_{\mu^{-1}}]$  are the Hodge matrices (3.55)–(3.56), which are diagonalized by means of trapezoidal integration in order to retrieve the explicit FDTD method on the completely fine grid.  $[\star_\varepsilon]_r$  and  $[\star_{\mu^{-1}}]_r$  are the restricted counterparts, which are not necessarily diagonal anymore. (5.2)–(5.3) is only valid if all nearest electric fields circulating a magnetic flux that is eliminated by restriction, are eliminated as well. Clearly, the restricted set of equations (5.2)–(5.3) features spatial reciprocity by construction, which is critical for the subgrid's numerical stability. Indeed, from our earlier stability analysis in Chapter 4, it is easily seen that (5.2)–(5.3) is stable for

$$\Delta t < \frac{2}{\|[\star_\varepsilon]_r^{-1/2} C_r [\star_{\mu^{-1}}]_r^{1/2}\|_2} . \quad (5.7)$$

Although (5.2)–(5.6) is of no further importance for the actual implementation of the final subgridding algorithm, it is an attractive form to deduce conservation properties (see [1]).

In the general 3-D case, (5.2)–(5.6) is not explicit. If the coarse Whitney elements are chosen to form an interpolatory basis, that is, if every basis function is zero in all

anchor points except for one, then it is always possible to diagonalize the restricted Hodges (5.5)–(5.6) by judiciously introducing zeros on the diagonal of the original Hodge, hereby increasing the remaining diagonal elements as to preserve the trace [2, p. 74-76]. The resulting subgridding scheme is fully explicit and still possesses the same conservation properties. Although the chosen basis functions only yield first-order accuracy along the subgrid boundaries, quadratic supraconvergence is observed in practice. In [2, p. 77-78], coupling weights explicitly depending on the refinement ratio are listed for some specific subgridding configurations, namely a straight interface, a convex corner and a concave corner. The key finding of this chapter is that these coefficients can be interpreted in terms of finite integrations, such that more complex subgridding configurations can be build easily.

We start from the most simple configuration where only one cell is refined by the same factor  $r_x = r_y = r_z = r$  in all three dimensions. This is the convex (or “exterior”) corner in [2, p. 77-78]. For simplicity, we consider a uniform main grid with cell size  $\Delta x = \Delta y = \Delta z = \Delta$  and a homogeneous medium with permittivity  $\varepsilon$  and permeability  $\mu$ . For each of the twelve primary edges of the refined cell, there is a non-trivial update equation for the associated coarse-grid electric field. For example, in case of the edge depicted in Fig. 5.1, where the refinement ratio is chosen to be  $r = 5$ , the update equation of  $E_z$ , with “half-integer notation”, is

$$\begin{aligned} \frac{\varepsilon\mu}{\Delta t} (E_z|_{i,j,k+\frac{1}{2}}^{n+1} - E_z|_{i,j,k+\frac{1}{2}}^n) = \\ \alpha_n B_y|_{i+\frac{1}{2},j,k+\frac{1}{2}}^{n+\frac{1}{2}} - \alpha_s B_y|_{i-\frac{1}{2},j,k+\frac{1}{2}}^{n+\frac{1}{2}} + \alpha_w B_x|_{i,j-\frac{1}{2},k+\frac{1}{2}}^{n+\frac{1}{2}} - \alpha_e B_x|_{i,j+\frac{1}{2},k+\frac{1}{2}}^{n+\frac{1}{2}} \quad (5.8) \\ + \sum_{p=1}^{r-1} \sum_{q=1}^r \left( \beta_{en}^p B_y|_{i+\frac{1}{2r},j+1-\frac{p}{r},k-\frac{1}{2r}+\frac{q}{r}}^{n+\frac{1}{2}} - \beta_{ne}^p B_x|_{i+1-\frac{p}{r},j+\frac{1}{2r},k-\frac{1}{2r}+\frac{q}{r}}^{n+\frac{1}{2}} \right), \end{aligned}$$

with heuristically determined coefficients [2, p.77-78]

$$\alpha_n = \alpha_e = \frac{2r^2 + 2r}{3r^2 + 2r - 1} \frac{1}{\Delta} = \frac{75}{105} \frac{1}{\Delta} \quad (5.9)$$

$$\alpha_s = \alpha_w = \frac{4r^2}{3r^2 + 2r - 1} \frac{1}{\Delta} = \frac{125}{105} \frac{1}{\Delta} \quad (5.10)$$

$$\beta_{ne}^p = \beta_{en}^p = \frac{4p/r}{3r^2 + 2r - 1} \frac{1}{\Delta} = \frac{p}{105} \frac{1}{\Delta} \quad (5.11)$$

For  $r = 1$ , the double summation in (5.8) drops out and (5.9)–(5.10) reduce to the standard FDTD coefficients. Although exhaustively derived from finite elements, the coarse-grid coefficients  $\alpha$  can be simply interpreted in terms of finite integrations. They are the ratio of the partial lengths and the (pink) area indicated in

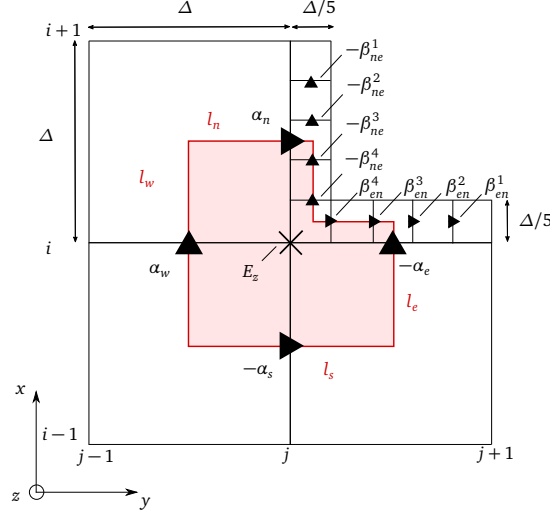


**Figure 5.1:** Update coefficients for the coarse-grid electric field along a subgrid corner with refinement ratio  $r = 5$ . The triangles denote the fine- and coarse-grid magnetic flux densities of interest. The remaining unknowns and grid lines are omitted to enhance the readability. Although only the  $xy$ -plane is shown, the actual geometry is 3-D and the upper-right cell is refined in the  $z$ -dimension. The subscripts refer to the cardinal directions north, east, south and west.

Fig. 5.1. More specifically,

$$\alpha_n = l_n / A \quad (5.12)$$

$$\alpha_e = l_e / A \quad (5.13)$$

$$\alpha_s = l_s / A \quad (5.14)$$

$$\alpha_w = l_w / A \quad (5.15)$$

with

$$l_n = l_e = \Delta(1 - \nu) \quad (5.16)$$

$$l_s = l_w = \Delta \quad (5.17)$$

$$A = \Delta^2(1 - \nu^2), \quad (5.18)$$

where we used

$$\nu = \frac{1}{2} - \frac{1}{2r}. \quad (5.19)$$

It is left as an exercise to the reader to verify that, indeed, the FIT theory put forward in Section 3.3.2, with partial edges and partial faces, justifies the  $\alpha$  coefficients. Moreover, these coefficients could also be retrieved by filling the subgrid with perfect magnetic conducting material and then applying the Dey-Mitra (DM)

conformal technique [4]. As is the case for DM, the  $\alpha$  coefficients are most efficiently implemented by making  $\varepsilon$  and  $\mu$  inhomogeneous, such that the original FDTD update stencil is preserved.

The fine-grid coefficients are given by

$$\beta_{ne}^p = p/r^3 \times \Delta/A . \quad (5.20)$$

Since the fine-grid flux densities are summed over the  $z$ -dimension, an explanation for these coefficients solely based on finite integrations is impossible. Some averaging should come into play. Indeed, the ratio of partial length  $\Delta/r$  and partial area  $A$  are again clearly observed in (5.20), and the remaining factor  $p/r^2$  constitutes a uniform averaging over the  $z$ -dimension and a linearly weighted averaging over the  $x$ - or  $y$ -dimension depending on the Cartesian component. As such, it upholds the linear-tangent/constant-normal nature of the Whitney two-forms used in the finite-element derivation.

Update equations analogous to (5.8) can be constructed for the other electric field components along the edges of the subgridded cell. For the coarse-grid magnetic flux densities along the faces of the subgridded cell, the finite integrations reduce to standard finite differences. The fields inside the bulk of the subgrid use the standard FDTD update coefficients, which differ from the ones inside the bulk of the main grid by a factor  $r$ . For the updates of the outermost fine-grid magnetic flux densities, the adjacent coarse-grid electric field is extended uniformly along its tangent direction and linearly along its normal direction, in agreement with the underlying Whitney one-forms used in the finite-element derivation.

The proposed finite-integration insights allow to derive coupling weights for more intricate cell-by-cell refinement schemes such as, for example, the one depicted in Fig. 5.2. Here, the refinement is inhomogeneous and anisotropic: a triplet of refinement ratios  $(r_x, r_y, r_z)$  is assigned to every coarse cell. Via (5.19), they give rise to triplets  $(v_x, v_y, v_z)$ . It is left as an exercise to the reader to verify that

$$l_n = \Delta(1 - v_y|_{nw} - v_y|_{ne}) = 7\Delta/20 \quad (5.21)$$

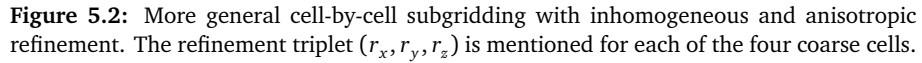
$$l_e = \Delta(1 - v_x|_{ne} - v_x|_{se}) = \Delta/5 \quad (5.22)$$

$$l_s = \Delta(1 - v_y|_{sw} - v_y|_{se}) = 11\Delta/56 \quad (5.23)$$

$$l_w = \Delta(1 - v_x|_{nw} - v_x|_{sw}) = 5\Delta/12 \quad (5.24)$$

$$A = \Delta^2(1 - v_x|_{nw} v_y|_{nw} - v_x|_{ne} v_y|_{ne} - v_x|_{se} v_y|_{se} - v_x|_{sw} v_y|_{sw}) = 1357\Delta^2/2800 \quad (5.25)$$

where again the cardinal directions are used to indicate each of the four coarse cells. The corresponding coefficients that need to be inserted in (5.8) are (5.12)–


$$\beta_{nw}^p = p/(r_x^2 r_z)|_{nw} \times \Delta/A \quad p = 1, \dots, r_x|_{nw} - 1 \quad (5.26)$$

$$\beta_{ne}^p = p/(r_x^2 r_z)|_{ne} \times \Delta/A \quad p = 1, \dots, r_x|_{ne} - 1 \quad (5.28)$$

$$\beta_{s_e}^p = p/(r_x^2 r_z)|_{s_e} \times \Delta/A \quad p = 1, \dots, r_x|_{s_e} - 1 \quad (5.30)$$

$$\beta_{sw}^p = p/(r_x^2 r_z)|_{sw} \times \Delta/A \quad p = 1, \dots, r_x|_{sw} - 1 \quad (5.32)$$

$$\beta_{ws}^p = p/(r_v^2 r_z)|_{sw} \times \Delta/A \quad p = 1, \dots, r_v|_{sw} - 1 \quad (5.33)$$

$$\begin{aligned} \alpha_w + \sum_{p=1}^{r_x|nw-1} \sum_{q=1}^{r_z|nw} \beta_{nw}^p + \sum_{p=1}^{r_x|sw-1} \sum_{q=1}^{r_z|sw} \beta_{sw}^p \\ = \alpha_e + \sum_{p=1}^{r_x|ne-1} \sum_{q=1}^{r_z|ne} \beta_{ne}^p + \sum_{p=1}^{r_x|se-1} \sum_{q=1}^{r_z|se} \beta_{se}^p = \Delta/A, \end{aligned} \quad (5.34)$$

such that the discrete derivative of a constant flux density is indeed zero.

### 5.3 Numerical example: ridge waveguide

The transmission through the rectangular waveguide depicted in Fig. 5.3 is extracted from our novel FDTD subgridding approach via mode orthogonality, where the modes are numerically computed by solving the symmetric eigenvalue problem corresponding to the discrete Helmholtz equation in the waveguide's cross section [5, Eq. 4.19]. This yields the normalized discrete field distribution  $E_x^{\text{TE}_{10}}(x, y)$  and the cut-off wavenumber  $k_c^{\text{TE}_{10}}$  of the  $\text{TE}_{10}$  mode. The latter is used to determine the propagation constant

$$\Gamma(\omega) = \sqrt{\omega^2 \epsilon_0 \mu_0 - (k_c^{\text{TE}_{10}})^2} . \quad (5.35)$$

The  $E_x(x, y)$  distribution recorded in the waveguide cross section is projected onto  $E_x^{\text{TE}_{10}}(x, y)$  at four different locations  $z_k$  along the  $z$ -axis, as depicted in Fig. 5.4. This is simply realized by computing the inner product

$$V_k(t) = \sum_{i,j} E_x(z_k, t)|_{i,j} E_x^{\text{TE}_{10}}|_{i,j} \quad k = 1, 2, 3, 4 , \quad (5.36)$$

where the summation runs over the  $x$ - and  $y$ -indices. Since all propagating and evanescent modes inside the waveguide are orthogonal with respect to each other,  $V_k(t)$  is the superposition of forward and backward propagating  $\text{TE}_{10}$  modes. Hence, after application of a discrete Fourier transformation, we end up with the set of equations

$$V_1(\omega) = A(\omega) e^{-j\Gamma(\omega)z_1} + B(\omega) e^{j\Gamma(\omega)z_1} \quad (5.37)$$

$$V_2(\omega) = A(\omega) e^{-j\Gamma(\omega)z_2} + B(\omega) e^{j\Gamma(\omega)z_2} \quad (5.38)$$

$$V_3(\omega) = C(\omega) e^{-j\Gamma(\omega)z_3} + D(\omega) e^{j\Gamma(\omega)z_3} \quad (5.39)$$

$$V_4(\omega) = C(\omega) e^{-j\Gamma(\omega)z_4} + D(\omega) e^{j\Gamma(\omega)z_4} . \quad (5.40)$$

As is shown in Fig. 5.4, we choose  $z_2 = z_1 + \Delta z$  and  $z_4 = z_3 + \Delta z$ . Now, we can solve for the amplitudes of the forward propagating modes:

$$A(\omega) = \frac{V_1(\omega) e^{j\Gamma(\omega)\Delta z} - V_2(\omega)}{e^{j\Gamma(\omega)\Delta z} - e^{-j\Gamma(\omega)\Delta z}} e^{j\Gamma(\omega)z_1} \quad (5.41)$$

$$C(\omega) = \frac{V_3(\omega) e^{j\Gamma(\omega)\Delta z} - V_4(\omega)}{e^{j\Gamma(\omega)\Delta z} - e^{-j\Gamma(\omega)\Delta z}} e^{j\Gamma(\omega)z_3} . \quad (5.42)$$

Their ratio is the desired transmission scattering parameter

$$S_{21}(\omega) = \frac{C(\omega)}{A(\omega)} = \frac{V_3(\omega) e^{j\Gamma(\omega)\Delta z} - V_4(\omega)}{V_1(\omega) e^{j\Gamma(\omega)\Delta z} - V_2(\omega)} e^{j\Gamma(\omega)(z_3 - z_1)} . \quad (5.43)$$

Since the  $\text{TE}_{10}$  mode is propagating in the frequency range of interest, i.e.  $\Gamma(\omega) \in \mathbb{R}$ , the amplitude of the transmission in decibel units is given by

$$|S_{21}(\omega)|_{\text{dB}} = 20 \log_{10} \left| \frac{V_3(\omega) e^{j\Gamma(\omega)\Delta z} - V_4(\omega)}{V_1(\omega) e^{j\Gamma(\omega)\Delta z} - V_2(\omega)} \right| . \quad (5.44)$$

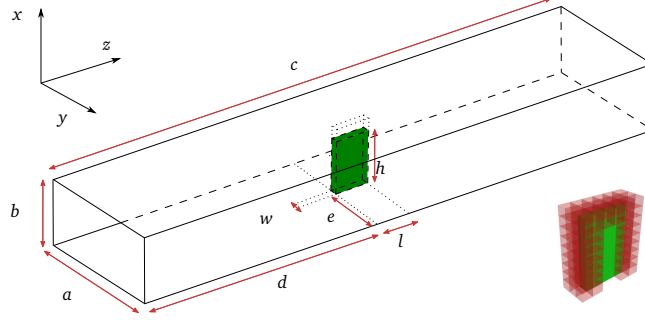


**Figure 5.3:** Rectangular waveguide with  $E$ -plane ridge discontinuity ( $a = 19.050$  mm,  $b = 9.525$  mm,  $c = 81.280$  mm,  $d = 38.100$  mm,  $e = 9.017$  mm,  $w = 1.016$  mm,  $h = 7.620$  mm,  $l = 5.080$  mm). The PEC ridge (green) is discretized by  $8 \times 1 \times 4$  coarse cells. The waveguide is discretized by  $10 \times 19 \times 64$  coarse cells. Small nonuniformities in the  $y$ -dimension are needed to match the geometry. The waveguide is terminated by 15 CFS-PML layers along the two planes normal to the  $z$ -axis. The inset on the right indicates the refined cells (red) w.r.t. the ridge (green).

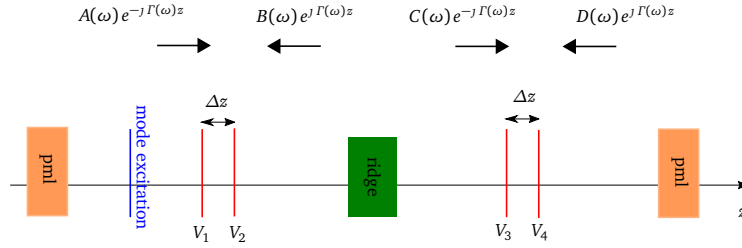


**Figure 5.4:** Scattering parameter extraction via mode orthogonality for the rectangular waveguide with ridge discontinuity. The electric fields in the cross section of the waveguide are projected onto the  $TE_{10}$  eigenvector for four different  $z$ -coordinates; two on the left and two on the right of the ridge. This allows to extract the amplitudes of the forward propagating  $TE_{10}$  modes in both waveguide sections. Their ratio yields the transmission  $S_{21}$ .

This quantity is plotted in Fig. 5.5. The cells adjacent to the edges and corners of the ridge, as shown in the inset of Fig. 5.3, are locally refined by a factor  $r$ . The time step equals the Courant limit of the smallest cell occurring in the grid, including the subgrids, and the total simulated time is 40 ns. Besides isotropic refinement, we also examine the effect of refinement solely in the direction normal to the ridge faces, in a PML-like fashion with overlapping corners. The FDTD results are compared to the experimental data from [6] and the subgridding algorithm is clearly found to succeed in accurately capturing the field singularities near the ridge.

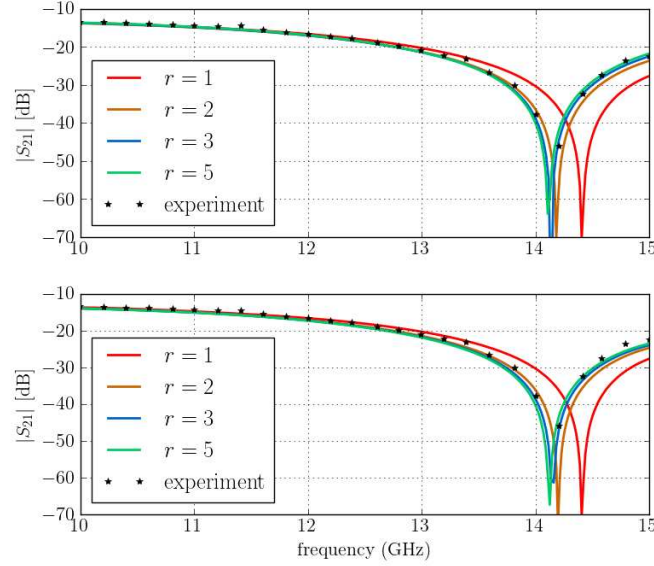


**Figure 5.5:** Transmission through the ridge waveguide shown in Fig. 5.3 for isotropic (*top*) and PML-like anisotropic (*bottom*) refinement.

## 5.4 Conclusion

Alike Maslow's hammer, the widely used finite differences are too limited to unravel the physically correct interpolation rules required for subgridding. Therefore, an accurate, easily implementable, cell-by-cell subgridding algorithm based on finite elements and interpreted in terms of finite integrations is described in this chapter. Unlike many finite-difference-based approaches, this algorithm preserves energy and charge by construction and is provably conditionally stable. The proposed subgridding method is successfully validated on a waveguide example with field singularity. Future work focuses on reducing the number of time samples in the coarse grid with a local time stepping approach and the extension to other coordinate systems alike [7].

## References

- [1] R. A. Chilton and R. Lee, “Conservative and provably stable FDTD subgridding”, *IEEE Transactions on Antennas and Propagation*, vol. 55, no. 9, pp. 2537–2549, 2007.
- [2] R. Chilton, “H-, P- and T-refinement strategies for the Finite-Difference-Time-Domain (FDTD) method developed via Finite-Element (FE) principles”, PhD thesis, Ohio State University, 2008.
- [3] M. Clemens and T. Weiland, “Discrete electromagnetism with the finite integration technique”, *Journal of Electromagnetic Waves and Applications*, vol. 15, no. 1, pp. 79–80, 2001.
- [4] S. Dey and R. Mittra, “A locally conformal finite-difference time-domain (FDTD) algorithm for modeling three-dimensional perfectly conducting objects”, *IEEE Microwave and Guided Wave Letters*, vol. 7, no. 9, pp. 273–275, 1997.
- [5] W. Yu, X. Yang, Y. Liu, and R. Mittra, *Electromagnetic Simulation Techniques Based on the FDTD Method*. John Wiley & Sons, Inc., 2009.
- [6] R. R. Mansour, R. S. K. Tong, and R. H. MacPhie, “Simplified description of the field distribution in finlines and ridge waveguides and its application to the analysis of E-plane discontinuities”, *IEEE Transactions on Microwave Theory and Techniques*, vol. 36, no. 12, pp. 1825–1832, 1988.
- [7] W. Tierens and D. De Zutter, “BOR-FDTD subgridding based on finite element principles”, *Journal of Computational Physics*, vol. 230, no. 12, pp. 4519–4535, 2011.



# 6

## The Fully-Collocated Implicit FDTD Method

*“With four parameters I can fit an elephant,  
and with five I can make him wiggle his trunk.”*

John Von Neumann

★ ★ ★

*This chapter elaborates on the fully-collocated implicit (FCI) FDTD method. This method is very promising with regard to multiscale modeling of complex materials. Despite its many great properties, it does not have a positive resonance in the finite-difference community. Much of the scepticism about the method is believed to originate from an improper finite-element analysis that expands the fields in discrete zero-forms (scalars) in the original paper [1]. This chapter proposes a correct finite-element derivation where the fields are one-forms (polar vectors) in the 3-D space. This explains the excellent accuracy of the results generated with this method in [1], [2]. Although the new finite-element insights do not alter the finite-difference scheme itself, it is of utmost importance with regard to hybridization techniques, e.g. subgridding. In view of the latter, we shortly experiment with Huygens subgridding to embed a small collocated grid in an overall Yee grid in 2-D. This method is used to examine the shielding effectiveness of an anisotropic dielectric slab.*

## 6.1 Introduction

Although the FDTD method's strength resides in its second-order accurate staggered grid with explicit leapfrog time integration, this is, at the same time, its main weakness as it imposes a stability limit on the time step, it downgrades the accuracy to merely first order upon nonuniform gridding, it requires material parameters to be averaged even across straight material boundaries, and it thwarts the numerical modeling of the constitutive relations of complex media [3]. These inconveniences are resolved by the fully-collocated implicit (FCI) FDTD method, presented in [1] to simulate electromagnetic waves in fusion plasmas. In the FCI-FDTD method, all electric and magnetic state variables are anchored to the nodes of a cubic grid (see Fig. 3.2(a)), whereas the actual evaluation of Maxwell's equations happens in the centers of the cell faces by means of a correct mixture of interpolations and differentiations. In contrast to virtually all other collocated schemes, the resulting finite-difference stencil is second-order accurate without odd-even decoupling. In fact, it even features enhanced accuracy compared to the traditional Yee scheme, since the second-order accuracy is preserved for nonuniform discretizations. This property makes the FCI-FDTD method attractive with regard to multiscale electromagnetic problems since the grid can be highly nonuniform without a restricting grading ratio as is the case for the traditional Yee scheme. Also, its unconditional stability enhances multiscale modeling. Especially in 3-D, however, the FCI-FDTD method is computationally inefficient due to the large sparse matrix system that needs to be solved.

In the remainder of this chapter, we first deduce the FCI-FDTD scheme starting from a finite-element expansion in Whitney one-forms. In Section 6.3, the actual finite-difference update equation is analyzed and some of the key properties of the FCI-FDTD method are recapitulated, in order to convince the reader of the fact that this method has a wide range of applications that reach far beyond the capabilities of standard Yee-FDTD. In Section 6.4, a hybrid Yee/FCI-FDTD method is applied to an anisotropic dielectric slab in 2-D.

In the next chapter, a more efficient scheme with collocation along one instead of three axes will be proposed, specially geared at multiscale problems that require a higher resolution in only one dimension, e.g. thin conductive layers.

## 6.2 Finite-element derivation

The method proposed in [1] is essentially an  $(E,H)$ -scheme where the electric and magnetic fields are expanded in nodal Whitney one-forms

$$\begin{aligned}\mathcal{N}_x^1|_{i,j,k} &= \Pi_i^*(x) \Lambda_j(y) \Lambda_k(z) \\ \mathcal{N}_y^1|_{i,j,k} &= \Lambda_i(x) \Pi_j^*(y) \Lambda_k(z) \\ \mathcal{N}_z^1|_{i,j,k} &= \Lambda_i(x) \Lambda_j(y) \Pi_k^*(z) \quad ,\end{aligned}\tag{6.1}$$

$$\mathcal{N}_z^1|_{i,j,k} = \Lambda_i(x) \Lambda_j(y) \Pi_k^*(z) \quad ,\tag{6.2}$$

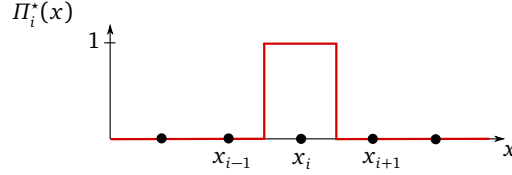


Figure 6.1: Shifted (or dual) pulse function.

with the shifted pulse function (Fig. 6.1)

$$\Pi_i^*(x) = \begin{cases} 1 & x_{i-1}^* \leq x < x_i^* \\ 0 & \text{elsewhere} \end{cases} . \quad (6.3)$$

At this point, it is recommended to return to Fig. 3.4 in order to understand the spatial indexing. In vectorized form, after the appropriate normalization of the pulse functions by the associated dual-grid step, the finite-element expansion of the fields reads

$$\mathbf{E}(x, y, z, t) = (\hat{\mathbf{n}}^1(x, y, z))^T \sum_n \hat{\Pi}_n(t) \hat{\mathbf{e}}_n \quad (6.4)$$

$$\mathbf{H}(x, y, z, t) = (\hat{\mathbf{n}}^1(x, y, z))^T \sum_n \hat{\Pi}_n(t) \hat{\mathbf{h}}_n . \quad (6.5)$$

In 4-D spacetime, the state variables are two-forms, which justifies the double-hat notation. This simply means that the variable is rescaled by the product of two lengths. For example, for one of the elements of the electric-field state vector  $\hat{\mathbf{e}}_n$  pertaining to the  $x$ -component, we have

$$\hat{\hat{e}}_x|_{i,j,k}^n = \Delta t \hat{e}_x|_{i,j,k}^n = \Delta t \Delta x_i^* e_x|_{i,j,k}^n . \quad (6.6)$$

Testing Faraday's and Ampère's law with  $\hat{\mathbf{w}}^2(x, y, z) \Lambda_n(t)$ , which correctly spans the range space of the curl and effectively evaluates Maxwell's equations in the face centers, yields

$$\begin{aligned} & \iiint \hat{\mathbf{w}}^2 \nabla \times (\hat{\mathbf{n}}^1)^T dx dy dz \sum_{n'} \int \hat{\Pi}_{n'}(t) \Lambda_n(t) dt \hat{\mathbf{e}}_{n'} \\ &= \iiint \hat{\mathbf{w}}^2 [\mu] (\hat{\mathbf{n}}^1)^T dx dy dz \sum_{n'} \int \partial_t \hat{\Pi}_{n'}(t) \Lambda_n(t) dt \hat{\hat{\mathbf{h}}}_{n'} , \end{aligned} \quad (6.7)$$

and

$$\begin{aligned} & \iiint \hat{\mathbf{w}}^2 \nabla \times (\hat{\mathbf{n}}^1)^T dx dy dz \sum_{n'} \int \hat{\Pi}_{n'}(t) \Lambda_n(t) dt \hat{\mathbf{h}}_{n'} \\ &= \iiint \hat{\mathbf{w}}^2 [\varepsilon] (\hat{\mathbf{n}}^1)^T dx dy dz \sum_{n'} \int \partial_t \hat{\Pi}_{n'}(t) \Lambda_n(t) dt \hat{\mathbf{e}}_{n'} , \end{aligned} \quad (6.8)$$

respectively. The time derivative of the pulse function is shifted to the triangle function by means of integration by parts. Hence, (6.7)–(6.8) give rise to

$$[\star_\mu^\circ] \frac{\hat{\mathbf{h}}_n - \hat{\mathbf{h}}_{n-1}}{\Delta t} = [\star_c^\circ] \frac{\hat{\mathbf{e}}_n + \hat{\mathbf{e}}_{n-1}}{2} \quad (6.9)$$

$$[\star_\varepsilon^\circ] \frac{\hat{\mathbf{e}}_n - \hat{\mathbf{e}}_{n-1}}{\Delta t} = [\star_c^\circ] \frac{\hat{\mathbf{h}}_n + \hat{\mathbf{h}}_{n-1}}{2} , \quad (6.10)$$

with

$$[\star_\varepsilon^\circ] = \iiint \hat{\mathbf{w}}^2[\varepsilon] (\hat{\mathbf{n}}^1)^T dx dy dz \quad (6.11)$$

$$[\star_\mu^\circ] = \iiint \hat{\mathbf{w}}^2[\mu] (\hat{\mathbf{n}}^1)^T dx dy dz \quad (6.12)$$

$$[\star_c^\circ] = \iiint \hat{\mathbf{w}}^2 \nabla \times (\hat{\mathbf{n}}^1)^T dx dy dz . \quad (6.13)$$

The Hodge operators (6.11)–(6.13) are highlighted by a circle to indicate that the collocated grid is most naturally terminated by periodic boundary conditions (PBCs) in order to end up with a well-posed set of update equations. Nonetheless, PEC and PMC boundary conditions are easily realized as well, but they require an asymmetrical use of image theory [2, Sec. 3.5.4]. Also, the circle notation facilitates the distinction between Yee- and FCI-operators.

Besides the triangle-triangle mass lumping (3.58), the occurring collocated pulse-triangle inner products are also determined by means of the trapezoidal quadrature rule applied to the primary-grid nodes. More specifically,

$$\int_{-\infty}^{+\infty} \hat{\Pi}_{i_1}^*(x) \Lambda_{i_2}(x) dx \approx \begin{cases} 1 & \text{if } i_1 = i_2 = i \\ 0 & \text{else} \end{cases} . \quad (6.14)$$

The staggered pulse-triangle inner products give rise to two-point interpolations

$$\int_{-\infty}^{+\infty} \hat{\Pi}_{i_1}(x) \Lambda_{i_2}(x) dx = \begin{cases} \frac{1}{2} & \text{if } i_2 \in \{i_1, i_1 + 1\} \\ 0 & \text{else} \end{cases} , \quad (6.15)$$

as do the staggered pulse-pulse inner products

$$\int_{-\infty}^{+\infty} \hat{\Pi}_{i_1}(x) \hat{\Pi}_{i_2}^*(x) dx = \begin{cases} \frac{1}{2\Delta x_{i_2}^*} & \text{if } i_2 \in \{i_1, i_1 + 1\} \\ 0 & \text{else} \end{cases} . \quad (6.16)$$

The grid is assumed to consist of  $N = N_x N_y N_z$  cells terminated by PBCs. Then, upon closer inspection of (6.13), it is found that

$$[\star_c^\circ] = [\delta^*][\tilde{\star}_c^\circ][\delta^*]^{-1} , \quad (6.17)$$

with the mixed interpolation-differentiation curl operator

$$[\tilde{\star}_c^\circ] = \begin{bmatrix} 0 & -I_{N_x} \otimes A_y^\circ \otimes \delta_z^{-1} D_z^\circ & I_{N_x} \otimes \delta_y^{-1} D_y^\circ \otimes A_z^\circ \\ A_x^\circ \otimes I_{N_y} \otimes \delta_z^{-1} D_z^\circ & 0 & -\delta_x^{-1} D_x^\circ \otimes I_{N_y} \otimes A_z^\circ \\ -A_x^\circ \otimes \delta_y^{-1} D_y^\circ \otimes I_{N_z} & \delta_x^{-1} D_x^\circ \otimes A_y^\circ \otimes I_{N_z} & 0 \end{bmatrix}_{3N \times 3N} , \quad (6.18)$$

the diagonal step-size matrix

$$[\delta^*] = \begin{bmatrix} \delta_x^* \otimes I_{N_y} \otimes I_{N_z} & & \\ & I_{N_x} \otimes \delta_y^* \otimes I_{N_z} & \\ & & I_{N_x} \otimes I_{N_y} \otimes \delta_z^* \end{bmatrix}_{3N \times 3N} , \quad (6.19)$$

the circulant 1-D difference incidence matrix

$$D_d^\circ = \begin{bmatrix} -1 & 1 & & & \\ & -1 & 1 & & \\ & & \ddots & \ddots & \\ 1 & & & -1 & 1 \\ & & & & -1 \end{bmatrix}_{N_d \times N_d} \quad d \in \{x, y, z\} , \quad (6.20)$$

the circulant 1-D averaging operator

$$A_d^\circ = \frac{1}{2} \begin{bmatrix} 1 & 1 & & & \\ & 1 & 1 & & \\ & & \ddots & \ddots & \\ & & & 1 & 1 \\ 1 & & & & 1 \end{bmatrix}_{N_d \times N_d} \quad d \in \{x, y, z\} , \quad (6.21)$$

and  $\delta_d$  and  $\delta_d^*$  the diagonal primary and dual step-size matrices of rank  $N_d$ . Despite the use of the trapezoidal rule, the Hodge matrices (6.11)–(6.12) are not diagonal. Moreover, the material matrices  $[\varepsilon]$  and  $[\mu]$  are not necessarily diagonal either in the case of anisotropic media. For example,

$$[\star_\varepsilon^\circ] = A[\varepsilon] = \begin{bmatrix} I_{N_x} \otimes A_y^\circ \otimes A_z^\circ & & \\ & A_x^\circ \otimes I_{N_y} \otimes A_z^\circ & \\ & & A_x^\circ \otimes A_y^\circ \otimes I_{N_z} \end{bmatrix} \begin{bmatrix} [\varepsilon_{xx}] [\varepsilon_{xy}] [\varepsilon_{xz}] \\ [\varepsilon_{yx}] [\varepsilon_{yy}] [\varepsilon_{yz}] \\ [\varepsilon_{zx}] [\varepsilon_{zy}] [\varepsilon_{zz}] \end{bmatrix} . \quad (6.22)$$

Each constituent block of  $[\varepsilon]$ , e.g.  $[\varepsilon_{xx}]$ , is diagonal. To derive (6.22), nine different types of inner products were calculated, one for each block in  $[\varepsilon]$ . In fact, it is stunning how simple (6.22) is, given the preceeding mathematical derivation, which, indeed, shows that the FCI-FDTD method is well suited to model anisotropic media. An expression similar to (6.22) exists for  $[\star_\mu^\circ]$ . Interestingly,  $[\star_\varepsilon^\circ]$  and  $[\star_\mu^\circ]$  do not feature any information about the grid's metric. This information is all collected in  $[\star_c^\circ]$ , even though this operator does not originate from a constitutive

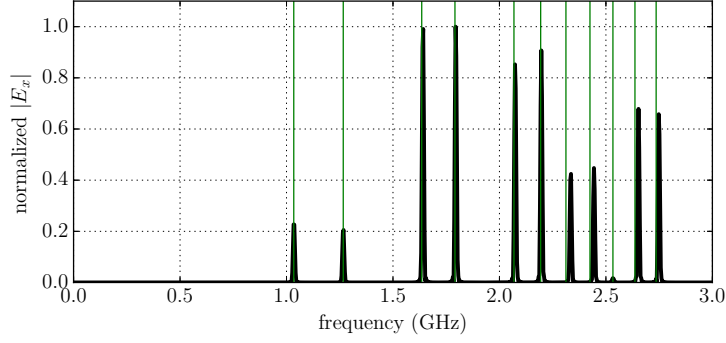


**Figure 6.2:** Resonances inside a cubic cavity of size 205 mm filled with vacuum. The cavity is divided into  $20 \times 20 \times 20$  cells of size 10 mm. The use of image theory, which is required to construct the PEC boundary conditions, adds half a cell to the cavity. The cavity is excited by an electric dipole current source with differentiated-gaussian time signature placed close to its center. The highest frequency (3 GHz) corresponds to ten samples per wavelength. The electric field component parallel to the dipole is recorded in a random point inside the cavity. The time signal is multiplied by a Hanning window prior to the Fourier transform. The resonance frequencies computed by the FCI-FDTD method (*black*) agree well with the analytical solutions (*green*). No additional peaks owing to spurious solutions pop up.

relation. Nevertheless, the star notation is used for the curl operator  $[\star_c^\circ]$  to highlight the metric content. It should be noted that, in contrast to the Yee scheme,  $[\star_\epsilon^\circ]$  and  $[\star_\mu^\circ]$  are not symmetric. However, they are almost symmetric since

$$(A_d^\circ)^T = S^T A_d^\circ, \quad (6.23)$$

with  $S$  the primary circulant matrix or circular upshift matrix [4, Fact 5.16.7].

Interestingly, this fully collocated method features the correct continuity of the tangential electric and magnetic fields across material discontinuities. This last fact is very important and cannot be deduced from the finite-element analysis based on zero-forms performed in [1]. In contrast to conventional nodal finite elements that are indeed based on zero-forms, there is no reason to doubt the physical correctness of the FCI-FDTD method. From a theoretical perspective, the method is not suspected to support spurious solutions. Indeed, this is corroborated by the numerical computation of the resonance frequencies inside a vacuum cavity as depicted in Fig. 6.2.

### 6.3 Properties

First of all, it should be noted that, after switching from the state variables  $(\hat{\mathbf{e}}_n, \hat{\mathbf{h}}_n)$  to  $(\mathbf{e}_n, \mathbf{h}_n)$ , the FCI-FDTD scheme derived in previous section is found to be equiv-

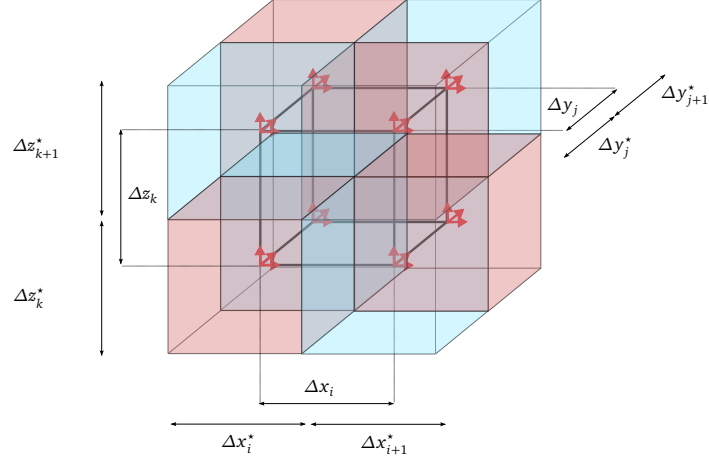


**Figure 6.3:** Material mapping in the fully collocated grid. Each node of the cubic grid is an anchor point for all six state variables ( $E_x, E_y, E_z, H_x, H_y, H_z$ ). Materials are assigned to cuboid volumes such that each grid node is exactly in the center of a cuboid material piece. Hence, material boundaries are right in the middle between grid nodes, where Maxwell's equations are effectively evaluated. Moreover, the updated fields are aligned to the material boundaries such that tangential field continuity is guaranteed.

alent to the scheme proposed in [1], [2]. More specifically, the update equation reads

$$\begin{bmatrix} \frac{A[\tilde{\epsilon}]}{\Delta t} & -\frac{[\tilde{\kappa}_c^\circ]}{2} \\ \frac{[\tilde{\kappa}_c^\circ]}{2} & \frac{A[\tilde{\mu}]}{\Delta t} \end{bmatrix} \begin{bmatrix} \mathbf{e}_{n+1} \\ \mathbf{h}_{n+1} \end{bmatrix} = \begin{bmatrix} \frac{A[\tilde{\epsilon}]}{\Delta t} & \frac{[\tilde{\kappa}_c^\circ]}{2} \\ -\frac{[\tilde{\kappa}_c^\circ]}{2} & \frac{A[\tilde{\mu}]}{\Delta t} \end{bmatrix} \begin{bmatrix} \mathbf{e}_n \\ \mathbf{h}_n \end{bmatrix}, \quad (6.24)$$

with rescaled dielectric tensors

$$[\tilde{\epsilon}] = [\delta^\star]^{-1} [\epsilon] [\delta^\star] \quad (6.25)$$

$$[\tilde{\mu}] = [\delta^\star]^{-1} [\mu] [\delta^\star], \quad (6.26)$$

which only differ from the original tensors  $[\epsilon]$  and  $[\mu]$  if anisotropic media with non-zero off-diagonal blocks are considered. The dual-grid steps in  $[\delta^\star]$  determine the size of the discretized material voxels (see Fig. 6.3). The FCI-FDTD method displays the well-known Crank-Nicolson time integration scheme, which is very inefficient for large problems, especially in 3-D, as the system matrix scales proportionally with the total number of cells  $N$ . As a matter of fact, the spatial interpolations present in  $A$  and in  $[\tilde{\kappa}_c^\circ]$  constitute a spatial analog of the Crank-Nicolson scheme, which makes the system matrix less sparse than its Yee-grid counterpart. However, owing to the structured cubic grid, it should be possible to build an efficient iterative solver with proper preconditioner.

The interpolations and differentiations that happen under the hood of the FCI-FDTD method are visualized in Fig. 6.4. In the center of each face of the FCI

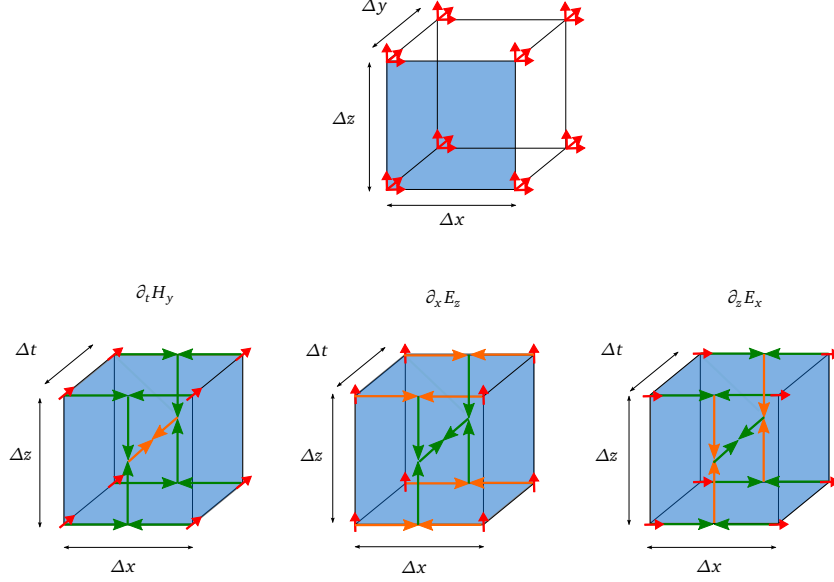


**Figure 6.4:** Visualization of the interpolations (green) and differentiations (orange) used in Faraday's law  $\mu \partial_t H_y = \partial_x E_z - \partial_z E_x$ , which is evaluated in the center of a face of the collocated cell normal to the  $y$ -axis (blue).

cell, the normal electric and magnetic field components are updated. Hence, these updated components, corresponding to the time-differentiated fields in Maxwell's equations, are spatially interpolated along their two normal directions. The remaining fields that circulate the updated field according to Maxwell's curl equations, are differentiated along their normal direction and interpolated along their tangential direction such that the spatial derivatives occurring in Maxwell's equations are evaluated in the face center as well. To evaluate the updated field and the circulating fields at the same time instance, the latter need to be interpolated in time as well, such that, eventually, every field component is differentiated once and interpolated twice with respect to different dimensions per update equation. Since both central differences and central interpolations are second-order accurate, the FCI-FDTD method is *unconditionally* second-order accurate, i.e. even for nonuniform gridding. Besides, owing to the collocation, axis-aligned materials are inserted unambiguously without requiring additional material averaging along the boundaries. As is depicted Fig. 6.3, the boundaries of the piecewise medium after discretization cross the face centers. As such, they are aligned with the updated fields in their evaluation point, i.e. after the double spatial interpolation, such that, indeed, the FCI-FDTD method guarantees tangential electric and magnetic field continuity, as could be expected from the expansion in one-forms. Hence, in contrast to the  $(E, B)$  Yee-FDTD method, which ensures the continuity of three components, the  $(E, H)$  FCI-FDTD method has four continuous components, which

again improves the accuracy.

The numerical dispersion relation of the fully-collocated implicit FDTD method with homogeneous isotropic medium and uniform grid is

$$\left[ \frac{\tan\left(\frac{\omega\Delta t}{2}\right)}{c\Delta t} \right]^2 = \left[ \frac{\tan\left(\frac{\tilde{k}_x\Delta x}{2}\right)}{\Delta x} \right]^2 + \left[ \frac{\tan\left(\frac{\tilde{k}_y\Delta y}{2}\right)}{\Delta y} \right]^2 + \left[ \frac{\tan\left(\frac{\tilde{k}_z\Delta z}{2}\right)}{\Delta z} \right]^2, \quad (6.27)$$

which converges to its continuous counterpart for dense discretizations. Owing to the infinite range of the tangent function, the FCI-FDTD method is stable for any time step. A rigorous stability proof for general nonuniform grids with different kinds of boundary conditions is provided in [2, Sec. 3.5.5].

In summary, the main advantages of the FCI-FDTD method are

- unconditional stability,
- unconditional second-order accuracy yielding huge geometrical flexibility,
- enhanced modeling of anisotropic materials,
- enhanced modeling of axis-aligned material boundaries,
- tangential electric and magnetic field continuity,

whereas the main disadvantages are

- inefficiency due to a CN-like implicit update scheme,
- PEC boundary conditions use image theory which cannot be directly applied to anisotropic media [5],
- large code refactoring cost for commercial FDTD solvers based on the Yee scheme.

## 6.4 Numerical example: 2-D anisotropic slab

By way of example, the shielding effectiveness of an anisotropic slab with off-axis dielectric tensor is resolved by means of the FCI-FDTD method, embedded in an overall Yee grid via Huygens subgridding (HSG) [6], and compared to the solution obtained by a full Yee grid where the geometry is rotated to align the dielectric tensor with the Cartesian axes (Fig. 6.5).

For the HSG-FCI method, the spatial resolution of the Yee grid is  $\Delta x = \Delta y = 2.5$  mm and the time step is chosen to be the 2-D Courant limit  $\Delta t = 5.897$  ps. The collocated subgrid is nonuniform and resolves the slab by  $\Delta x = 1$  mm and

$\Delta y = 1.25$  mm. The axis-aligned 10 mm-slab is characterized by the dielectric tensor

$$\varepsilon_r^{\text{fci}} = \begin{bmatrix} 10 & 6 \\ 6 & 10 \end{bmatrix} . \quad (6.28)$$

The simulation counts  $N_t = 1500$  iterations. For the conventional Yee-FDTD simulation, we used  $\Delta x = \Delta y = 0.707$  mm,  $\Delta t = 1.668$  ps and  $N_t = 2400$ . The slab is rotated by  $45^\circ$  such that its boundary is staircased but the dielectric tensor is axis-aligned, i.e.

$$\varepsilon_r^{\text{yee}} = \begin{bmatrix} 16 & 0 \\ 0 & 4 \end{bmatrix} . \quad (6.29)$$

The magnetic line source produces a Gaussian-modulated sine wave with sufficient spectral content in the 0-26 GHz frequency band, and it is located 50 mm in front of the slab. The magnetic field is recorded in the observation point at the back of the slab, as is indicated in Fig. 6.5. Two simulations are run: one where the slab is made of the anisotropic dielectric and one where it is made of vacuum (as is the ambient medium). The ratio of the discrete Fourier transforms of the two recorded signals yields the shielding effectiveness (SE). Fig. 6.6 shows that the SE obtained by both approaches coincides perfectly for frequencies lower than 6 GHz. It has to be noted that at  $f = 6$  GHz, the spatial resolution reaches twenty samples per wavelength. Hence, beyond this frequency, numerical dispersion largely affects the solution.

The Huygens subgridding technique does not fit in the “keep it simple” spirit. We refer the reader to [7] for some extra explanation. Moreover, it is believed that with the finite-element analysis provided in Section 6.2, a better hybridization of the Yee- and the FCI-FDTD method should be possible. In fact, this is achieved for collocation in one direction in the next chapter.

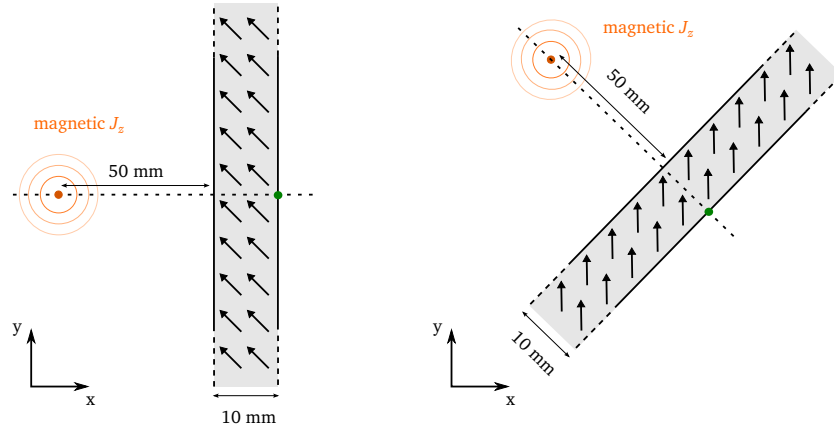


**Figure 6.5:** Two numerical approaches to compute the shielding effectiveness of an anisotropic slab illuminated by a near-field magnetic line source. Left: The slab is resolved by the FCI-FDTD method, which can easily handle the non-diagonal dielectric tensor. Right: The entire geometry is rotated such that the dielectric tensor is aligned with the coordinate axes to allow a straightforward modeling via the traditional Yee-FDTD method. The observation point is indicated by a green dot.

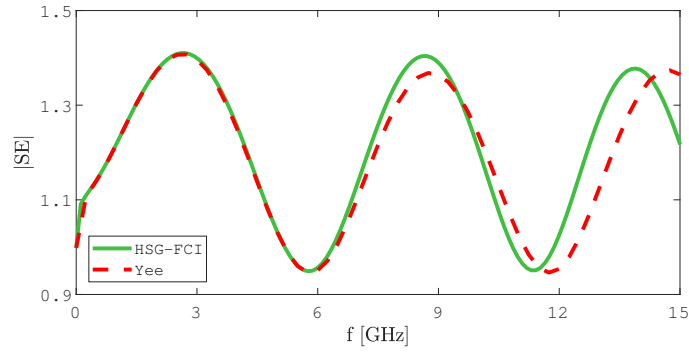


**Figure 6.6:** Magnitude of the shielding effectiveness of an anisotropic dielectric slab located in the near field of a magnetic line source.



## References

- [1] W. Tierens and D. De Zutter, “An unconditionally stable time-domain discretization on cartesian meshes for the simulation of nonuniform magnetized cold plasma”, *Journal of Computational Physics*, vol. 231, pp. 5144–5156, 2012.
- [2] W. Tierens, “Finite Element and Finite Difference Based Approaches for the Time-Domain Simulation of Plasma-Wave Interactions”, PhD thesis, Ghent University, 2013.
- [3] M. Nauta, M. Okoniewski, and M. Potter, “FDTD method on a Lebedev grid for anisotropic materials”, *Transactions on Antennas and Propagation*, vol. 61, no. 6, pp. 3161–3171, 2013.
- [4] D. Bernstein, *Matrix Mathematics (2nd edition)*. Princeton University Press, 2009.
- [5] B. Rao and T. Wu, “On the applicability of image theory in anisotropic media”, *IEEE Transactions on Antennas and Propagation*, vol. 13, no. 5, pp. 814–815, 1965.
- [6] J.-P. Bérenger, “Extension of the FDTD Huygens subgridding algorithm to two dimensions”, *IEEE Transactions on Antennas and Propagation*, vol. 57, no. 12, pp. 3860–3867, 2009.
- [7] A. Van Londersele, D. De Zutter, and D. Vande Ginste, “Huygens subgridding combined with the 2D fully collocated implicit FDTD method”, in *2016 IEEE International Symposium on Antennas and Propagation (APSURSI)*, Fajardo, Puerto Rico, 26 June - 1 July 2016, pp. 2025–2026.



# 7

## The Unidirectionally-Collocated Hybrid Implicit-Explicit FDTD Method

“Shut up and calculate!”  
David Mermin

★ ★ ★

*This chapter proposes a novel hybrid implicit-explicit (HIE) FDTD method with collocation in the direction of implicitization. In this direction, the method features increased accuracy, the reason being twofold: 1) the applied combination of interpolations and differentiations preserves second-order accuracy upon nonuniform discretization; 2) material boundaries are more accurately approximated by the grid. The proposed unidirectionally collocated HIE-FDTD method is specifically geared at multiscale problems that require refinement in one dimension, such as thin conductive layers. The method is extended with a uniaxial perfectly matched layer (UPML) to mimic open space, an auxiliary differential equation (ADE) to model dispersive Drude media, and the possibility to hybridize with the classical Yee scheme. The method's stability and accuracy are verified by several numerical examples, such as a 3-D microstrip line, a metal grating scatterer, and a graphene shield.*

## 7.1 Introduction

The proposed unidirectionally collocated hybrid implicit-explicit (UCHIE) FDTD technique eliminates one of the spatial dependencies from the time step's stability limit at the expense of more computational complexity. This is most lucrative when simulating planar multilayered structures which indeed require a higher sampling density in one dimension. The plethora of documented HIE methods, e.g. [1]–[8], stick to the conventional Yee cell, though this discretization scheme is merely first-order accurate if applied nonuniformly. Furthermore, its staggering introduces additional errors when approximating material boundaries. We cope with these inconveniences by projecting the Yee cell onto a plane normal to the direction of implicitization, such that we get a layered discretization scheme which accurately resolves the material boundaries. This is demonstrated in Fig. 3.2(b) for implicitization in the  $x$ -dimension. Using an interpolation strategy similar to [9], second-order accuracy is preserved upon nonuniform discretization in this particular direction. Furthermore, using an interfacing rule similar to the one proposed in [10] in 1-D, the UCHIE-FDTD method can be hybridized with the traditional Yee-FDTD method.

In this chapter, the UCHIE-FDTD method is first briefly sketched in terms of finite elements. Then, in Section 7.3, the interfacing with the classical Yee scheme is established. Next, in Section 7.4, Drude media and a UPML are added. In Section 7.5, the stability of the UCHIE method is discussed by means of complex-frequency analysis (CFA). The stability of the 2-D UCHIE subgridding scheme is numerically validated. Section 7.6 elaborates on the numerical dispersion error of the UCHIE-FDTD method, which is not unexpectedly found to be an anisotropic mixture of the dispersion errors occurring in the conventional FDTD method and the FCI-FDTD method. Finally, in Section 7.7, several numerical examples are provided to demonstrate the accuracy and stability of the proposed method. The numerical reflections arising from the UPML and from the interface between UCHIE grid and Yee grid are both quantified. Furthermore, the SE of a thin conductive layer and a graphene sheet are compared to their analytical solution. The characteristic impedance of a 3-D microstrip line and the far-field scattering pattern from a metal grating are compared to the solution of an in-house MoM solver.

## 7.2 Finite-element interpretation

The UCHIE-FDTD method is a mixed  $(E, B)$ – $(D, H)$  scheme with, for collocation in the  $x$ -dimension, the following set of 4-D spacetime finite-element expansions:

$$B_x(x, y, z, t) = \sum_{i,j,k,n} \hat{b}_x|_{i,j,k}^n \Lambda_i(x) \hat{\Pi}_j(y) \hat{\Pi}_k(z) \Lambda_n(t) \quad (7.1)$$

$$E_y(x, y, z, t) = \sum_{i,j,k,n} \hat{e}_y|_{i,j,k}^n \Lambda_i(x) \hat{\Pi}_j(y) \Lambda_k(z) \hat{\Pi}_n(t) \quad (7.2)$$

$$E_z(x, y, z, t) = \sum_{i,j,k,n} \hat{e}_z|_{i,j,k}^n \Lambda_i(x) \Lambda_j(y) \hat{\Pi}_k(z) \hat{\Pi}_n(t) \quad (7.3)$$

$$D_x(x, y, z, t) = \sum_{i,j,k,n} \hat{d}_x|_{i,j,k}^n \Lambda_i(x) \hat{\Pi}_j^*(y) \hat{\Pi}_k^*(z) \Lambda_n(t) \quad (7.4)$$

$$H_y(x, y, z, t) = \sum_{i,j,k,n} \hat{h}_y|_{i,j,k}^n \Lambda_i(x) \hat{\Pi}_j^*(y) \Lambda_k^*(z) \hat{\Pi}_n(t) \quad (7.5)$$

$$H_z(x, y, z, t) = \sum_{i,j,k,n} \hat{h}_z|_{i,j,k}^n \Lambda_i(x) \Lambda_j^*(y) \hat{\Pi}_k^*(z) \hat{\Pi}_n(t) \quad (7.6)$$

The Maxwell equations that differentiate  $x$ -components with respect to time are satisfied in the strong sense, resulting in two Yee-like explicit update equations. A weak formulation of Maxwell's equations is solved for the remaining  $y$ - and  $z$ -components. Similarly to the FCI-FDTD method, this is achieved by means of the face-centered two-form testing functions, which correctly model the range space of the curl:

$$T_{e_z}(x, y, z, t) = T_{h_y}(x, y, z, t) = \hat{\Pi}_i(x) \Lambda_j(y) \hat{\Pi}_k(z) \Lambda_n(t) \quad (7.7)$$

$$T_{e_y}(x, y, z, t) = T_{h_z}(x, y, z, t) = \hat{\Pi}_i(x) \hat{\Pi}_j(y) \Lambda_k(z) \Lambda_n(t) \quad (7.8)$$

Hence, the update equations for  $E_y$ ,  $E_z$ ,  $H_y$  and  $H_z$  are again evaluated in the face centers of the cell, giving rise to tangential field continuity across material discontinuities in the  $x$ -dimension, as could also be expected from the fact that all fields are expanded in linear triangle functions along the  $x$ -axis.

To avoid repetition, the update equations are not yet written down in this section, but they will in Section 7.4.2 with inclusion of Drude media and a UPML. In a nutshell, the UCHIE-FDTD method organizes the electromagnetic field components in unidirectionally collocated cells such as the one depicted in Fig. 3.2(b). It retains the conventional central differences, but it evaluates the Maxwell equations that contain a derivative with respect to the direction of collocation (here the  $x$ -dimension) right in the middle between two adjacent samples in that direction by means of linear interpolations. To end up with a consistent update scheme, similar field interpolations are needed in time. This principle is exemplified in Fig. 7.1. In the end, the two field components along the direction of collocation, i.e.  $D_x$  and  $B_x$ , are updated explicitly, whereas the remaining four field components are updated implicitly. Unlike traditional collocated finite-difference methods, the proposed

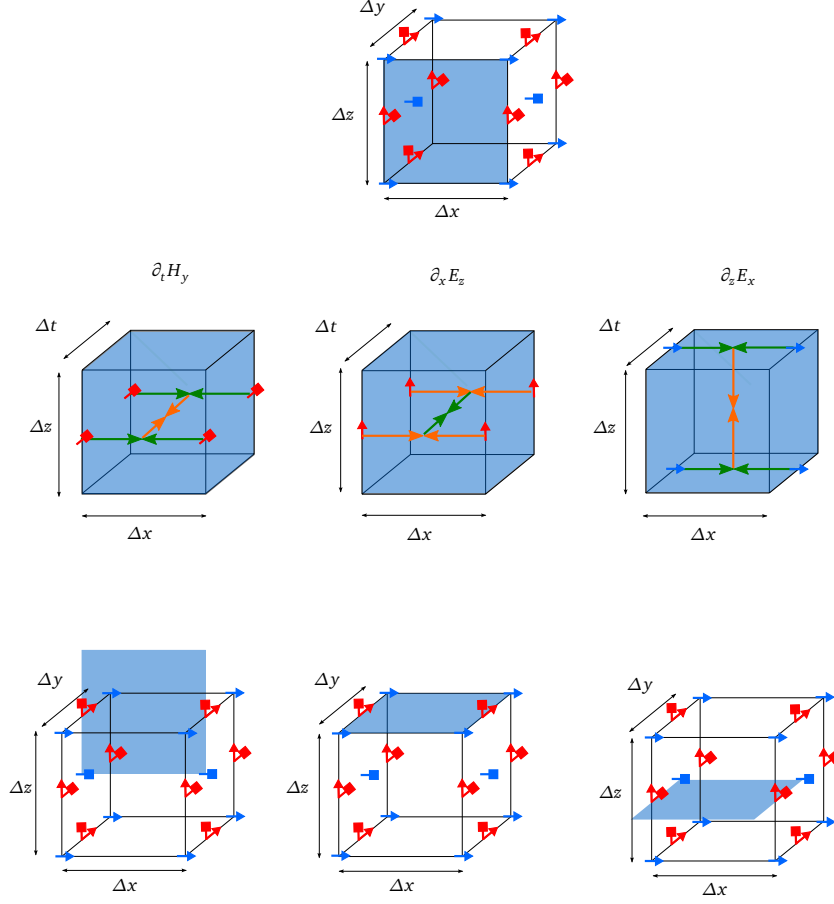


**Figure 7.1:** Visualization of the interpolations (*green*) and differentiations (*orange*) used by the UCHIE-FDTD method with collocation along the  $x$ -dimension. Electric and magnetic components are denoted by arrows and square arrows respectively. Differently colored markers are staggered in time. Faraday's law  $\mu \partial_t H_y = \partial_x E_z - \partial_z E_x$  is evaluated in the center of a face normal to the  $y$ -axis (*blue*). Similar interpolation-differentiation schemes exist for the three other (dual) faces indicated on the bottom row. The two remaining updates occurring in the faces normal to the  $x$ -axis do not require interpolations and are essentially conventional (Yee scheme) central-difference updates.

scheme ensures second-order accuracy, albeit at the cost of computationally more involved implicit update equations.

In the remainder of this chapter, we will use  $E_x$  and  $H_x$  instead of  $D_x$  and  $B_x$ , which is a straightforward change of variables since the permittivity and permeability matrices are diagonal (after mass lumping). Also, we adopt the “half-integer notation” to enhance the readability.

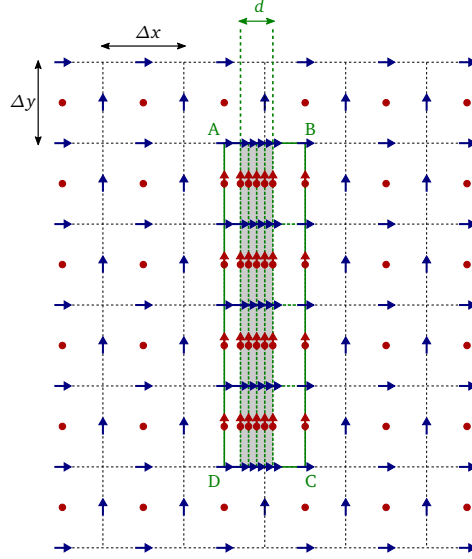


**Figure 7.2:** Embedding of the UCHIE subgrid, denoted by the rectangle ABCD, in a Yee grid in the 2-D TE case, i.e. the dots denote  $H_z$  variables and the arrows denote  $E_x$  and  $E_y$  variables. The gray-colored area indicates a conductor of thickness  $d$ , comprising four UCHIE cells in this example. The blue and red markers are discretized half a time step apart.

### 7.3 UCHIE/Yee hybridization

Below, the 2-D TE UCHIE-FDTD method is hybridized with the traditional Yee scheme for optimal efficiency. A dual 2-D TM scheme exists as well (see [11]). The typical configuration we want to tackle is depicted in Fig. 7.2. A thin, e.g. highly conductive, slab is embedded in a classical FDTD grid. This slab can be substantially smaller than the Yee cell of the global FDTD grid in one dimension, here the  $x$ -dimension, i.e.  $d \ll \Delta x$ , although, it encompasses several Yee cells in the other dimension.

To integrate the UCHIE grid into the classical FDTD grid, two sets of interfaces occur:

- the left and right interfaces, which require the transition from staggered, explicitly updated  $(E_y, H_z)$  values to collocated, implicitly updated  $(E_y, H_z)$  values, similar to the 1-D scheme described in [10];
- the upper and lower interfaces, which are only affected by explicit updates in main grid and subgrid, and which exhibit edge termination.

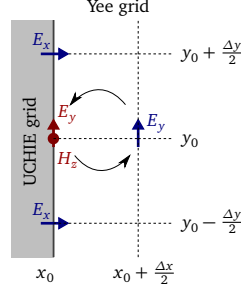


**Figure 7.3:** Visualization of the coupling scheme at the right interface. The synchronous update of  $H_z(x_0, y_0)$  and  $E_y(x_0, y_0)$  on the right edge of the subgrid requires input from the adjacent  $E_y(x_0 + \frac{\Delta x}{2}, y_0)$  in the Yee grid. In return, the explicit update of  $E_y(x_0 + \frac{\Delta x}{2}, y_0)$  requires input from  $H_z(x_0, y_0)$ .

The first set of interfaces needs to be included in the UCHIE update matrices as to retrieve a well-posed system. The necessary interface updates are obtained by testing Faraday's law, in the Yee part expanded in the traditional Whitney elements (3.44)–(3.45) and in the UCHIE part in the mixed Whitney elements (7.1)–(7.6), with the testing function (7.8), where the interpolatory character of the basis is preserved, i.e. the basis functions are zero in all points except for one. After some extensive calculations with mass lumping of triangle-triangle and collocated triangle-pulse inner products, and substitution of the update equation for  $H_z(x_0 + \Delta x, y_0)$ , this eventually yields the first-order accurate interface equation

$$\begin{aligned} \frac{\mu}{\Delta t} (H_z|_{x_0, y_0}^{t_0 + \frac{\Delta t}{2}} - H_z|_{x_0, y_0}^{t_0 - \frac{\Delta t}{2}}) &= \frac{1}{\Delta y} (E_x|_{x_0, y_0 + \frac{\Delta y}{2}}^{t_0} - E_x|_{x_0, y_0 - \frac{\Delta y}{2}}^{t_0}) \\ &\quad - \frac{1}{\Delta x} (2E_y|_{x_0 + \frac{\Delta x}{2}, y_0}^{t_0} - E_y|_{x_0, y_0}^{t_0 + \frac{\Delta t}{2}} - E_y|_{x_0, y_0}^{t_0 - \frac{\Delta t}{2}}) . \end{aligned} \quad (7.9)$$

The interested reader is referred to [12, Sec. 5.3] for similar calculations. Equation (7.9) is visualized in Fig. 7.3. The upper and lower interface use a standard reciprocal coupling scheme: the update of the fine-grid  $E_x$  requires a standard linear interpolation of the nearest coarse-grid  $H_z$ . The corresponding interpolation matrix is transposed and normalized to yield the restriction matrix needed for the updates of the adjacent coarse-grid  $H_z$ .

The UCHIE subgridding technique is easily added to existing FDTD codes. In case of a vertically oriented slab (see Fig. 7.2), the final subgridding algorithm obeys the following leapfrog time iteration scheme. First,  $H_z$  is updated in the FDTD region. This step uses input from the  $E_x$  located at upper and lower edges of the UCHIE region. Next,  $E_y$  and  $H_z$  are simultaneously updated in the UCHIE region with inclusion of the left and right interface conditions alike (7.9). Here,  $E_y$  values next to the interface are inserted into the implicit calculation. Then,  $E_x$  is explicitly updated in the UCHIE region. Along the upper and lower interface, this requires an interpolation of  $H_z$  values as explained before. Finally,  $E_x$  and  $E_y$  are updated in the FDTD region. The latter uses input from  $H_z$  along the left and right interface.

## 7.4 Drude media and uniaxial PML

### 7.4.1 Continuous equations

#### Drude medium

At optical frequencies, the electron motion inside metals interacts with the electromagnetic waves in a nonnegligible manner and is most efficiently taken into account by means of a dispersive Drude model

$$\sigma(\omega) = \frac{\sigma_{\text{DC}}}{1 + j\omega\gamma} , \quad (7.10)$$

where  $\sigma_{\text{DC}}$  is the conductivity at  $\omega = 0$ . Drude media are typically incorporated into Maxwell's equations by means of an auxiliary differential equation describing the time-domain behavior of the conduction current density  $\mathbf{J}$  [13, Eq. 9-56c]. Thus, a set of three differential equations needs to be solved, namely

$$\mu_0 \partial_t \mathbf{H} = -\nabla \times \mathbf{E} \quad (7.11)$$

$$\varepsilon_0 \partial_t \mathbf{E} + \mathbf{J} = \nabla \times \mathbf{H} \quad (7.12)$$

$$\gamma \partial_t \mathbf{J} + \mathbf{J} = \sigma_{\text{DC}} \mathbf{E} . \quad (7.13)$$

The substitutions

$$\mathbf{E} = Z_0 \tilde{\mathbf{E}} \quad (7.14)$$

$$\tau = c_0 t \quad (7.15)$$

$$\tilde{\sigma}_{\text{DC}} = Z_0 \sigma_{\text{DC}} \quad (7.16)$$

$$\tilde{\gamma} = c_0 \gamma , \quad (7.17)$$

simplify (7.11)–(7.13) to

$$\partial_\tau \mathbf{H} = -\nabla \times \tilde{\mathbf{E}} \quad (7.18)$$

$$\partial_\tau \tilde{\mathbf{E}} + \mathbf{J} = \nabla \times \mathbf{H} \quad (7.19)$$

$$\tilde{\gamma} \partial_\tau \mathbf{J} + \mathbf{J} = \tilde{\sigma}_{\text{DC}} \tilde{\mathbf{E}} . \quad (7.20)$$

#### UPML

In order to perform simulations in open space, a UPML is added [14]. Thereto, the electric and magnetic field each require one auxiliary equation to model the dispersive PML medium. Moreover, the electric field requires an additional auxiliary equation to prolong the Drude medium inside the PML. We highlight these auxiliary unknowns by single and double dots. The final set of equations, including all

these considerations, is

$$\kappa_{[yzx]} \partial_\tau \dot{\mathbf{H}} + \tilde{\sigma}_{[yzx]} \dot{\mathbf{H}} = -\nabla \times \tilde{\mathbf{E}} \quad (7.21)$$

$$\kappa_{[zxy]} \partial_\tau \mathbf{H} + \tilde{\sigma}_{[zxy]} \mathbf{H} = \kappa_{[xyz]} \partial_\tau \dot{\mathbf{H}} + \tilde{\sigma}_{[xyz]} \dot{\mathbf{H}} \quad (7.22)$$

$$\partial_\tau \ddot{\mathbf{E}} + \mathbf{J} = \nabla \times \mathbf{H} \quad (7.23)$$

$$\tilde{\gamma} \partial_\tau \mathbf{J} + \mathbf{J} = \tilde{\sigma}_{\text{DC}} \ddot{\mathbf{E}} \quad (7.24)$$

$$\kappa_{[yzx]} \partial_\tau \dot{\tilde{\mathbf{E}}} + \tilde{\sigma}_{[yzx]} \dot{\tilde{\mathbf{E}}} = \partial_\tau \ddot{\tilde{\mathbf{E}}} \quad (7.25)$$

$$\kappa_{[zxy]} \partial_\tau \tilde{\mathbf{E}} + \tilde{\sigma}_{[zxy]} \tilde{\mathbf{E}} = \kappa_{[xyz]} \partial_\tau \dot{\tilde{\mathbf{E}}} + \tilde{\sigma}_{[xyz]} \dot{\tilde{\mathbf{E}}} , \quad (7.26)$$

where a shorthand notation was adopted for the tensors, e.g.

$$\kappa_{[yzx]} = \begin{bmatrix} \kappa_y & & \\ & \kappa_z & \\ & & \kappa_x \end{bmatrix} \quad \tilde{\sigma}_{[yzx]} = Z_0 \begin{bmatrix} \sigma_y & & \\ & \sigma_z & \\ & & \sigma_x \end{bmatrix} , \quad (7.27)$$

with for the  $i^{\text{th}}$  PML layer

$$\kappa_d = 1 + (\kappa_d^{\text{max}} - 1)(i/n_{\text{pml}})^m \quad (7.28)$$

$$\sigma_d = \sigma_d^{\text{max}}(i/n_{\text{pml}})^m \quad d \in \{x, y, z\} . \quad (7.29)$$

This is the so-called polynomially graded PML with number of layers  $n_{\text{pml}}$  and power  $m$ . Here, we always choose the standard values  $n_{\text{pml}} = 10$  and  $m = 4$ . Also, from [14, Eq. 38], we borrow the optimal value

$$\sigma_d^{\text{max}} = \frac{m+1}{150 \pi \Delta d} \quad d \in \{x, y, z\} , \quad (7.30)$$

where  $\Delta d$  is the spatial step in the  $d$ -dimension (i.e.  $\Delta x$ ,  $\Delta y$  or  $\Delta z$ ). The UPML is mathematically perceived as a complex stretching of the Cartesian coordinates (and the fields) ensuring impedance matching across its interface. In other words, it is a reflectionless lossy medium. The real-stretch parameter  $\kappa_d$  aims to absorb the evanescent waves, whereas the imaginary-stretch parameter  $\sigma_d$  is responsible for the absorption of the traveling waves. They are one and zero respectively inside the simulation region of interest, and they are polynomially graded according to (7.28)–(7.29) inside the PMLs normal to the  $d$ -dimension. In the next section, (7.21)–(7.26) are discretized, giving rise to the UCHIE-FDTD update equations.

#### 7.4.2 Update equations

In line with conventional ADE schemes, the electric current density components have the exact same discretization as their associated electric field components.

Hence, we get the following set of explicit update equations

$$\begin{aligned} \beta_y^+ \dot{h}_x|_{i,j+\frac{1}{2},k+\frac{1}{2}}^{n+1} &= \beta_y^- \dot{h}_x|_{i,j+\frac{1}{2},k+\frac{1}{2}}^n \\ &\quad - \frac{1}{\Delta y} (\tilde{e}_z|_{i,j+1,k+\frac{1}{2}}^{n+\frac{1}{2}} - \tilde{e}_z|_{i,j,k+\frac{1}{2}}^{n+\frac{1}{2}}) + \frac{1}{\Delta z} (\tilde{e}_y|_{i,j+\frac{1}{2},k+1}^{n+\frac{1}{2}} - \tilde{e}_y|_{i,j+\frac{1}{2},k}^{n+\frac{1}{2}}) \end{aligned} \quad (7.31)$$

$$\beta_z^+ h_x|_{i,j+\frac{1}{2},k+\frac{1}{2}}^{n+1} = \beta_z^- h_x|_{i,j+\frac{1}{2},k+\frac{1}{2}}^n + (\beta_x^+ \dot{h}_x|_{i,j+\frac{1}{2},k+\frac{1}{2}}^{n+1} - \beta_x^- \dot{h}_x|_{i,j+\frac{1}{2},k+\frac{1}{2}}^n) \quad (7.32)$$

for the magnetic field and

$$\begin{aligned} \left( \frac{1}{\Delta \tau} + \frac{\tilde{\sigma}_{\text{DC}}}{2\alpha^+} \right) \ddot{e}_x|_{i,j,k}^{n+1} &= \left( \frac{1}{\Delta \tau} - \frac{\tilde{\sigma}_{\text{DC}}}{2\alpha^+} \right) \ddot{e}_x|_{i,j,k}^n - \frac{1}{2} \left( 1 + \frac{\alpha^-}{\alpha^+} \right) j_x|_{i,j,k}^n \\ &\quad + \frac{1}{\Delta y} (h_z|_{i,j+\frac{1}{2},k}^{n+\frac{1}{2}} - h_z|_{i,j-\frac{1}{2},k}^{n+\frac{1}{2}}) - \frac{1}{\Delta z} (h_y|_{i,j,k+\frac{1}{2}}^{n+\frac{1}{2}} - h_y|_{i,j,k-\frac{1}{2}}^{n+\frac{1}{2}}) \end{aligned} \quad (7.33)$$

$$\alpha^+ j_x|_{i,j,k}^{n+1} = \alpha^- j_x|_{i,j,k}^n + \tilde{\sigma}_{\text{DC}} (\ddot{e}_x|_{i,j,k}^{n+1} + \ddot{e}_x|_{i,j,k}^n) \quad (7.34)$$

$$\beta_y^+ \dot{e}_x|_{i,j,k}^{n+1} = \beta_y^- \dot{e}_x|_{i,j,k}^n + \frac{1}{\Delta \tau} (\ddot{e}_x|_{i,j,k}^{n+1} - \ddot{e}_x|_{i,j,k}^n) \quad (7.35)$$

$$\beta_z^+ \ddot{e}_x|_{i,j,k}^{n+1} = \beta_z^- \ddot{e}_x|_{i,j,k}^n + \beta_x^+ \dot{e}_x|_{i,j,k}^{n+1} - \beta_x^- \dot{e}_x|_{i,j,k}^n \quad (7.36)$$

for the electric field. Here, we used the notation

$$\alpha^\pm = \frac{2\tilde{\gamma}}{\Delta \tau} \pm 1 \quad (7.37)$$

$$\beta_d^\pm = \frac{\kappa_d}{\Delta \tau} \pm \frac{Z_0 \sigma_d}{2} \quad d \in \{x, y, z\} \quad (7.38)$$

There are two implicit update equations, i.e. (7.43) and (7.44). The PEC boundary conditions at the back of the PMLs require the exterior tangential electric fields to be zero. Consequently, for  $n_x$  cells in the  $x$ -dimension, there are  $n_x - 1$  electric field and  $n_x + 1$  magnetic field samples in (7.43)–(7.44). The bracket notation is used to denote diagonal matrices whose rank is  $n_x - 1$  or  $n_x + 1$  depending on whether they act on electric or magnetic field components respectively. We also introduced the  $x$ -interpolators

$$A_1 = \begin{bmatrix} 1 & 1 & & \\ & \ddots & \ddots & \\ & & 1 & 1 \end{bmatrix}_{n_x \times (n_x - 1)} \quad (7.39)$$

$$A_2 = \begin{bmatrix} 1 & 1 & & \\ & \ddots & \ddots & \\ & & 1 & 1 \end{bmatrix}_{n_x \times (n_x + 1)}, \quad (7.40)$$

and the  $x$ -differentiators

$$D_1 = \begin{bmatrix} \Delta x_1 & & \\ & \ddots & \\ & & \Delta x_{n_x} \end{bmatrix}^{-1} \begin{bmatrix} 1 & & \\ -1 & 1 & \\ & \ddots & \\ & & -1 & 1 \\ & & & -1 & 1 \end{bmatrix}_{n_x \times (n_x-1)} \quad (7.41)$$

$$D_2 = \begin{bmatrix} \Delta x_1 & & \\ & \ddots & \\ & & \Delta x_{n_x} \end{bmatrix}^{-1} \begin{bmatrix} -1 & 1 & \\ & \ddots & \\ & & -1 & 1 \end{bmatrix}_{n_x \times (n_x+1)} . \quad (7.42)$$

As suggested by the time-indices of the field samples, the time-stepping algorithm alternately performs sets of explicit and implicit updates. As one possible valid implementation, we opted to treat the update equations in the same order as they occur in this section.

### 7.4.3 Efficient solution method

In this section, an efficient strategy to solve the sparse linear system (7.43) is pointed out. First, the matrix in the l.h.s., which we will call  $M$  from now on, is partitioned as follows

$$M = \begin{bmatrix} M_{11} & M_{12} \\ M_{21} & M_{22} \end{bmatrix} = \left[ \begin{array}{ccc|ccc} [\alpha^+] & -[\tilde{\sigma}_{\text{DC}}] & 0 & 0 & 0 & 0 \\ \frac{A_1}{2} & \frac{A_1}{\Delta\tau} & 0 & 0 & D_2 & 0 \\ 0 & 0 & A_2[\beta_x^+] & 0 & 0 & D_1 \\ \hline 0 & -\frac{I}{\Delta\tau} & 0 & [\beta_z^+] & 0 & 0 \\ 0 & 0 & -[\beta_z^+] & 0 & [\beta_y^+] & 0 \\ 0 & 0 & 0 & -[\beta_y^+] & 0 & [\beta_x^+] \end{array} \right] . \quad (7.45)$$

Its inverse is given by [15, Prop. 2.8.7]

$$M^{-1} = \begin{bmatrix} S^{-1} & -S^{-1}M_{12}M_{22}^{-1} \\ -M_{22}^{-1}M_{21}S^{-1} & M_{22}^{-1} + M_{22}^{-1}M_{21}S^{-1}M_{12}M_{22}^{-1} \end{bmatrix} , \quad (7.46)$$

with

$$M_{22}^{-1} = \begin{bmatrix} [\beta_z^+]^{-1} & 0 & 0 \\ 0 & [\beta_y^+]^{-1} & 0 \\ [\beta_x^+]^{-1}[\beta_y^+][\beta_z^+]^{-1} & 0 & [\beta_x^+]^{-1} \end{bmatrix} , \quad (7.47)$$

and Schur complement

$$S = M_{11} - M_{12}M_{22}^{-1}M_{21} , \quad (7.48)$$

which is, in turn, partitioned as follows

$$S = \begin{bmatrix} S_{11} & S_{12} \\ S_{21} & S_{22} \end{bmatrix} = \left[ \begin{array}{c|cc} [\alpha^+] & -[\tilde{\sigma}_{\text{DC}}] & 0 \\ \hline \frac{A_1}{2} & \frac{A_1}{\Delta\tau} & D_2[\beta_y^+]^{-1}[\beta_z^+] \\ 0 & \frac{D_1}{\Delta\tau}[\beta_x^+]^{-1}[\beta_y^+][\beta_z^+]^{-1} & A_2[\beta_x^+] \end{array} \right] . \quad (7.49)$$

$$\begin{bmatrix} [\alpha^+] & -[\tilde{\sigma}_{\text{DC}}] & 0 & 0 & 0 & 0 \\ \frac{A_1}{2} & \frac{A_1}{\Delta\tau} & 0 & 0 & D_2 & 0 \\ 0 & 0 & A_2[\beta_x^+] & 0 & 0 & D_1 \\ 0 & -\frac{I}{\Delta\tau} & 0 & [\beta_z^+] & 0 & 0 \\ 0 & 0 & -[\beta_z^+] & 0 & [\beta_y^+] & 0 \\ 0 & 0 & 0 & -[\beta_y^+] & 0 & [\beta_x^+] \end{bmatrix} \begin{bmatrix} j_y \\ \ddot{e}_y \\ \dot{h}_z \\ \dot{e}_y \\ h_z \\ \tilde{e}_y \end{bmatrix}_{j+\frac{1}{2},k}^{n+\frac{1}{2}} = \begin{bmatrix} [\alpha^-] & [\tilde{\sigma}_{\text{DC}}] & 0 & 0 & 0 & 0 \\ -\frac{A_1}{2} & \frac{A_1}{\Delta\tau} & 0 & 0 & -D_2 & 0 \\ 0 & 0 & A_2[\beta_x^-] & 0 & 0 & -D_1 \\ 0 & -\frac{I}{\Delta\tau} & 0 & [\beta_z^-] & 0 & 0 \\ 0 & 0 & -[\beta_z^-] & 0 & [\beta_y^-] & 0 \\ 0 & 0 & 0 & -[\beta_y^-] & 0 & [\beta_x^-] \end{bmatrix} \begin{bmatrix} j_y \\ \ddot{e}_y \\ \dot{h}_z \\ \dot{e}_y \\ h_z \\ \tilde{e}_y \end{bmatrix}_{j+\frac{1}{2},k}^{n-\frac{1}{2}} + \begin{bmatrix} 0 \\ \frac{A_1}{\Delta x}(\mathbf{h}_{x_{j+\frac{1}{2},k+\frac{1}{2}}}^n - \mathbf{h}_{x_{j+\frac{1}{2},k-\frac{1}{2}}}^n) \\ \frac{A_2}{\Delta y}(\tilde{\mathbf{e}}_{x_{j+1,k}}^n - \tilde{\mathbf{e}}_{x_{j,k}}^n) \\ 0 \\ 0 \\ 0 \end{bmatrix} \quad (7.43)$$

$$\begin{bmatrix} [\alpha^+] & -[\tilde{\sigma}_{\text{DC}}] & 0 & 0 & 0 & 0 \\ \frac{A_1}{2} & \frac{A_1}{\Delta\tau} & 0 & 0 & -D_2 & 0 \\ 0 & 0 & A_2[\beta_z^+] & 0 & 0 & -D_1 \\ 0 & -\frac{I}{\Delta\tau} & 0 & [\beta_x^+] & 0 & 0 \\ 0 & 0 & -[\beta_x^+] & 0 & [\beta_z^+] & 0 \\ 0 & 0 & 0 & -[\beta_z^+] & 0 & [\beta_y^+] \end{bmatrix} \begin{bmatrix} j_z \\ \ddot{e}_z \\ \dot{h}_y \\ \dot{e}_z \\ h_y \\ \tilde{e}_z \end{bmatrix}_{j,k+\frac{1}{2}}^{n+\frac{1}{2}} = \begin{bmatrix} [\alpha^-] & [\tilde{\sigma}_{\text{DC}}] & 0 & 0 & 0 & 0 \\ -\frac{A_1}{2} & \frac{A_1}{\Delta\tau} & 0 & 0 & D_2 & 0 \\ 0 & 0 & A_2[\beta_z^-] & 0 & 0 & D_1 \\ 0 & -\frac{I}{\Delta\tau} & 0 & [\beta_x^-] & 0 & 0 \\ 0 & 0 & -[\beta_x^-] & 0 & [\beta_z^-] & 0 \\ 0 & 0 & 0 & -[\beta_z^-] & 0 & [\beta_y^-] \end{bmatrix} \begin{bmatrix} j_z \\ \ddot{e}_z \\ \dot{h}_y \\ \dot{e}_z \\ h_y \\ \tilde{e}_z \end{bmatrix}_{j,k+\frac{1}{2}}^{n-\frac{1}{2}} - \begin{bmatrix} 0 \\ \frac{A_1}{\Delta y}(\mathbf{h}_{x_{j+\frac{1}{2},k+\frac{1}{2}}}^n - \mathbf{h}_{x_{j-\frac{1}{2},k+\frac{1}{2}}}^n) \\ \frac{A_2}{\Delta x}(\tilde{\mathbf{e}}_{x_{j,k+1}}^n - \tilde{\mathbf{e}}_{x_{j,k}}^n) \\ 0 \\ 0 \\ 0 \end{bmatrix} \quad (7.44)$$

Analogously, the inverse of the Schur complement is given by

$$S^{-1} = \begin{bmatrix} S_{11}^{-1} + S_{11}^{-1} S_{12} S_s^{-1} S_{21} S_{11}^{-1} & -S_{11}^{-1} S_{12} S_s^{-1} \\ -S_s^{-1} S_{21} S_{11}^{-1} & S_s^{-1} \end{bmatrix}, \quad (7.50)$$

such that, in the end, solving the large sparse system (7.43) only requires the inversion of the rank- $2n_x$  matrix

$$\begin{aligned} S_s &= S_{22} - S_{21} S_{11}^{-1} S_{12} \\ &= \begin{bmatrix} A_1 \left( \frac{1}{\Delta\tau} + \frac{1}{2} [\alpha^+]^{-1} [\sigma_{DC}] \right) & D_2 [\beta_y^+]^{-1} [\beta_z^+] \\ \frac{D_1}{\Delta\tau} [\beta_x^+]^{-1} [\beta_y^+] [\beta_z^+]^{-1} & A_2 [\beta_x^+] \end{bmatrix}. \end{aligned} \quad (7.51)$$

The reordering matrix

$$[R]_{ij} = \begin{cases} 1 & i = 1, j = n_x \\ 1 & i = 2k, j = k \\ 1 & i = 2k + 1, j = n_x + k \\ 1 & i = 2n_x, j = 2n_x \\ 0 & \text{else} \end{cases} \quad (7.52)$$

$$k = 1, \dots, n_x - 1$$

together with the rank- $2n_x$  primary circulant matrix  $C$ , i.e. the circulant matrix whose first row has second element one and all other elements zero, allows to construct a banded matrix

$$B = C R S_s R^T, \quad (7.53)$$

which has four elements per row arranged in a staircase pattern. For example for  $n_x = 5$ , its sparsity pattern is

$$\begin{bmatrix} \times & \times & \times & & \\ \times & \times & \times & & \\ & \times & \times & \times & \\ \times & \times & \times & \times & \\ & \times & \times & \times & \times \\ & & \times & \times & \times & \times \\ & & \times & \times & \times & \times \\ & & & \times & \times & \times & \times \\ & & & \times & \times & \times & \times \\ & & & & \times & \times & \times & \times \\ & & & & & \times & \times & \times & \times \end{bmatrix}. \quad (7.54)$$

The LU factorization with row and column pivoting of  $B$ , i.e.

$$P B Q = L U, \quad (7.55)$$

is obtained at negligible cost. Once all necessary matrices are precomputed, (7.43) is updated via forward-backward substitutions and some sparse-matrix multiplications. More specifically, the final algorithm to update (7.43) inside the time-stepping loop goes as follows:

1. Compute the vector in the r.h.s. of (7.44) and split it into two parts  $\mathbf{v}_1$  and  $\mathbf{v}_2$  conforming to the partitioning applied in (7.45).
2. Compute  $\mathbf{p} = \mathbf{v}_1 - M_{12}M_{22}^{-1}\mathbf{v}_2$  and split this vector into two parts  $\mathbf{p}_1$  and  $\mathbf{p}_2$  conforming to the partitioning applied in (7.49).

3. Use forward and backward triangular sweeps to compute

$$[\ddot{\mathbf{e}}_y, \dot{\mathbf{h}}_z] = R^T Q U^{-1} L^{-1} P C R (\mathbf{p}_2 - S_{21}S_{11}^{-1}\mathbf{p}_1) \quad .$$

4. Compute  $\mathbf{j}_y = S_{11}^{-1}(\mathbf{p}_1 - S_{12}[\ddot{\mathbf{e}}_y, \dot{\mathbf{h}}_z])$ .

5. Compute  $[\dot{\mathbf{e}}_y, \mathbf{h}_z, \ddot{\mathbf{e}}_y] = M_{22}^{-1}(\mathbf{v}_2 - M_{21}[\mathbf{j}_y, \ddot{\mathbf{e}}_y, \dot{\mathbf{h}}_z])$ .

For clarity, we omitted the transposition superscripts above, because it should be quite clear that all occurring vectors are column vectors. Note that some matrix products can be computed prior to time-stepping. Compared to the conventional HIE-FDTD method [2], the proposed UCHIE-FDTD method requires the inversion of two pentadiagonal matrices of rank  $2n_x$  instead of two tridiagonal matrices of rank  $n_x$ . Hence, the improved accuracy of the UCHIE-FDTD method comes at a slightly higher computational cost.

## 7.5 Numerical stability

### 7.5.1 Complex-frequency analysis for standalone UCHIE

Substituting the discrete plane-wave solution in the update equations related to one vacuum UCHIE cell, yields the numerical dispersion relation

$$s_x^2 \frac{\tan^2\left(\frac{\tilde{k}_x \Delta x}{2}\right)}{\tan^2\left(\frac{\omega \Delta t}{2}\right)} + s_y^2 \frac{\sin^2\left(\frac{\tilde{k}_y \Delta y}{2}\right)}{\sin^2\left(\frac{\omega \Delta t}{2}\right)} + s_z^2 \frac{\sin^2\left(\frac{\tilde{k}_z \Delta z}{2}\right)}{\sin^2\left(\frac{\omega \Delta t}{2}\right)} = 1 \quad (7.56)$$

with the 1-D Courant numbers

$$s_x = \frac{\Delta \tau}{\Delta x} \quad , \quad s_y = \frac{\Delta \tau}{\Delta y} \quad , \quad s_z = \frac{\Delta \tau}{\Delta z} \quad . \quad (7.57)$$

Now, substitute

$$\frac{1}{\tan^2\left(\frac{\omega \Delta t}{2}\right)} = \frac{1}{\sin^2\left(\frac{\omega \Delta t}{2}\right)} - 1 \quad (7.58)$$

into (7.56) and move all  $\omega$ -dependency to one side of the equation. This yields

$$\sin^2\left(\frac{\omega\Delta t}{2}\right) = \frac{s_x^2 \tan^2\left(\frac{\tilde{k}_x \Delta x}{2}\right) + s_y^2 \sin^2\left(\frac{\tilde{k}_y \Delta y}{2}\right) + s_z^2 \sin^2\left(\frac{\tilde{k}_z \Delta z}{2}\right)}{s_x^2 \tan^2\left(\frac{\tilde{k}_x \Delta x}{2}\right) + 1} . \quad (7.59)$$

Hence, the dispersion relation only has real-valued solutions for  $\omega$  if the r.h.s. remains smaller than one. This requirement is clearly guaranteed for

$$s_{yz}^2 = s_y^2 + s_z^2 < 1 , \quad (7.60)$$

which is the Courant condition of the regular Yee grid in the 2-D space perpendicular to the direction of implicitization.

### 7.5.2 Numerical matrix stability analysis for UCHIE subgridding

Complex-frequency analysis is not a sufficient proof for the stability of the 2-D UCHIE subgridding technique. The Yee-FDTD method in the coarse grid and the UCHIE-FDTD method in the fine grid are both stable if the time step obeys the 2-D Courant limit, but yet, nothing is said about the effect of the interfacing between both grids.

As is the case for all linear time-domain methods, it is possible to express the UCHIE subgridding method in terms of one single time-stepping operator. This is a matrix  $A$ , also called the amplification or iteration matrix, that operates on a column vector  $\mathbf{v}^n$  that contains all unknowns at a specific time instant  $t = n\Delta t$ , or better said, after a specific number of iterations (since not all unknowns are discretized at the same point in time). The “future” quantities can then be found calculating

$$\mathbf{v}_{n+1} = A\mathbf{v}_n + \mathbf{s}_n , \quad (7.61)$$

where  $\mathbf{s}_n$  is a column vector representing the sources. This describes a linear system, which is known to be exponentially stable if none of the eigenvalues of  $A$  lie outside the unit circle. Eigenvalues inside the unit circle stem from losses, for example due to the presence of a non-perfect conductor. Eigenvalues with a small phase angle correspond to temporally well-resolved phenomena, i.e. with many  $\Delta t$  per period.

The matrix  $A$  can be extracted from a simulation as follows:

1. Assign the unit vector with only the  $i^{\text{th}}$  element being non-zero to  $\mathbf{v}_n$ .
2. Do the necessary calculations to advance one time step.
3. Store the resulting vector  $\mathbf{v}_{n+1}$  in the  $i^{\text{th}}$  column of  $A$ .
4. Repeat steps 1 to 3, iterating over all  $i$ .

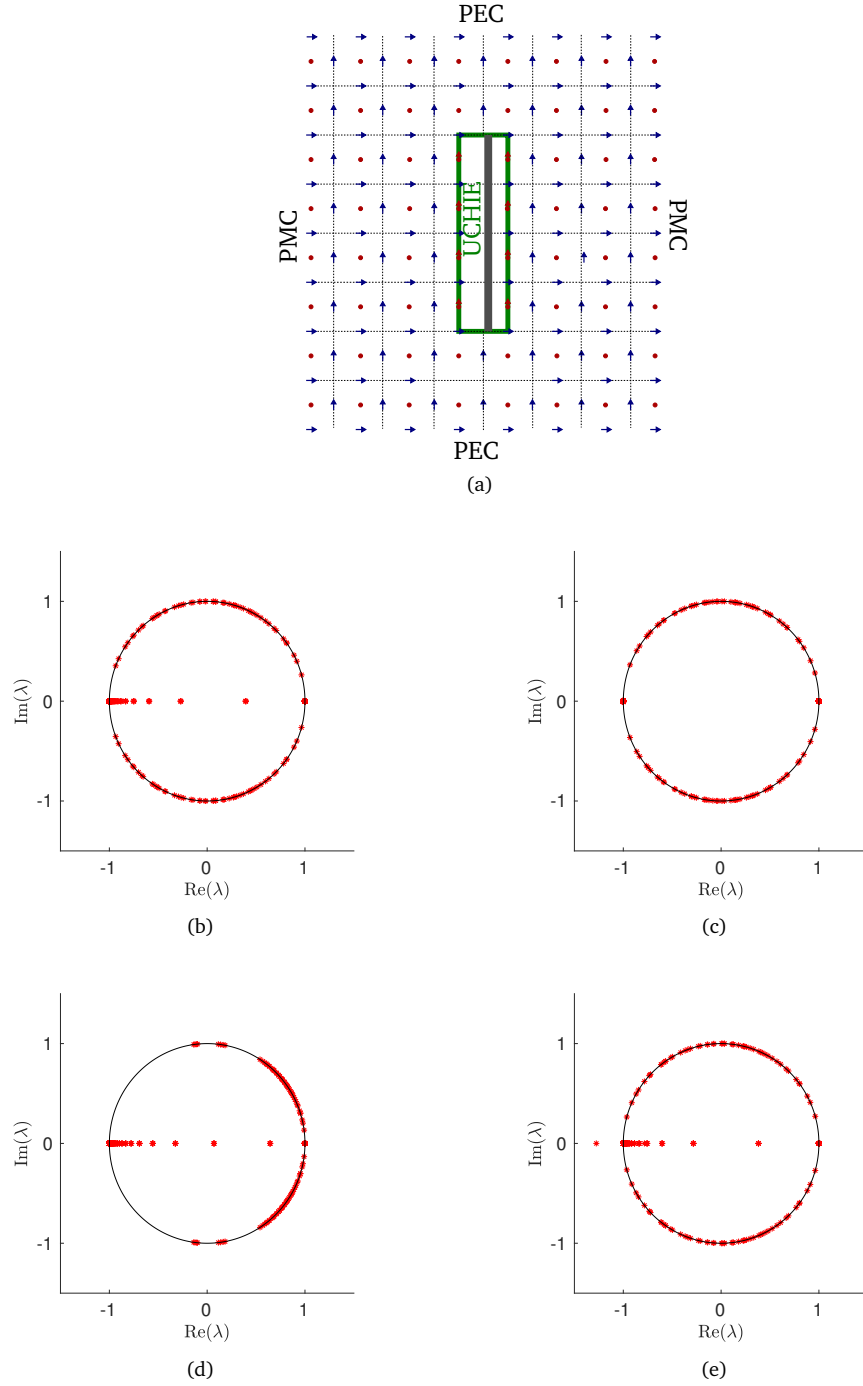


**Figure 7.4:** Eigenvalues  $\lambda$  of the iteration matrix  $A$  for the configuration of (a) with (b)  $s_{xy} = 1$ ; (c)  $s_{xy} = 1$  and vacuum everywhere; (d)  $s_{xy} = 0.5$ ; (e)  $s_{xy} = 1.03$ .

Fig. 7.4(b) shows a plot of the eigenvalues  $\lambda$  of the amplification matrix  $A$  for the test case depicted in Fig. 7.4(a). The overall FDTD grid measures 7 by 8 cells with  $\Delta x = 0.30$  m and  $\Delta y = 0.25$  m. This grid is terminated by PEC and PMC boundaries. The UCHIE grid covers 4 cells in the  $y$ -direction and is positioned centrally in the overall grid. In turn, a thin copper plate ( $\epsilon_r = 1$ ,  $\sigma = 5.8e7$  S/m) of thickness  $10 \mu\text{m}$  is itself positioned slightly towards the right of the center of the UCHIE grid (at a fraction 0.6 of the UCHIE region's width). The discretization step in the  $x$ -direction for this plate is chosen to be  $0.2 \mu\text{m}$  (50 divisions along the plate thickness). It should be emphasized that the aspect ratio of the refinement in the  $x$ -direction exceeds  $10^6$ ! For this example, the matrix  $A$  in (7.61) has rank 859. The time step is chosen such that the 2-D Courant number,

$$s_{xy} = \Delta\tau \sqrt{\frac{1}{\Delta x^2} + \frac{1}{\Delta y^2}} \quad , \quad (7.62)$$

equals one.

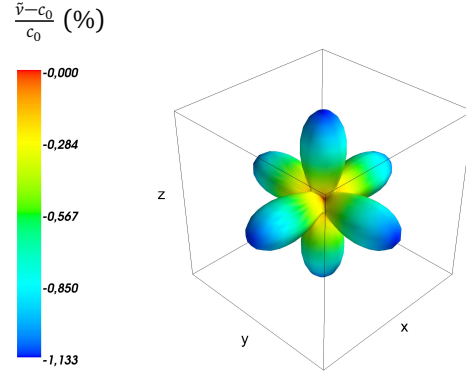
For the other plots, the following modifications were made:  $\sigma = 0$  (vacuum) in Fig. 7.4(c), a smaller Courant number ( $s_{xy} = 0.5$ ) in Fig. 7.4(d) and a larger one ( $s_{xy} = 1.03$ ) in Fig. 7.4(e). For the vacuum simulation, all eigenvalues are on the unit circle. For a smaller Courant number, i.e. for smaller  $\Delta t$ , the eigenvalues shift towards lower phase angles, whereas for a Courant number larger than one the simulation becomes unstable, since some eigenvalues are outside the unit circle.

## 7.6 Numerical dispersion

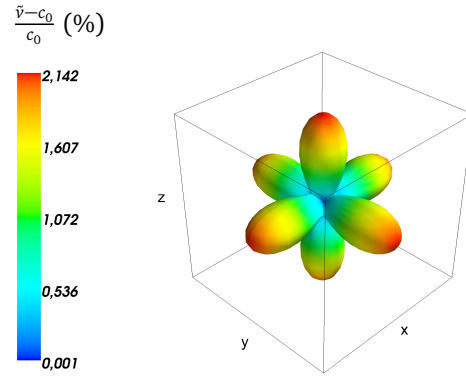
The numerical dispersion relation of the UCHIE-FDTD method in vacuum is given by (7.56). It exhibits tangent functions for the collocated-implicit dimension and sine functions for the staggered-explicit dimensions, conforming to the numerical dispersion relations of the conventional Yee-FDTD method (3.75) and the FCI-FDTD method (6.27). For all three methods, the numerical wavevector  $\tilde{\mathbf{k}}$  is transformed to spherical coordinates and its magnitude is iteratively computed with the Newton-Raphson root-finding routine. The relative phase error, defined as

$$\frac{\tilde{v} - c_0}{c_0} = \frac{k_0}{\tilde{k}} - 1 \quad , \quad (7.63)$$

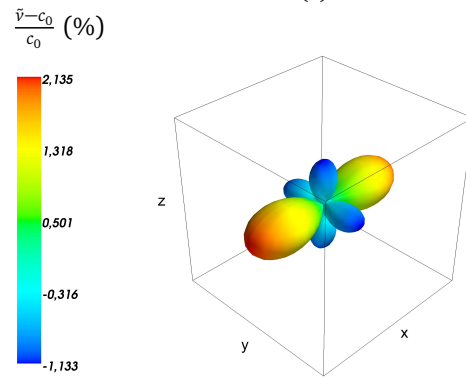
is plotted for different polar and azimuthal angles in Fig. 7.5 and for different sampling densities in Fig. 7.6. The phase error is anisotropic for all three finite-difference methods with the highest errors occurring along the cell edges and the lowest errors along the cell diagonals. In the Yee scheme, the numerical waves propagate slower than the real waves, whereas, in the FCI-FDTD method, they propagate faster with a relative error that is about twice as big. This can be ex-



(a)



(b)



(c)

**Figure 7.5:** Relative phase error for a uniform grid with ten samples per wavelength in each dimension and a time step equal to the Courant limit: **(a)** the conventional Yee scheme, **(b)** the FCI-FDTD method, and **(c)** the UCHIE-FDTD method.

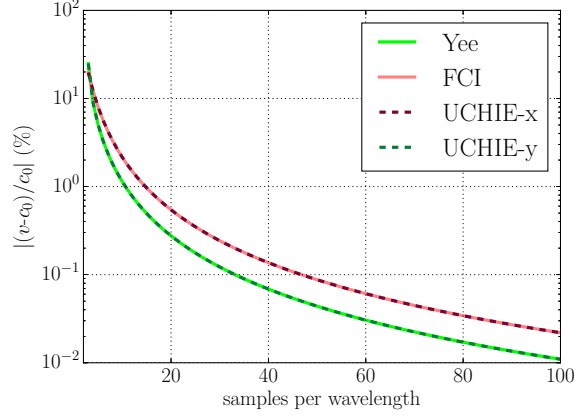


**Figure 7.6:** Absolute value of the relative phase error along the cartesian axes, again for a time step equal to the Courant limit.

plained by investigating the second term in the Taylor expansions

$$\sin(x) = x - \frac{x^3}{6} + \frac{x^5}{120} + \dots \quad (7.64)$$

$$\tan(x) = x + \frac{x^3}{3} + \frac{2x^5}{15} + \dots \quad (7.65)$$

The UCHIE phase error is found to behave identically to the Yee phase error along the staggered-explicit dimensions and identically to the FCI phase error along the collocated-implicit dimension. For all three methods, the numerical phase velocity converges to the speed of light with increasing sampling density.

## 7.7 Numerical examples

### 7.7.1 Spurious PML reflections

To assess the PML performance, a  $10 \times 10 \times 10$ -cell cavity fully covered by PMLs, is excited by an electric source  $j_x(t)$  located in the center of the cavity, and the electric field  $e_x^{\text{pml}}(t)$  is recorded at the exact same position. A uniform discretization  $\Delta x = \Delta y = \Delta z = \Delta = 1 \text{ mm}/\sqrt{\epsilon_r}$  is adopted in combination with the largest stable time step  $\Delta t = 2.36 \text{ ps}$ . The source  $j_x(t)$  is a differentiated Gaussian pulse with bandwidth 50 GHz. Each PML has five layers. The damping parameter (7.29) is polynomially graded to the fourth power up to  $\sigma_{\max} = \sigma_{\text{opt}} = (30\pi\Delta\sqrt{\epsilon_r})^{-1}$ , corresponding to (7.30). Evanescent waves are not further damped by the PMLs, that is,  $\kappa_{\max} = 1$ . A second simulation uses the same set-up but replaces each PML with

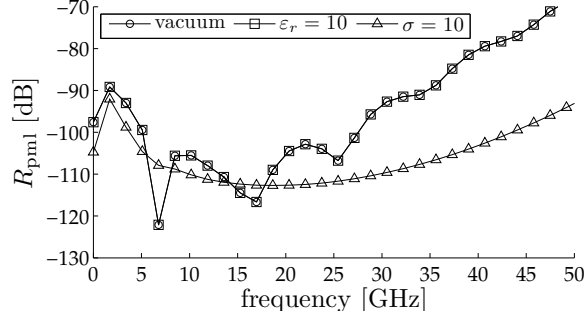


Figure 7.7: PML reflection error for different background media.

90 extra cells terminated by PECs. The recorded field  $E_x^{\text{ref}}(t)$  serves as a reference. Both simulations execute 250 iterations. The two time signals are Fourier transformed and the PML reflection coefficient, defined as

$$R_{\text{pml}}(\omega) = 20 \log_{10} \left| \frac{E_x^{\text{pml}}(\omega) - E_x^{\text{ref}}(\omega)}{E_x^{\text{ref}}(\omega)} \right|, \quad (7.66)$$

is computed and plotted in Fig. 7.7 for three different homogeneous background media. As could be expected according to [14, Eq. 37], the curves for vacuum and dielectric background media coincide. At 30 GHz, the wavelength is resolved by 10 samples. Above this frequency, the PML performance is compromised by numerical dispersion. Overall, the reflection is very low.

### 7.7.2 Spurious subgrid reflections

In analogy to [16], [17], the spurious reflections originating from the interface between the coarse FDTD grid and the UCHIE subgrid are quantified by exciting a vacuum parallel plate waveguide by a TEM pulse which propagates towards a vacuum UCHIE subgrid. The configuration is shown in the inset of Fig. 7.8. The separation between the two plates is 10 mm, the subgrid measures 4 mm in the  $y$ -direction and has a thickness  $\Delta x$  of one coarse FDTD cell. The UCHIE subgrid consists of 50 subdivisions in the  $x$ -dimension with  $\Delta x_f = 0.2 \mu\text{m}$ , completed by two padding areas in order to obtain one  $\Delta x$ . The subgrid reflection coefficient,

$$R_{\text{sg}}(\omega) = 20 \log_{10} \left| \frac{H_z^{\text{sg}}(\omega) - H_z^{\text{ref}}(\omega)}{H_z^{\text{ref}}(\omega)} \right|, \quad (7.67)$$

is plotted in Fig. 7.8 for two different coarse-grid cell sizes:  $\Delta x = \Delta y = 0.5 \text{ mm}$  and  $\Delta x = 2\Delta y = 2 \text{ mm}$ . The field  $H_z^{\text{sg}}(t)$  is recorded in an observation point  $P$  placed five cells in front of the subgrid. An auxiliary simulation without subgrid provides the reference field values  $H_z^{\text{ref}}(t)$ . Fig. 7.8 confirms that UCHIE subgridding can easily compete with other subgridding methods such as the conservative

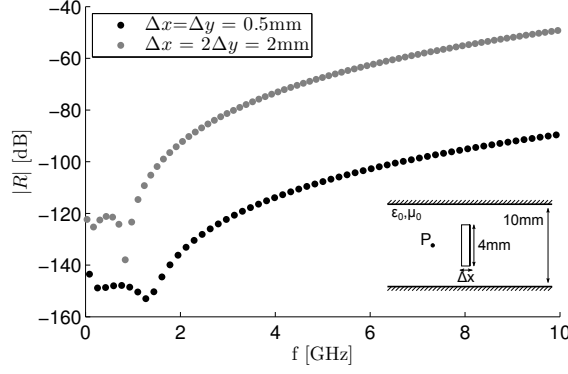


**Figure 7.8:** Quantization of spurious reflections: magnitude of the reflection coefficient of a vacuum UCHIE subgrid in a vacuum parallel plate waveguide excited by its TEM mode. The physical configuration is presented as an inset.

subgridding scheme described in [16]. Indeed, it was stated in [10] that the 1-D hybrid staggered-collocated refinement scheme has no reflections for the magic time step, that is, for the Courant number equal to one. Given the analogous interface condition, this property holds in 2-D as well, but only for normally incident plane waves and for the 1-D magic time step associated to the normal direction, which cannot be picked in 2-D due to instability. Also, only two out of four interfaces have this accurate interface condition. The two remaining interfaces, which exhibit edge termination, have less accurate standard subgridding interpolation rules that cause additional reflections. This explains the very low but non-zero amount of spurious reflections observed in Fig. 7.8. As the frequency increases, the sampling density of the grid relative to the wavelength drops and the discrepancy between the dispersion relations in both grids augments, which unavoidably results in higher reflections. For the same reason, the coarser discretization of the FDTD region results in a higher reflection coefficient.

### 7.7.3 Shielding effectiveness of a thin conductive layer

Consider the 2-D geometry of Fig. 7.9. A conducting slab with thickness  $d$  and height  $h$  resides in free space. A magnetic line source  $g(t)\mathbf{u}_z$  illuminates the slab in the near field. To validate our new UCHIE subgridding method on this 2-D TE problem, simulation results are compared with the analytical results obtained by extending the slab to infinity, i.e.  $h \rightarrow \infty$ . This analytical solution is derived using a well-known frequency-domain approach [18] for layered media by introducing a spatial Fourier transform of Maxwell's equations along the  $y$ -coordinate. This

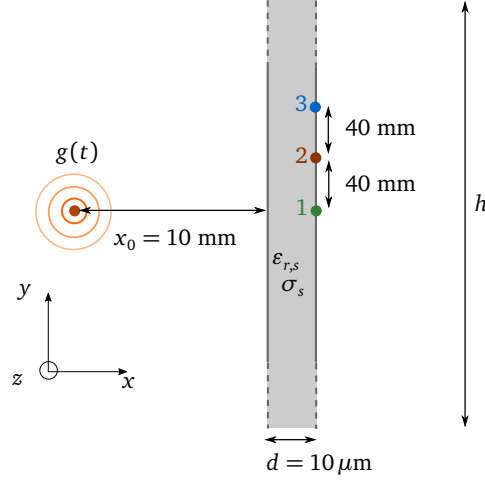


**Figure 7.9:** A magnetic line source (*orange*) is shielded by a thin copper slab (*gray*) in 2-D. The magnetic field is observed at three different locations at the back of the slab (*green, brown, blue*).

yields the transmitted magnetic field at the back of the slab:

$$H_z^t(\omega, y) = \frac{1}{2\pi} \int_{-\infty}^{+\infty} H_z^t(\omega, k_y) e^{jk_y y} dk_y, \quad (7.68)$$

with

$$H_z^t(\omega, k_y) = -\frac{2Z_s e^{-j\Gamma_0 x_0}}{(Z_0 + Z_s)^2 e^{j\Gamma_s d} - (Z_0 - Z_s)^2 e^{-j\Gamma_s d}} g(\omega), \quad (7.69)$$

and  $g(\omega)$  the time-domain Fourier transform of  $g(t)$ . Furthermore, the impedances  $Z_0$  and  $Z_s$  are

$$Z_0 = \frac{\Gamma_0}{\omega \epsilon_0} \quad Z_s = \frac{\Gamma_s}{\omega \epsilon_0 \epsilon_{r,\text{eff}}}, \quad (7.70)$$

whereas the wavenumbers  $\Gamma_0$  and  $\Gamma_s$  are given by

$$\Gamma_0 = \sqrt{k_0^2 - k_y^2} \quad \Gamma_s = \sqrt{k_0^2 \epsilon_{r,\text{eff}} - k_y^2}. \quad (7.71)$$

They depend on the vacuum wavenumber  $k_0$  and the effective relative permittivity of the conductive slab

$$\epsilon_{r,\text{eff}} = \epsilon_{r,s} + \frac{\sigma_s}{j \omega \epsilon_0}. \quad (7.72)$$

Both wavenumbers must have a phase angle in the fourth quadrant in order to ensure that the exponentials in (7.69) are damped. As a consequence, the integrand

of (7.68) is discontinuous at  $k_y$ -values for which  $\Gamma_0$  and/or  $\Gamma_s$  become zero. To resolve this behavior adequately, we use a tanh-sinh quadrature rule [19, Sec. 4.1]. In the case of a vacuum slab, the transmitted magnetic field of the line source is a Hankel function [20, Eq. 11-15b]

$$H_{z0}^t(\omega, y) = -\frac{k_0^2}{4\omega\mu_0} \mathcal{H}_0^{(2)}(k_0 r) g(\omega) , \quad (7.73)$$

with  $r$  the distance between the excitation and the observation point. From the above, we derive the dimensionless shielding effectiveness:

$$SE(\omega, y) = 20 \log_{10} \left| \frac{H_{z0}^t(\omega, y)}{H_z^t(\omega, y)} \right| . \quad (7.74)$$

For the numerical results discussed below,  $SE(\omega, y)$  is first calculated using the new UCHIE subgridding technique. This requires two different runs: one with conductive and one with vacuum slab. At every time step, the value of  $H_z$  is recorded in different observation points located at the back of the slab. The data of both runs are Fourier transformed with respect to  $t$  and then divided by each other. The length  $h$  is chosen large enough as to ensure that the recorded fields are not yet influenced by diffraction at the top and bottom of the slab. This implies that the numerically obtained  $SE(\omega, y)$  values can be compared to the corresponding analytical values for  $h \rightarrow \infty$  obtained by calculating (7.68).

The waveform  $g(t)$  is a differentiated Gaussian pulse with a bandwidth of 7.5 GHz. The overall FDTD grid counts 40 by 1800 divisions with  $\Delta x = \Delta y = 4$  mm. It is terminated by a ten-cell split-field PML along its four exterior boundaries. The UCHIE subgrid is positioned in the center of the overall FDTD grid. It comprises one coarse cell in the  $x$ -direction, but extends along the full  $y$ -dimension from one cell above the lower PML to one cell below the upper PML. The copper slab inside the UCHIE grid has a width  $d = 10$   $\mu\text{m}$  and counts 60 uniform cells along the  $x$ -axis. Hence, the slab is refined by a factor 24 000 in this direction. The UCHIE subgrid exhibits two more segments along the  $x$ -axis as to pad one step  $\Delta x$  in the main grid. The slab's left surface is exactly in the middle of the UCHIE grid such that the source, which is placed two cells to the left of the UCHIE grid, is 10 mm removed from the slab, i.e.  $x_0 = 10$  mm. The time step is the 2-D Courant limit  $\Delta t = 9.4345$  ps and the number of iterations is  $N_t = 2000$ . With these choices, diffraction effects at the upper and lower edges of the slab do not influence the presented data.

Fig. 7.10 shows that the shielding effectiveness of a thin copper slab, i.e.,  $\epsilon_r = 1$  and  $\sigma = 5.8 \cdot 10^7$  S/m, is accurately computed for the frequency range that is covered by the source, even for  $f = 7.5$  GHz corresponding to merely ten samples per wavelength in the main grid. Additionally, the results for an infinitesimally thin conductive layer with impedance network boundary condition (INBC), based on [21], [22], are plotted. The cotangent and cosecant arising in the self-impedance

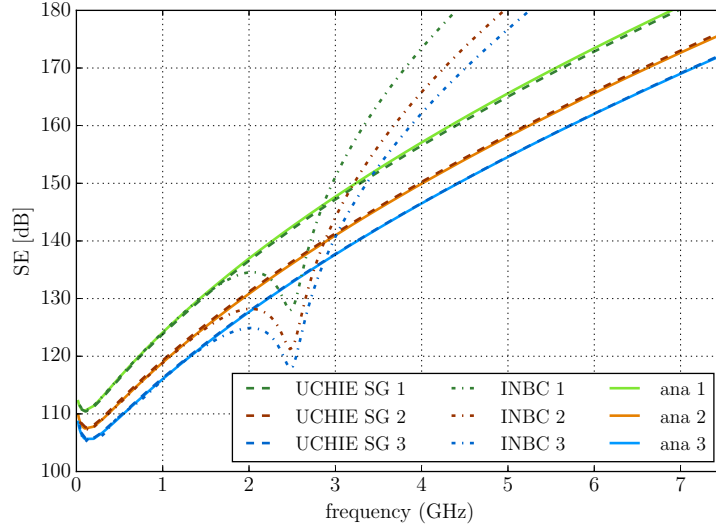


**Figure 7.10:** Shielding effectiveness of a copper slab ( $d = 10 \mu\text{m}$ ,  $\epsilon_r = 1$ ,  $\sigma = 5.8 \cdot 10^7$  S/m) for a near-field magnetic line source at  $x_0 = 10$  mm. The three observation points are indicated in Fig. 7.9.

and mutual impedance of the INBC, respectively, are expanded in their Taylor series, truncated after seven terms, and a partial fraction routine is applied to derive the update coefficients, as is described in [21]. The  $H$ -node shift issue is resolved by the spatially first-order accurate scheme proposed in [22]. In contrast to the INBC approach, the UCHIE subgridding method is not restricted to good and homogeneous conductors ( $\sigma \gg \omega\epsilon$ ), but can handle any type of material. Also, it does not depend on the fact that a 1-D thin sheet approximation is introduced. As could be expected, the INBC approach is unreliable for the higher frequencies where the thin-layer assumption no longer holds.

Fig. 7.11 shows the SE for exactly the same configuration, except for the fact that the slab is made of highly doped silicon with  $\epsilon_r = 11.7$  and  $\sigma = 10^3$  S/m. Again, the accuracy of the UCHIE subgridding technique is striking.

#### 7.7.4 Skin effect

One of the purposes of the new subgridding method is to accurately model thin good conductor effects. We again turn to the set-up of Fig. 7.9, but now with a finite slab having  $h = 10$  mm. The slab is made of copper and has thickness  $d = 10 \mu\text{m}$ . It is discretized with a  $0.2 \mu\text{m}$  increment in the  $x$ -direction. The FDTD cell dimensions are  $\Delta x = 0.253$  mm and  $\Delta y = 0.250$  mm. The source is again placed at a distance  $x_0 = 10$  mm in front of the copper slab. Fig. 7.12 displays the normalized

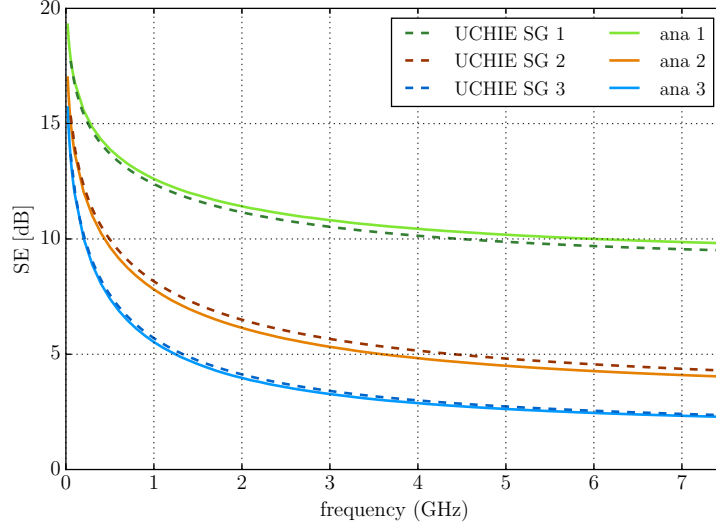


**Figure 7.11:** Shielding effectiveness of a highly doped silicon slab ( $d = 10 \mu\text{m}$ ,  $\epsilon_r = 11.7$ ,  $\sigma = 10^3 \text{ S/m}$ ). The three observation points are indicated in Fig. 7.9.

magnitude of the current density at 2.45 GHz in the normal cross section at the height of observation point 1. At this frequency, the skin depth  $\delta_{\text{skin}}$  is  $1.3351 \mu\text{m}$ . Two exponentials are fitted (in the least-squares sense) to the data points that lie within one skin depth distance from the left and right conductor surface, resulting in the dashed lines in Fig. 7.12. The fitting leads to the following numerical data for the skin depth:  $\delta_{\text{skin}}^{\text{left}} = 1.3353 \mu\text{m}$  and  $\delta_{\text{skin}}^{\text{right}} = 1.3342 \mu\text{m}$ , i.e. a relative error of less than one per thousand.

### 7.7.5 Field solutions compared to MoM

For exactly the same setup as in Section 7.7.4, the magnetic fields along the left and right surface of the copper slab are compared to the output of the noncommercial MoM-solver described in [23]. Fig. 7.13 again confirms the accuracy of the UCHIE subgridding technique.

### 7.7.6 Far-field radiation pattern of a metal grating

The scattering width (SW) of a five-strip metal grating is simulated, where each conductive strip is modeled by a separate UCHIE subgrid. The total-field scattered-field (TFSF) formalism is used in combination with an incident field array look-up table to excite a sinusoidal TM-polarized plane wave with a frequency of 2.45 GHz and an angle of incidence of  $25^\circ$ . The whole simulation space is delimited by a five-layer split-field PML [24]. A conventional near-to-far-field (NTFF) transformation

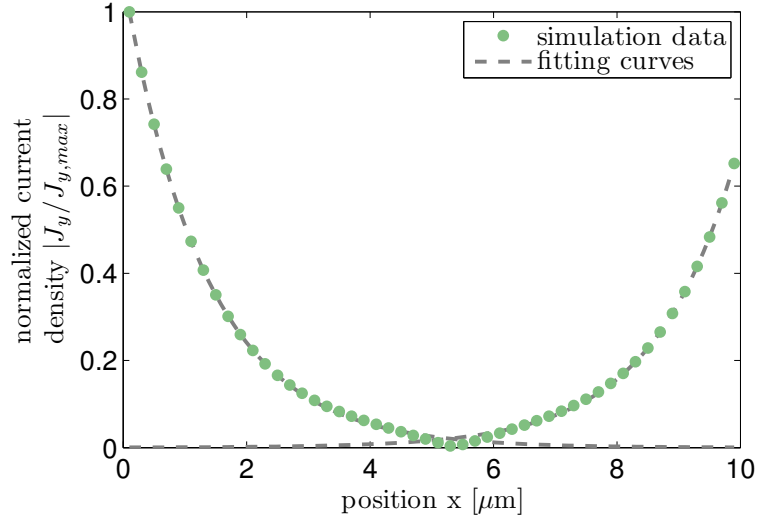


**Figure 7.12:** Current density in the cross section of a thin copper slab ( $d = 10\ \mu\text{m}$ ,  $h = 10\ \text{mm}$ ,  $\sigma = 5.8 \cdot 10^7\ \text{S/m}$ ) at  $f = 2.45\ \text{GHz}$ .

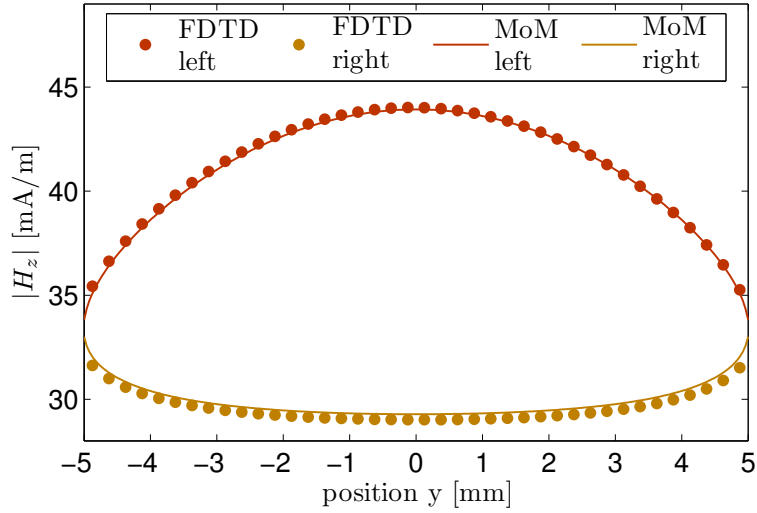


**Figure 7.13:** Field solutions on the slab's left and right surfaces compared to the MoM solution.

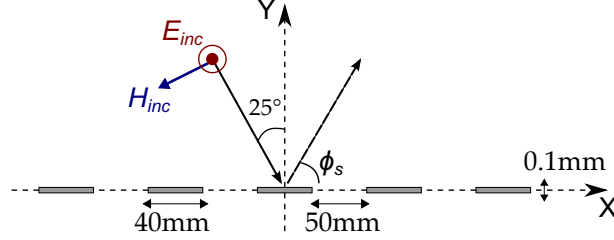


Figure 7.14: A plane TM-wave is incident on a five-strip metal grating.

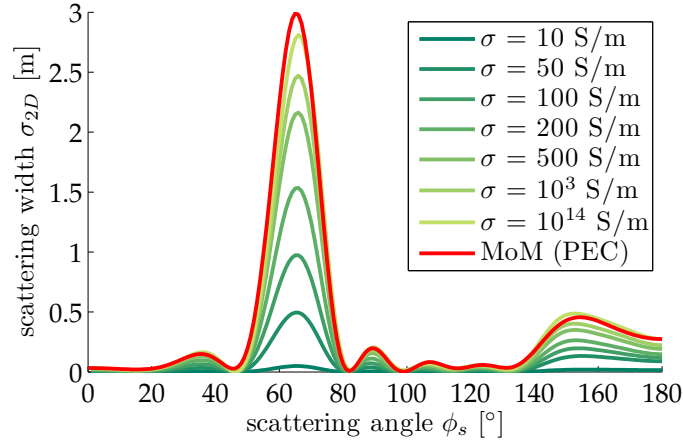


Figure 7.15: Scattering width for several conductivities of the strips.

is used to project the scattered fields from a near-field rectangle in the SF region to a far-field observation circle [25, Sec. 8.3.2]. The configuration of the grating is depicted in Fig. 7.14: the strips measure 0.1 mm by 40 mm and extend infinitely in the  $z$ -direction. They are separated by a 50 mm gap. The Yee grid employs a uniform step size  $\Delta x = \Delta y = 2.5$  mm and runs at the Courant limit  $\Delta t = 5.9$  ps. The strips contain 50 UCHIE cells in their smallest dimension in order to capture the skin effect properly. This corresponds to a refinement factor of 1250. The SW, which is defined as

$$\sigma_{2D} = \lim_{\rho \rightarrow \infty} 2\pi\rho \left| \frac{E_z(\rho)}{E_{inc}} \right|^2, \quad (7.75)$$

is plotted in Fig. 7.15 for several values of the conductivity  $\sigma$  inside the strips. The lion's share of the radiation is reflected in the specular direction  $\phi_s = 65^\circ$ . The array factor reveals the presence of additional lobes at  $\phi_s = \arccos(\sin(25^\circ) + m\frac{\lambda}{a})$ , where  $m$  is an integer,  $\lambda$  the wavelength of the incident wave, and  $a$  the period of the grating, here 90 mm. This shows that more radiation is expected at  $\phi_s = 159.55^\circ$ , as is confirmed by Fig. 7.15. The red curve is produced by the non-commercial MoM solver [23], which approximates the strips by PEC, i.e.  $\sigma = \infty$ .

### 7.7.7 Shielding effectiveness of a graphene sheet

Graphene, a carbon monolayer with honeycomb pattern, is a promising material to manufacture high-speed transistors and other switching devices thanks to its thinness, its mechanical strength and its extraordinarily high electron mobility. Consequently, it has attracted lots of research interests, also with regard to the development of CEM tools. At microwave and THz frequencies, the conductivity of graphene is mainly attributed to intraband electron transitions. In that case, the graphene sheet is typically characterized by a Drude model with effective relative permittivity

$$\varepsilon_{r_g}(\omega) = 1 + \frac{\sigma_g / j \omega \varepsilon_0}{1 + j \omega / 2\Gamma_{\text{scat}}} , \quad (7.76)$$

where the volumetric DC conductivity of graphene is (see e.g. [26])

$$\sigma_g = \frac{q^2 k_B T}{\pi \hbar^2 \Gamma_{\text{scat}} d} \ln \left( 2 \cosh \left( \frac{\mu_c}{2k_B T} \right) \right) , \quad (7.77)$$

with  $q$  the electron charge,  $\hbar$  the reduced Planck constant,  $k_B$  the Boltzmann constant,  $T$  the temperature,  $\Gamma_{\text{scat}}$  the scattering rate,  $\mu_c$  the chemical potential, and  $d$  the sheet thickness. Note that (7.76) corresponds to (7.10) with  $\gamma = 1/(2\Gamma_{\text{scat}})$ .

The graphene sheet under investigation has  $d = 1$  nm,  $T = 300$  K,  $\mu_c = 0.05$  eV, and  $\Gamma_{\text{scat}} = 0.5$  THz. Hence, according to (7.77), the sheet has a DC conductivity  $\sigma_g = 6.7$  S/ $\mu\text{m}$ . In order to validate the stability and accuracy of the dispersive 3-D UCHIE-FDTD method with UPML, the shielding effectiveness is determined for normal plane-wave incidence on an infinite graphene sheet. Thereto, a similar configuration as the one in [7], [8] is adopted and depicted in Fig. 7.16. A plane wave is generated by a TFSF surface placed at one side of the graphene sheet, whereas the transmitted field  $E_{z_g}(t)$  is recorded in one point at the other side of the sheet. The source is a differentiated Gaussian pulse with bandwidth  $b = 0.55$  THz, temporal width  $t_w = 2/\pi b$  and delay  $t_d = 6 t_w$ . The spatial invariance in the  $y$ - and  $z$ -dimension is fulfilled by imposing periodic boundary conditions (PBCs). Both the transmitted and the back-scattered plane waves are absorbed by UPMLs with  $\kappa_x^{\text{max}} = 1$ . The overall grid is uniformly discretized with steps  $\Delta x = \Delta y = \Delta z \approx 27 \mu\text{m}$ , whereas the graphene sheet is locally resolved by two small cells of size  $d$  along the  $x$ -axis as depicted in Fig. 7.17. The time step equals the Courant limit in the  $yz$ -plane, more specifically

$$\Delta\tau = \frac{1}{\sqrt{\frac{1}{\Delta y^2} + \frac{1}{\Delta z^2}}} \approx 19 \mu\text{m} , \quad (7.78)$$

which is about 19 000 times larger than the time step that would have to be used by the classical FDTD method. The recorder is placed  $136 \mu\text{m}$  beyond the graphene sheet. The simulation performs 10 000 iterations. An auxiliary simulation uses the same configuration, but replaces the graphene sheet by a vacuum layer as to record

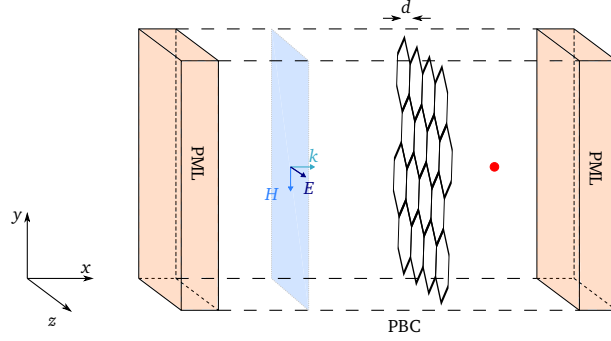


**Figure 7.16:** The TFSF plane (blue) excites a plane wave with non-zero components  $H_y$  and  $E_z$  which normally impinges upon a thin graphene sheet (hexagons) of thickness  $d = 1$  nm. The electric field  $E_z$  is recorded a few cells behind the graphene sheet (red). Infiniteness in the  $y$ - and  $z$ -dimension is mimicked by PBCs along four of the exterior faces. The remaining two faces are covered by PMLs to absorb outgoing waves in the  $x$ -dimension.

the reference field  $E_{z_0}(t)$ . The time-domain data are then Fourier transformed and their ratio determines the shielding effectiveness

$$SE_{\text{num}}(\omega) = 20 \log_{10} \left| \frac{E_{z_0}(\omega)}{E_{z_g}(\omega)} \right|. \quad (7.79)$$

The analytical solution for the SE is known to be

$$SE_{\text{ana}}(\omega) = 20 \log_{10} \left| \frac{1 - R_f^2 e^{-jk_g 2d}}{1 - R_f^2} e^{jk_g d} \right|, \quad (7.80)$$

with  $R_f$  the Fresnel reflection coefficient of a single vacuum-graphene interface

$$R_f = \frac{1 - \sqrt{\epsilon_{r_g}}}{1 + \sqrt{\epsilon_{r_g}}}, \quad (7.81)$$

and wavenumber

$$k_g = \frac{\omega}{c_0} \sqrt{\epsilon_{r_g}}. \quad (7.82)$$

The resulting SEs are plotted in Fig. 7.18. Despite the enormous refinement ratio of 27 000, the analytical and numerical curves are indistinguishable, confirming the accuracy of the UCHIE-FDTD method. The shielding is mainly ascribed to reflections from the two interfaces rather than to the skin effect. At 0.5 THz, the skin depth, hereby meaning the thickness that the graphene sheet should have to reduce the amplitude of a plane wave by 63%, is 360 nm and this value increases towards DC.

A similar simulation is repeated but this time a dipole of length  $\Delta z$  is excited at a distance  $d_s = 409 \mu\text{m}$  from the left side of the graphene sheet. All six exterior

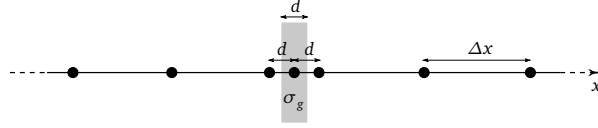


**Figure 7.17:** Discretization along the  $x$ -axis. The vacuum part of the grid is uniformly discretized with step  $\Delta x \approx 27 \mu\text{m}$ . The graphene sheet is approximated by two small UCHIE cells of size  $d = 1 \text{ nm}$ . The graphene conductivity  $\sigma_g = 6.7 \text{ S}/\mu\text{m}$  is solely assigned to the single discretization point enclosed by these two small cells and does not need to be averaged as is the case for the conventional Yee grid.

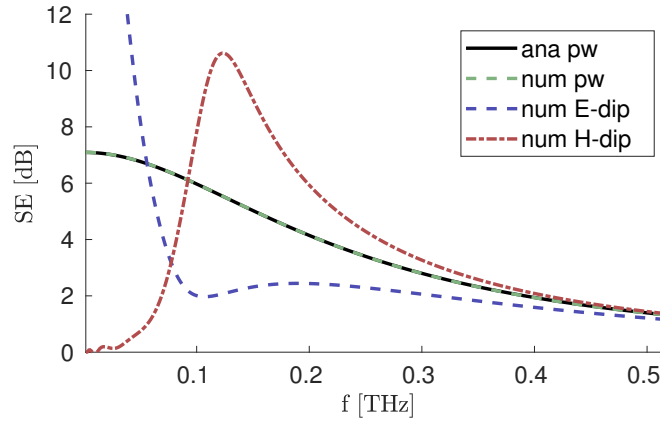


**Figure 7.18:** Shielding effectiveness of the 1 nm graphene sheet illuminated by a normally incident plane wave, an  $E$ -dipole and an  $H$ -dipole. The analytical plane-wave solution is plotted as well.

faces of the grid are covered by UPMLs, this time with  $\kappa_x^{\max} = \kappa_y^{\max} = \kappa_z^{\max} = 10$  in order to absorb the evanescent waves radiated by the dipole source as well as the evanescent waves inside the graphene sheet. Indeed, the graphene sheet extends inside the PMLs in order to exclude reflections from its outer edges, such that we are again modeling an infinite graphene sheet. For the  $E$ -dipole, the SE is again determined by recording  $E_z$  and taking the ratio defined in (7.79), whereas, for the  $H$ -dipole, the dual definition of the SE is adopted where  $E_z$  is replaced by  $H_z$ . The resulting SEs for both the  $E$ - and the  $H$ -dipole are shown in Fig. 7.18. Below 0.12 THz, which corresponds to  $k_0 d_s < 1$ , the graphene sheet experiences the reactive near field of the dipole. For this frequency range, the wave impedances of the  $E$ - and  $H$ -dipole are approximately  $Z_E = Z_0/k_0 d_s > Z_0$  and  $Z_H = Z_0 k_0 d_s < Z_0$  respectively. The graphene sheet behaves like a classical good conductor at low frequencies. As such, it has a very low wave impedance. Consequently, the  $E$ -dipole experiences a higher contrast resulting in more reflections, whereas the  $H$ -dipole does the opposite. This is exactly what we observe in Fig. 7.18: At low frequen-

cies, the  $E$ -dipole is better shielded by the graphene sheet due to strong reflections, whereas the  $H$ -dipole does not even notice the graphene sheet because their wave impedances have the same order of magnitude. At higher frequencies, both dipoles are electrically further removed from the graphene sheet and, consequently, they resemble a plane wave as demonstrated by the convergence of the three curves in Fig. 7.18.

### 7.7.8 Characteristic impedance of a 3-D microstrip line

Finally, the new UCHIE-FDTD method is used to simulate the  $y$ -invariant microstrip line depicted in Fig. 7.19. The line is excited by a hard field source approximating a quasi-TEM pulse with Gaussian time signature at one end, and disappears 10 mm further inside a UPML at the other end. This UPML's damping parameter  $\sigma_y$  is rescaled by the square root of the effective relative permittivity of the microstrip line to yield better impedance matching. The remaining four exterior boundaries of the simulation space are terminated with standard vacuum-matched UPMLs. All UPMLs consist of five layers with  $\kappa_{\max} = 1$  and  $\sigma_{\max} = \sigma_{\text{opt}}$ , defined earlier in (7.30). The microstrip line is surrounded by five vacuum cells in the  $xz$ -plane. The  $x$ -dimension is implicitized with ten divisions inside each of the two conductors to accurately capture the skin effect, and five divisions inside the dielectric to deal with this thin layer. To resolve the fringing fields, an area of three times the strip width is sampled with a step  $\Delta z_1 = 7.5 \mu\text{m}$ . The remainder of the microstrip is sampled with  $\Delta z_2 = 75 \mu\text{m}$ , and the cells outside the microstrip have  $\Delta z_3 = \Delta y = 500 \mu\text{m}$ . The simulation runs for  $10^5$  iterations at 0.99 times the 2-D Courant limit. A total of 108 banded matrices with rank 88 are LU factorized prior to time-stepping, taking less than 0.0006% of the total CPU time. The forward-backward substitutions inside the time-stepping loop only take 22.3% of the CPU time. At present, our Matlab script uses over 1.4 million unknowns, but could be made more efficient by eliminating the auxiliary unknowns in the non-PML region. Assuming quasi-static conditions, the voltage between the conductors and the current inside the strip are computed at the end of the line using the usual line integral over the electric fields and contour integral over the magnetic fields respectively. They are Fourier transformed after which their ratio yields the characteristic impedance  $Z_c$ . The phase difference between two voltages shifted by one step  $\Delta y$  is used to determine the wavenumber  $k = \beta - j\alpha$ . All relevant quantities are plotted in Fig. 7.20, and are compared to the numerical solution of an in-house solver leveraging the Dirichlet-to-Neumann (DtN) operator [27]. The high degree of resemblance between the UCHIE and the DtN solution shows that all details, including the thin layer and skin effect, are correctly predicted.

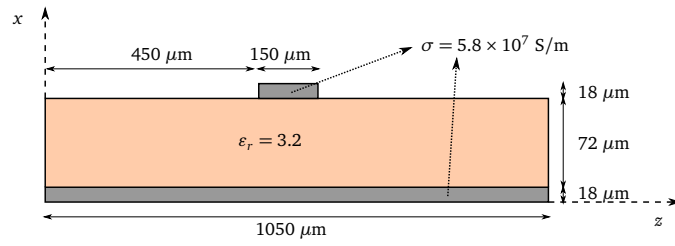
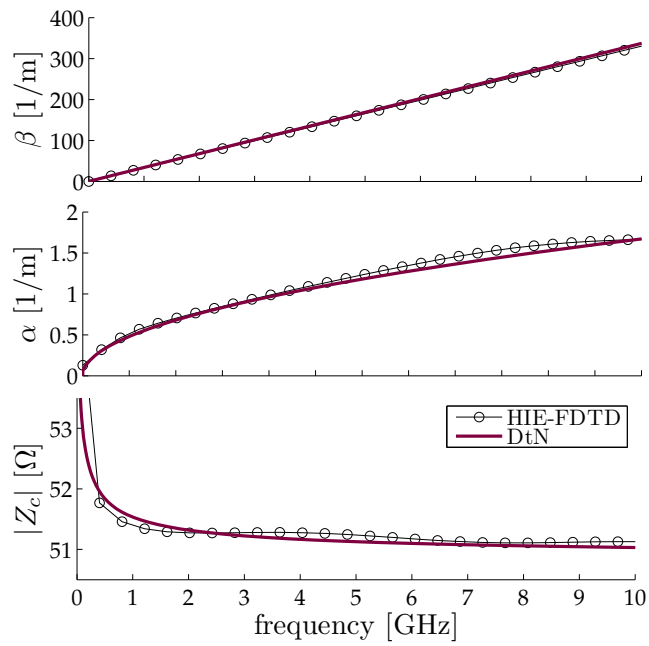


Figure 7.19: Microstrip cross section.

Figure 7.20: Propagation constant  $\beta$ , attenuation constant  $\alpha$  and magnitude of the characteristic impedance  $Z_c$  of the microstrip depicted in Fig. 7.19.



## References

- [1] B. Huang, G. Wang, Y. Jiang, and W. Wang, "A hybrid implicit-explicit FDTD scheme with weakly conditional stability", *Microwave and optical technology letters*, vol. 39, no. 2, pp. 97–101, 2003.
- [2] J. Chen and J. Wang, "A 3D hybrid implicit-explicit FDTD scheme with weakly conditional stability", *Microwave and Optical Technology Letters*, vol. 48, no. 11, pp. 2291–2294, 2006.
- [3] —, "A three-dimensional semi-implicit FDTD scheme for calculation of shielding effectiveness of enclosure with thin slots", *IEEE Transactions on Electromagnetic Compatibility*, vol. 49, no. 2, pp. 354–360, 2007.
- [4] J. Chen and J. Wang, "Improved hybrid implicit-explicit finite-difference time-domain method with higher accuracy and user-defined stability condition", *International Journal of Electronics and Communications*, vol. 65, no. 3, pp. 265–267, 2011.
- [5] Q. Zhang, B. Zhou, and J. Wang, "A Novel Hybrid Implicit-Explicit FDTD Algorithm with More Relaxed Stability Condition", *IEEE Antennas and Wireless Propagation Letters*, vol. 12, pp. 1372–1375, 2013.
- [6] J. Wang, B. Zhou, L. Shi, C. Gao, and B. Chen, "A novel 3-D HIE-FDTD method with one-step leapfrog scheme", *IEEE Transactions on Microwave Theory and Techniques*, vol. 62, no. 6, pp. 1275–1283, 2014.
- [7] M. L. Zhai, H. L. Peng, X. H. Wang, X. Wang, Z. Chen, and W. Y. Yin, "The conformal HIE-FDTD method for simulating tunable graphene-based couplers for THz applications", *IEEE Transactions on Terahertz Science and Technology*, vol. 5, no. 3, pp. 368–376, 2015.
- [8] J. Chen, J. Li, and Q. H. Liu, "Designing graphene-based absorber by using HIE-FDTD method", *IEEE Transactions on Antennas and Propagation*, vol. 65, no. 4, pp. 1896–1902, 2017.
- [9] W. Tierens and D. De Zutter, "An unconditionally stable time-domain discretization on cartesian meshes for the simulation of nonuniform magnetized cold plasma", *Journal of Computational Physics*, vol. 231, pp. 5144–5156, 2012.
- [10] W. Tierens and D. D. Zutter, "Implicit local refinement for evanescent layers combined with classical FDTD", *IEEE Microwave and Wireless Components Letters*, vol. 23, no. 5, pp. 225–227, 2013.
- [11] A. Van Londersele, D. De Zutter, and D. Vande Ginste, "HIE-subgridding for TM scattering problems", in *2016 IEEE International Symposium on Antennas and Propagation (APSURSI)*, Fajardo, Puerto Rico, 26 June - 1 July 2016, pp. 2029–2030.

- [12] W. Tierens, “Finite Element and Finite Difference Based Approaches for the Time-Domain Simulation of Plasma-Wave Interactions”, PhD thesis, Ghent University, 2013.
- [13] S. Taflovie and S. C. Hagness, *Computational Electrodynamics: The Finite-Difference Time-Domain Method (Third Edition)*. Artech House, 2005.
- [14] S. D. Gedney, “An anisotropic perfectly matched layer-absorbing medium for the truncation of FDTD lattices”, *IEEE Transactions on Antennas and Propagation*, vol. 44, no. 12, pp. 1630–1639, 1996.
- [15] D. Bernstein, *Matrix Mathematics (2nd edition)*. Princeton University Press, 2009.
- [16] R. A. Chilton and R. Lee, “Conservative and provably stable FDTD subgridding”, *IEEE Transactions on Antennas and Propagation*, vol. 55, no. 9, pp. 2537–2549, 2007.
- [17] R. Chilton, “H-, P- and T-refinement strategies for the Finite-Difference-Time-Domain (FDTD) method developed via Finite-Element (FE) principles”, PhD thesis, Ohio State University, 2008.
- [18] N. Faché and D. De Zutter, “Full-wave analysis of a perfectly conducting wire transmission line in a double-layered conductor-backed medium”, *IEEE Transactions on Microwave Theory and Techniques*, vol. 37, no. 3, pp. 512–518, 1989.
- [19] D. Bailey, J. Borwein, N. Calkin, R. Girgensohn, R. Luke, and V. Moll, *Experimental Mathematics In Action*. A. K. Peters, 2006.
- [20] A. Balanis, *Advanced Engineering Electromagnetics (2nd edition)*. Wiley, 2012.
- [21] S. V. den Berghe, F. Olyslager, and D. D. Zutter, “Accurate modeling of thin conducting layers in FDTD”, *IEEE Microwave and Guided Wave Letters*, vol. 8, no. 2, pp. 75–77, 1998.
- [22] V. Nayyeri, M. Soleimani, and O. Ramahi, “A method to model thin conductive layers in the finite-difference time-domain method”, *IEEE Transactions on Electromagnetic Compatibility*, vol. 56, no. 2, pp. 385–392, 2014.
- [23] D. Dobbelaere, H. Rogier, and D. De Zutter, “Accurate 2.5-D boundary element method for conductive media”, *Radio Science*, vol. 49, no. 6, pp. 389–399, 2014.
- [24] J.-P. Bérenger, “A perfectly matched layer for the absorption of electromagnetic waves”, *Journal of Computational Physics*, vol. 114, no. 2, pp. 185 – 200, 1994.
- [25] S. D. Gedney, *Introduction to the Finite-Difference Time-Domain (FDTD) Method for Electromagnetics*. Morgan & Claypool publishers, 2011.
- [26] D. L. Sounas and C. Caloz, “Gyrotropy and nonreciprocity of graphene for microwave applications”, *IEEE Transactions on Microwave Theory and Techniques*, vol. 60, no. 4, pp. 901–914, 2012.

- 
- [27] T. Demeester and D. De Zutter, “Construction of the Dirichlet to Neumann boundary operator for triangles and applications in the analysis of polygonal conductors”, *IEEE Transactions on Microwave Theory and Techniques*, vol. 58, no. 1, pp. 116–127, 2010.



PART III

Conclusion



# 8

## Conclusion

*“Our work is never over.”*  
Daft Punk

### 8.1 Comparative overview

Throughout this doctoral research, several hybrid implicit-explicit and collocated-staggered techniques were proposed to improve the FDTD method’s performance with regard to electromagnetic problems encompassing disparate geometric scales. They are listed in Table 8.1, where they are compared to each other in terms of

1. *Provable stability*: Is it possible to analytically prove that the method is stable, albeit under certain constraints such as a time step limit?
2. *Accuracy*: Does the numerical solution converge to the real solution within several tenths of percents for a reasonably small number (e.g. 20 to 30) of samples per wavelength?
3. *Anisotropy*: Does the method allow a natural discretization of complicated constitutive relations such as those pertaining to anisotropic media?
4.  *$n$ -D refinement*: Is it recommended to use the method for refinement in more than one dimension?
5. *Time efficiency*: Does the method yield significant time savings compared to the conventional FDTD method in the case of multiscale problems?
6. *Memory efficiency*: Does the method yield significant memory savings compared to the conventional FDTD method in the case of multiscale problems?

	chapter	provably stable	accurate	anisotropy	$n$ -D refinement	time efficient	memory efficient	parallelizable	scalable	compatible
FCI	6	✓	✓	✓						
UCHIE	7	✓	✓			✓		✓		
$N\beta$ HIE	4	✓	✓			✓		✓	✓	
CNHIE	4	✓	✓			✓	✓	✓	✓	✓
ADHIE	4	✓	✓		✓	✓	✓	✓	✓	✓
<hr/>										
2-D UCHIE-SG	7		✓			✓		✓		
2-D FCI-HSG	6		✓	✓						
3-D FIT-SG	5	✓	✓			✓	✓	✓	✓	✓

**Table 8.1:** Comparative overview of the proposed multiscale techniques. The methods above the dashed line are mainly meant for nonuniform gridding, whereas the ones below the dashed line are subgridding methods.

7. *Parallelizability*: Is it possible to divide the computations needed to advance one time step into a number of parallel processes that scales with the number of unknowns?
8. *Scalability*: Is the linear time complexity of the conventional FDTD method preserved?
9. *Compatibility*: Is the method easily added to existing FDTD software based on Yee's scheme?

This is definitely not a rigorous exposition. The story is not always “black or white” as is the case with the presence or absence of a check mark in Table 8.1. For example,

- The  $N\beta$ HIE and CNHIE methods are both scalable as long as their use is restricted to one-dimensional refinement.
- The UCHIE method is not scalable if the currently implemented standard LU factorization is adopted to solve the pentadiagonal stencils, but less common algorithms that resemble the well-known Thomas algorithm for tridiagonal matrices, featuring linear time complexity exist as well [1].
- The  $N\beta$ HIE method could have check marks in the memory efficiency and compatibility columns too, but these marks are left out because the CNHIE method scores better for these properties. In fact, due to the three-level instead of two-level update scheme and due to the wave impedance error as

a consequence of the asymmetrical time integration of the curls, the  $N\beta$ HIE method is always inferior to the CNHIE method in terms of accuracy, efficiency and compatibility.

- The Yee-cell based methods rely on second-order supraconvergence, which only occurs if a sufficiently small maximum grading ratio is imposed to the sizes of adjacent cells. The FCI and UCHIE methods, on the other hand, feature unconditional second-order accuracy, such that they typically require a much smaller number of cells to resolve the same multiscale problem with the same level of accuracy. However, their update equations are less sparse than the Yee-cell based ones, such that the memory efficiency comparison between staggered and collocated schemes is, in fact, dependent on the problem at hand.
- The FIT-SG method is fully explicit but does not allow to tune the time step as is the case with all other presented techniques, which makes it difficult to compare them to each other.

From Table 8.1, it is clear that the ADHIE-FDTD method is by far the best solution to speed up FDTD simulations that encompass multiscale geometries. The FIT subgridding method is also very promising, in particular if it could benefit from a local time-stepping scheme for even better accuracy and efficiency.

It has to be emphasized that some of the numerical examples presented in this work are infeasible to reproduce with the conventional FDTD method on a standard computer due to memory shortage and/or an excessive number of iterations.

## 8.2 Overall conclusion

In this doctoral thesis, several approaches are proposed to improve the efficiency of the finite-difference time-domain (FDTD) method when it comes to modeling multiscale problems arising in many present-day electronics products. Well-known nonuniform gridding and subgridding techniques composed of traditional Yee cells are extended with locally applied hybrid implicit-explicit time integration (Newmark- $\beta$ , Crank-Nicolson and alternating-direction implicit schemes) as to remove the smallest occurring cell sizes from the Courant stability limit, such that the time dimension is not needlessly oversampled. Much care has been taken to provide rigorous algebraic stability proofs for each of these methods, taking into account the inhomogeneity of the background medium, the nonuniformity of the grid, the boundary conditions, etcetera. Especially the newly developed leapfrog alternating-direction hybrid implicit-explicit (ADHIE) method outshines in terms of computational efficiency as the occurring matrices only scale with the number of cells in one dimension. Since the ADHIE method is applied locally to features that are much smaller than the relevant wavelengths, the splitting error, which is proportional to the field gradient, is low.

Since finite differences are not sufficient to understand the behavior of grid anomalies such as subgridding, which are mostly the cause of many undesired numerical artifacts (e.g. spurious reflections, spurious charges, instability, aliasing), much effort has been put in finite-integration and finite-element analysis throughout this doctoral thesis. Their main asset, apart from being applicable to any type of grid, is that they inherently comply to the differential-geometric principles that underpin Maxwell's equations, such that important physical conservation properties are preserved on the discrete level. A theoretically well-supported subgridding method, based on Whitney brick elements and mass lumping, was found to be closely related to finite integrations, which allowed to extend the method to a very flexible cell-by-cell subgridding scheme for inhomogeneous and anisotropic refinement without buffer zone.

Another part of this doctoral research has been devoted to the hybridization of the classical Yee scheme with the fully-collocated implicit (FCI) FDTD method, which features unconditional stability and unconditional second-order accuracy at the cost of a large sparse matrix inversion. A more efficient unidirectionally-located hybrid implicit-explicit (UCHIE) FDTD method was developed and hybridized with the Yee grid in 2-D. It was found to be a very effective approach to model thin conductive layers. A standalone 3-D version of the UCHIE-FDTD method was found to be excellent in tackling geometries that are highly multiscale in one dimension such as graphene sheets, and does this with a minimal number of variables, owing to the unconditional second-order accuracy and the unambiguous discretization of the material boundaries with the correct tangential-field continuity.

Most work presented in this doctoral thesis focuses on academic examples that have an analytical solution, this to verify the accuracy of the proposed methods. The emphasis of this work is thus on accuracy rather than efficiency, with the underlying premise that the proposed techniques quickly outperform existing techniques for problems that are highly multiscale.

## 8.3 Possible future work

### 8.3.1 FCI-FDTD

The fully-located implicit FDTD method naturally treats anisotropic media without the need for additional interpolations. It should be possible to extend the stability proof provided in [2] to anisotropic and even bianisotropic media. Then, once a good anisotropic solver is at our disposal, transformation optics can be used to transform complex geometries to complex materials. This could, for example, be used to accurately model cylindrical through-silicon vias (TSVs) [3]. Here, the unconditional stability of the FCI-FDTD method plays out very well, because the double coordinate transformation could possibly introduce faster-than-light media, which require a lower time step. At that point, the inefficient matrix solution should be tackled: since the grid is well-structured, it should be possible to con-

struct an efficient iterative solver [4] with proper preconditioner. Another solution could be to expand the Schur complement of the update matrix in a truncated Neumann series [5, Eq. 7.2.45] (possibly accelerated with an Euler or Van Wijngaarden transformation [6, Sec. 5.3.2]) or a truncated Euler series [5, Eq. 7.2.46] that can be computed recursively, which essentially yields a fully explicit method with a time step upper bound. Yet another avenue would be to find some ADI-type solution. However, the occurring interpolators are believed to create overly large splitting errors. At last, the adequate embedding of the FCI-FDTD method in an overall Yee grid can be attempted. Moreover, the finite-element insights mentioned in this dissertation are quite new and it is believed that they could lead to a robust grid stitching scheme. One inconvenience, however, could be the well-posedness. Also, the 2-D UCHIE-subgridding method could be extended to 3-D with the help of the new finite-element insights.

### 8.3.2 Cell-by-cell subgridding

If the cell-by-cell subgridding algorithm with arbitrary refinement ratio [7] could be extended with local time-stepping in a provably stable way, this would finally put an end to the FDTD subgridding quest, thanks to its flexibility combined with its strong physical backbone. First of all, however, the scheme should be tested for simple dielectric and lossy media. From a finite-integration point of view, this should work properly. It could be interesting to verify with Gershgorin's circle theorem [8, Fact 4.10.16], if the coarse-grid updates next to the subgrid can become unstable. The cell-by-cell subgridding scheme could be easily extended to other coordinate systems (e.g. cylindrical and/or body-of-revolution systems [9]). Also, an error measure could be defined such that the cell-by-cell subgridding method can be used for adaptive mesh refinement purposes. At last, the hybrid implicit-explicit methods developed in this dissertation go hand in hand with this subgridding algorithm (one acts on space, the other on time, and this in a well-separated manner). Hence, a provably stable implicit subgridding method, for example based on Crank-Nicolson time integration, could be constructed.

### 8.3.3 Graphene

In [10], graphene was examined in the microwave and THz regime. Only the *intraband* electron interactions needed to be considered. At higher frequencies such as the near infrared, however, also the *interband* interactions should be taken into account. The frequency-domain characteristic for this contribution is not a plain Drude model, though, and should thus be tweaked as to be suitable for the FDTD method. As is proposed in [11], this could be achieved with Padé fitting. This same strategy could be repeated for the UCHIE-FDTD method and is expected to yield increased accuracy owing to the collocated grid and second-order accuracy.

The modeling of graphene by an intraband and an interband conductivity is based on the Kubo formula and only holds in the non-ballistic regime. In the ballistic

regime, e.g. for a graphene field-effect transistor (FET), a multiphysics approach is necessary that harmonizes Maxwell's equations and the Dirac equation [12].

## References

- [1] S. Askar and A. Karawia, "On solving pentadiagonal linear systems via transformations", *Mathematical Problems in Engineering (Hindawi)*, vol. 2015, Article ID 232456, 9 pages, 2015.
- [2] W. Tierens, "Finite Element and Finite Difference Based Approaches for the Time-Domain Simulation of Plasma-Wave Interactions", PhD thesis, Ghent University, 2013.
- [3] B. K. Kaushik, V. R. Kumar, M. K. Majumder, and A. Alam, *Through Silicon Vias*. Taylor & Francis Group, 2017.
- [4] H. K. Rouf, "Improvement of computational performance of implicit finite difference time domain method", *Progress In Electromagnetics Research M*, vol. 43, pp. 1–8, 2015.
- [5] G. Dahlquist and A. Bjorck, *Numerical Methods in Scientific Computing*. Society for Industrial and Applied Mathematics (SIAM), 2008.
- [6] W. H. Press, S. A. Teukolsky, W. T. Vetterling, and B. P. Flannery, *Numerical Recipes in C: The Art of Scientific Computing (Third Edition)*. Cambridge University Press, 2007.
- [7] A. Van Londersele, R. Lee, F. L. Teixeira, D. De Zutter, and D. Vande Ginste, "Systematic cell-by-cell FDTD subgridding in 3-D", *IEEE Microwave and Wireless Components Letters*, accepted.
- [8] D. Bernstein, *Matrix Mathematics (2nd edition)*. Princeton University Press, 2009.
- [9] W. Tierens and D. De Zutter, "BOR-FDTD subgridding based on finite element principles", *Journal of Computational Physics*, vol. 230, no. 12, pp. 4519–4535, 2011.
- [10] A. Van Londersele, D. De Zutter, and D. Vande Ginste, "Full-wave analysis of the shielding effectiveness of thin graphene sheets with the 3D unidirectionally collocated HIE-FDTD method", *International Journal of Antennas and Propagation*, vol. 2017, Article ID 5860854, 8 pages, 2017.
- [11] J. Chen, J. Li, and Q. H. Liu, "Designing graphene-based absorber by using HIE-FDTD method", *IEEE Transactions on Antennas and Propagation*, vol. 65, no. 4, pp. 1896–1902, 2017.
- [12] L. Pierantoni, *Multiphysics modeling of the electromagnetic-transport problems in nanodevices: A new challenge in computational engineering*, IEEE Distinguished Microwave Lecturers: <http://tc25.mtt-tcc.org/luca-pierantoni>, Phoenix, United States, 2015.





